COUPLING OF A RADIATION MODEL WITH SYSTEM MODEL OF
BUBBLING FLUIDIZED BED COMBUSTORS

A THESIS SUBMITTED TO
THE GRADUATE SCHOOL OF NATURAL AND APPLIED SCIENCES
OF
MIDDLE EAST TECHNICAL UNIVERSITY

BY

MEHMET SONER YAŞAR

IN PARTIAL FULFILLMENT OF THE REQUIREMENTS
FOR
THE DEGREE OF DOCTOR OF PHILOSOPHY
IN
CHEMICAL ENGINEERING

DECEMBER 2023

Approval of the thesis:

COUPLING OF A RADIATION MODEL WITH SYSTEM MODEL OF BUBBLING FLUIDIZED BED COMBUSTORS

submitted by **MEHMET SONER YAŞAR** in partial fulfillment of the requirements for the degree of **Doctor of Philosophy** in **Chemical Engineering, Middle East Technical University** by,

Prof. Dr. Halil Kalıpçılar
Dean, Graduate School of **Natural and Applied Sciences**　　＿＿＿＿＿＿＿＿＿＿

Prof. Dr. Pınar Çalık
Head of the Department, **Chemical Engineering**　　＿＿＿＿＿＿＿＿＿＿

Prof. Dr. Görkem Külah
Supervisor, **Chemical Engineering, METU**　　＿＿＿＿＿＿＿＿＿＿

Prof. Dr. Nevin Selçuk
Co-Supervisor, **Chemical Engineering, METU**　　＿＿＿＿＿＿＿＿＿＿

Examining Committee Members:

Prof. Dr. Murat Köksal
Mechanical Engineering, Hacettepe University　　＿＿＿＿＿＿＿＿＿＿

Prof. Dr. Görkem Külah
Chemical Engineering, METU　　＿＿＿＿＿＿＿＿＿＿

Prof. Dr. Nimeti Döner
Mechanical Engineering, Gazi University　　＿＿＿＿＿＿＿＿＿＿

Assoc. Prof. Dr. Harun Koku
Chemical Engineering, METU　　＿＿＿＿＿＿＿＿＿＿

Asst. Prof. Dr. Necip Berker Üner
Chemical Engineering, METU　　＿＿＿＿＿＿＿＿＿＿

Date: 25.12.2023

I hereby declare that all information in this document has been obtained and presented in accordance with academic rules and ethical conduct. I also declare that, as required by these rules and conduct, I have fully cited and referenced all material and results that are not original to this work.

Name Last name : Yaşar, Mehmet Soner

Signature :

ABSTRACT

COUPLING OF A RADIATION MODEL WITH SYSTEM MODEL OF BUBBLING FLUIDIZED BED COMBUSTORS

Yaşar, Mehmet Soner
Doctor of Philosophy, Chemical Engineering
Supervisor : Prof. Dr. Görkem Külah
Co-Supervisor: Prof. Dr. Nevin Selçuk

December 2023, 438 pages

Currently, none of the steady-state and transient bubbling fluidized bed combustor models couples the solution of the radiative transfer equation with the solution of conservation equations of other transport processes although thermal radiation is of considerable importance in such systems, as such an objective requires both accurate and computationally efficient methods for not only the solution of radiative transfer but also the estimation of radiative properties of particle-laden combustion gases. Therefore, in this study, 1-D steady-state and transient comprehensive system models for combustion of lignite and co-combustion of lignite and cotton residue with limestone addition is coupled with a 3-D radiation model based on the method of line solution of discrete ordinates method utilizing spectral radiative properties of combustion gases, particles, and walls. Furthermore, a 2-D computational fluid dynamics model for the combustion of lignite only is developed using the commercial software ANSYS Fluent and coupled with both accurate and computationally efficient methods for the estimation of radiative properties of particle-laden combustion gases. Predictive accuracies of all models are validated

against measurements obtained from METU 0.3 MW$_t$ atmospheric bubbling fluidized bed (ABFBC) combustion test rig firing lignite or co-firing lignite with cotton residue and limestone addition.

The outcome of this study provides comprehensive, accurate, and computationally efficient tools for simulation of steady-state and transient bubbling fluidized bed combustors and reveals the significant impact of radiative heat transfer in modeling of industrial boilers. Moreover, this study revealed the importance of the combustion gases, soot particles, fine and coarse fly ash particles and proper treatment of their radiative properties for the radiative heat transfer predictions under the conditions of bubbling fluidized bed combustors firing lignite or co-firing lignite with biomass and limestone addition. Finally, the predictions of the coupled steady state and transient bubbling fluidized bed combustor models indicate that using a sophisticated radiation model provides more accurate temperature predictions for the freeboard of METU 0.3 MW$_t$ ABFBC test rig compared to the bubbling fluidized bed combustor models without coupling.

Keywords: Radiative Heat Transfer, Non-Gray Gas Radiation, Mathematical Modeling, Bubbling Fluidized Bed Combustors, Coal/Biomass Co-Combustion, CFD

ÖZ

KABARCIKLI AKIŞKAN YATAKLI YAKICILARIN SİSTEM MODELİ İLE RADYASYON MODELİNİN BİRLEŞTİRİLMESİ

Yaşar, Mehmet Soner
Doktora, Kimya Mühendisliği
Tez Yöneticisi: Prof. Dr. Görkem Külah
Ortak Tez Yöneticisi: Prof. Dr. Nevin Selçuk

Aralık 2023, 438 sayfa

Dinamik ve yatışkın kabarcıklı akışkan yataklı yakıcı (KAYY) modellerinin hiçbiri, ısıl ışıma bu tür sistemlerde oldukça önemli olmasına rağmen, ışınım transfer denkleminin çözümünü diğer taşıma işlemlerinin korunum denklemlerinin çözümü ile birleştirmez çünkü böyle bir amaç, yalnızca ışınım transfer denkleminin çözümü için değil, aynı zamanda parçacık yüklü yanma gazlarının ışınım özelliklerinin tahmini için hem doğru hem de hesaplama açısından verimli yöntemler gerektirir. Bu nedenle, bu çalışmada, linyitin yanması ve linyitin pamuk küspesi ve kireç taşı ile birlikte yanması için kapsamlı 1 boyutlu dinamik ve yatışkan sistem modelleri, spektral gaz, parçacık ve duvar özelliklerini kullanan belirli yönler yönteminin çizgiler metoduyla çözümüne dayalı bir 3 boyutlu radyasyon modeli ile birleştirilmiştir. Bunlara ek olarak, ANSYS Fluent ticari yazılımı kullanılarak yalnızca linyitin yanması için 2 boyutlu bir hesaplamalı akışkanlar dinamiği modeli geliştirilmiş ve parçacık yüklü yanma gazlarının ışınımsal özelliklerinin tahmini için hem doğru hem de hesaplama açısından verimli yöntemlerle birleştirilmiştir. Modellerin tahmin doğruluğu linyit yakan veya linyiti pamuk küspesi ve kireç taşı

ile birlikte yakan ODTÜ 0,3 MWt atmosferik kabarcıklı akışkan yataklı yanma test düzeneğinden elde edilen ölçümlere karşı doğrulanmıştır.

Bu çalışmanın sonucu, dinamik ve yatışkın KAYY'lerin simülasyonu için kapsamlı, doğru ve hesaplama açısından verimli bir araç sağlar ve endüstriyel kazanların modellenmesinde ışınım ısı transferinin etkisini vurgular. Ayrıca bu çalışma, linyit yakan veya linyiti biyokütle ve kireçtaşı ile birlikte yakan kabarcıklı akışkan yataklı yakıcıların koşulları altında ışınımsal ısı transferi tahminleri için yanma gazlarının, is partiküllerinin, ince ve kaba uçucu kül teneciklerinin ve bunların ışınımsal özelliklerinin uygun şekilde işlenmesinin önemli olduğunu ortaya koymuştur. Son olarak, birleştirilmiş yatışkın ve dinamik kabarcıklı akışkan yataklı yakıcı modellerinin tahminleri, gelişmiş bir radyasyon modeli kullanmanın ODTÜ 0,3 MW_t ABFBC test teçhizatının serbest bölgesinde, birleştirilmemiş kabarcıklı akışkan yataklı yakıcı modellerine göre, daha doğru sıcaklık tahminleri sağladığını göstermektedir.

Anahtar Kelimeler: Işınımsal Isı Transferi, Gri Olmayan Gaz Radyasyonu, Matematiksel Modelleme, Kabarcıklı Akışkan Yataklı Yakıcılar, Kömür/Biyokütle Birlikte Yakma, HAD

To My Mother

ACKNOWLEDGMENTS

TABLE OF CONTENTS

LIST OF TABLES

xviii

xix

LIST OF FIGURES

FIGURES

xxxii

LIST OF ABBREVIATIONS

1D	One-Dimensional
2D	Two-Dimensional
3D	Three-Dimensional
8D	Eight-Dimensional
ABFBC	Atmospheric Bubbling Fluidized Bed Combustor
BFBC	Bubbling Fluidized Bed Combustor
CFBC	Circulating Fluidized Bed Combustor
CFD	Computational Fluid Dynamics
CR	Cotton Residue
DDPM	Dense Dicrete Phase Model
DOM	Discrete Ordinates Method
DPM	Dicrete Phase Model
DSS012	Two-Point Upwind Differencing Scheme
DSS014	Three-Point Upwind Differencing Scheme
FBC	Fluidized Bed Combustor
FC	Fixed Carbon
FDM	Finite Difference Method
FVM	Finite Volume Method
GG	Gray Gas
GNB	Gray Narrow Band Model
GWB	Gray Wide Band Model
HF	Heat Flux
HS	Hazelnur Shell
LBL	Line-by-Line

LHV	Lower Heating Value
MOL	Method of Lines
NSTOP	terminating step in Mie solution
ODE	Ordinary Differential Equation
OR	Olive Residue
PDE	Partial Differential Equation
PSD	Particle Size Distribution
RI	Complex Index of Refraction
RTE	Radiative Transfer Equation
RHT	Radiative Heat Transfer
SLW	Spectral Line-Based Weighted Sum of Gray Gases
SLW-1	One Gas Spectral Line-Based Weighted Sum of Gray Gases
ST	Source Term
VM	Volatile Matter
WSGG	Weighted sum of Gray Gases

LIST OF SYMBOLS

SYMBOLS

a — Decay constant (m^{-1}), gray gas weight; volume fraction

$\tilde{a}$ — Normalized gray gas weight

A — Cross-sectional area (m^2); surface area (m^2); pre-exponential factor of Arrhenius rate expression ($(m^3 \ kmol^{-1})^{1-n}$)

Ar — Archimedes number

B — Particle load ($kg \ m^{-3}$)

c_p — Specific heat capacity ($J \ kg^{-1} \ K^{-1}$)

c — Speed of light in vacuum ($m \ s^{-1}$)

C — Concentration ($mol \ m^{-3}$)

C_{abs} — Absorption cross section ($m^2 \ mol^{-1}$)

$\tilde{C}_{abs}$ — Supplemental absorption cross section ($m^2 \ mol^{-1}$)

C_D — Drag Coefficient

d — Diameter (m)

d_p — Particle diameter (m)

D — Diffusion coefficient ($m^2 \ s^{-1}$)

e — Restitiution coefficient

E — Activation energy ($J \ mol^{-1}$)

E_b — Blackbody emissive power ($W \ m^{-2}$)

E_p — Particle emissive power ($W \ m^{-2}$)

$E(r)$ — Elutriation rate constant (s^{-1})

f — Friction factor; scattering factor

f_v — Volume fraction of soot particles

F — Mass flow rate of solid streams ($kg \ s^{-1}$); Force (N)

F_D — Drag force (N)

F_z Upward flow rate of entrained particles at any height in freeboard (kg s^{-1})

$f(E)$ Activation energy distribution function for devolatilization (mol J^{-1})

g Gravitational acceleration (m s^{-2}); k-distribution function; asymmetry factor

G Incident radiation (W m^{-2})

h Individual heat transfer coefficient (W m^{-2} K^{-1}); Planck's constant; Specific enthalpy (J/kg)

H Height (m)

ΔH^0 Heat of reaction at standard state (J mol^{-1})

I Radiative intensity (W m^{-2} sr^{-1})

I_b Blackbody intensity (W m^{-2} sr^{-1})

k Reaction rate constant; thermal conductivity (W m^{-1}); Boltzmann's constant; absorption index; turbulent kinetic energy (J/kg)

$k(E)$ First order reaction rate constant for devolatilization (s^{-1})

k_f Film mass transfer coefficient (m s^{-1})

k_s First order surface reaction rate constant for char combustion (m s^{-1})

k_t Time constant with dimension (m^{-1} s^{-1})

K_{be} Mass transfer coefficient (m s^{-1})

K_{be} Film mass transfer coefficient (m s^{-1})

K_i^* Total flux of entrained particles in size i (kg m^{-2} s^{-1})

$K_{i,h}^*$ Cluster flux of entrained particles in size i (kg m^{-2} s^{-1})

$K_{i,\infty}^*$ Dispersed non-cluster flux of entrained particles in size i (kg m^{-2} s^{-1})

ℓ Direction cosine

L Length (m); mean beam length (m)

L_e Spectrally dependent mean beam length (m)

L_m Spectrally averaged mean beam length (m)

m Mass flow rate (kg s^{-1}); complex index of refraction

$\dot{m}$ Mass transfer rate (kg s^{-1})

M	Hold-up in the bed (kg)
MW	Molecular or atomic weight (g mol^{-1})
n	Molar flow rate (mol s^{-1}); molar generation/ consumption rate (mol s^{-1}); refractive index
N	Molar density (mol m^{-3})
NB	Number of wide bands for particles
ND	Number of octants
NM	Number of ordinates specified by the order of angular quadrature
NGC	Number of gray gases for CO_2
NGW	Number of gray gases for H_2O
NX, NY, NZ	Number of nodes along x, y and z directions
N_t	Number of discrete sizes in particle size measurement
P	Pressure (Pa)
$P_0(r)$	Size distribution of inlet fuel particles (m^{-1})
$P_{bd}(r)$	Size distribution of bed drain particles (m^{-1})
$P_{bed}(r)$	Size distribution of char particles in the bed (m^{-1})
$P_{CO}(r)$	Size distribution of carry over char particles (m^{-1})
$P_z(r)$	Size distribution of entrained char particles at any height in freeboard (m^{-1})
Pr	Prandtl number
q	Radiative heat flux (W m^{-2})
$\nabla \cdot q$	Radiative source term (W m^{-3})
Q	Volumetrix flow rate (m^3 s^{-1}); energy generation/loss rate (J s^{-1}); Heat transfer rate (J s^{-1})
Q_a	Absorption efficiency
Q_e	Extinction efficiency
Q_s	Scattering efficiency
r	Spatial independent variable (m); rate of reaction (mol m^{-3} s^{-1})
r	Position vector

r_C	Carbon consumption rate on the surface of char particle (mol m^{-2} s^{-1})
R	Ideal gas constant (J mol^{-1} K^{-1}); radius (m)
$\boldsymbol{R}$	Energy generation/loss rate in freeboard (J m^{-3} s^{-1})
$\mathfrak{R}$	Species generation/depletion rate (mol m^{-3} s^{-1})
$\mathfrak{R}(r)$	Shrinkage rate of particles (m s^{-1})
Re	Reynold's number
s	direction of intensity
S	External sorbent surface area (m^2)
Sc	Schmidt number
t	Time (s)
T	Temperature (K)
u	Velocity (m s^{-1})
u_0	Superficial gas velocity (m s^{-1})
u_{mf}	Minimum fluidization velocity (m s^{-1})
U_{ff}	Throughflow velocity (m s^{-1})
U	Overall heat transfer coefficient (W m^{-2} K^{-1})
V	Volume (m^3)
w	Quadrature weight
w_i	Differential weight of particle size i
x	Mass fraction; spatial independent variable (m); size parameter
x_{fc}	Mass fraction of fixed carbon in fuel
x_a	Mass fraction of ash in fuel
x_{vl}	Fraction of volatiles released in the bed
χ_{CO_2}	Mole fraction of CO_2
χ_{H_2O}	Mole fraction of H_2O
y	Mole fraction
Y	Mass fraction of gaseous species
z	Spatial independent variable (m)

GREEK LETTERS

α	Thermal diffusivity (m^2 s^{-1}); absorptivity
β	Extinction coefficient (m^{-1})
δ	Bubble phase volume fraction; Kronecker delta
ε	Voidage; emissivity; turbulent kinetic energy dissipation rate (m^2 s^{-3})
ε_{mf}	Voidage of the bed at minimum fluidization velocity
ϵ	Convergence criterion
η	Contact efficiency; direction cosine
θ	Polar angle (rad)
Θ	Scattering angle (rad); granular temperature (J kg^{-1})
κ	Absorption coefficient (m^{-1})
λ	Latent heat of vaporization at standard state (J kg^{-1}); wavelength (μm)
μ	Viscosity (kg m^{-1} s^{-1}); direction cosine
ξ	Direction cosine
v	Volatile released (%)
v_∞	Ultimate yield of volatile releases, %
ρ	Density (kg m^{-3}); reflectivity
σ	Standard deviation of activation energy distribution (J mol^{-1}); Stephan-Boltzmann constant (W m^{-2} K^{-4}); Fractional sorbent surface area; scattering coefficient (m^{-1})
τ	Residence time; optical thickness; transmissivity; shear stress (N)
φ	Sphericity, azimuthal angle (rad)
Φ	Scattering phase function (sr^{-1})
Ω	Direction vector of radiation intensity
Ω'	Direction vector of incident radiation intensity

SUBSCRIPTS

0	Initial; feed
a	Air; ash
avg	Average
b	Bubble, blackbody
bd	Bed drain
bed	Bed
bio	Biomass originated
bw	Bed wall
c	Carbon dioxide index
C	Carbon
CO	Carry over
coal	Coal originated
cw	Cooling water
ct	Cooling tubes
d	Char
e	Emulsion
elut	Elutriation
ent	Entrainment
ext	External
f	Freeboard; feed fuel; fluidization
fc	Fixed carbon
fw	Freeboard wall
g	Gas
i	Inert; inner
j	Species index, spectral band index
k	Water vapour index in SLW model
l	Carbon dioxide index in SLW model; lignite
ℓ	Index for a discrete direction
ℓ'	Index for a discrete incoming direction

lst	Limestone
λ	Wavelength index
m	Medium; ordinate index
m′	Incoming ordinate
max	Maximum
maxe	Maximum elutriated
min	Minimum
o	Outer
p	Particle
P	Products
r	Radiation
ref	Reference
rxn	Reaction
R	Reactant
s	Surface; solid
T	Tube
t	Turbulent
td	Turbulent dissipation
vm	Virtual mass
w	Wall; water

SUPERSCRIPTS

a	Aggregate
ℓ	Index for a discrete direction
ℓ′	Index for a discrete incoming direction
m	Ordinate index
m′	Incoming ordinate
p	Particle
tr	Modified parameter in transport approximation

CHAPTER 1

INTRODUCTION

Currently, coal is the most abundant fossil fuel in the world, with reserves that are around two to three times greater than those of oil and gas [1]. It is therefore commonly used for energy production, in an attempt to cope with the world's energy demand. There also exist widespread lignite reserves in Turkey; however, those lignites are generally characterized by their high ash, moisture, volatile matter, and sulfur contents.

The urgent need to extend the life of existing fossil fuel resources and the progressive implementation of environmental legislations that are more stringently regulating emissions from burning fossil fuels have increased interest in renewable energy sources. Among them, biomass can be considered as a promising alternative against fossil fuels due to the fact that it is CO_2-neutral and an effective remedy to reduce emissions of this greenhouse gas. In addition to that, 10% of the world's energy is produced by biomass, making it the second-largest energy source after fossil fuels. [2]. However, utilizing biomass exclusively could result in serious operational issues and unplanned shutdowns in industrial and utility boilers such as corrosion, ash deposition, and bed agglomeration. These problems in the combustion of biomass alone can be alleviated (i) by the use of additives such as kaolin, dolomite, alumina, etc. [3,4] (ii) by the use of different bed materials containing alumina, magnesite, ferric oxide, etc. [5–7] (iii) by co-firing biomass with coal [8–10]. The third alternative is considered to be the most promising one as it offsets the negative effects of firing coal and biomass individually by reducing the gaseous emissions originating from coal combustion and hindering ash-related issues encountered in biomass combustion. Bubbling fluidized bed combustion technology is a good candidate for the co-combustion of coal and biomass owing to its fuel flexibility and

1

low operation temperatures. Other attractive features of bubbling fluidized bed combustors (BFBCs) are high system efficiency, in-situ desulfurization, and low NO_x emissions. Fluidized bed combustors (FBCs) are readily used for the combustion of lignites, which is one of the major indigenous energy sources of Turkey. Furthermore, olive residue (OR), hazelnut shell (HS), and cotton residue (CR) are three important sources of biomass in Turkey with estimated quantities of 321 000, 332 000, and 709 000 tons of annual production, respectively [11–14]. Nevertheless, the diverse and versatile nature of biomass makes its combustion complicated and necessitates a detailed understanding of the co-combustion of biomass and coal in FBCs. Such a goal necessitates both experimental research and mathematical modeling studies.

Apart from biomass, solar and wind energy have an increased interest against fossil fuels nowadays as they are environmentally friendly and become more cost-efficient day by day. However, these energy sources are characterized as non-dispatchable due to their unpredictable and intermittent nature. The problems originating from the intermittent nature of solar and wind energy can be alleviated by the utilization of a backup fuel together with these sources. During the time periods when solar and wind energy are available at high levels, these sources are regarded as favorable in the energy market owing to their low operation cost. When those sources are not available, producing energy from the backup fuel in a thermal power plant becomes more beneficial. However, this requires a technology, which can handle frequent load changes. For this purpose, transient operations of the thermal power plants need to be investigated and analyzed which can be achieved by dynamic modeling.

One of the most commonly used approaches for modeling FBCs is computational fluid dynamics (CFD) [15–17] where equations of mass, momentum, and energy are solved explicitly by utilizing sub-models for the implementation of turbulence, drying and devolatilization, char combustion, transport and reaction of gaseous species, etc. Despite the fact that CFD models are regarded as one of the most appropriate tools for the simulation of FBCs, those approaches suffer from extreme computational source requirements and sometimes are not affordable in practical

2

engineering applications. Alternatively, one-dimensional system models, which utilize empirical correlations to describe complex multiphase flow in FBCs, provide sufficient accuracy by improving computational efficiency significantly [18,19]. Aside from hydrodynamics, thermal radiation is also an important phenomenon for the modeling of BFBCs as radiative heat transfer (RHT) makes up the majority of heat transfer in those systems due to the existence of radiating particles and gases.

There exists a limited number of BFBC modeling studies in the literature involving the coupled steady-state solution of RHT in conjunction with conservation equations of other transport processes. Scala and Salatino [20] developed a steady-state, 1-D system model for atmospheric BFBC burning a high volatile solid fuel. The system model consists of three regions which are the fluidized bed, splash zone, and the freeboard, and accounts for hydrodynamics, volatile release and combustion, char combustion, char comminution, elutriation, and heat transfer. However, the model does not consider the formation and reduction of gaseous pollutants such as SO_2, NO_x, and N_2O. Moreover, the RHT was taken into account using the zone method where the system consists of four gray, absorbing, emitting zones which are the bed, the freeboard, ejected particles, and absorbing/emitting gas. In an attempt to investigate the performances of different global NH_3 reaction mechanisms, a CFD-based model for BFBC firing biomass sludge with methane was developed by Saario and Oksanen [21] using ANSYS Fluent software. Special emphasis was given to the selective non-catalytic reduction process. k-ε and eddy dissipation combustion models were used for consideration of turbulence and turbulence – chemistry interaction, respectively. The radiative transfer equation (RTE) was solved with the finite volume method whereas the weighted sum of gray gases (WSGG) model was used for the estimation of gas radiative properties. However, absorption, emission, and scattering due to particles were neglected. Finally, the model was validated against the temperature and NO and NH_3 measurements obtained from an industrial scale boiler. In another study carried out by Alagoz et al. [22], a 1-D comprehensive system model of a BFBC firing Turkish lignites with and without fly ash recycling was coupled with a 3-D radiation model based on the method of line (MOL) solution

of discrete ordinates method (DOM). The model is composed of two regions, namely the bed and the freeboard regions, and takes hydrodynamics, volatile release and combustion, char particle combustion and size distribution, heat transfer, elutriation, and entrainment, sulfur retention into consideration. Radiative properties of the medium were estimated using Leckner's correlation for combustion gases and Mie theory for particles whereas particle scattering was taken to be isotropic. However, the medium was treated as gray, absorbing, emitting, and isotropically scattering medium bounded by gray and diffuse refractory lined walls. Furthermore, a high order polynomial obtained from wall temperature measurements was given to the model as input data. The validity of the model was tested by comparing its predictions with incident heat flux (HF), temperature, and O_2, CO_2, and CO measurements. Hu et al. [23] coupled the zone method of radiation with a 1-D system model for BFBC developed in Aspen Plus software. The system model accounts only for hydrodynamics, volatile release and combustion, char combustion, and heat transfer. Radiative properties of combustion gases were estimated using the WSGG model whereas gray particle properties were calculated using Mie theory at the wavelength where blackbody radiation intensity at the system temperature is the highest. El-Sayed and Noseir [24] developed a 2-D CFD model for only the freeboard zone of a pilot-scale BFBC firing sesame stalk and broad bean stalk using ANSYS Fluent software. Input data and boundary conditions for the freeboard modeling were taken from the experiments carried out in the pilot-scale BFBC. The model does not account for the formation and reduction of pollutants such as SO_2, NO_x, and N_2O. RHT was taken into account utilizing P-1 approximation where the medium was considered to be gray, absorbing, emitting, and isotropically scattering. Finally, a CFD model for bubbling fluidized bed combustion of two biomasses (wood pellet and olive stone) was developed by Diba et al. [25] using AVL Fire software. Their model accounts for gas-solid hydrodynamics, drying, devolatilization, combustion of char and volatiles, and heat transfer but does not consider the formation and reduction of gaseous pollutants such as NO, N_2O, SO_2

4

and particle size distribution (PSD). RTE, on the other hand, is solved using the discrete transfer method utilizing gray gas and particle emissivities.

Regarding the transient BFBC models in the literature, there are a limited number of studies investigating the transient operation of coal- or biomass-fired BFBCs using dynamic modeling. The pioneering work on dynamic modeling of BFBCs was carried out by Beasley and Golan [26]. In their study, a classical first-order system response model was developed to predict dynamic temperature characteristics of a combusting bed for step changes in coal and air flow rates. Predictions of the model were validated against the transient temperature measurements obtained from the 3517 kW fluidized bed combustor HF unit. Later, Ikonen and Cortela [27] developed a simple model consisting of seven differential equations describing the dynamic behavior of the bed fuel inventory, bed emulsion phase oxygen content, flue gas oxygen content, bed temperature, freeboard temperature, power output, and drum pressure. The dynamic behavior of a 30 MW power plant was tested by imposing step changes to air flow rate and fuel feed rate. However, RHT was not taken into account in the freeboard energy conservation equation. Selcuk and Degirmenci [28] developed a 1-D comprehensive transient model for 0.3 MW_t atmospheric bubbling fluidized bed combustion (ABFBC) test rig, which accounts for bed and freeboard hydrodynamics, volatile release and combustion, char combustion, PSD, and heat transfer. Thermal radiation in the combustor is taken into account by the implementation of Stefan-Boltzmann law between particles and gaseous medium. Validation of the model was carried out against the steady-state and transient temperature and concentration measurements obtained from the 0.3 MW_t ABFBC test rig firing lignite. Another dynamic model for ABFBC is developed by Galgano et al. [29]. Their model consists of three regions, namely bubbling bed, splashing region, and freeboard, and takes into account hydrodynamics, volatile release and combustion, char particles combustion and size distribution, elutriation, and entrainment, and heat transfer. The RHT was taken into account using Stefan-Boltzmann law. The dynamic response of the system to the changes in flow rate and moisture content of the fuel was investigated. The model was not validated against

the measurements. In an attempt to investigate the transient operation of a bubbling fluidized bed boiler firing high volatile solid fuel, Kataja and Majanne [30] developed a dynamic model including both air-flue gas line and water-steam circuit. Their model consists of four different regions, namely fluidized bed, splashing region, secondary zone, and freeboard, and takes into account bed hydrodynamics, volatile release and combustion, char particles combustion and size distribution, elutriation and entrainment, and heat transfer. Stefan-Boltzmann law is used to represent RHT. The model was found to well describe the dynamic responses of the bubbling fluidized bed boiler to flow rate and moisture content of the fuel based on its validation against the measured process data including drum and steam pressure. In the study carried out by Surasani et al. [31], a model for dynamic simulation of fluidized bed combustion of biomass was developed. The model included three different regions in series which are well-mixed fluidized bed, plug flow freeboard, and well-mixed cyclone. In the model, RHT was not taken into consideration. Transient predictions of the model were validated against the temperature and flue gas composition measurements obtained from a laboratory-scale BFBC indicating that the model is appropriate to be coupled with a thermodynamic cycle to simulate the operation of power plants. In an attempt to deal with the difficulties in FBC control arising from nonlinearity and frequent disturbances, Sun et al. [32] tested the performance of a disturbance observer-enhanced PI controller by applying it to a non-linear FBC model. The dynamic FBC model considered the differential equations for the transient behaviors of fuel inventory, bed and freeboard oxygen contents, bed and freeboard temperatures, and thermal power. As a result of this, the suggested control strategy was found to be comparable even with Model Predictive Control (MPC). Huttunen et al. [33] investigated the effect of changes in boiler load of a 79 MW wood-firing bubbling fluidized bed boiler by developing a computational fluid dynamics model using ANSYS Fluent software. In the model, thermal radiation was taken into account using DOM whereas the radiative property estimation methods for particles and combustion gases were not described. Finally, in an attempt to simulate the transient operation of both large-scale BFBCs and

6

circulating fluidized bed combustors (CFBCs), Castilla et al. [34] developed a model which considers hydrodynamics, volatile release and combustion, char particles combustion, entrainment, and heat transfer. In their model, RHT is taken into consideration by Stephan-Boltzmann law using gray emissivities and absorptivities for the freeboard medium and the walls. However, freeboard medium absorptivity is determined by fitting the absorptivity to the operational data for different furnace loads. The model was validated against the steady-state and transient measurements obtained from 130 MW BFBC and 80 MW CFBC.

None of the above-mentioned studies coupled comprehensive steady-state and transient system models for a BFBC with a sophisticated radiation model where RTE is explicitly solved together with mass, momentum and energy conservation equations. However, the performance of a BFBC system strongly depends upon the heat recovery in the freeboard section which is characterized by a low particle load. Previous works regarding the heat transfer characteristics of the FBCs state that RHT becomes significant when particle load is low [34,35]. Furthermore, during fluidized bed co-combustion of coal and biomass with limestone addition, the number of fine particles in the freeboard increases [36,37]. Therefore, RHT may become more important in such cases as fine particles interact with radiation more than coarse particles owing to their high projected surface area. For this purpose, coupling comprehensive BFBC system models for combustion and/or co-combustion applications with a radiation model is needed.

Coupling of a radiation model with the system models of BFBCs requires the solution of RTE, where radiation intensity is described as a function of seven independent variables (three location variables, two-direction variables, a spectral variable, and time), together with mass, momentum and energy conservation equations. Therefore, robust methods are needed both for the solution of RTE and for the estimation of radiative properties of combustion gases, particles and walls. Previous works on the determination of the most computationally efficient and accurate solution method for RTE revealed that MOL solution of DOM meets all the requirements based on its validation against Monte Carlo method, zonal method, and

measurements [38,39]. Nevertheless, the solution of RTE becomes further complicated in the presence of spectral absorption, emission, and scattering properties of the medium. Studies involving thermal radiation in the FBCs have already taken into account the spatial, temporal, directional, and spectral dependence of fly ash particles [40–45]. However, less effort is devoted to find out both sufficiently accurate and computationally efficient gas radiative property models for BFBCs in the presence of non-gray particles and boundaries.

Proper treatment of complex spectral dependence of gas radiative properties is one of the most challenging aspects of the solution of RTE as radiative properties of combustion gases oscillate wildly throughout the thermal spectrum. Therefore, within the last few decades, a wide variety of studies have been devoted to develop robust spectral gas radiative property models which are summarized in [46–48]. Among the wide variety of gas radiative property models, line-by-line (LBL) method is the most accurate one and is considered to be the exact treatment of gas radiative properties. However, LBL method is extremely computationally expensive, especially for large-scale combusting systems, as it requires millions of RTE solutions. Narrow band models such as statistical narrow bands (SNB) and narrow band correlated-k (NBCK), on the other hand, simplify the estimation of spectral gas behavior by averaging spectral gas properties over narrow wavenumber intervals of the order of a few dozen cm^{-1} [48]. Although narrow band models are capable of achieving LBL accuracy [46,49], their computational time requirements are still too high for multidimensional engineering problems. Therefore, applications of narrow band models and LBL are restricted to providing benchmark solutions and data required by other simpler approaches. Alternatively, wide band models, in which the blackbody intensity does not change substantially across an entire vibration-rotation band, were developed to reduce the computational cost requirement [46]. In those approaches, spectral properties across the wide bands are evaluated by using correlations obtained by integrating narrow band solutions over those bands. However, these models generally result in approximately $\pm$ 30 % errors [46] despite the fact that they significantly improve computational efficiency compared to narrow

band models and LBL. For the sake of improving computational efficiency without reducing accuracy, global models which utilize spectrally integrated gas radiative properties over the entire spectrum instead of wavenumber intervals were developed. Amongst them, the most popular ones are the WSGG model [50], spectral line based weighted sum of gray gases (SLW) model [51–53], and full spectrum correlated-k (FSCK) model [54]. Those models have been applied to a wide variety of problems [51,53–60] where they have been validated against LBL and narrow band models and found successful in terms of accuracy and computational efficiency. A drawback of these models is that their applications with non-gray particles and/or non-gray boundaries are restricted [61].

Among the wide variety of spectral gas radiative property models, SLW model developed by Denison and Webb [51–53] and further extended and improved by Webb and co-workers [62–66] is a promising alternative that provides an accurate mean for total RHT calculations with considerable savings in computational requirements. The predictive performance and computational efficiency of SLW model were validated against the benchmark solutions in a wide range of problems including absorbing, emitting, and scattering media [51–53,55,60,66,67]. In recent studies, Webb and co-workers [68–71] improved SLW for modeling thermal radiation in non-isothermal and/or non-homogeneous gaseous media where modeling of thermal radiation is challenging due to spatial variation of thermodynamic states and difficulties associated with radical variations of local radiative properties. SLW model was also implemented into coupled natural convection-radiation problems [72–75] and CFD software such as ANSYS Fluent or OpenFOAM [76–80]. In an attempt to further reduce the computational requirements of SLW for convection-radiation problems which require repeated solutions of RTE, Solovjov et al. [81,82] developed the efficient and minimal formulation of SLW by representing the spectrum as a mixture of single gray gas and a clear gas which is referred as SLW-1.

Predictions of SLW-1 model were first validated by Solovjov et al. [81] against LBL method and SLW method with a large number of gray gases on 1-D plane layer

problems consisting of only water vapor bounded by gray walls. Furthermore, they implemented several approaches for the estimation of spectral parameters of SLW-1 which are absorption coefficient (κ_1) and gray gas weight (a_1) of the gray gas. Among them, a simple method based on two emissivities where κ_1 and a_1 are determined by fitting the total gas emissivities calculated at two different path lengths L_1 and L_2, was found to provide reasonable accuracy. However, the accuracy of the predictions of SLW-1 was found to be sensitive to the selected path lengths (L_1 and L_2). Regarding selection of L_1 and L_2 values, they recommended that those values should capture a range of path lengths that are both smaller and greater than the length defined by the physical boundaries. Solovjov et al. [82] also tested the predictive accuracy of SLW-1 model on 1-D plane layer problems consisting of non-isothermal, non-homogenous H_2O and CO_2 mixtures with non-gray soot bounded by black or gray walls by comparing the predictions of SLW-1 with those of LBL method, SLW model with a large number of gray gases and SNB model. It was found that SLW-1 model yields very good accuracy in those 1-D plane layer problems. Further assessments of predictive accuracy of SLW-1 model were conducted in 1-D test cases consisting of water vapor [83] and mixtures of H_2O, CO_2 and soot [84] bounded by gray or black walls. In those studies, the predictive performance of SLW-1 model was compared with other spectral gas radiative property models such as LBL, SLW, wide band correlated-k (WBCK), WSGG and SLW-3. In conclusion, SLW-1 yielded acceptable accuracy for the 1-D test cases investigated. Implementation of SLW-1 model into a 2-D radiation model was achieved by Amiri and Lari [85]. In their study, SLW-1 model was applied to 2-D test cases consisting of homogeneous or non-homogeneous H_2O and/or CO_2 gases bounded by black walls and was validated against the LBL predictions. As a result of this, SLW-1 model was found to provide acceptable accuracy with much lower computational requirements compared to LBL, SLW and FSCK models. Recently, SLW-1 model was applied to a combined convection-radiation in a square enclosure consisting of non-gray H_2O, CO_2 and N_2 mixture [86]. The effects of mole fraction of the gas

mixture, wall emissivity, Rayleigh number and convection radiation interaction were studied.

The above-mentioned studies consider the application of SLW-1 model only to 1-D and 2-D test cases without absorbing, emitting, and scattering particles. However, predictive accuracy and computational efficiency of SLW-1 model should also be tested in large-scale coal combustors involving absorbing, emitting, and scattering particles to bring further clarity to the benefits of utilization of SLW-1 as spectral gas radiative property model in industrial applications. For this purpose Ozen et al. [87] extended SLW-1 model to 3-D gray enclosures containing non-gray absorbing, emitting gases, and non-gray absorbing, emitting and anisotropically scattering fly ash particles referred as 'banded SLW-1'. Spectral parameters of banded SLW-1 were found by matching the gas mixture total emissivities calculated at two different path lengths L_1 and L_2 which are 0.50 and 1.25 times the freeboard height, respectively. Their results indicated that the predictive accuracy of banded SLW-1 deteriorates in the presence of non-gray particles compared to the presence of gray particles. Therefore, Ozen et al. [87] recommended band-wise selection of path lengths (L_1 and L_2) for the estimation of spectral parameters of banded SLW-1 as a further investigation. Furthermore, optimization of path length (L_1 and L_2) values should be carried out as the accuracy of banded SLW-1 model strongly depends on those values [81]. Finally, Ozen et al. [87] assessed the predictive accuracy of banded SLW-1 model in gray enclosures involving non-gray absorbing, emitting, and scattering medium. However, that assessment needs to be carried out in the presence of non-gray walls as correct treatment of RHT in such systems requires utilization of non-gray boundaries.

Recently, Bordbar and Hyppänen [88] developed a simple banded approach for radiative properties of combustion gases which supports the incorporation of non-gray wall emissivities. In this model, for a gas mixture of H_2O and CO_2, the thermal spectrum was divided into 31 bands, whose limits were determined based on LBL spectral absorption coefficient profile. Each band was assumed to contain a single gray gas mixture of H_2O and CO_2. Predictions of the model were found to be as

accurate as LBL solutions for three test cases containing only non-gray combustion gases bounded by black or non-gray walls. To improve the computational efficiency of the 31 band model, Bordbar et al. [61] further simplified the banded gas radiative property model by dividing the thermal spectrum into 10 bands based on band dividing scheme of Maximov [89]. Absorption coefficient of each band was calculated using a correlation formed from a database provided by SNB at a wide range of temperature, path length, and H_2O and CO_2 mole fractions. The model was applied to 1-D and 3-D benchmark problems representing typical air and oxy-fuel combustion conditions. The model was found to provide sufficiently good accuracy with significantly low computational time compared to LBL and Bordbar's 31 band model. Based on these findings, Bordbar's 10 band model was applied to back pass channel of a CFBC where contribution of particle radiation is assumed to be negligible compared to gas radiation due to low particle concentration. However, recent studies considering both radiating particles and radiating gases indicate that particle radiation may become as important as gas radiation or even dominate the RHT [44,57,90,91]. Hence, the assessment of the accuracy of Bordbar's 10 band model for gas radiative properties needs to be tested in presence of high particle concentration such as the freeboard sections of BFBCs.

Therefore, absence of steady-state and transient BFBC system models coupled with a radiation model both for the combustion of lignite and co-combustion of lignite with CR and limestone addition on one hand, necessity to establish both computationally efficient and sufficiently accurate spectral radiative property models on the other, lead this study to the following objectives which are (i) assessment of the accuracy and computational efficiency of two spectral gas radiative property models, namely Bordbar's 10 band model [61] and banded SLW-1 [81,87] in 0.3 MWt ABFBC test rig by comparing their predictions with measurements and benchmark solutions (ii) comparison of RHT predictions of gray and non-gray wall emissivities of different type of wall materials common in industry and utility boilers (iii) coupling a 1-D comprehensive transient system model for BFBC firing lignite with a 3-D radiation code based on MOL of DOM utilizing both

12

computationally efficient and sufficiently accurate spectral radiative property models (iv) coupling a 1-D comprehensive steady-state system model for BFBC co-firing lignite with CR and limestone addition with the 3-D radiation code based on MOL of DOM utilizing spectral radiative property models and (v) coupling gas and particle radiative property models with a 2-D CFD model for BFBC firing lignite. To accomplish such objectives, comprehensive steady-state and transient system models for METU 0.3 MW_t ABFBC test rig, developed by Selcuk and co-workers [18,28,92–97] are chosen as basis. The CFD model, on the other hand, is developed using the commercial software ANSYS Fluent 2022 R1 [98] within the scope of this study. After completion of those objectives, the 3-D radiation model will be applied to a test case representing the typical conditions of solid rocket motor exhaust plumes to investigate RHT in solid rocket plumes where radiation is an important mechanism of heat transfer.

To achieve the above-mentioned objectives, the main tasks were set as follows:

1. Developing a 3-D radiation model utilizing MOL of DOM for the simulation of RHT of the freeboard of BFBCs where non-gray gas and particles are bounded by non-gray walls.
2. Creating a benchmark solution, which involves spectral particle, gas, and wall properties.
3. Quantifying the contribution of spectral gas and particle radiation to RHT under BFBC conditions in the presence of spectral walls.
4. Assessment of the accuracy and computational efficiency of spectral gas radiative property models in the presence of spectral particles and walls for BFBCs by comparing their predictions with experimental measurements and benchmark solutions.
5. Comparison of RHT predictions with gray and non-gray wall emissivities of different types of wall materials common in industry and utility boilers.
6. Investigating the effect of fine fly ash particles on thermal radiation in BFBCs.

7. Investigating the effect of soot particles and aggregates on thermal radiation in BFBCs.

8. Coupling a 1-D comprehensive steady-state system model for a BFBC firing lignite with a 3-D radiation model utilizing MOL of DOM with spectral radiative property models.

9. Validating the steady-state coupled model by comparing its predictions with temperature and O_2, CO_2, and CO concentration measurements.

10. Investigating the effect of using spectral radiative properties of particles, gases, and walls in the coupled model on RHT, temperature, and O_2, CO_2, and CO concentration predictions.

11. Coupling a 1-D comprehensive transient system model for a BFBC firing lignite with a 3-D radiation code based on MOL of DOM utilizing a sufficiently accurate and computationally efficient radiative property model for combustion gases, particles, and walls.

12. Validating the transient coupled model by comparing its predictions with transient temperature and O_2 and CO concentration measurements.

13. Investigating the effect of using a sophisticated radiation model where RTE is explicitly solved in conjunction with conservation equations of other transport processes on temperature and O_2 and CO concentration predictions.

14. Quantifying the contribution of radiation to total heat transfer in the freeboards of BFBCs.

15. Coupling a 1-D comprehensive steady-state system model for BFBC co-firing lignite with CR and limestone addition with a 3-D radiation code based on MOL of DOM utilizing spectral radiative property models for combustion gases, particles, and walls.

16. Validating the steady-state coupled model by comparing its predictions with measured temperature and gaseous emissions of the species O_2, CO_2, CO, SO_2, NO, and N_2O.

17. Developing a 2-D CFD model for BFBCs using the commercial software ANSYS Fluent accounting for gas-solid multiphase flow, turbulence, chemical reactions and radiation.

18. Validating the 2-D CFD model by comparing its predictions with measured temperatures and concentration profiles of the species O_2, CO_2, CO.

19. Assessment of the accuracy and computational efficiency of gas and particle radiative property models coupled with the 2-D CFD model for BFBCs by comparing their predictions with experimental measurements.

CHAPTER 2

RADIATION MODEL

The objective in RHT calculations is to determine the amount of energy leaving one surface and reaching another after traveling through a medium. If the medium interacts with radiation, as in the case of Earth's atmosphere or a coal-combustion chamber, then the attenuation of each beam along its path and its redirection needs to be considered. The main idea in the RHT calculations is that radiative energy loses some of its strength as it propagates through a path due to out-scattering and absorption and gains additional strength because of in-scattering of radiation and emission in the direction as illustrated by Figure 2.1. Along this direction and path, the change in radiative energy can be tallied, which provides a conservation equation of radiative energy called the 'radiative transfer equation (RTE)'. However, the solution of RTE is not straightforward as its radiation intensity is described as a function of seven independent variables (three location variables, two direction variables, a spectral variable, and time). Another challenging aspect of the solution of RTE is the proper consideration of complex spectral and directional dependence of thermal radiation due to combustion gases and particles. Therefore, modeling of radiation necessitates robust methods both for the solution of RTE and the estimation of radiative properties of particle-laden combustion gases.
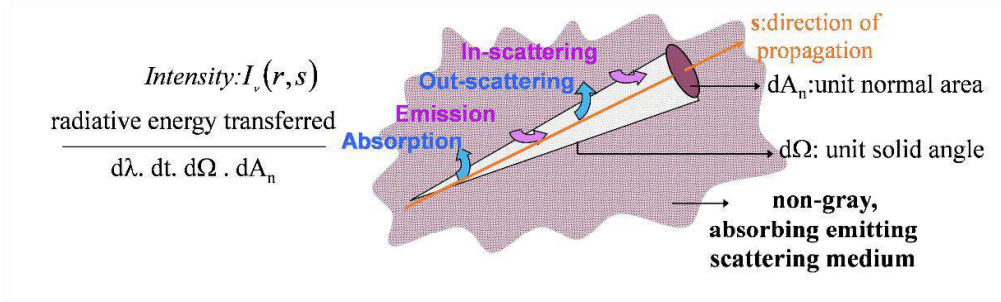
Figure 2.1. Schematic representation of RHT calculations

In this chapter, the details of the radiation models utilized in the present work are summarized. Starting from the RTE for the 3-D rectangular geometry, the derivation of the RTE in the form of MOL solution of DOM are provided together with its numerical solution techniques. In the next part of this chapter, the methods for the estimation of radiative properties of combustion gases, particles and walls are described in detail.

2.1 Solution of Radiative Transfer Equation (RTE)

2.1.1 Radiative Transfer Equation (RTE)

For the representation of RHT in combusting systems, solution of radiative transfer equation (RTE) is of significant importance. It is written as a conservation equation in a specified direction (ds) through a small volume element of non-gray, absorbing, emitting, scattering uniform media in the following form:

$$\frac{1}{c}\frac{dI_\lambda}{dt} + \frac{dI_\lambda}{ds} = \frac{1}{c}\frac{I_\lambda(r,\Omega)}{dt} + (\Omega \cdot \nabla)I_\lambda(r,\Omega)$$

$$= -(\kappa_\lambda + \sigma_\lambda)I_\lambda(r,\Omega) + (\kappa_\lambda)I_{\lambda,b}(r) + \frac{\sigma_\lambda}{4\pi}\int_{4\pi}\Phi_\lambda(\Omega',\Omega)I_\lambda(r,\Omega')d\Omega' \qquad (2.1)$$

where $I_\lambda(\mathbf{r},\mathbf{\Omega})$ is the spectral radiation intensity at position $\mathbf{r}$ in the direction $\mathbf{\Omega}$ defined as the quantity of radiant energy passing in a specified direction $\mathbf{\Omega}$ along a path s per unit solid angle $d\mathbf{\Omega}$ about the direction $\mathbf{\Omega}$, per unit area normal to the

direction of travel, per unit time. κ_λ and σ_λ are the spectral absorption and spectral scattering coefficients of the medium, respectively. $I_{\lambda,b}(r)$ is the spectral black-body radiation intensity at position **r** and $\Phi_\lambda(\Omega', \Omega)$ is the spectral phase function for scattering which describes the fraction of energy scattered from the incoming direction Ω' to the outgoing direction Ω. Ω denotes the direction of solid angle and c is the speed of light. The term on the left-hand side represents the change of intensity in the specified direction s and solid angle Ω. The terms on the right-hand side (RHS) stand for absorption and out-scattering, emission and in-scattering, respectively.

However, the radiation phenomena can be taken to be quasi-steady state as the light travels so fast that radiative equilibrium is reached before any notable temperature change takes place as in the vast majority of engineering problems. By simply neglecting the time rate of change of radiation intensity (dI_λ/dt), the quasi-steady form of the spectral RTE is written as:

$$\frac{dI_\lambda}{ds} = (\Omega \cdot \nabla) I_\lambda(r, \Omega)$$

$$= -(\kappa_\lambda + \sigma_\lambda) I_\lambda(r, \Omega) + (\kappa_\lambda) I_{\lambda,b}(r) + \frac{\sigma_\lambda}{4\pi} \int_{4\pi} \Phi_\lambda(\Omega', \Omega) I_\lambda(r, \Omega') d\Omega' \qquad (2.2)$$

For a rectangular coordinates (x, y, z), the radiative intensity gradient can be defined by the following expression by applying the chain rule;

$$\frac{dI_\lambda}{ds} = \frac{\partial I_\lambda}{\partial x}\frac{dx}{ds} + \frac{\partial I_\lambda}{\partial y}\frac{dy}{ds} + \frac{\partial I_\lambda}{\partial z}\frac{dz}{ds} \qquad (2.3)$$

where the direction cosines are represented as functions of zenith angle (θ) and azimuthal angle (φ) as shown in Figure 2.2:

$$\frac{dx}{ds} = \mu = \cos(\theta) \qquad (2.4)$$

$$\frac{dy}{ds} = \eta = \sin(\theta)\sin(\varphi) \qquad (2.5)$$

19

$$\frac{dz}{ds} = \xi = \sin(\theta)\cos(\varphi) \tag{2.6}$$
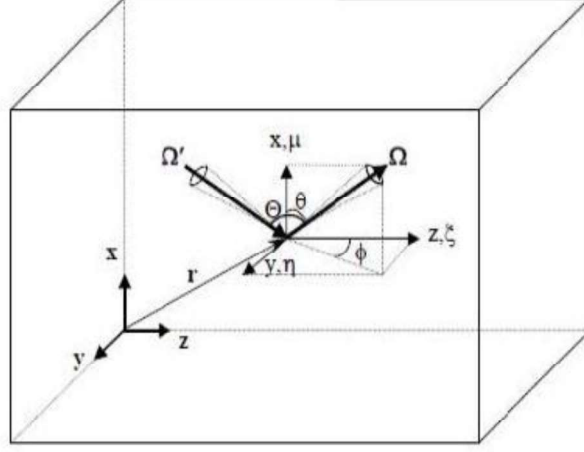
Figure 2.2. Directional cosines for rectangular geometries (Θ is the angle between radiation intensities at incoming and outgoing directions)

For rectangular geometry, the final form of the quasi-steady form of RTE can be written as follow:

$$\mu\frac{\partial I_\lambda}{\partial x} + \eta\frac{\partial I_\lambda}{\partial y} + \xi\frac{\partial I_\lambda}{\partial z} =$$

$$-(\kappa_\lambda + \sigma_\lambda)I_\lambda(\boldsymbol{r},\boldsymbol{\Omega}) + (\kappa_\lambda)I_{\lambda,b}(\boldsymbol{r}) + \frac{\sigma_\lambda}{4\pi}\int_{4\pi}\Phi_\lambda(\boldsymbol{\Omega'},\boldsymbol{\Omega})I_\lambda(\boldsymbol{r},\boldsymbol{\Omega'})d\boldsymbol{\Omega'} \tag{2.7}$$

For opaque, diffuse, and non-gray boundaries, the following boundary conditions can be used for Eq. (2.7):

$$I_\lambda(\boldsymbol{r_w},\boldsymbol{\Omega}) = \varepsilon_{w,\lambda}I_{b,w,\lambda} + \frac{(1-\varepsilon_{w,j})}{\pi}\int_{\boldsymbol{n}\cdot\boldsymbol{\Omega'}<0} I_\lambda(\boldsymbol{r_w},\boldsymbol{\Omega'})|\boldsymbol{n}\cdot\boldsymbol{\Omega'}|d\boldsymbol{\Omega'} \tag{2.8}$$

Once the intensity field can be evaluated by solving RTE [Eq. (2.7)] in conjuction with the boundary conditions [Eq. (2.8)], radiative HF and source term (ST) fields can be determined as follows;

$$q_\lambda = \int\limits_{4\pi} (\boldsymbol{e_i} \cdot \boldsymbol{\Omega}) I_\lambda d\boldsymbol{\Omega} \tag{2.9}$$

$$\nabla \cdot q_\lambda = \kappa_\lambda \left(4\pi I_{b,\lambda}(\boldsymbol{r}) - G_\lambda(\boldsymbol{r}) \right) \tag{2.10}$$

where G_λ is the incident spectral radiation defined as:

$$G_\lambda(\boldsymbol{r}) = \int\limits_{4\pi} I_\lambda(\boldsymbol{r}, \boldsymbol{\Omega}) d\boldsymbol{\Omega} \tag{2.11}$$

2.1.2 Discrete Ordinates Method (DOM)

In the discrete ordinates method (DOM), the entire angular domain is represented by finite number of discrete solid angles panning the total solid angle of 4π steradians. With the help of this approach, the in-scattering term in the RTE [Eq. (2.7)] is represented as the summation of quadratures over the ordinate directions, which means, the RTE that is an integro-differential equation is transformed into partial differential equations (PDEs) involving only spatial coordinates as independent variables. Spatial discretization can then be accomplished by using a variety of methods including finite volume method (FVM), finite element method (FEM), or finite difference method (FDM). For the classical implementation of DOM [99,100], spatial derivatives are discretized by using standard cell–centered, FVM.

In the DOM implementation, the spectral RTE involving absorbing, emitting and scattering mediums for a rectangular coordinate system can be written as follows;

$$\mu_{m,\ell} \frac{\partial I_\lambda^{m,\ell}}{\partial x} + \eta_{m,\ell} \frac{\partial I_\lambda^{m,\ell}}{\partial y} + \xi_{m,\ell} \frac{\partial I_\lambda^{m,\ell}}{\partial z} = -\left(\kappa_{g,\lambda} + \kappa_{p,\lambda} + \sigma_{p,\lambda} \right) I_\lambda^{m,\ell}$$

$$+ \left(\kappa_{g,\lambda} + \kappa_{p,\lambda} \right) I_{b,\lambda}$$

$$+ \frac{\sigma_{p,\lambda}}{4\pi} \sum_{m',l'} \Phi_\lambda(\boldsymbol{\Omega}_{m',\ell'}, \boldsymbol{\Omega}_{m,\ell}) w_{m',\ell'} I_\lambda^{m',\ell'} \tag{2.12}$$

where $I_\lambda^{m,\ell}$ [$\equiv I_\lambda(\mathbf{r}; \mu_{m,\ell}, \eta_{m,\ell}, \xi_{m,\ell})$] is the spectral radiation intensity at position $\mathbf{r}$ (x, y, z) in the discrete direction $\boldsymbol{\Omega}_{m,\ell}$ as represented by Figure 2.3, m and ℓ denote the discrete ordinate (m = 1,2,…,M and ℓ = 1,2,…,N), M and N are the total number of ordinates used in the approximation, $\mu_{m,\ell}$, $\eta_{m,\ell}$, and, $\xi_{m,\ell}$ are the direction cosines of $\boldsymbol{\Omega}_{m,\ell}$ with x, y, z axis, respectively and $w_{m',\ell'}$ is the angular quadrature weight associated with the incoming direction $\boldsymbol{\Omega}_{m',\ell'}$.
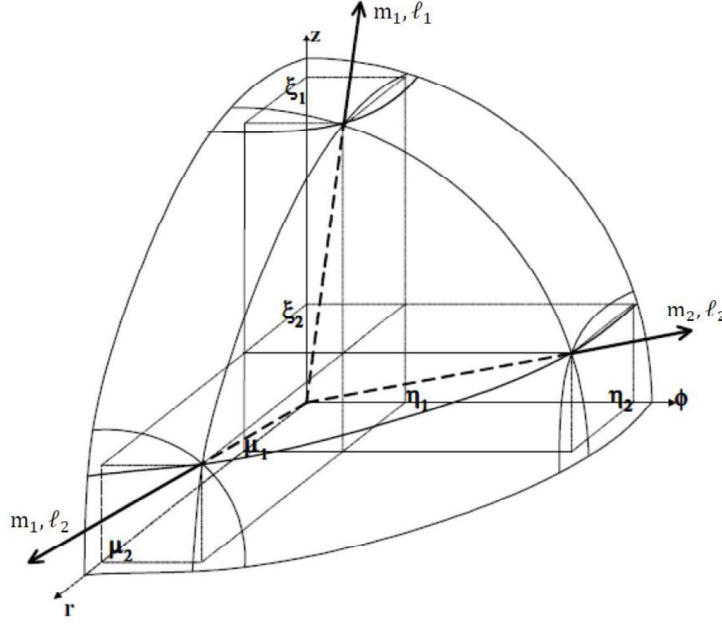
Figure 2.3. Schematic representation of discrete directions represented by m, ℓ in one octant of a unit sphere for S$_4$ order of approximation

For a diffuse and spectral wall at a certain temperature, the boundary conditions given by Eq. (2.13) can be utilized:

$$\text{at } x = 0, \ I_\lambda^m = \varepsilon_{w,\lambda} I_{b,w,\lambda} + \frac{(1 - \varepsilon_{w,\lambda})}{\pi} \sum_{\mu_{m'} < 0} I_\lambda^{m'} w_{m'} |\mu_{m'}|, \quad \mu_m > 0 \qquad (2.13)$$

$$\text{at } x = L, \ I_\lambda^m = \varepsilon_{w,\lambda} I_{b,w,\lambda} + \frac{(1 - \varepsilon_{w,\lambda})}{\pi} \sum_{\mu_{m'} > 0} I_\lambda^{m'} w_{m'} |\mu_{m'}|, \quad \mu_m < 0 \qquad (2.14)$$

22

Similar conditions can be applied to the boundaries for the other directions.

Once the intensity field is obtained by the solution of Eq. (2.12) in conjuction with the boundary conditions [Eqs. (2.12) and (2.14)], radiative HF and ST fields can be determined as follows:

$$\boldsymbol{q}_{\lambda,inc} = \sum_{m'=1}^{M} w_{m'}\ell_{m'}I_{\lambda}^{m'} \tag{2.15}$$

$$\boldsymbol{q}_{\lambda,net} = \sum_{m'=1}^{M} w_{m'}\ell_{m'}I_{\lambda}^{m'} - \sum_{m=1}^{M} w_{m}\ell_{m}I_{\lambda}^{m} \tag{2.16}$$

$$\nabla \cdot \boldsymbol{q}_{\lambda} = \kappa_{\lambda}\left(4\pi I_{\lambda,b} - \sum_{m} w_{m}I_{\lambda}^{m}\right) \tag{2.17}$$

For the angular discretization, S_N and T_N schemes are most commonly utilized. Carlson and Lathrop [101] first developed the S_N angular discretization scheme in which a number of key moments of the radiative intensity are satisfied. The directions for the S_2, S_4, S_6, S_8, and S_{10} approximations are illustrated in Figure 2.4. As illustrated in the figure, discrete directions are ordered in levels and the number of directions is different at each level. The details of the S_N angular quadrature scheme can be found elsewhere [102].
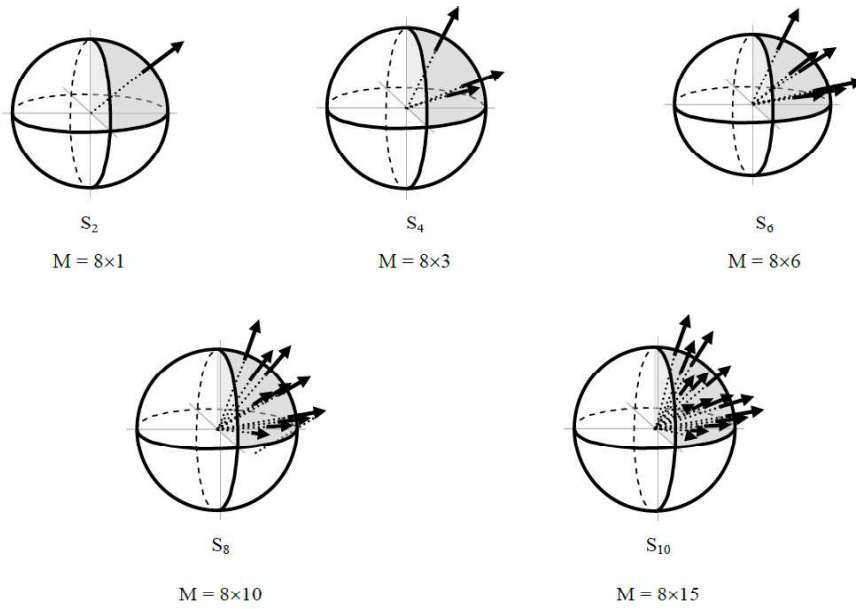
Figure 2.4. Orders of approximation for S_N

On the other hand, Thurgood and his co-workers [103] developed T_N angular discretization scheme which provides more accurate results and eliminates the ray effect. T_N angular discretization scheme utilizes the basal equilateral triangle of vertices at (1,0,0), (0,1,0), and (0,0,1) to map each octant. This basal triangle is then represented as N^2 smaller equilateral triangles. The direction of each ray that passes through the smaller triangles' centroids is defined as the direction of smaller triangles. The tessellations of the basal triangle and the sphere triangles for the T_4 quadrature set are demonstrated by Figure 2.5.
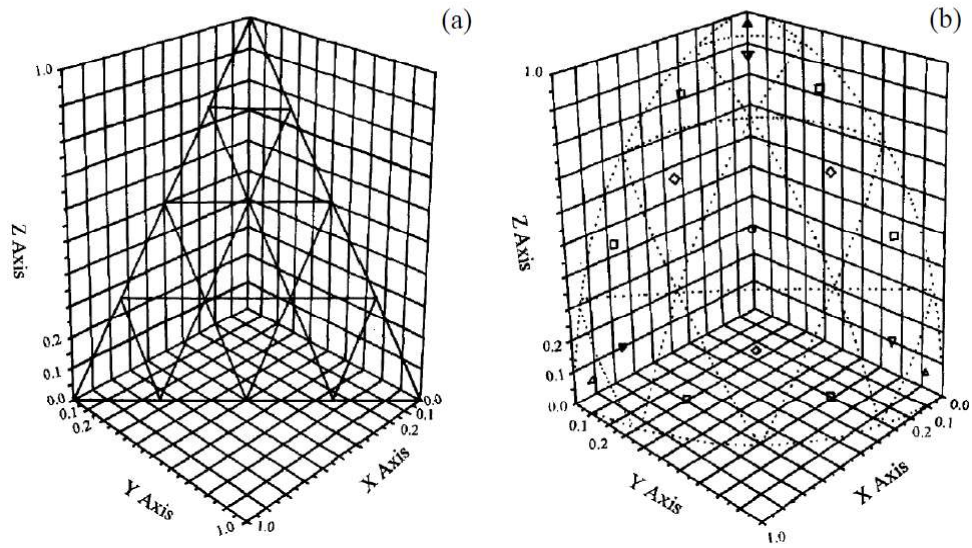
Figure 2.5. Orders of approximation for T_4 (a) Tessellation of basal equilateral triangle (b) sphere triangles [103]

The number of ordinates per octant and for all sphere for S_N and T_N angular discretization schemes and for a 3-D rectangular geometry are listed in Table 2.1. The details of the S_N and T_N angular discretization schemes involving quadrature weights and direction cosines are provided in Appendix A.

Table 2.1 Number of ordinates for S_N and T_N quadratures in 3-D systems

Angular Discretization Scheme	Number of ordinates per octant	Total number of ordinates
S_N	$N(N+2)/8$	$M=2^D N(N+2)/8$
T_N	N^2	$M=8 N^2$

2.1.3   Method of Lines (MOL) Solution of Discrete Ordinates Method (DOM)

For the MOL solution of DOM, the false-transients approach [104] is adopted by incorporating a pseudo-time derivative of intensity into the DOM representation of RTE:

$$k_t \frac{\partial I_\lambda^{m,\ell}}{\partial t} = -\mu_{m,\ell} \frac{\partial I_\lambda^{m,\ell}}{\partial x} - \eta_{m,\ell} \frac{\partial I_\lambda^{m,\ell}}{\partial y} - \xi_{m,\ell} \frac{\partial I_\lambda^{m,\ell}}{\partial z} - (\kappa_{g,\lambda} + \kappa_{p,\lambda} + \sigma_{p,\lambda}) I_\lambda^{m,\ell}$$

$$+ (\kappa_{g,\lambda} + \kappa_{p,\lambda}) I_{b,\lambda}$$

$$+ \frac{\sigma_{p,\lambda}}{4\pi} \sum_{m',l'} \Phi_\lambda (\Omega_{m',\ell'}, \Omega_{m,\ell}) w_{m',\ell'} I_\lambda^{m',\ell'} \tag{2.18}$$
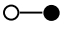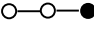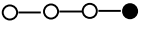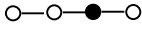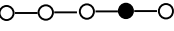
where t is the pseudo-time variable, k_t is introduced to maintain dimensional consistency in the equation which is taken as unity in this study. The set of discrete ordinates equations [Eq. (2.18)] is transformed into a set of initial value problems (ODEs) by discretizing the spatial derivatives in Eq. (2.18) using well known spatial discretization techniques such as finite differencing schemes. The resulting set of ODE can be solved by using a powerful ODE solver which is ROWMAP [105], based on ROW-methods of order four (a class of linearly implicit Runge-Kutta methods) utilizing Krylov techniques for the solution of linear systems. The selection of time steps is carried out by the ODE solver in such a way that the accuracy and stability of the solution is guaranteed. Since the steady state intensity profiles are not influenced by the initial conditions, the integration of ODEs can be started with any initial conditions. The ODE propagates in time by solving for the intensities at a time step, "n", calculating the time derivatives, and integrating again to solve for intensities at the new time step, "n+1". The solution is terminated when the radiative intensities for each ordinates and spatial grids comply with the condition given by the Eq. (2.19) and the intensity field is taken as the steady-state intensity field:

$$\frac{|I_n - I_{n-1}|}{I_{n-1}} < \epsilon \tag{2.19}$$

where ϵ is the error tolerance and subscript (n-1) stands for the intensity field at the previous time step.

For the discretization of spatial derivatives in DOM, FVM is utilized. In FVM, the set of differential equations is integrated over a control volume, and the resultant equation is discretized using a spatial differencing scheme. The details of FVM discretization of DOM can be found elsewhere [106]. On the other hand, for the discretization of spatial derivatives in MOL of DOM representation of RTE, two-point and three-point upwind differencing schemes (DSS012, DSS014), which are presented in Table 2.2 together with higher order approximations, are employed.

Table 2.2 Spatial differencing schemes with FDM utilized in MOL solution of DOM [107,108]

Name of the Scheme	Stencil	Formulation dI(λ_l)/d$\lambda \approx$	Order of Accuracy
2-point upwind (DSS012)	○—●	$(I_i - I_{i-1})/ \Delta \lambda$	$O(\Delta\lambda)$
3-point upwind (DSS014)	○—○—●	$(3I_i - 4I_{i-1} + I_{i-2})/ 2\Delta \lambda$	$O(\Delta\lambda^2)$
4-point upwind (DSS016)	○—○—○—●	$(11I_i - 18I_{i-1} + 9I_{i-2} - 2I_{i-3})/ 6\Delta \lambda$	$O(\Delta\lambda^3)$
4-point biased upwind (DSS018)	○—○—●—○	$(2I_{i+1} + 3I_i - 6I_{i-1} + I_{i-2})/ 6\Delta \lambda$	$O(\Delta\lambda^3)$
5-point biased upwind (DSS020)	○—○—○—●—○	$(3I_{i+1} + 10I_i - 18I_{i-1} + 6I_{i-2} - I_{i-3})/ 12\Delta \lambda$	$O(\Delta\lambda^4)$

2.1.4 Structure and Operation of the In-House Developed Code for the MOL Solution of DOM

Figure 2.6 and Figure 2.7 illustrate the algorithm of the computer code of MOL solution of DOM for a non-gray absorbing, emitting, and scattering medium (MOLSDOM - NGAESM) bounded by non-gray walls.
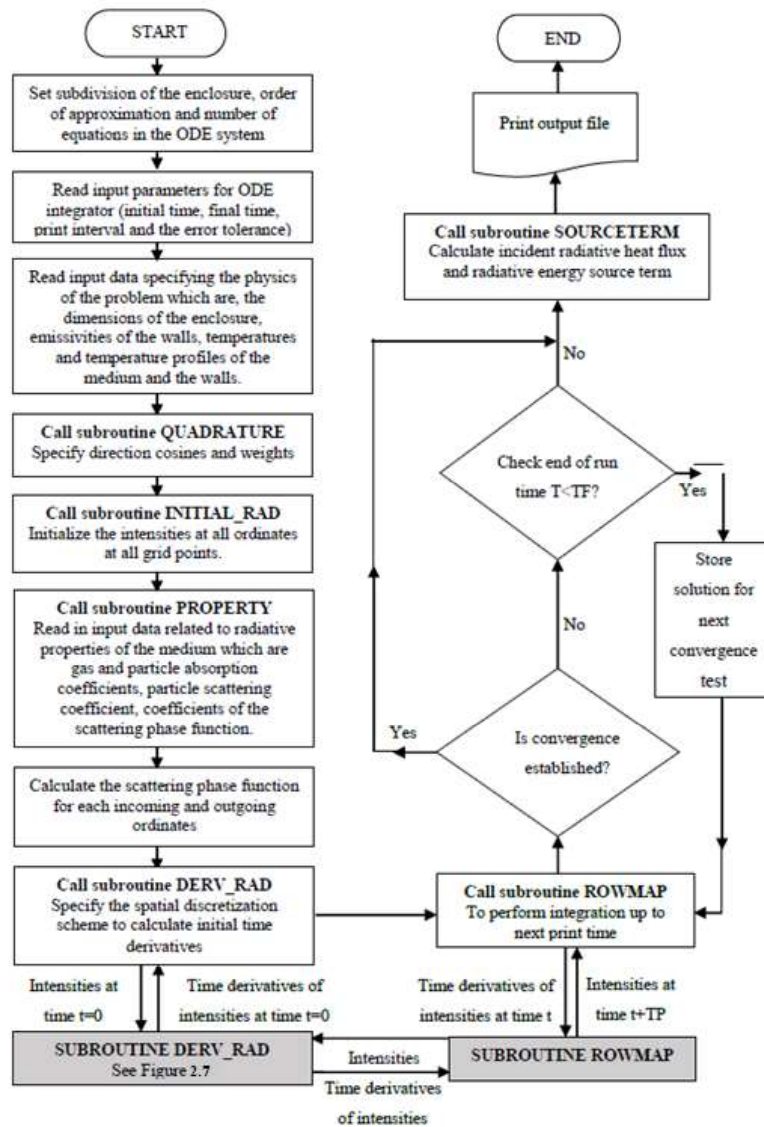
Figure 2.6. Flowchart for MOL solution of DOM for a non-gray absorbing, emitting, and scattering medium bounded by non-gray walls
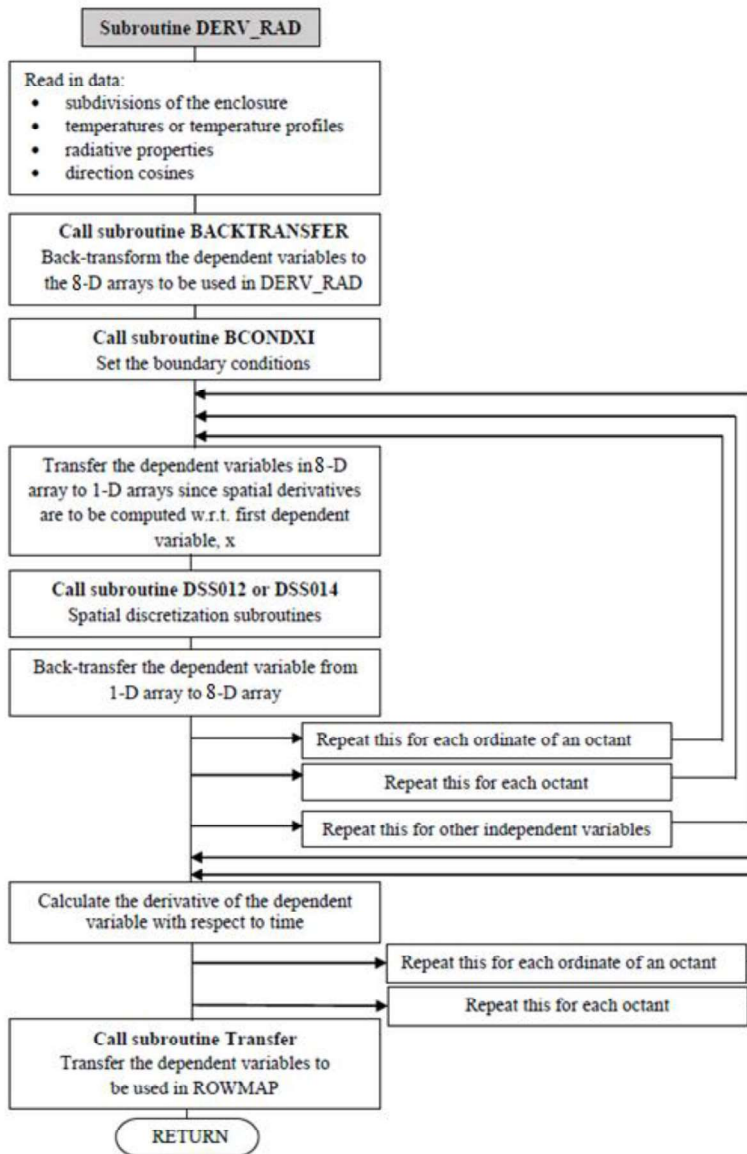
Figure 2.7. Algorithm of the subroutine DERV_RAD

2.2   Radiative Property Models for Combustion Gases

One of the major challenges of modeling of thermal radiation in FBCs is the accurate treatment of the radiative properties of the combustion gases (H_2O and CO_2) as they oscillate wildly throughout the thermal spectrum. Therefore, within the last few

decades, a wide variety of studies have been devoted to develop robust spectral gas radiative property models which are summarized in [46–48].

To summarize, line-by-line (LBL) and narrow band models [such as statistical narrow bands (SNB) and narrow band correlated-k (NBCK)] are considered to be the most accurate ones but they are computationally inefficient for large-scale engineering problems. Alternatively, wide-band models are developed to improve computational efficiency but with the cost of decreased level of accuracy. Nowadays, global models, involving the weighted sum of gray gases (WSGG) model [50], the spectral line-based weighted sum of gray gases (SLW) model [51–53], and the full spectrum correlated-k (FSCK) model [54], become popular for large-scale engineering problems as they improve the computational efficiency without a major loss in the accuracy. However, one of the major drawbacks of these models is that their application with non-gray particles and/or non-gray boundaries is limited [61].

One of the objectives of this study is to assess the accuracy and CPU efficiency of different radiative property models for combustion gases in order to find the best method. Therefore, throughout the study, 7 spectral and 1 gray gas radiative property models are utilized in conjuction with the 3-D radiation model described above. In the following sub-section, these models are described in detail.

2.2.1   Gray Gas Model Based on Gray Wide Band

For the estimation of gray gas radiative properties, the gray wide band (GWB) approach with a single wide band is utilized. In this approach, the absorption coefficient of the gas mixture in the gray wide band is represented as the Planck mean of spectral absorption coefficients obtained from narrow band models. Spectral absorption coefficients of the combustion gases can then be found as follows;

$$\kappa_{g_\lambda} = \left(\frac{1}{L}\right) ln\,(\tau_\lambda) \tag{2.20}$$

31

where $\tau_\lambda = 1 - \varepsilon_{g_\lambda}$ is the spectral gas transmissivity which can be calculated over an isothermal and homogeneous path by the expression proposed by Ludwig et al. [109];

$$\tau_\lambda(L) = \left[-\frac{\pi B}{2} \left(\sqrt{1 + \frac{4SL}{\pi B}} - 1 \right) \right] \tag{2.21}$$

where $B = 2\bar{\beta}_v/\pi^2$, $S = \bar{k}_v X p$, L is spectrally averaged mean beam length (= 3.6 volume/surface area), X is the mole fraction of radiating gas, p is the pressure, $\bar{k}_v$ is the mean line-intensity to spacing ratio, $\bar{\beta}_v = 2\pi\bar{\gamma}/\bar{\delta}_v$ is the mean line width to spacing ratio, $\bar{\gamma}$ is the mean collision half-width of an absorption line and $\bar{\delta}_v$ is the equivalent line spacing. $\bar{k}_v$, $\bar{\delta}_v$ and $\bar{\gamma}$ for H_2O and CO_2 can be obtained from [110].

The gray gas absorption coefficient can then be calculated by averaging over Planck distribution;

$$\kappa_g = \frac{\sum_{j'=1}^{NB} \kappa_{\lambda,j'} \Delta f_{j'}}{\sum_{j'=1}^{NB} \Delta f_{j'}} \tag{2.22}$$

where Δf is the fraction of blackbody emissive power in any wavelength interval;

$$\Delta f_{j'} = f(n\lambda_{j'+1}T) - f(n\lambda_{j'}T) \tag{2.23}$$

where f is the fraction of blackbody emissive power contained between 0 and $n\lambda T$ which is defined by Modest [46]:

$$f(n\lambda T) = \frac{\int_0^\lambda E_{b,\lambda} d\lambda}{\int_0^\infty E_{b,\lambda} d\lambda} \tag{2.24}$$

The term $E_{b,\lambda}$ in Eq. (2.24) is spectral blackbody emissive power and can be determined by Planck's law [46]. Further details are given in Appendix B.

2.2.2 Statistical Narrow Band Correlated-k (SNBCK)

The main idea of the SNBCK is that in a narrow band, any radiative quantity, φ_η, depends only on the gas absorption coefficient, and integration of that quantity over the wavenumber interval can be replaced with integration over the absorption coefficient;

$$\bar{\varphi}_\eta = \frac{1}{\Delta\eta} \int_{\Delta\eta} \varphi(\kappa_\eta)d\eta = \int_0^\infty f(k)\,\varphi(k)dk \tag{2.25}$$

where $f(k)$ is called k-distribution function and represents weighted sum of the number of spectral points where $\kappa_\eta = k$ in the wavenumber interval under consideration. As the k-distribution function behaves erratically at the local minima and maxima ($d\eta/d\kappa_\eta = 0$); a cumulative k-distribution function, $g(k)$, is introduced such that;

$$g(k) = \int_0^k f(k')dk' \tag{2.26}$$

$$\bar{\varphi}_\eta = \int_0^\infty f(k)\,\varphi(k)dk = \int_0^1 \varphi(k(g))dg \tag{2.27}$$

where $k(g)$ is the inverse of $g(k)$.

If accurate narrow band transmissivity data is available, k-distribution function can be determined by the inverse Laplace transformation of the transmissivity data [46]. For this purpose, the expression proposed by Ludwig et al. [109] [Eq. (2.21)] for the estimation of gas transmissivity over an isothermal and homogeneous path is adopted in this study.

By taking the inverse Laplace transform of Eq. (2.21) and using Eq. (2.26), the analytical expression for the cumulative k-distribution function is obtained [111]:

$$g(k) = \frac{1}{2}\left[1 - erf\left(\frac{a}{\sqrt{k}} - b\sqrt{k}\right)\right] + \frac{1}{2}\left[1 - erf\left(\frac{a}{\sqrt{k}} + b\sqrt{k}\right)\right]e^{\pi B} \tag{2.28}$$

where $a = \frac{1}{2}\sqrt{\pi BS}$, $b = \frac{1}{2}\sqrt{\pi B/S}$, and erf(x) is called error function.

The intensity field for narrow band can be obtained by applying the seven-point Gauss-Labatto quadrature to Eq. (2.21);

$$I_\eta = \sum_{i=1}^{N} w_i I(k(g_i)) \tag{2.29}$$

where N is the number of quadrature points which is 7 in this study, w_i is the weight parameter and $k(g_i)$ is the inverse of the cumulative k-distribution function, $g(k)$, in the quadrature point, i. $k(g_i)$ can easily be found by utilizing the Newton-Raphson method. The details of the SNBCK model can be found in [60,111,112].

2.2.3   Weighted Sum of Gray Gases (WSGG) Model

The LBL model and narrow band models such as NBCK or SNBCK are computationally inefficient for large-scale engineering problems as they require the solution of thousands or millions of RTE due to complex spectral dependence of gas radiative properties. Fortunately, it was shown that the absorption cross-section values are roughly reproduced in numerous wavelength intervals. For this reason, those absorption cross-sections can be grouped together and handled as separate gray gases with certain absorption cross-sections, $C_{abs,j}$. The representative illustration of the approximation of real spectrum with 4 gray gases is shown by Figure 2.8.
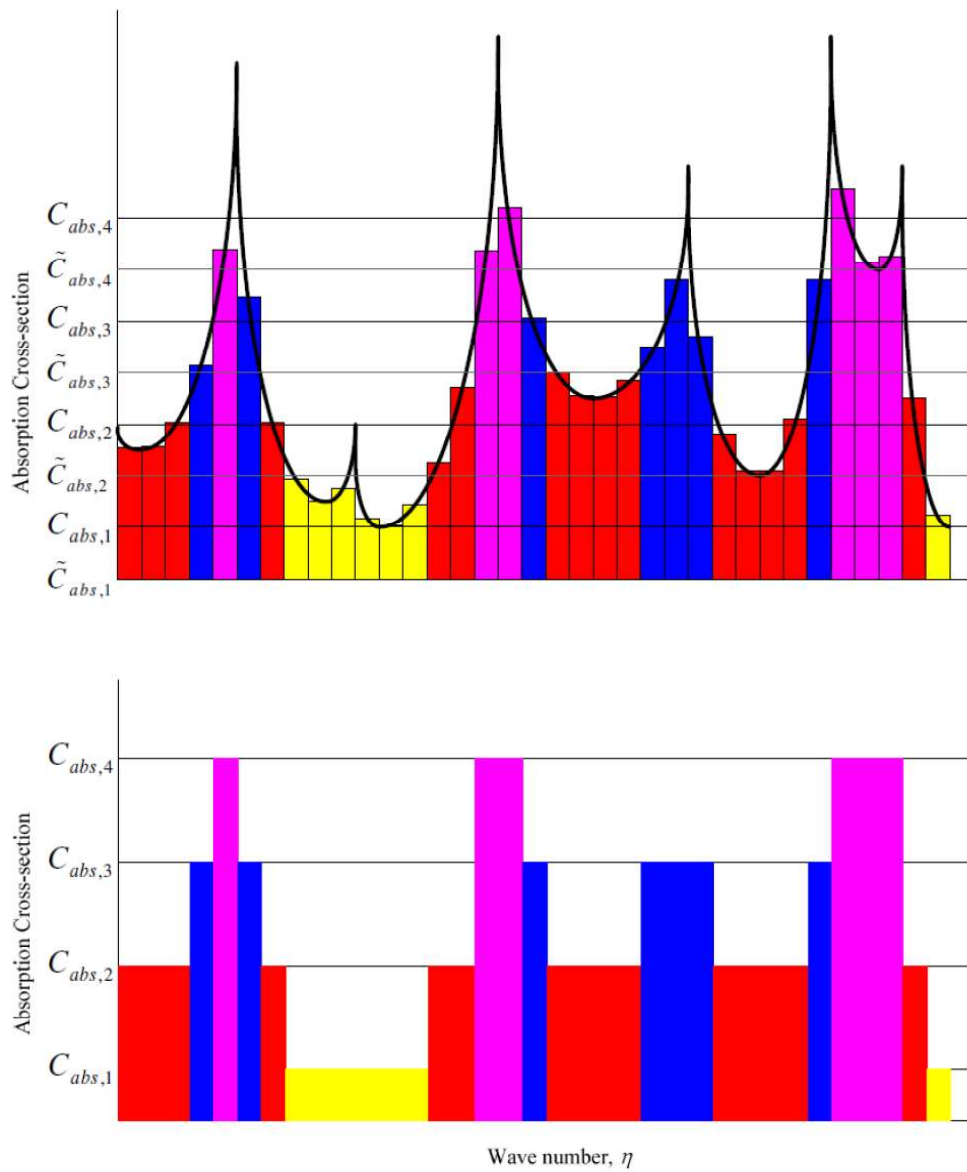
Figure 2.8. Approximation of a real spectrum by grouping into 4 gray gases [52]

The representation of the real non-gray radiating gases in terms of a certain number of gray gases is first suggested by Hottel and Sarofim [50], and commonly known as the Weighted Sum of Gray Gases (WSGG) model in the radiation literature. Due to its simplicity, sufficient accuracy, and CPU efficiency, WSGG has gained growing attention and is further improved.

The gas mixture in the WSGG is originally represented as a mixture of 1 clear gas and 4 gray gases, and the RTE is solved for each gas denoted by the subscript j in Eq. (2.30);

$$k_t \frac{\partial I_j^{m,\ell}}{\partial t} = -\mu_{m,\ell} \frac{\partial I_j^{m,\ell}}{\partial x} - \eta_{m,\ell} \frac{\partial I_j^{m,\ell}}{\partial y} - \xi_{m,\ell} \frac{\partial I_j^{m,\ell}}{\partial z} - \left(\kappa_{g,j} + \kappa_{p,j} + \sigma_{p,j} \right) I_j^{m,\ell}$$

$$+ \left(\kappa_{g,j} + \kappa_{p,j} \right) \alpha_j I_b$$

$$+ \frac{\sigma_{p,j}}{4\pi} \sum_{m',\ell'} \Phi_j(\Omega_{m',\ell'}, \Omega_{m,\ell}) w_{m',\ell'} I_j^{m',\ell'} \qquad (2.30)$$

where $\kappa_{g,j}$ and α_j are the absorption coefficients of the gray gas and gray gas weight, respectively. There are various techniques in the literature to determine the absorption coefficients and the weight of each gray gas. In the present work, 3 different approaches for the WSGG are used. These techniques are further explained in the following sub-sections.

2.2.3.1 Weighted Sum of Gray Gases Model of Bordbar et al. (WSGG – Bordbar)

One of the improvements of WSGG is achieved by Bordbar et al. [113] by generating a new set of coefficients to extend the WSGG model to oxy-fired combustion systems. For this purpose, Bordbar et al. [113] developed correlations for the absorption coefficients and gray gas weights as a function of temperature and CO_2 and H_2O mole fraction from the HITEMP 2010 database [114].

In this model, the gas mixture is represented as a mixture of 1 clear gas and 4 gray gases. As denoted earlier, the RTE is solved for each gas. It should be highlighted at this point that the ANSYS Fluent implementation of this model is carried out by using 5 spectral bands each representing clear or gray gases with a certain absorption coefficient and gray gas weight. The weight of each gray gas can be estimated by the following expression;

$$\alpha_j(T) = \sum_{k=1}^{4} b_{j,k} T_r^{\ k} \tag{2.31}$$

where T_r is the normalized temperature ($= T/T_{ref}$) with T_{ref} as 1200 K, j denotes gray gases, $b_{j,k}$ is the polynomial function of the molar fraction ratio ($M_r = X_{H_2O}/X_{CO_2}$);

$$b_{j,k} = \sum_{l=0}^{4} c_{j,k,l} M_r^{\ l} \tag{2.32}$$

The weight of the clear gas can then be found by subtracting the weight of each gray gas from unity:

$$\alpha_0(T) = 1 - \alpha_1(T) - \alpha_2(T) - \alpha_3(T) - \alpha_4(T) \tag{2.33}$$

Similarly, the absorption coefficient of each gray gas (in m^{-1}atm^{-1}) can be found by the following expression;

$$k_j = \sum_{l=1}^{4} d_{j,l} M_r^{\ l} \tag{2.34}$$

The coefficients suggested by Bordbar et al. [113], which are $d_{j,l}$ and $c_{j,k,l}$, are listed in Tables 2.3 and 2.4.

Table 2.3 $d_{j,l}$ coefficients of Bordbar et al. [113]

j	$l = 0$	$l = 1$	$l = 2$	$l = 3$	$l = 4$
1	0.034043	0.065230	-0.046369	0.013868	-0.001445
2	0.350946	0.746514	-0.529309	0.159442	-0.016633
3	4.570740	2.168067	-1.498901	0.491717	-0.054300
4	109.816900	-50.923590	23.432360	-5.163892	0.439389

Table 2.4 $c_{j,k,l}$ coefficients of Bordbar et al. [113]

j	k	$l = 0$	$l = 1$	$l = 2$	$l = 3$	$l = 4$
1	0	0.7412956	-0.5244441	0.5822860	-0.2096994	0.0242031
1	1	-0.9412652	0.2799577	-0.7672319	0.3204027	-0.0391017
1	2	0.8531866	0.0823075	0.5289430	-0.2468463	0.0310940
1	3	-0.3342806	0.1474987	-0.4160689	0.1697627	-0.0204066
1	4	0.0431436	-0.0688622	0.1109773	-0.0420861	0.0049188
2	0	0.1552073	-0.4862117	0.3668088	-0.1055508	0.0105857
2	1	0.6755648	1.4092710	-1.3834490	0.4575210	-0.0501976
2	2	-1.1253940	-0.5913199	0.9085441	-0.3334201	0.0384236
2	3	0.6040543	-0.0553385	-0.1733014	0.0791608	-0.0098934
2	4	-0.1105453	0.0464663	-0.0016130	-0.0035398	0.0006121
3	0	0.2550242	0.3805403	-0.4249709	0.1429446	-0.0157408
3	1	-0.6065428	0.3494024	0.1853509	-0.1013694	0.0130244
3	2	0.8123855	-1.1020090	0.4046178	-0.0811822	0.0062981
3	3	-0.4532290	0.6784475	-0.3432603	0.0883088	-0.0084152
3	4	0.0869309	-0.1306996	0.0741446	-0.0202929	0.0020110
4	0	-0.0345199	0.2656726	-0.1225365	0.0300151	-0.0028205
4	1	0.4112046	-0.5728350	0.2924490	-0.0798077	0.0079966
4	2	-0.5055995	0.4579559	-0.2616436	0.0764841	-0.0079084
4	3	0.2317509	-0.1656759	0.1052608	-0.0321935	0.0033870
4	4	-0.0375491	0.0229519	-0.0160047	0.0050463	-0.0005364

2.2.3.2　WSGG Model of Smith et al. (WSGG – Smith)

Another implementation of WSGG is suggested by Smith et al. [115] prior to the work of Bordbar et al. [113]. Although the WSGG model of Smith et al. [115] is a less sophisticated version of the WSGG model, it is commonly utilized especially in combustion studies. However, this model is limited to air-fired scenarios. Since the

system under investigation in this study is an air-fired system, the predictive accuracy of the WSGG model of Smith et al. [115] is also tested.

In the WSGG model of Smith et al. [115], the gas mixture is represented as a mixture of 1 clear gas and 3 gray gases, and the RTE is solved for each gray gas. Similar to the WSGG implementation of Bordbar et al. [113], the ANSYS Fluent implementation of this model is carried out by using 4 spectral bands each representing clear or gray gases with a certain absorption coefficient and gray gas weight.

The difference in the WSGG implementation of Smith et al. [115] is that the weights of the gray gases are only functions of temperature and do not depend on gas compositions. Instead, the effect of gas composition is imposed by the utilization of different coefficients for different mole fraction ratios of CO_2 and H_2O. The temperature-dependent gray gas weights for the WSGG model of Smith et al. [115] can be determined by the following expression:

$$\alpha_j(T) = \sum_{k=1}^{4} b_{j,k} T^{k-1} \tag{2.35}$$

The weight of the clear gas can then be found by subtracting the weight of each gray gas from unity:

$$\alpha_0(T) = 1 - \alpha_1(T) - \alpha_2(T) - \alpha_3(T) \tag{2.36}$$

The coefficients suggested by Smith et al. [113], $b_{j,k}$, are listed in Table 2.5 together with the absorption coefficients of each gray gas.

Table 2.5 $b_{j,k}$ coefficients and gas absorption coefficients of Smith et al. [113]

j	k_j (m^{-1}atm^{-1})	$b_{j,1} \times 10^1$	$b_{j,2} \times 10^4$	$b_{j,3} \times 10^7$	$b_{j,4} \times 10^{11}$
1	0.4303	5.150	-2.303	0.9779	-1.494
2	7.055	0.7749	3.399	-2.297	3.770
3	178.1	1.907	-1.824	0.5608	-0.5122

2.2.3.3   Domain-based WSGG (DBWSGG)

The domain-based WSGG is the implementation of the WSGG model by ANSYS Fluent software and is a readily available gas radiative property model in the software. Although its name implies otherwise, the model is actually a gray model in nature. For this model, the emissivity of the gas mixture (ε_g), consisting of 1 clear and 3 gray gases, is calculated by the following expression;

$$\varepsilon_g = \sum_{j=0}^{3} \alpha_j(T)\left(1 - exp\left(-k_j P_g (X_{CO_2} + X_{H_2O}) L_e\right)\right) \tag{2.37}$$

where P_g is the total absolute gas pressure, X_{CO_2} and X_{H_2O} are the mole fractions of CO_2 and H_2O, respectively, L_e is the mean beam length ($= 3.6 \times Volume/Surface\ area$), and j is the index for each gray gas. The absorption coefficient and gray gas weight of each gray gas [k_j and $\alpha_j(T)$] are determined by the same expressions and coefficients of Smith et al. [113] (see Eqs. (2.35) and (2.36) and Table 7). Finally, the overall absorption coefficient of the gas mixture (κ_g) to be used to solve the gray RTE is calculated by the following expression:

$$\kappa_g = -\frac{\ln(1 - \varepsilon_g)}{L_e} \tag{2.38}$$

2.2.4   Spectral Line-Based Weighted Sum of Gray Gases (SLW) Model

Denison and Webb [51–53] further improved the WSGG model by introducing a new parameter called absorption-line blackbody distribution function (ALBDF) from the HITRAN and HITEMP databases in order to accurately represent the gray gas weights. This extension is referred to as spectral line-based weighted sum of gray gases (SLW) and is considered to be a state-of-the-art gas property model [46]. The SLW model consists of two major steps. One of them is determination of gas absorption coefficients and estimation of their gray gas weights whereas the other

one is the solution of RTE for each gray gas mixture. In the following sections, these steps are explained in detail.

2.2.4.1   Calculation of Absorption Coefficients

Each gray gas represents the space between two consecutive supplemental absorption cross-sections ($\tilde{C}_{abs,j}$ and $\tilde{C}_{abs,j+1}$) and their absorption cross-sections are calculated as follows:

$$\tilde{C}_{abs,j} = exp\left(\frac{ln\left(\tilde{C}_{abs,j}\right) + ln\left(\tilde{C}_{abs,j+1}\right)}{2}\right) \tag{2.39}$$

Based on the recommendations of Dennison and Webb [52], the upper and lower limits of absorption cross-sections are selected as 3×10^{-5} and 60 m^2/mole for H_2O and 3×10^{-5} and 120 m^2/mole for CO_2 within the scope of this study. The absorption coefficient of gray gases can then be determined as follows;

$$\kappa_{g_j} = N C_{abs,j} \tag{2.40}$$

where molar density (*N*) is calculated utilizing the ideal gas equation of state. It should be highlighted at this point that one of the gray gases has a "zero absorption coefficient" and represents the transparent regions of the thermal spectrum.

2.2.4.2   Calculation of Gray Gas Weights

In the SLW model, an ALBDF (F_s) is introduced by Denison and Webb [51–53] for the efficient representation of gray gas weights. The ALBDF refers to the fraction of the blackbody emissive power ($E_{b,\eta}$) where the absorption cross-section ($C_{abs,\eta}$) is smaller than defined value C_{abs};

$$F_s(C_{abs}, T_b, T_g, P_T, Y_s) = \frac{1}{\sigma T_b^4} \int_{\Delta \eta_i(C_{abs}, T_b, T_g, P_T, Y_s)} E_{b,\eta}(\eta, T_b) d\eta \qquad (2.41)$$

where $E_{b,\eta}$ is determined by the Planck's law as a function of wave number (η) and blackbody temperature, T_b. The subscript i stands for the ith spectral band.

The blackbody weights (α_j) are determined by subtracting the two ALBDF representing two consecutive supplemental absorption cross-sections ($\tilde{C}_{abs,j}$ and $\tilde{C}_{abs,j+1}$):

$$a_j = F_s(\tilde{C}_{abs,j+1}, T_b, T_g, P_T, Y_s) - F_s(\tilde{C}_{abs,j}, T_b, T_g, P_T, Y_s) \qquad (2.42)$$

For the estimation of ALBDF for H_2O and CO_2, the hyperbolic tangent correlations suggested by Denison and Webb [51–53] are utilized. For H_2O vapor, the ALBDF is provided as follows;

$$F_w = \frac{1}{2} tanh(P_w(T_b, T_g, \xi - \xi_{sb})) + \frac{1}{2} \qquad (2.43)$$

where P_w is calculated by the following expression;

$$P_w(T_b, T_g, \xi - \xi_{sb}) = \sum_{m=0}^{3} \sum_{n=0}^{3} \sum_{l=0}^{3} b_{lmn} \left(\frac{T_g}{2500}\right)^n \left(\frac{T_b}{2500}\right)^m (\xi - \xi_{sb})^l \qquad (2.44)$$

where

$$\xi = ln(C_{abs}) \qquad (2.45)$$

$$\xi_{sb} = \sum_{m=0}^{3} \sum_{n=0}^{2} \sum_{l=0}^{3} c_{lmn} \left(\frac{T_b}{2500}\right)^n \xi^m (y_{H_2O})^{l+1} \qquad (2.46)$$

In a similar manner, the ALBDF for CO_2 is provided by;

$$F_c = \frac{1}{2} tanh(P_c(T_b, T_g, \xi)) + \frac{1}{2} \qquad (2.47)$$

where P_c is calculated by the following expression;

$$P_c(T_b, T_g, \xi) = \sum_{m=0}^{3} \sum_{n=0}^{3} \sum_{l=0}^{3} d_{lmn} \left(\frac{T_g}{2500}\right)^n \left(\frac{T_b}{2500}\right)^m (\xi)^l \qquad (2.48)$$

where

$$\xi = ln\,(C_{abs}) \qquad (2.49)$$

In Eqs. (2.43) to (2.49), the terms b_{lmn}, c_{lmn}, and d_{lmn} are the coefficients deduced from the HITRAN database and given in Tables 2.6, 2.7, and 2.8, respectively.

Table 2.6 b_{lmn} coefficients used for H_2O [52]

$$l = 0$$

n/m	0	1	2	3
0	1.61030	-0.81812	2.60010	-1.31710
1	-4.09310	15.55250	-21.20400	9.65240
2	5.14350	-21.81900	31.08280	-14.47400
3	-2.08570	9.87750	-14.27900	6.67470

$$l = 1$$

n/m	0	1	2	3
0	0.44019	-0.82164	1.51490	-0.81023
1	-0.63348	5.02390	-7.80320	3.72700
2	0.87163	-5.98180	9.86420	-4.87400
3	-0.38798	2.63550	-4.19310	1.98680

$$l = 2$$

n/m	0	1	2	3
0	0.10665	-0.38573	0.57835	-0.28014
1	-0.43116	1.88650	-2.62180	1.17850
2	0.68960	-2.97120	4.26980	-1.95680
3	-0.29831	1.28340	-1.79290	0.78725

$$l = 3$$

n/m	0	1	2	3
0	0.00825	-0.03106	0.04393	-0.02037
1	-0.03286	0.12337	-0.15792	0.06611
2	0.06816	-0.26154	0.35095	-0.15283
3	-0.03048	0.11745	-0.15308	0.06340

Table 2.7 c_{lmn} coefficients used for H_2O [52]

$$l = 0$$

n/m	0	1	2	3
0	4.72000	-0.84969	-0.03472	0.00058
1	-8.54820	0.31248	0.04025	0.00394
2	5.23940	-0.13804	-0.05801	-0.00529

$$l = 1$$

n/m	0	1	2	3
0	-8.96150	1.58610	0.04347	0.00287
1	16.95470	-2.01660	-0.67133	-0.07068
2	-10.76000	1.46000	0.63323	0.06237

$$l = 2$$

n/m	0	1	2	3
0	9.14610	-1.39750	0.08464	0.00715
1	-17.32700	1.99650	0.59999	0.06621
2	11.18640	-1.69350	-0.70054	-0.06873

$$l = 3$$

n/m	0	1	2	3
0	-3.55040	0.48539	-0.06775	-0.00593
1	6.62400	-0.70710	-0.18179	-0.02047
2	-4.30580	0.68911	0.26931	0.02564

Table 2.8 d_{lmn} coefficients used for CO_2 [52]

$$l = 0$$

n/m	0	1	2	3
0	2.45702	-4.02320	7.54549	-3.63104
1	-5.45334	15.67297	-23.80230	11.90780
2	6.53751	-24.32470	39.51896	-20.36060
3	-2.52344	11.33757	-19.11370	9.97877

$$l = 1$$

n/m	0	1	2	3
0	0.076568	0.290182	-0.642820	0.394216
1	2.361840	-12.004100	21.500300	-11.581800
2	-3.950610	22.443420	-40.866700	22.051760
3	2.174820	-13.046700	23.667620	-12.653600

$$l = 2$$

n/m	0	1	2	3
0	-0.03306	0.36730	-0.69811	0.38312
1	0.43677	-3.52466	6.60703	-3.65683
2	-0.72533	6.74885	-12.96670	7.19415
3	0.41386	-3.96295	7.58713	-4.16496

$$l = 3$$

n/m	0	1	2	3
0	-0.00188	0.02850	-0.05496	0.03042
1	0.01921	-0.22354	0.43709	-0.24779
2	-0.03259	0.44027	-0.88149	0.49908
3	0.01985	-0.26267	0.52196	-0.29157

2.2.4.3 Treatment of Non-Isothermal and Non-Homogeneous Media in SLW

Modeling RHT in non-isothermal and/or non-homogeneous gaseous media is challenging due to spatial variation of thermodynamic states and difficulties associated with radical variations of local radiative properties. Non-isothermal and/or non-homogeneous gaseous media is treated utilizing the reference approach in this study. In this approach, first, a reference state is chosen as the average of temperatures and CO_2 and H_2O concentration fields. Then, local absorption cross-sections (C_{abs}) can be estimated by equating the ALBDF evaluated at reference and local states;

$$F_s\left(\tilde{C}_{abs,j}, T_b = T_{ref}, T_g = T_{local}, Y_s = Y_{local}\right)$$
$$= F_s\left(\tilde{C}_{abs,j,ref}, T_b = T_{ref}, T_g = T_{ref}, Y_s = Y_{ref}\right) \tag{2.50}$$

where T_{local} is the local value of the temperature and T_{ref} and $Y_{s,ref}$ are the reference temperature and mole fraction, respectively. This implicit equation is solved by using an iterative solution method, which is bisection method in this study.

Then the local gray gas absorption cross-sections and blackbody weight of each gray gas are evaluated by the following expressions:

$$\kappa_{g_j} = N(T_{local}, Y_{s,local})C_{abs,j}(T_{local}, Y_{s,local}) \tag{2.51}$$

$$a_j = F_s\left(\tilde{C}_{abs,j+1}, T_b = T_{local}, T_g = T_{ref}, Y_s = Y_{s,ref}\right)$$
$$- F_s(\tilde{C}_{abs,j}, T_b = T_{local}, T_g = T_{ref}, Y_s = Y_{s,ref}) \tag{2.52}$$

2.2.4.4 Treatment of Binary Gas Mixtures in SLW

For modeling of heat transfer accurately for a medium involving binary gases such as CO_2 and H_2O, the RTE for rectangular domains is modified as follows:

$$k_t \frac{\partial I_{k,l}^{m,\ell}}{\partial t} = -\mu_{m,\ell} \frac{\partial I_{k,l}^{m,\ell}}{\partial x} - \eta_{m,\ell} \frac{\partial I_{k,l}^{m,\ell}}{\partial y} - \xi_{m,\ell} \frac{\partial I_{k,l}^{m,\ell}}{\partial z} - \left(\kappa_{g,k,l} + \kappa_p + \sigma_p\right) I_{k,l}^{m,\ell}$$

$$+\left(\kappa_{g,k,l} + \kappa_p\right)\alpha_{k,l} I_b$$

$$+\frac{\sigma_p}{4\pi} \sum_{m',\ell'} \Phi(\mathbf{\Omega}_{m',\ell'}, \mathbf{\Omega}_{m,\ell}) w_{m',\ell'} I_{k,l}^{m',\ell'} \tag{2.53}$$

where the indices k and l denote the kth and lth gray gas for H_2O and CO_2, respectively and $\alpha_{k,l}$ is the joint gray gas weights and can be found by the multiplication approach:

$$\alpha_{k,l} = \alpha_k \alpha_l \tag{2.54}$$

The summation of these joint gray gas weights must be unity:

$$\sum_l \sum_k \alpha_{k,l} = 1 \tag{2.55}$$

The absorption coefficients of the gas mixture ($\kappa_{g,k,l}$) are given as follows;

$$\kappa_{g,k,l} = N_k C_{abs,k} + N_l C_{abs,l} \tag{2.56}$$

where N_k and N_l are the molar densities of H_2O and CO_2, respectively.

2.2.5 Banded Spectral Line-Based Weighted Sum of Gray Gases (banded SLW)

Originally, SLW requires gray particle and wall properties as it is a global model. For this reason, it cannot be utilized with non-gray particles and non-gray walls [52]. Nevertheless, SLW weights can be related to the cumulative k-distributions through integration of Planck's function, which allows the calculation of gray gas weights for an arbitrary spectral band [52].

For modeling of heat transfer accurately for a medium involving binary gases such as CO_2 and H_2O together with non-gray particles and boundaries, the thermal

spectrum is divided into a certain number of spectral intervals where properties of particles and walls are taken to be constant. In an arbitrary j^{th} band, RTE given in Eq. (2.53) takes the following form;

$$k_t \frac{\partial I_{j,k,l}^{m,\ell}}{\partial t} = -\mu_{m,\ell} \frac{\partial I_{j,k,l}^{m,\ell}}{\partial x} - \eta_{m,\ell} \frac{\partial I_{j,k,l}^{m,\ell}}{\partial y} - \xi_{m,\ell} \frac{\partial I_{j,k,l}^{m,\ell}}{\partial z} - \left(\kappa_{g,j,k,l} + \kappa_{p,j} + \sigma_{p,j}\right) I_{j,k,l}^{m,\ell}$$

$$+ \left(\kappa_{g,j,k,l} + \kappa_{p,j}\right) \tilde{a}_{j,k} \tilde{a}_{j,l} \Delta f_j I_b$$

$$+ \frac{\sigma_{p,j}}{4\pi} \sum_{m',\ell'} \Phi_j(\Omega_{m',\ell'}, \Omega_{m,\ell}) w_{m',\ell'} I_{j,k,l}^{m',\ell'} \tag{2.57}$$

where the indices k and l denote the kth and l^{th} gray gas for H_2O and CO_2, respectively. Δf_j is the fraction of blackbody emissive power of the jth band. Gray gas weights $(\tilde{a}_{j,k} \tilde{a}_{j,l})$ utilized in Eq. (2.57) are normalized weights of the kth and l^{th} gray gases in the jth band. Normalization of the gray gas weights in the jth band can be achieved by the following expressions:

$$\tilde{a}_{j,k} = \frac{a_{j,k}}{\Delta f_j}, \quad \tilde{a}_{j,l} = \frac{a_{j,l}}{\Delta f_j} \tag{2.58}$$

Blackbody weights $(a_{j,k}, a_{j,l})$ within the jth band [Eq. (2.58)] are determined by using k-distributions (g_w and g_c) as follows;

$$a_{j,k} = \frac{1}{\sigma T^4} \left[\int_{\eta_j}^{\eta_{j+1}} g_w(\tilde{C}_{abs,k+1}, T, P, \eta) E_b(T, \eta) d\eta \right.$$

$$\left. - \int_{\eta_j}^{\eta_{j+1}} g_w(\tilde{C}_{abs,k}, T, P, \eta) E_b(T, \eta) d\eta \right] \tag{2.59}$$

$$a_{j,l} = \frac{1}{\sigma T^4} \left[\int_{\eta_j}^{\eta_{j+1}} g_c(\tilde{C}_{abs,l+1}, T, P, \eta) E_b(T, \eta) d\eta \right.$$

$$\left. - \int_{\eta_j}^{\eta_{j+1}} g_c(\tilde{C}_{abs,l}, T, P, \eta) E_b(T, \eta) d\eta \right] \tag{2.60}$$

$$E_b(T, \eta) = \frac{2\pi h c_0 \eta^3}{n^2 \left[exp\left(\frac{hc_0\eta}{nkT}\right) - 1 \right]} = \frac{3.7419 \times 10^{-8}\, \eta (cm^{-1})^3}{exp\left(\frac{1.4388\,\eta}{T}\right) - 1} \tag{2.61}$$

in which the integrations are performed by using Simpson's rule. The k-distribution functions g_w and g_c of H_2O and CO_2 for banded SLW model is calculated based on the hyperbolic tangent correlations suggested by Dennison and Webb [52];

$$g_{w,\iota}(\tilde{C}_{abs,k}, T) = \frac{1}{2} tanh(P_{w,\iota}) + \frac{1}{2} \tag{2.62}$$

$$P_{w,\iota}(T, \xi - \xi_{sb}) = \sum_{l=0}^{3} \sum_{m=0}^{3} \tilde{b}_{lm\iota} \left(\frac{T}{2500}\right)^m (\xi - \xi_{sb})^l \tag{2.63}$$

$$\xi = ln\,(\tilde{C}_{abs,k}) \tag{2.64}$$

$$\xi_{sb} = \sum_{l=0}^{3} \sum_{m=0}^{3} \tilde{c}_{lm\iota}\, \xi^m (y_{H_2O})^{l+1} \tag{2.65}$$

$$g_{c,\iota}(\tilde{C}_{abs,l}, T) = \frac{1}{2} tanh(P_{c,\iota}) + \frac{1}{2} \tag{2.66}$$

$$P_{c,\iota}(T, \xi) = \sum_{l=0}^{4} \sum_{m=0}^{3} \tilde{d}_{lm\iota} \left(\frac{T}{2500}\right)^m (\xi)^l \tag{2.67}$$

$$\xi = ln\,(\tilde{C}_{abs,l}) \tag{2.68}$$

where the index, ι, refers to the k-distribution function of the ιth spectral location which is given as $400\,\iota$ cm^{-1} and $300\,\iota$ cm^{-1} for H_2O and CO_2, respectively. The coefficients $\tilde{b}_{lm\iota}$, $\tilde{c}_{lm\iota}$, and $\tilde{d}_{lm\iota}$ are given in Appendix C. It should be noted that Eq.

(2.68) needs modification at 2400 cm^{-1} ($\eta=300\iota=300\times8=2400$ cm^{-1}) for the strongest CO_2 absorption band [52]. At this wavenumber, the k-distribution function is given as [52]:

$$g_{c,8}(\tilde{C}_{abs,l}, T, P) = 0.2535 \, tanh(P_{c,a}) + 0.2465 \, tanh(P_{c,b}) + \frac{1}{2} \qquad (2.69)$$

where functions $P_{c,a}$ and $P_{c,b}$ are calculated by using Eq. (2.67) with the coefficients $\tilde{d}_{lm\iota}$.

Finally, the absorption coefficient of the gas mixture ($\kappa_{g_{j,k,l}}$) in Eq. (2.57) can be found using Eq. (2.56) for each spectral band.

Gas emissivity in the jth band can be calculated by using the following expression;

$$\varepsilon_{g,j} = \sum_{l=1}^{NGC} \sum_{k=1}^{NGW} a_{j,k} a_{j,l} (1 - e^{-\kappa_{g_{k,l}} L}) \qquad (2.70)$$

where L is the spectrally averaged mean beam length and NGW and NGC are the numbers of gray gases for H_2O and CO_2, respectively. Total gas emissivity is then determined by spectral averaging of gas emissivities in each band:

$$\varepsilon_g = \frac{\sum_{j=1}^{NB} \varepsilon_{g,j} \Delta f_j}{\sum_{j=1}^{NB} \Delta f_j} \qquad (2.71)$$

2.2.6   One-Gas Spectral Line-Based Weighted Sum of Gray Gases (SLW-1)

In the banded SLW model, repeated solution of RTE for each gas mixture in each band is necessary. For this reason, CPU time requirements significantly increase for especially multi-dimensional engineering problems due to the increase in the number of RTE (N_{RTE}) to be solved;

$$N_{RTE} = N_{time} \times N_{grid} \times N_{direction} \times N_{band} \times N_{gray \, gas \, k} \times N_{gray \, gas \, l} \qquad (2.72)$$

where N_{time} denotes the number of time steps in the MOL approach, N_{grid} is the number of grids, $N_{direction}$ is the number of discrete directions, N_{band} is the number of bands and $N_{gray\ gas\ k}$ and $N_{gray\ gas\ l}$ are the number of gray gases for H_2O and CO_2, respectively.

The efficient and minimal formulation of SLW can be achieved by representing the thermal spectrum as a mixture of single gray gas and a clear gas, which is referred to as SLW-1 [81,116]. One of the main challenges to this model is to determine the absorption coefficient (κ_1) and gray gas weight (a_1) of the gray gas. Among various methods for the determination of these properties, the approach based on two emissivities [81,116], where κ_1 and a_1 are determined by fitting the total gas emissivities calculated at two different path lengths L_1 and L_2, as in $\varepsilon_1 = \alpha_1(1 - e^{-\kappa_1 L_1})$ and $\varepsilon_2 = \alpha_1(1 - e^{-\kappa_1 L_2})$, is utilized owing to its simplicity and sufficient accuracy [81]. Using the double integration SLW, the total emissivity of the binary mixture for two different path lengths can be calculated with a sufficient number of gray gases;

$$\varepsilon_{mix}(L_1) = \sum_{k=1}^{NGW}\sum_{l=1}^{NGC} a_k a_l (1 - e^{-\kappa_{g_{k,l}}L_1}) \tag{2.73}$$

$$\varepsilon_{mix}(L_2) = \sum_{k=1}^{NGW}\sum_{l=1}^{NGC} a_k a_l (1 - e^{-\kappa_{g_{k,l}}L_2}) \tag{2.74}$$

where the gray gas weights are found by using Eq. (2.42) and the absorption coefficients of the gas mixtures are obtained from Eq. (2.56). The gray gas parameters (κ_1 and a_1) are then found by solving the following system of algebraic equations, which has a unique solution for $\kappa_l > 0$:

$$\varepsilon_{mix}(L_1) = \alpha_1(1 - e^{-\kappa_1 L_1}) \tag{2.75}$$

$$\varepsilon_{mix}(L_2) = \alpha_1(1 - e^{-\kappa_1 L_2}) \tag{2.76}$$

Dividing Eq. (2.75) by Eq. (2.76), a_1 can be eliminated and κ_1 can be found using Newton's method with an error tolerance of 10^{-4}. Finally, clear gas parameters can be determined by the following expressions:

$$\kappa_0 = 0 \tag{2.77}$$

$$\alpha_0 = 1 - \alpha_1 \tag{2.78}$$

2.2.7 Banded One-Gas Spectral Line-Based Weighted Sum of Gray Gases (SLW-1)

Similar to the SLW model, the SLW-1 model also is not applicable for media involving non-gray particles and/or boundaries in its original form. However, this problem can be alleviated by dividing the thermal spectrum into several spectral bands where properties of particles and walls are taken to be constant and representing each band as a mixture of single gray gas and a clear gas, which is referred to as banded SLW-1 [87].

Using the double integration to banded SLW, the total emissivity of the binary mixture for two different path lengths for each spectral band, j, can be calculated with a sufficient number of gray gases;

$$\varepsilon_{j,mix}(L_1) = \sum_{k=1}^{NGW} \sum_{l=1}^{NGC} \tilde{a}_{j,k}\tilde{a}_{j,l}(1 - e^{-\kappa_{g_{j,k,l}}L_1}) \tag{2.79}$$

$$\varepsilon_{j,mix}(L_2) = \sum_{k=1}^{NGW} \sum_{l=1}^{NGC} \tilde{a}_{j,k}\tilde{a}_{j,l}\left(1 - e^{-\kappa_{g_{j,k,l}}L_2}\right) \tag{2.80}$$

where the gray gas weights are found by using Eqs. (2.59) and (2.60), and the absorption coefficients of the gas mixtures are obtained from Eq. (2.56). For each band, the gray gas parameters ($\kappa_{j,1}$ and $a_{j,1}$) are then found by solving the following system of algebraic equations, which has a unique solution for $\kappa_{j,l} > 0$:

$$\varepsilon_{j,mix}(L_1) = \alpha_{j,1}(1 - e^{-\kappa_{j,1}L_1}) \tag{2.81}$$

$$\varepsilon_{j,mix}(L_2) = \alpha_{j,1}(1 - e^{-\kappa_{j,1}L_2}) \qquad\qquad (2.82)$$

Clear gas parameters can be determined for each band using the same expressions for SLW-1 [Eqs. (2.77) and (2.78)].

For the approach based on two emissivities to determine gray gas parameters of the SLW-1 model, $\varepsilon_{j,mix}(L_1)$ and $\varepsilon_{j,mix}(L_2)$ in Eqs. (2.79) and (2.80) are calculated for 10 x 10 (H_2O x CO_2) gray gas mixtures. Furthermore, based on the recommendations of Solovjov et al. [81], all L_1 and L_2 values utilized in this study are selected to capture a range of path lengths that are both smaller and greater than the length defined by the physical boundaries. In order to define the physical boundaries of the system under consideration, three different definitions are utilized, and their predictive accuracies are tested against the benchmark solutions and measurements. The physical boundary definitions tested in this study are the height of the freeboard, spectrally averaged mean beam length (L_m) and spectrally dependent mean beam length (L_e). Their calculation methods are given in Appendix D.

2.2.8   Bordbar's 10 Band Model

In an attempt to develop a simple and accurate banded gas radiative property model, Bordbar et al. [61] divided the thermal radiation spectrum into 10 bands based on the band dividing scheme of Maximov [89] who demonstrated that those 10 bands (shown in Table 2.9) represent the spectral regions where the most significant contributions of H_2O and CO_2 to absorption and emission of thermal radiation occur in the thermal conditions corresponding to combusting systems. The contribution of H_2O and CO_2 to absorption and emission in the remaining spectral parts, on the other hand, were assumed to be negligible. In fact, those regions were considered as windows.

Table 2.9 Band intervals recommended by Maximov [89] for combusting systems

Band No.	Start (µm)	End (µm)
1	1.338	1.465
2	1.770	2.105
3	2.454	2.632
4	2.632	2.878
5	4.167	4.706
6	5.263	5.970
7	6.154	7.843
8	8.889	12.90
9	12.90	16.67
10	16.67	66.67

Bordbar et al. [61] provided simple correlations for the determination of the band gas absorption coefficients covering operating conditions corresponding to practical combusting systems using databases of band gas absorption coefficients obtained by implementing the statistical narrow band model. Correlations for band gas absorption coefficients were obtained for different molar fraction ratios ($M_r = \chi_{H_2O}/\chi_{CO_2}$) of 1/8, 1/4, 1/2, 1 and 2 and for pure H_2O and CO_2 covering the temperature range between 500 and 2400 K and path length range between 10 cm and 15 m.

The following form of correlation was suggested by Bordbar et al. [61] to approximate the gas absorption coefficients for the active bands:

$$\kappa_{g,j} = a_1 + a_2 \ln(T) + a_3 \ln(PL) + a_4 ln^2(T) + a_5 ln^2(PL)$$
$$+ a_6 \ln(T) \ln(PL) \tag{2.83}$$

where $PL = (\chi_{H_2O} + \chi_{CO_2})P_i L$ in which L is the spectrally averaged mean beam length. The coefficients of Eq. (2.83) (a_1 to a_6) for each spectral interval were determined by a curve fitting procedure, based on a non-linear least square method,

utilizing the band absorption coefficient database obtained by implementing the statistical narrow band model. Details of the statistical narrow band model and curve-fitting procedure can be found elsewhere [61,89]. Coefficients of Eq. (2.83) for an H_2O-CO_2 mixture with M_r = 1 and 1/8, representing the air-fired and oxy-fired combustion systems, are tabulated in Tables 2.10 and 2.11, respectively whereas the coefficients for the mixtures with different molar fraction ratios can be found in [61].

Table 2.10 Coefficients for the correlations of the band gas absorption coefficient of an H_2O-CO_2 mixture with M_r = 1 [61]

Band	a_1	a_2	a_3	a_4	a_5	a_6
1	0.919122	-0.050875	-0.339151	-0.00672	-0.002178	0.042970
2	0.877775	-0.158920	-0.197953	0.009788	-0.001119	0.022207
3	9.613162	-1.987588	-1.360774	0.108578	0.026032	0.146709
4	12.89373	-2.377743	-2.992425	0.138231	0.049245	0.307937
5	37.16659	-14.80333	6.976153	1.655044	0.794430	-1.86095
6	11.92844	-2.417743	-1.792236	0.129435	0.040327	0.190125
7	9.502207	-1.881765	-1.542546	0.110609	0.065159	0.130306
8	9.472530	-3.357394	0.751424	0.297754	-0.001391	-0.122498
9	19.34950	-6.853713	1.623699	0.701101	0.224327	-0.523703
10	4.952210	-1.433418	-0.075431	0.176454	0.210895	-0.204262

Table 2.11 Coefficients for the correlations of the band gas absorption coefficient of an H_2O-CO_2 mixture with $M_r = 1/8$ [61]

Band	a_1	a_2	a_3	a_4	a_5	a_6
1	0.199322	0.002452	-0.081722	-0.00318	-0.000569	0.010554
2	0.460116	-0.066706	-0.120368	0.002554	-0.001168	0.015310
3	2.567918	-0.485771	-0.460969	0.023309	0.003067	0.054005
4	10.55948	-2.613615	-1.550354	0.219032	0.043157	0.107953
5	56.53518	-22.67026	11.456380	2.512294	1.195645	-2.908978
6	4.556402	-0.988243	-0.605158	0.056484	0.006011	0.069641
7	2.413270	-0.407942	-0.546100	0.019668	0.010303	0.055666
8	3.523753	-1.456466	0.436200	0.146622	-0.002814	-0.073248
9	23.16641	-7.684319	0.816435	0.768879	0.270188	-0.473434
10	1.890447	-0.937951	0.448627	0.131430	0.067787	-0.151218

Bordbar's 10 band model [61] is originally developed for systems involving combustion gases only. To adopt Bordbar's 10 band gas radiative property model into this study which contains particle-laden combustion gases, windows between the active bands are also considered together with the active bands as contributions of particles to absorption, emission, and scattering in those windows cannot be neglected in the freeboard of a BFBC. However, contributions of H_2O and CO_2 to absorption and emission in those windows are neglected i.e., gas absorption coefficients in the windows are taken to be zero to comply with Bordbar's 10 band model. Furthermore, the regions including $\lambda < 1.338$ μm and $\lambda > 16.67$ μm are discarded due to the absence of spectral properties of particles and walls. That neglection of spectral regions will not have a significant effect on RHT predictions as the spectral region between 1.338 μm and 16.67 μm was found to cover 97 % of the thermal radiation in the system under consideration within the scope of this study. This is why 15 wavelength intervals (9 active bands and 6 windows) presented in Table 2.12 are utilized in this study.

Table 2.12 Band dividing scheme utilized in this study

Band No.	Start (μm)	End (μm)
1 (Active Band)	1.338	1.465
2 (Window)	1.465	1.770
3 (Active Band)	1.770	2.105
4 (Window)	2.105	2.454
5 (Active Band)	2.454	2.632
6 (Active Band)	2.632	2.878
7 (Window)	2.878	4.167
8 (Active Band)	4.167	4.706
9 (Window)	4.706	5.263
10 (Active Band)	5.263	5.970
11 (Window)	5.970	6.154
12 (Active Band)	6.154	7.843
13 (Window)	7.843	8.889
14 (Active Band)	8.889	12.90
15 (Active Band)	12.90	16.67

As Bordbar's 10 band model utilizes a single gray gas mixture in each band, gas emissivity in an arbitrary spectral band can be found as follows:

$$\varepsilon_{g,j} = (1 - e^{-\kappa_{g,j}L}) \tag{2.84}$$

Finally, the total gas emissivity can be determined by spectral averaging of band gas emissivities by the following expression:

$$\varepsilon_g = \frac{\sum_{j=1}^{NB} \varepsilon_{g,j}\Delta f_j}{\sum_{j=1}^{NB} \Delta f_j} \tag{2.85}$$

2.3 Radiative Property Models for Particles, Particle Clouds, and Aggregates

Another challenging aspect of modeling RHT in FBCs is to estimate the radiative properties of particles in the system. Although particle's radiative properties do not have a complex spectral dependence, they have a complex directional dependence due to their type, composition, shape, size, and optical properties.

Particles in the combusting systems continuously emit and absorb thermal radiation in the whole thermal spectrum and may also scatter thermal radiation depending on particle size. Generally, interaction between particles and radiation is considered to be dictated by four main factors: (i) shape of the particle, (ii) ratio of particle size to the wavelength, (size parameter, $x = \pi d_p / \lambda$), (iii) optical properties of particle and (iv) the relative distance between the particles (c/λ).

In general, interaction between particles and incident radiation depends on four major factors:

Although FBCs, due to their low operation temperatures, lead to insufficient melting of fly ash particles to be shaped as spherical [14], in modeling of thermal radiation, particles are generally taken to be in the ideal shapes like spheres or cylinders. This approach leads to very accurate results as non-symmetry caused by the irregular shape of particles is evened by the clouds. To test this hypothesis, Gronarz et al. [16] investigated the effect of the non-sphericity of particles on the radiative properties of particle clouds. The radiative properties of non-spherical particles, with sphericities ranging from 0.5 to 2.0, were calculated using T-matrix whereas those of spherical particles were calculated using Mie theory. Their results show that the non-sphericity of particles leads to insignificant deviations (less than 10 %) in absorption and scattering properties, and Mie theory can be utilized to estimate those properties.

Combusting systems involve particles of various size from nanometres (soot) to millimeters (coal particles in FBCs). For ash particles, this range is between around

1 and 1000 μm for FBCs (with a mean diameter usually less than 50 μm and 300 μm, for BFBC and CFBC, respectively). Under the operating conditions of FBCs, majority (99 %) of the thermal radiation is between 1-20 μm corresponding to a size parameter range of 0.1-3000. This large particle size range of FBCs leads to differences in interaction between particles and thermal radiation. Therefore, the dependence of the interaction between particles and thermal radiation on particle size must be treated carefully.

The most important particle optical property in RHT calculations is the complex index of refraction (m = n-ik) which is the combination of refractive (n) and absorption indices (k) of particles. The refractive index (n) dictates the scattering of thermal radiation by particles whereas the absorption index (k) is related with the absorption of thermal radiation by particle and emission of particles. The complex index of refraction (RI), in general, depends on wavelength, temperature, and chemical composition and directly influences the spectral dependence of the particles' radiative properties. Therefore, its proper treatment is of substantial importance.

Distance between the particles, in other words, the concentration of particles, defines particle-radiation interactions in the presence of particle clouds. The scattering may be independent or dependent when scattering by a single particle is not affected or affected by the neighboring particles, respectively. For the independent scattering, cloud properties can be determined by utilizing the properties of single particles, on the other hand, scattering of thermal radiation by particles is represented with a different probability distribution. In other words, when the particles are close enough to each other, they typically absorb more than when they absorb individually. Figure 2.9 illustrates the different scattering regimes as a function of particle volume fraction and size parameter. As highlighted by the figure, particles in combusting systems tend to show independent scattering behavior, hence, particle radiative property model described in the following sections are only for the independent regimes.
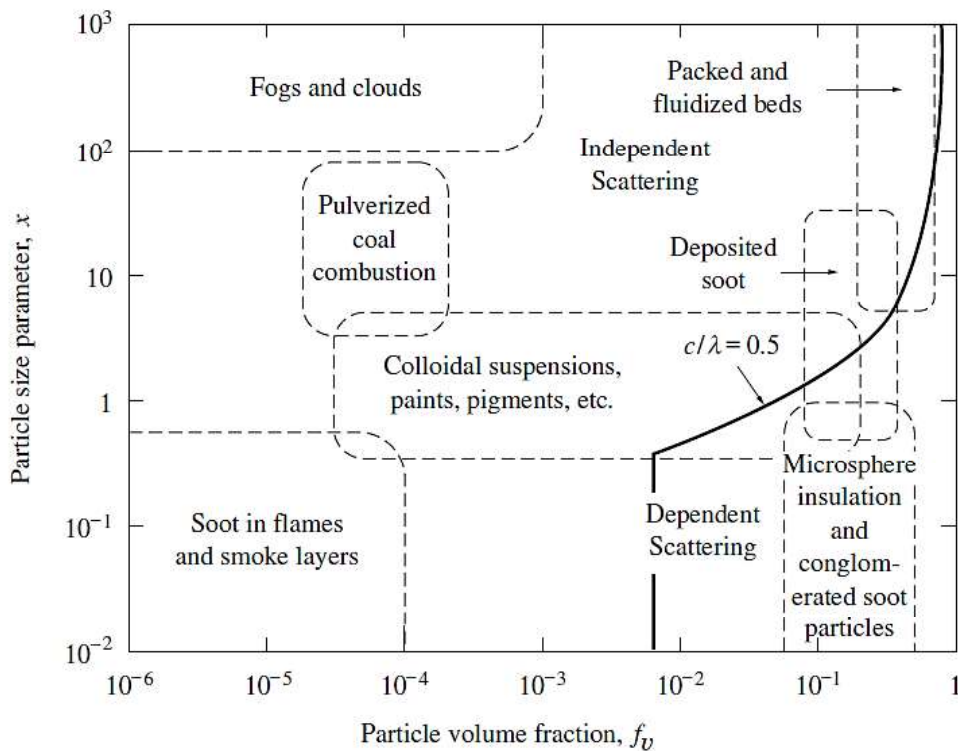
Figure 2.9. Dependent and independent scattering regimes [46]

2.3.1   Radiative Properties of a Single Spherical Particle

Lord Rayleigh first investigated the interaction between single spherical particles with thermal radiation in the nineteenth century. He developed a simple solution for very small spheres compared to the wavelength of thermal radiation (x << 1). This solution for the very small particles is generally referred to as the 'Rayleigh scattering theory in the literature'. Later, in 1908, Gustav Mie developed an equivalent analytical solution to Maxwell's equations which is valid for all sizes of spherical particles. This theory describing absorption and scattering behaviors of spherical particles is generally referred to as 'Mie theory' or 'Lorenz-Mie theory'. This solution gives the extinction cross-section ($C_e(n, k, x, \lambda)$), scattering albedo

$(\omega_0(n, k, x, \lambda))$ and the phase function $(\Phi(n, k, x, \theta, \lambda))$ as functions of size parameter $(x = \pi d_p/\lambda)$ and RI $(m(\lambda) = n(\lambda) - ik(\lambda))$.

The extinction cross-section is defined as the summation of absorption and scattering cross-sections $(C_a(n, k, x, \lambda)$ and $C_s(n, k, x, \lambda)))$ as follows:

$$C_e(n, k, x, \lambda) = C_a(n, k, x, \lambda) + C_s(n, k, x, \lambda) \tag{2.86}$$

Particles' interaction with the thermal radiation is generally described as a function of efficiencies instead of cross sections. The absorption and scattering efficiencies can be found by dividing the cross-sections to the projectile surface area of particles:

$$Q_e(n, k, x, \lambda) = C_e(n, k, x, \lambda)/\pi R^2 \tag{2.87}$$

$$Q_a(n, k, x, \lambda) = C_a(n, k, x, \lambda)/\pi R^2 \tag{2.88}$$

$$Q_s(n, k, x, \lambda) = C_s(n, k, x, \lambda)/\pi R^2 \tag{2.89}$$

The scattering phase function (Φ), on the other hand, describes the probability of scattering of the incident radiation from its direction. Furthermore, in the modeling of thermal radiation in FBCs, scattering of thermal radiation by particles is taken to be elastic which means that the wavelength does not alter during scattering.

2.3.1.1   Limiting Solutions of Maxwell Equations

As mentioned above, Mie theory is valid for all sizes of spherical particles, however, it is computationally intensive. For this purpose, some more CPU-efficient limiting solutions of Maxwell equations can be solved to estimate the particles' radiative properties for specific cases. These limiting solutions are Rayleigh scattering theory $(x|n - 1| \ll 1)$, Rayleigh-Gans scattering $(x|n - 1| \ll 1$ and $k \ll 1)$, Anomalous Diffraction $(x \gg 1$ and $n \approx 1)$, and geometric optics approximation (GOA) with diffraction $(x \gg 1$ and $x|n - 1| \gg 1)$. Among them, Rayleigh scattering theory is commonly used in the estimation of radiative properties of soot. Furthermore, Ates et al. [40,42] showed that GOA provides accurate predictions for the particles'

radiative properties in CFBC. In the present work, special emphasis is given to the RHT calculations for BFBCs involving fly ash, coal/char, and soot particles and exhaust plumes of solid rocket motors involving alumina particles. Therefore, only the details of Rayleigh scattering theory and Mie theory are provided in the following sub-sections.

2.3.1.2   Rayleigh Scattering Theory

The interaction between thermal radiation and very small spheres was investigated long before the development of Mie theory. For such particles (x << 1) the spectral absorption and scattering coefficients of the soot particles can be estimated using the following expressions [117,118];

$$\kappa_{p,\lambda} = \frac{6\pi f_v}{\lambda} Im\left\{\frac{m^2-1}{m^2+2}\left[1 + \frac{x^2}{15}\left(\frac{m^2-1}{m^2+2}\right)\frac{m^4+27m^2+38}{2m^2+3}\right]\right\} \tag{2.90}$$

$$\sigma_{p,\lambda} = \frac{4\pi^4 d_p^4 f_v}{\lambda^4}\left|\left(\frac{m^2-1}{m^2+2}\right)\right|^2 \tag{2.91}$$

where f_v is the particles volume fraction, d_p is the particle diameter, λ is the wavelength, x is the particle size parameter ($= \pi d_p/\lambda$) and m is the RI. As can be seen from the Eqs. (2.90) and (2.91), the absorption coefficient is diversely proportional to λ whereas the scattering coefficient is diversely proportional to λ^4. In other words, for very small particles, the scattering of thermal radiation becomes very small or negligible compared to absorption. Furthermore, gas molecules tend to scatter the light with shorter wavelengths, as represented by Rayleigh scattering theory, which explains the color of the sky.

The scattering phase function for the very small particles (x << 1) is calculated as follows:

$$\Phi_p(\theta) = \frac{3}{4}(1 + cos^2\theta) \tag{2.92}$$

However, it was observed that this scattering phase function does not deviate from the isotropic scattering significantly.

2.3.1.3   Mie Theory

In Mie theory, complex amplitude functions $S_1(\theta)$ and $S_2(\theta)$ are utilized to express the extinction cross-section and scattering cross-section of particles. These amplitude functions are defined as functions of RI (m) and size parameter (*x*);

$$S_1(\theta) = \sum_{n=1}^{\infty} \frac{(2n+1)}{n(n+1)} [a_n \pi_n(\cos \theta) + b_n \tau_n(\cos \theta)] \tag{2.93}$$

$$S_2(\theta) = \sum_{n=1}^{\infty} \frac{(2n+1)}{n(n+1)} [b_n \pi_n(\cos \theta) + a_n \tau_n(\cos \theta)] \tag{2.94}$$

where π_n and τ_n are the Legendre polynomials;

$$\pi_n(\cos \theta) = \frac{dP_n(\cos \theta)}{d\cos \theta} \tag{2.95}$$

$$\tau_n(\cos \theta) = \cos \theta \, \pi_n(\cos \theta) - \sin^2\theta \, \frac{d\pi_n(\cos \theta)}{d\cos \theta} \tag{2.96}$$

and a_n and b_n are the Mie scattering coefficients:

$$a_n = \frac{\psi_n{}'(mx)\psi_n(x) - m\psi_n(mx)\psi_n{}'(x)}{\psi_n{}'(mx)\xi_n(x) - m\psi_n(mx)\xi_n{}'(x)} \tag{2.97}$$

$$b_n = \frac{m\psi_n{}'(mx)\psi_n(x) - \psi_n(mx)\psi_n{}'(x)}{m\psi_n{}'(mx)\xi_n(x) - \psi_n(mx)\xi_n{}'(x)} \tag{2.98}$$

ψ_n and ξ_n are referred to as the Ricatti-Bessel functions and defined by the following expressions [46],

$$\psi_n(z) = \left(\frac{\pi z}{2}\right)^{\frac{1}{2}} J_{n+\frac{1}{2}}(z) \tag{2.99}$$

$$\xi_n(z) = \left(\frac{\pi z}{2}\right)^{\frac{1}{2}} H_{n+\frac{1}{2}}(z)$$ (2.100)

where the functions J and H represent the Bessel and Hankel functions, respectively.

The Legendre polynomial P_n is defined as follows;

$$P_n(i) = \frac{1}{2} \sum_{k=0}^{n} \binom{n}{k}^2 (i-1)^{n-k}(i+1)^k$$ (2.101)

such that P_n becomes as given by Eqs. (2.102) to (2.105) for n = 0, 1, 2, 3 …,

$$P_0(\cos\theta) = 1$$ (2.102)

$$P_1(\cos\theta) = \cos\theta$$ (2.103)

$$P_2(\cos\theta) = \frac{1}{2}(3(\cos\theta)^2 - 1)$$ (2.104)

$$P_3(\cos\theta) = \frac{1}{2}(5(\cos\theta)^3 - 3\cos\theta)$$ (2.105)

The amplitude functions $S_1(\theta)$ and $S_2(\theta)$ given by Eqs. (2.93) and (2.94) are utilized to represent extinction and scattering cross-sections as follows [46];

$$C_e = \frac{4\pi R^2}{x^2} \mathfrak{R}(S(0))$$ (2.106)

$$C_s = \frac{\pi R^2}{x^2} \int_0^\pi (i_1 + i_2)\sin(\theta)\,d\theta$$ (2.107)

where $\mathfrak{R}(S(0))$ is the real part of $S(0)$ and i_j is represented by the following expression:

$$i_j = |S_j|^2$$ (2.108)

If $S_1(\theta)$ and $S_2(\theta)$ are inserted into Eqs. (2.106) and (2.107), then the individual particle radiative properties become functions of a_n and b_n;

65

$$C_e = \frac{2\pi R^2}{x^2} \sum_{n=1}^{\infty} (2n+1)\Re(a_n + b_n) \tag{2.109}$$

$$C_s = \frac{2\pi R^2}{x^2} \sum_{n=1}^{\infty} (2n+1)(|a_n|^2 + |b_n|^2) \tag{2.110}$$

The following expression defines the ratio of scattered energy to a certain direction θ to the total incident radiation:

$$\frac{I_{scattered}(\theta)}{I_{incident}} = \frac{1}{2}\frac{i_1 + i_2}{x^2} \tag{2.111}$$

By dividing (Eq. (2.111)) to the total scattering incident radiation, the scattering phase function can be found:

$$\Phi = \frac{\dfrac{I_{scattered}(\theta)}{I_{incident}}}{\dfrac{1}{\pi} \int_{4\pi} \dfrac{I_{scattered}(\theta)}{I_{incident}} d\Omega} = \frac{i_1 + i_2}{\dfrac{1}{4\pi} \int_{4\pi} (i_1 + i_2) d\Omega} = 2\frac{i_1 + i_2}{Q_s} \tag{2.112}$$

Nevertheless, the solution of Eq. (2.112) is too time consuming. Scattering phase function can also be expressed by Legendre polynomials as follows;

$$\Phi = 1 + \sum_{n=1}^{\infty} A_n P_n(cos\,\theta) \tag{2.113}$$

where A_n coefficients are calculated only once from a_n and b_n. On the other hand, this procedure using Legendre polynomials to determine the scattering phase function is still laborious for many practical engineering applications. For this purpose, scattering phase function is generally expressed by the asymmetry factor (g) which is defined as follows;

$$g = \overline{cos\,\theta} = \frac{1}{4\pi} \int_{4\pi} \Phi(\theta)\,cos\,\theta\,d\Omega \tag{2.114}$$

where g ranging from -1 to +1 which stands for the purely backward scattering and purely forward scattering, respectively.

66

In the present study, the radiative properties of particles are calculated by extending the BHMIE code based on Mie theory [46].

2.3.2   Radiative Properties of Polydisperse Particle Clouds

In many engineering applications, especially in combusting systems, it has to be dealt with a large collection of particles which are called clouds. If the scattering is independent, as in the case of this study, the effect of the existence of such clouds is simply additive. These clouds may include uniform size particles. However, in real-life engineering problems, particles in the clouds have a PSD.

Solution of RTE in FBCs requires the radiative properties of particle clouds such as absorption coefficient, scattering coefficient, and scattering phase function in addition to gas absorption coefficient rather than the radiative properties of single particles which are absorption and scattering efficiency. In this section, the determination of radiative properties of uniform-size and non-uniform-size particle clouds by using the radiative properties of single particles is described.

For a uniform size particle cloud, the cloud properties can be calculated by multiplying the total number of particles (N_T) with the absorption, scattering, and extinction cross-sections:

$$\kappa_{p,\lambda} = N_T C_a = \pi R^2 N_T Q_{a,\lambda} \tag{2.115}$$

$$\sigma_{p,\lambda} = N_T C_s = \pi R^2 N_T Q_{s,\lambda} \tag{2.116}$$

$$\beta_{p,\lambda} = N_T C_e = \pi R^2 N_T Q_{e,\lambda} \tag{2.117}$$

where $\kappa_{p,\lambda}$, $\sigma_{p,\lambda}$ and $\beta_{p,\lambda}$ are the spectral absorption, scattering, and extinction coefficients. If the particles in the cloud have a uniform size, the scattering phase function and the asymmetry factor do not change with respect to the particle size such that:

$$\Phi_\lambda(\theta) = \Phi_{\lambda,\text{single}}(\theta) \tag{2.118}$$

$$g_\lambda(\theta) = g_{\lambda,\text{single}}(\theta) \tag{2.119}$$

However, when the particles are present in a cloud of non-uniform size distribution as in practical systems, properties of the particle cloud can be found by the summation of the particle properties of each size, which yields [46];

$$\kappa_{p,\lambda} = \int_0^\infty \frac{\pi d_p^2}{4} Q_{a,\lambda}(d_p) N(d_p) d d_p \tag{2.120}$$

$$\sigma_{p,\lambda} = \int_0^\infty \frac{\pi d_p^2}{4} Q_{s,\lambda}(d_p) N(d_p) d d_p \tag{2.121}$$

$$\overline{g_\lambda} = \frac{1}{\sigma_{p,\lambda}} \int_0^\infty \frac{\pi d_p^2}{4} Q_{s,\lambda}(d_p) g_\lambda(d_p) N(d_p) d d_p \tag{2.122}$$

$$\overline{\Phi_\lambda} = \int_0^\infty \frac{\pi d_p^2}{4} Q_{s,\lambda}(d_p) \Phi_\lambda(d_p) N(d_p) d d_p \Big/ \int_0^\infty \frac{\pi d_p^2}{4} Q_{s,\lambda}(d_p) N(d_p) d d_p \tag{2.123}$$

where $N(d_p) d d_p$ is the number of particles with a diameter between d_p and $d_p + d d_p$. The total number of particles and particle volume fraction are defined as:

$$N_T = \int_0^\infty N(d_p) d d_p \tag{2.124}$$

$$f_v = \frac{4}{3}\pi \int_0^\infty \frac{d_p^3}{8} N(d_p) d d_p \tag{2.125}$$

Eqs. (2.120) − (2.122) require a continuous PSD function such as Rosin-Rammler size distribution function. In the presence of experimentally measured data providing a discrete size distribution of particles, Eqs. (2.120) − (2.122) can be rewritten as follows:

$$\kappa_{p,\lambda} = \frac{3}{2} \sum_{i=1}^{N_t} \frac{Q_{a,\lambda}(d_{p_i}) B w_i}{\rho_p d_{p_i}} \tag{2.126}$$

$$\sigma_{p,\lambda} = \frac{3}{2} \sum_{i=1}^{N_t} \frac{Q_{s,\lambda}(d_{p_i}) B w_i}{\rho_p d_{p_i}} \tag{2.127}$$

$$\overline{g_\lambda} = \sum_{i=1}^{N_t} \frac{g_\lambda(d_{p_i}) B w_i}{\rho_p d_{p_i}} \bigg/ \sum_{i=1}^{N_t} \frac{B w_i}{\rho_p d_{p_i}} \tag{2.128}$$

where B is the total particle load and w_i is the differential weight of particles in the ith size interval.

2.3.3 Scattering Phase Function Simplifications

Generally large particles are present in FBCs leading to strong forward scattering tendencies (g ~ 0.5 – 0.95). In such systems, Henyey-Greenstein phase function [46] has been found to provide successful approximations of scattering phase functions as a function of g and θ;

$$\Phi_\lambda(\theta) = \frac{1 - {g_\lambda}^2}{(1 + {g_\lambda}^2 - 2g_\lambda \cos\theta)^{1.5}} \tag{2.129}$$

where g_λ is the spectral asymmetry factor. Henyey-Greenstein phase function has a non-oscillatory smooth behavior while the acute forward scattering peak increases with the increasing asymmetry factor.

Nevertheless, much simpler approaches such as transport approximation [119] in which the forward scattering peak is taken into account by a Dirac-delta function whereas isotropic scattering is used to represent rest of the scattering angles. To achieve this objective, a modified scattering coefficient which is given by the Eq. (2.130) is utilized for the solution of RTE:

$$\sigma_{p_j}{}^{tr} = \sigma_{p_j}\left(1 - g_j\right) \tag{2.130}$$

Within the scope of this thesis study, both approaches are used to represent the anisotropy in the scattering of thermal radiation by particles.

2.3.4   Radiative Properties of Soot Aggregates

Soot particles are masses of carbon with some impurities originating from incomplete combustion of hydrocarbons. Those particles are usually spherical and small, between around 5 nm to 80 nm in size. Furthermore, thermal radiation emitted by soot particles is considerably stronger compared to that emitted by combustion gases. Therefore, absorption and scattering of radiation by soot particles are needed to be considered for the modeling of RHT in combusting systems.

Generally, the diameter of soot particles is very small compared to the wavelengths in infrared radiation. Under these circumstances, Rayleigh's theory is expected to hold for the estimation of the radiative properties of soot particles. However, soot particles can combine into large aggregates resembling mass fractals consisting of hundreds of particles as highlighted by Figure 2.10, which in turn makes the use of both Rayleigh's theory and spherical-particle assumption questionable.
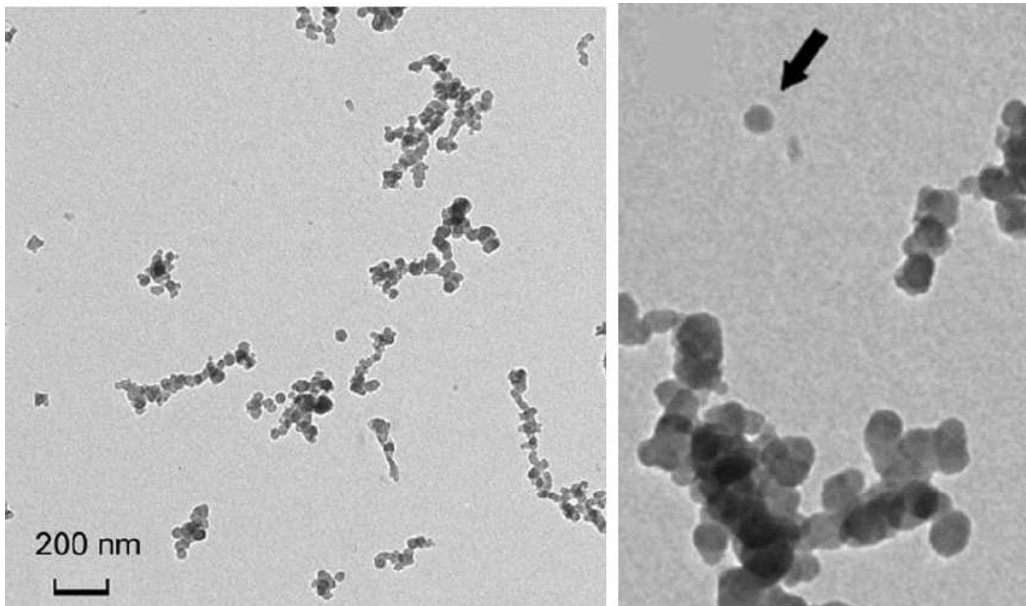
Figure 2.10. TEM images of soot particles and aggregates [120]

Recently, some numerically exact simulations for the determination of radiative properties of soot aggregates have been conducted using T-matrix and generalized

multisphere Mie (GMM) solutions; however, they are computationally intensive. Later, Mackowski [121] calculated absorption cross-sections of soot aggregates (C_a^a) using electrostatic approximation (ESA) with different indices of refraction and found that absorption cross-sections of the soot aggregates are well correlated by the following expression by confirming the results against the exact GMM formulation;

$$\frac{C_a^a}{NC_a^p} = \frac{3}{2N+1} + \frac{2(N-1)}{2N+1}\left(\frac{C_a^a}{NC_a^p}\right)_\infty \tag{2.131}$$

where C_a^p is the absorption cross-section of a single soot particle, N is the number of soot particles in the aggregate and $\left(C_a^a/NC_a^p\right)_\infty$ is the limiting value for $N \to \infty$. For typical soot, $\left(C_a^a/NC_a^p\right)_\infty$ value can be taken as 1.06 [46]. However, this expression cannot represent the effect of agglomeration of scattering cross-section (C_s^a) as it also depends on the primary particle size of soot. Effect of agglomeration on scattering cross-section for large-agglomerate (for $N \to \infty$) is well represented by fractal Rayleigh–Debye–Gans (RDG) formulation:

$$\left(\frac{C_s^a}{NC_s^p}\right)_\infty = \frac{k_f}{(2\alpha)^{D_f}}\left[\frac{3}{2-D_f} - \frac{12}{(6-D_f)(4-D_f)}\right] \tag{2.132}$$

where C_s^p is the scattering cross-section of a single soot particle, D_f is the mass fractal dimension, k_f is fractal prefactor. It has been shown that D_f and k_f values are almost universal and ranging between $1.6 - 1.9$ and $2.0 - 2.6$ [46], respectively.

For intermediate values of N, the scattering cross-section of soot aggregates can be estimated accurately using the simple power-law expression developed by Farias et al. [122]:

$$\frac{C_s^a}{NC_s^p} = \left(\frac{C_s^a}{NC_s^p}\right)_\infty^{1-N^{-1/4}} \tag{2.133}$$

Banded radiative soot particles' properties and aggregates is found by using Eq. (2.134);

$$\varphi_j = \frac{\sum_{j'=1}^{NB} \varphi_{\lambda,j'} \Delta f_{j'}}{\sum_{j'=1}^{NB} \Delta f_{j'}} \qquad (2.134)$$

where φ_j represents either $\kappa_{p,j}$ or $\sigma_{p,j}$.

Finally, Planck-mean properties are utilized as gray radiative properties of soot particles and aggregates.

2.3.5 Complex Index of Refraction Models for Particles

The radiative properties of particles are strong functions of particles' RI. Therefore, accurate and proper treatment of the RI of particles is of significant importance. In the literature, particles' RI data are generally presented as experimental measurements or empirical/semi-empirical models. In the present work, RHT calculations are applied to the systems involving fly ash particles, soot particles and aggregates, and alumina particles. For this purpose, only the estimation of the RI of these particles is provided in the following sub-sections.

2.3.5.1 Complex Index of Refraction of Fly Ash Particles

Within the last few decades, a significant amount of effort has been devoted to measure the RI of fly ash particles which are summarized in [45,102]. Among them, Goodwin [123] reported the first comprehensive measurements of the RI of coal slags as a function of wavelengths, temperatures, and ash compositions under the typical conditions of combusting systems. Based on these measurements covering a wavelength range of 0.7-13 μm, Goodwin suggested semi-empirical correlations to estimate the absorption and refractive indices of ash particles with respect to ash compositions, density, wavelength and temperature. The input parameters for the correlation of Goodwin are listed in Table 2.13. As shown by the table, the correlation of Goodwin depends on the ash composition which makes it difficult to be coupled with a radiation model. Another important aspect of Goodwin's model of

RI is that it requires the oxidation state of iron atoms which is rarely known. However, Goodwin's measurements and correlations are commonly used as benchmark in the thermal radiation literature [45,102].

Table 2.13 Input Parameters for Goodwin's Model Equations

Wavelength Interval (µm)	Input Parameters	
	Refractive Index, n	Absorption Index, k
1-4	Mass fractions of SiO_2, Al_2O_3, Fe_2O_3, CaO, MgO and TiO_2 Particle density	Fe_2O_3 mass fraction Oxidation state of iron atoms $(Fe^{+2}/(Fe^{+2}+Fe^{+3}))$ $g(\lambda)$; tabulated data
4-8		SiO_2 mass fraction k_0; tabulated data
8-13	SiO_2 mass fraction	SiO_2 mass fraction

Another semi-empirical model is developed by Ebert [124] as an extension of Goodwin's study to extend Goodwin's model of RI to elevated temperatures and for a wider range of ash compositions. In particular, this model is valid for ash particles with SiO_2 content less than 95 % and Fe_2O_3 content less than 30 % and for operating temperatures up to 1600 °C. Moreover, the summation of mass fractions of SiO_2, Al_2O_3, Fe_2O_3, CaO, MgO, and TiO_2 is needed to be more than 0.80.

The details and equations of Goodwin's and Ebert's models for RI of coal slags can be found in Appendix E.

2.3.5.2   Complex Index of Refraction of Soot

The optical properties of soot have been investigated by many researchers using different forms of carbon and measurement techniques which are briefly summarized in [46]. Among these studies, the measurements of Chang and Charalampopoulos [125] for the soot produced by propane flames have received very much attention. Chang and Charalampopoulos [125] also provided a polynomial expression deduced from their measurements which is applicable for the wavelength interval of $0.4 - 30$ μm:

$$n = 1.811 + 0.1263 ln\lambda + 0.0270 ln^2\lambda + 0.0417 ln^3\lambda \qquad (2.135)$$

$$k = 0.5821 + 0.1213 ln\lambda + 0.2309 ln^2\lambda - 0.0100 ln^3\lambda \qquad (2.136)$$

It should be noted at this point that Tien and Lee [126] stated that the   optical properties of soot do not significantly affect by flames of different fuels with different H/C ratios. This is why, the polynomial expression deduced from their measurements of Chang and Charalampopoulos [125] where soot produced by propane flames is used for the coal flames.

2.3.5.3   Complex Index of Refraction of Alumina Particles

Alumina particles are present in the typical exhausts of solid rocket motors as the addition of alumina to the propellant stabilizes the combustion process due to the micron size of aluminum particles and greatly raises the thrust level. However, exhaust plumes of such systems are characterized by high infrared emission owing to the presence of alumina which makes them prone to be detected by infrared space or airborne surveillance sensors. For this purpose, several researchers measured the optical properties of alumina [127–133]. Although the refractive index of alumina is found to be consistent in all studies, it was concluded that the absorption indices of alumina vary several orders of magnitude [134]. The strong discrepancies between the absorption indices of alumina reported earlier are considered to be due to the

phase and crystal structure of alumina and the presence of impurities in alumina [135–137]. In a recent study [131], it was stated that the liquid phase alumina transforms into a metastable phase which is γ-Al₂O₃. This metastable phase is then transformed into α-Al₂O₃ which is referred to as the stable phase. On the other hand, another study carried out by [138] states that the formation of γ and α phases probably depends on the temperature-time history of the particles. Furthermore, they [138] have stated that smaller particles tend to be made by the gamma phase.

Based on the above-mentioned discussion, it is considered necessary to investigate the effect of optical properties of different phases and crystal structures of alumina on RHT under rocket plume conditions. For this purpose, refractive and absorption indices of γ-Al₂O₃ are taken from Anfimov et al. [131] as given in Eqs. (2.137) to (2.143);

$$n = \left\{ 1 + \lambda^2 \left(\frac{1.02378}{\lambda^2 - 0.00377588} + \frac{1.058264}{\lambda^2 - 0.0122544} + \frac{5.280792}{\lambda^2 - 321.36164} \right) \right\}^{0.5}$$
$$\times \left[1 + 0.029 \left(\frac{T}{1000} - 0.473 \right) \right] \tag{2.137}$$

$$k = \zeta_0 + \zeta_1 + \zeta_2 + \zeta_3 \tag{2.138}$$

where ζ_0, ζ_1, ζ_2 and ζ_3 are terms stand for the absorption by vibration band, by the free electrons, by the edge fundamental band, and Urbach edge absorption, respectively;

$$\zeta_0 = 7.93 \times 10^{-4} \lambda exp \left[-\frac{6.07 \times 10^{-3}}{T} \left(\frac{10^4}{\lambda} - 1333 \right)^2 \right]$$
$$\times \left[1 - exp \left(-\frac{1.917 \times 10^3}{T} \right) \right] \tag{2.139}$$

$$\zeta_1 = 1.0 \times 10^{-2} \frac{\lambda}{n} \exp \left(-\frac{7.2 \times 10^3}{T \lambda_g} \right) \tag{2.140}$$

$$\zeta_2 = 2.1 \times 10^{-9} \lambda \left(\frac{1}{\lambda} - \frac{2}{\lambda_g} \right)^2 T^2 + 1.5 \times 10^{-2} \frac{\lambda_g}{2} \tag{2.141}$$

$$\zeta_3 = 1.5 \times 10^{-2} \lambda \exp\left[-\frac{2.8 \times 10^3}{T}\left(\frac{2}{\lambda_g} - \frac{1}{\lambda}\right)\right] \qquad (2.142)$$

where:

$$\frac{1}{\lambda_g} = 0.6916\left(\frac{1.289 \times 10^4}{T} - 3.233\right) \qquad (2.143)$$

The refractive and absorption indices of α-Al$_2$O$_3$ are taken from Querry [127]. On the other hand, for liquid alumina, two different RI data are used. The first one is the combination of Anfimov et al. [131] (given in Eq. (2.137)) and Bakhir et al. [132]:

$$k = 0.002(0.06\lambda^2 + 0.7\lambda + 1)exp[1.847(T/1000 - 2.95)] \qquad (2.144)$$

The second one is taken from the study of Kuzmin et al. [129]:

$$n = 1.747 + 0.0066\lambda - 0.0068\lambda^2 + 0.00003T \qquad (2.145)$$

$$log(k) = -2.19 + 0.089\lambda^{0.95} - 0.00056(3200 - T)\lambda^{-0.45} \qquad (2.146)$$

Using the spectral refractive and absorption indices given above, the medium is treated as a mixture of an absorbing-emitting gas and absorbing-emitting-scattering particles. The spectral and gray representations of alumina particles' refractive and absorption indices are demonstrated by Figure 2.11. As shown by the figure, gray and spectral refractive indices of alumina are quite similar in the wavenumber range between $2000 - 4000$ cm^{-1}.
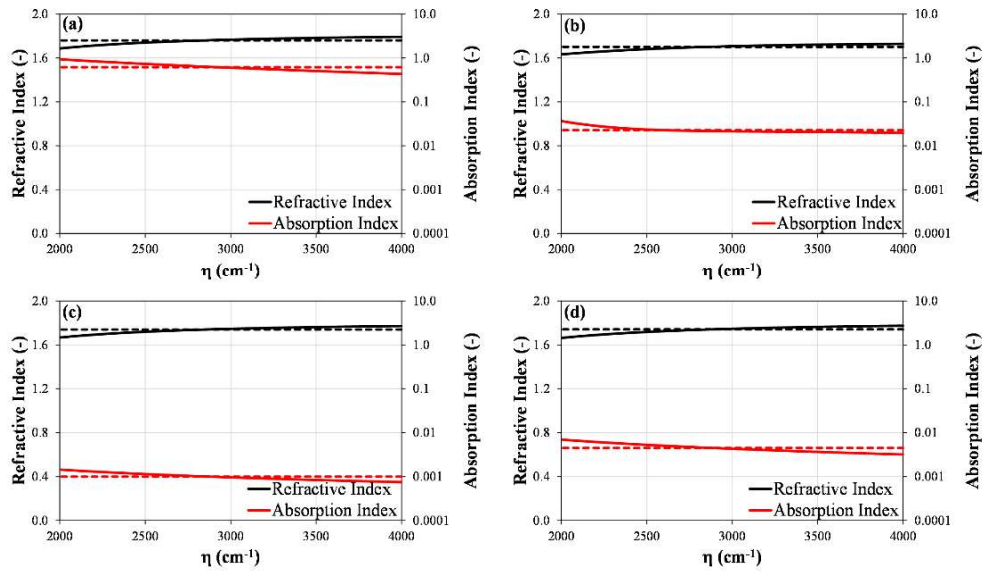
Figure 2.11. Spectral and gray representations of the refractive and absorption indices of (a) γ-Al_2O_3 (b) α-Al_2O_3 (c) liquid alumina with Anfimov et al. [131] and Bakhir et al. [132] (d) liquid alumina with Kuzmin et al. [129] (solid lines: spectral indices; dashed lines: gray indices)

2.4 Radiative Properties of Wall Materials

As denoted by the boundary conditions for the RTE [Eqs. (2.13) and (2.14)], the accuracy in the RHT predictions also depends on the radiative properties of the boundaries which are the emissivities of the walls. Therefore, spectral wall emissivities for different types of wall materials commonly used in industry and utility boilers are needed to investigate the RHT in combusting systems as the correct treatment of RHT in such systems requires the utilization of non-gray boundaries. In FBCs, commonly used wall materials are refractories (owing to their endurance to high temperatures and thermal insulation capability) and membrane tube walls or water walls (to extract the heat released during combustion). However, water walls are sometimes covered by coal slags, which influences the radiative properties of the walls significantly.

One of the wall materials used in this study is the alumina silicate refractory. Calculation of the spectral optical properties of alumina silicate refractories is difficult due to their complex surface characteristics. Therefore, utilizing experimentally measured spectral wall emissivities of such materials becomes more effective. Previously, Jackson and Yen [139] measured the spectral emissivities of different types of refractory materials at different temperatures. Among the refractory materials, the spectral emissivity of alumina-silicate refractory (70 % Al_2O_3 and 26 % SiO_2) is utilized in this study. The spectral and gray representations of the wall emissivities of alumina-silicate refractory are demonstrated by Figure 2.12. As demonstrated by the figure, the spectral wall emissivities significantly deviate from the gray emissivities.
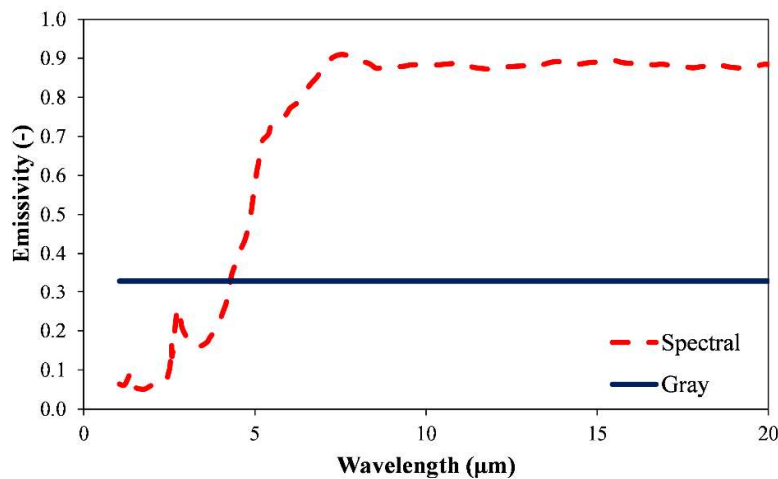
Figure 2.12. The spectral and gray representations of the wall emissivities of alumina-silicate refractory (70 % Al_2O_3 and 26 % SiO_2) [139]

For the FBCs in industries, the main objective is to extract the heat released to the freeboard section by the combustion of fuel. Therefore, such systems are covered by water walls instead of refractory to extract the released heat and generate superheated steam. For this purpose, additional parametric studies are carried out by replacing the refractory-lined side walls of the test rig under investigation with a cold (537 K) water wall made up of thermally oxidized SA508 carbon steel. The spectral

emissivity of thermally oxidized SA508 carbon steel is taken from the measurements of Jo et al. [140]. The spectral and gray representations of the emissivity of thermally oxidized SA508 carbon steel are shown by Figure 2.13. As shown by the figure, spectral and gray wall emissivity for thermally oxidized SA508 carbon steel is very similar between $1 - 15$ µm whereas they differ significantly between $15 - 20$ µm.
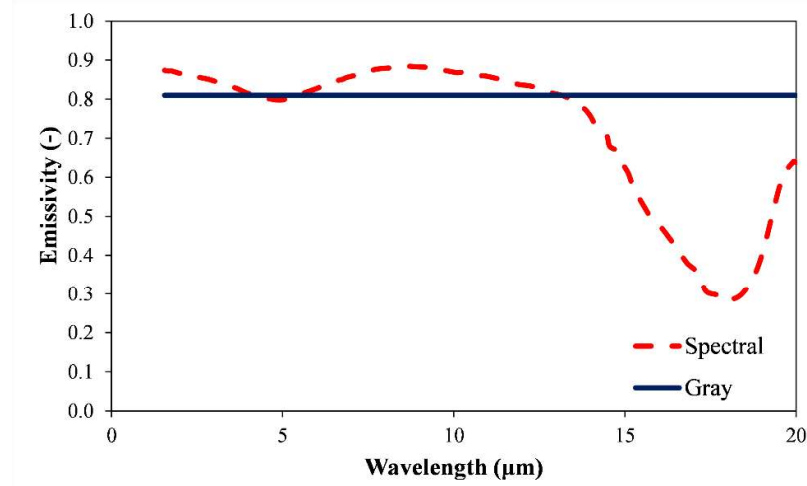
Figure 2.13. The spectral and gray representations of the wall emissivities of thermally oxidized SA508 carbon steel [140]

During the operation of industry or utility boilers, fly ash particles in the freeboard section become sticky due to high temperatures. These particles stick to cooler surfaces such as water walls building up an insulating layer of coal slag. This effect is investigated by conducting a parametric study where the side water walls at 537 K are assumed to be covered by coal slag, with the compositions of fly ashes.

The spectral emissivities of slag-covered water walls can be estimated by using Fresnel's relation and utilizing the estimated RI of coal slags as follows;

$$\varepsilon_\lambda = 1 - \rho_\lambda \tag{2.147}$$

$$\rho_\lambda = \frac{\rho_{\perp,\lambda} + \rho_{/\!/,\lambda}}{2} \tag{2.148}$$

79

$$\rho_{\perp,\lambda} = \frac{(\cos\theta_1 - p)^2 + q^2}{(\cos\theta_1 + p)^2 + q^2} \tag{2.149}$$

$$\rho_{\parallel,\lambda} = \frac{(p - sin\theta_1 tan\theta_1)^2 + q^2}{(p + sin\theta_1 tan\theta_1)^2 + q^2}\rho_{\perp,\lambda} \tag{2.150}$$

$$p^2 = 0.5\left[\left(\sqrt{(n^2 - k^2 - sin^2\theta_1)^2 + 4n^2k^2}\right) + (n^2 - k^2 - sin^2\theta_1)\right] \tag{2.151}$$

$$q^2 = 0.5\left[\left(\sqrt{(n^2 - k^2 - sin^2\theta_1)^2 + 4n^2k^2}\right) - (n^2 - k^2 - sin^2\theta_1)\right] \tag{2.152}$$

where Ebert's model of RI [124] is used to calculate spectral refractive (n) and absorptive (k) indices of coal slags covering water walls using fly ash compositions and wall temperatures of the combustion tests. Details of Ebert's model of refractive indices are given in section 2.3.5.1. and Appendix E.

CHAPTER 3

1-D STEADY-STATE SYSTEM MODEL FOR ABFBC CO-FIRING LIGNITE AND COTTON RESIDUE

3.1   General

The 1-D steady-state ABFBC model for the co-combustion of lignite and CR is first developed and extended by Selcuk and her colleagues [92–97,142]. The system model is based on species and energy conservation equations in the bed and freeboard sections and consists of sub-models for the treatment of bed and freeboard hydrodynamics, volatile release and combustion, char particle combustion and size distribution, heat transfer, elutriation and entrainment, sulfur retention, and NO and N_2O formation and reduction.

Figures 3.1 and 3.2 illustrate the model assumptions of bed and freeboard sections, respectively. The chemical species taken into account in the model are *O_2, CO, CO_2, H_2O, SO_2, NH_3, NO, HCN, CNO, N_2O* which undergo a complex reaction scheme consisting of 26 chemical reactions. In the model for the co-combustion of lignite with CR, both fuels have their own paths for devolatilization and char combustion whereas the products of those steps are mixed and undergo the same reaction path in the gas phase.
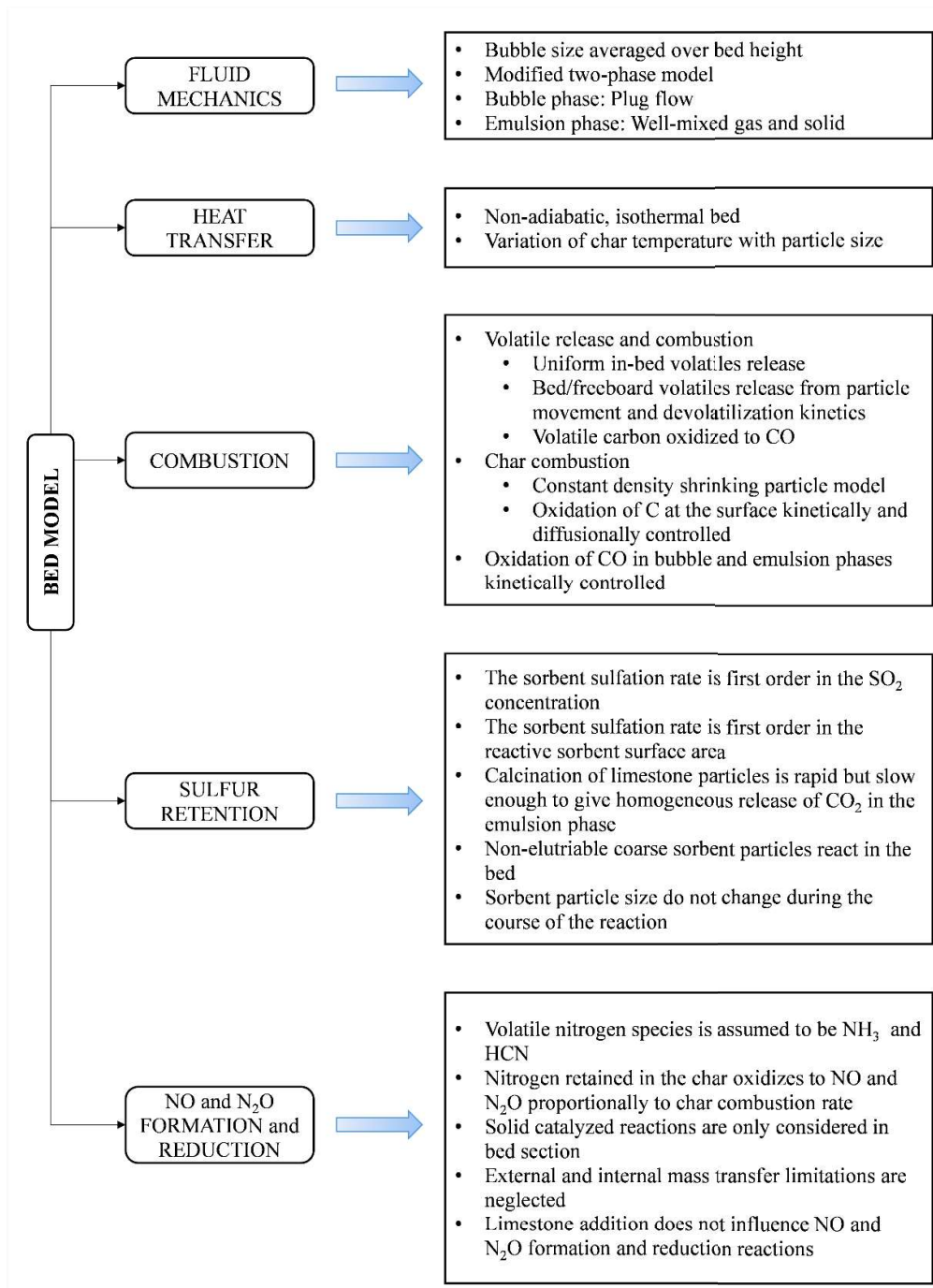
Figure 3.1. An overview of the steady state bed model assumptions

```
FREEBOARD MODEL
├── FLUID MECHANICS ⟹  • Plug flow
│                        • Exponential decay of solids
│
├── HEAT TRANSFER ⟹   • Non-adiabatic, non-isothermal
│
├── COMBUSTION ⟹
│      • Volatile release and combustion
│          • Volatile not released in the bed releases with a
│            logarithmic pattern to the freeboard
│          • Bed/freeboard volatiles release from particle
│            movement and devolatilization kinetics
│      • Char combustion
│          • Oxidation of C at the surface kinetically and
│            diffusionally controlled
│      • Oxidation of CO in the gas phase kinetically
│        controlled
│
├── SULFUR RETENTION ⟹
│      • The sorbent sulfation rate is first order in the SO₂
│        concentration
│      • The sorbent sulfation rate is first order in the
│        reactive sorbent surface area
│      • Elutriable fine sorbent particles and coarse sorbent
│        particles carried by bubble bursting react in the
│        freeboard
│      • Sorbent particle size do not change during the
│        course of the reaction
│
└── NO and N₂O FORMATION and REDUCTION ⟹
       • Volatile nitrogen species is assumed to be NH₃ and
         HCN
       • Only homogeneous reactions are considered
```

Figure 3.2. An overview of the steady state freeboard model assumptions

83

In the present work, a radiation model, where RTE is directly solved, is coupled with energy conservation equations of only the freeboard section. The performance of the FBC system model coupled with the radiation model will be tested against the same FBC system model without coupling it with the radiation model. The components of the system model developed prior to this study are described in detail in the literature [92–97,142]. However, all components of the system model will be explained briefly in the following sections for the sake of integrity.

3.2 ABFBC Model Description

3.2.1 Bed and Freeboard Hydrodynamics

Modified two-phase theory of fluidization by Grace and Clift [143] is used to represent the fluid and particle motion in the bubbling bed;

$$u_0 = \frac{Q_b}{A_{bed}} + u_{tf} + u_e(1 - \delta) \tag{3.1}$$

where throughflow velocity, u_{tf}, is expressed by the n-type two-phase theory suggested by Grace and Harrison [144];

$$u_{tf} = (n + 1)u_e\delta \tag{3.2}$$

where $n = 2$ for three-dimensional beds. The emulsion phase gas velocity is estimated using the expression of Gogolek and Becker [145]:

$$u_e = \frac{u_{mf}}{1 - 1.5\delta^{2/3}} \tag{3.3}$$

On the other hand, the velocity of the bubbles is determined by the following relation of Davidson and Harrison [146]:

$$u_b = 0.711(gd_b)^{1/2} + u_0 - u_{mf} \tag{3.4}$$

84

An integrated average mean bubble size is found from the bubble size expression proposed by Mori and Wen [147].

In the present model, the mass transfer coefficient between the bubbles, which are solid-free, and emulsion is calculated using the relation suggested by Davidson and Harrison [146]:

$$K_{be} = 4.5\frac{u_e}{u_b} \tag{3.5}$$

In the freeboard section, the hold-up of solid particles decreases exponentially along the height in the freeboard with decay constant a:

$$\frac{\varepsilon_p}{\varepsilon_{p,0}} = exp\left(-a \times z_f\right) \tag{3.6}$$

Particle load in the freeboard can then be calculated as follows:

$$B = \varepsilon_p \times \rho_p \tag{3.7}$$

Choi et al. [148] suggested an emprical relation of decay constant as a function of column size, gas velocity, temperature, particle size, and density:

$$a = \frac{1}{d_p} \times exp\left(-11.2 + 210\frac{d_p}{d_{bed} - d_p}\right) \times \left(\frac{d_p\rho_g\left(u_0 - u_{mf}\right)}{\mu}\right)^{-0.492}$$
$$\times \left(\frac{d_p g \rho_p}{\rho_g\left(u_0 - u_{mf}\right)^2}\right)^{0.725} \times \left(\frac{\rho_p - \rho_g}{\rho_g}\right)^{0.731} \times C_D^{-1.47} \tag{3.8}$$

The use of the empirical correlation of Choi et al. [148] directly for particle volume fraction distribution in the model leads to deviations in the particle load predictions at the exit as the expression is originally developed for sand particles. For this purpose, the decay constant expression of Choi et al. [148] for the fly ash particles is multiplied by 4.2 to predict the experimental particle load at the exit as it is the usual practice [97,149].

At the top of the bubbling bed, the solids volume fraction, $\varepsilon_{p,0}$, is determined as follows:

$$\varepsilon_{p,0} = 1 - \varepsilon_f \tag{3.9}$$

The entrainment flux of particles, K_i^*, is calculated by assuming that it consists of a cluster flux, $K_{i,h}^*$, and a dispersed, non-cluster flux, $K_{i,\infty}^*$, as suggested by Hazlett and Bergougnou [150];

$$K_i^* = K_{i,h}^* + K_{i,\infty}^* \tag{3.10}$$

where $K_{i,h}^*$ stands for the cluster flux of entrained particles which is obtained from the empirical correlations proposed by Choi et al. [148]. The elutriation rate constant, $E(r)$, used to calculate carry over flow rate, is then calculated from:

$$E(r) = \frac{A_{bed}}{M_d} K_{i,\infty}^* \tag{3.11}$$

Entrained particles' size distribution at any freeboard height can be determined by assuming that it is proportional to their size distribution at the bed section with a proportionality constant $K_{i,h}^*$;

$$P_{z,p}(r) = A_{bed} \times K_{i,h}^* \times P_{bed,p}(r)/F_{z,p} \tag{3.12}$$

where $P_{z,p}(r)$ is the size distribution of entrained particles, $P_{bed,p}(r)$ is the PSD in the bed section. It should be noted that the PSD of ashes in the bed section is not calculated, instead, it is assumed to be equal to the measured size distribution of bed ash particles collected after the combustion test [8]. $F_{z,p}$ term in Eq. (3.12) is the flow rate of entrained particles which can be determined as follows:

$$F_{z,p} = A_{bed} \times \int_{r_{min}}^{r_{max}} K_{i,h}^* \times P_{bed,p}(r) dr \tag{3.13}$$

3.2.2 Volatile Release and Combustion

In the 1-D steady state system model for co-combustion of lignite and CR, volatiles released are taken to be uniformly distributed in the bed section. The fraction of volatiles released to the bed section is estimated utilizing the model of Stubington et al. [151] whereas the kinetics of devolatilization is represented by the parallel independent reaction model of Anthony and Howard [152]. Assuming the presence of a radial temperature distribution and uniformly distributed volatile matter in the fuel particles, the total amount of volatile matter released with respect to time is given by:

$$\frac{v_{avg}}{v_\infty} = \frac{3}{R^3} \int_0^R \left[1 - \int_0^\infty exp\left(-\int_0^t k(E)dt \right) f(E)dE \right] r^2 dr \tag{3.14}$$

Devolatilization history of the particle yields the fraction of volatiles released in bed (x_{vl}). The rest of the volatiles are taken to be released to the freeboard based on a logarithmic distribution function as a function of height above bed surface. Regarding the combustion of volatile species, all carbon, hydrogen, and sulfur are assumed to be converted into CO, H_2O, and SO_2, respectively. On the other hand, the majority of the nitrogen in the volatiles is converted into N_2 where the remaining ones are released as NH_3 and HCN. The kinetics of CO oxidation occurring both in the bubbles and emulsion is described by the expression of Hottel et al. [153]. Further details of the volatiles release sub-model can be found elsewhere [92,154].

3.2.3 Char Combustion

The product of char combustion of lignite and CR are taken to be CO only considering the operation temperatures of typical FBCs. In this model, for modeling of char combustion, shrinking particle model is utilized. Both film mass transfer and kinetic resistances are taken into account. Therefore, the expression for the carbon oxidation rate takes the following form:

$$r_{C,e} = \frac{2}{\frac{1}{k_f} + \frac{2}{k_s}} \bar{C}_{O_2,e} \tag{3.15}$$

The film mass transfer coefficient, k_f, is estimated based on the correlations of Jung and La Nauze [155]. On the other hand, the kinetic law of Field et al. [156] and Adanez et al. are employed for the reaction kinetics of the char oxidation of lignite and CR, respectively.

The shrinkage rate of char particles, which is required for the calculation of PSD, can be determined by noting that the rate of carbon removal from the surface of char must be equal to the rate of combustion of carbon at the particle surface:

$$\frac{d}{dt}\left[\frac{4}{3}\pi r^3 \rho_d \frac{x_{fc}}{x_{fc} + x_a}\right] = -4\pi r^2 M_C r_{C,e} \tag{3.16}$$

Rearranging Equation (3.16) leads to the final form of shrinkage rates of lignite and CR chars:

$$\Re(r) = -\frac{dr}{dt} = \frac{1}{\rho_d} \frac{x_{fc} + x_a}{x_{fc}} M_C r_{C,e} \tag{3.17}$$

Finally, the temperate of the char particles in the bed as a function of particle diameter can be found by solving the energy balance accounting for reaction enthalpy of char combustion, convective heat transfer and radiative heat transfer:

$$\frac{\rho_d}{M_C} \frac{x_{fc}}{x_{fc} + x_a} \Delta H_{R1}^0 \Re(r) - \left[h_p(T_d - T_{bed}) + \sigma\varepsilon(T_d^4 - T_{bed}^4)\right] = 0 \tag{3.18}$$

3.2.4   Particle Size Distribution

The char particles' size distribution is determined by solving the population balance separately for lignite and CR. The following assumptions are made for the derivation of population balance:

88

1. Char particles enter the bed at a rate of F_0 with a size distribution of $P_0(r)$ which is expressed by Rosin-Rammler size distribution function.

2. As char particles are well-mixed, bed drain char size distribution represents the bed char size distribution.

3. The rate of elutriation of char particles of size r is directly proportional to their concentration in the bed.

4. The densities of char particles do not change during the burn-out.

5. Char particles are considered to shrink by combustion according to the shrinking particle model.

Therefore, the final form of the equation can be written as follows:

$$\frac{dW(r)}{dr} = -W(r)\left[\frac{F_{bd}}{M_d \Re(r)} + \frac{E(r)}{\Re(r)} - \frac{3}{r}\right] + F_0 P_0(r) \tag{3.19}$$

where $W(r)$ is:

$$W(r) = M_d P_{bed}(r)\Re(r) \tag{3.20}$$

Eq. (3.19) is solved separately to calculate the char hold-up of lignite and CR. Details of Eq. (3.19) are given by [154].

The following boundary condition is applied to Eq. (3.19):

$$@ \quad r = r_{max} \quad \quad W(r) = 0 \tag{3.21}$$

The PSD of the inert ashes in the bed are given as input data deduced from the experimental measurements of bottom ash particles.

3.2.5   Desulfurization Model

In this study, desulfurization is represented as two consecutive steps consisting of instantaneous calcination and sulfation. The sulfation rate is taken to be first order in

SO$_2$ concentration and proportional to the reactive external surface area of the particles [94].

Assuming constant size of sorbent particles due to negligible attrition, the sulfation rate for each particle with size r, can be written as:

$$r_{SO_2} = kC_{SO_2}S(t) \tag{3.22}$$

Therefore, the reactive external surface area, $S(t)$, is taken to decrease with time exponentially due to pore blocking by the sulfation reaction:

$$\frac{S(t)}{S_0} = \sigma(t) = exp\left[-\frac{6M_{CaCO_3}kC_{SO_2}}{x_{CaCO_3}\rho_{lst}d_p}t\right] \tag{3.23}$$

As the model is developed for steady-state conditions, average fractional external surface area, σ_{avg}, is defined as a function of residence time distribution, and time-dependent fractional external surface area $\sigma(t)$.

$$\sigma_{avg} = \frac{1}{\left[1 + \frac{6M_{CaCO_3}kC_{SO_2}}{x_{CaCO_3}\rho_{lst}d_p}\tau\right]}\left[1 - exp\left(-\left\{\frac{1}{\tau} + \frac{6M_{CaCO_3}kC_{SO_2}}{x_{CaCO_3}\rho_{lst}d_p}\right\}\tau_{max}\right)\right] \tag{3.24}$$

Calculation of average fractional external surface area, σ_{avg}, and determination of the residence time of sorbent particles, τ, is given in detail elsewhere [158].

Finally, the sulfation rate becomes:

$$r_{SO_2} = kC_{SO_2}S_0\sigma_{avg} \tag{3.25}$$

It should be noted at this point that the rate expression in Eq. (3.25) is just for a single sorbent size. The total sulfation rate becomes equal to the summation of the rates for different sorbent sizes.

For the freeboard, sulfation due to both fine elutriable sorbent particles and coarse sorbent particles carried by bursting bubbles are taken into account. The details for the sulfation reaction in the freeboard are given in [159].

3.2.6   NO and N₂O Formation and Reduction

In this model, NO and N₂O emissions is taken to be solely caused by the nitrogen in the fuel owing to the low operation temperatures of FBCs, in other words, thermal and prompt mechanisms are neglected. The reaction path of the fuel nitrogen utilized in this study is illustrated in Figure 3.3.
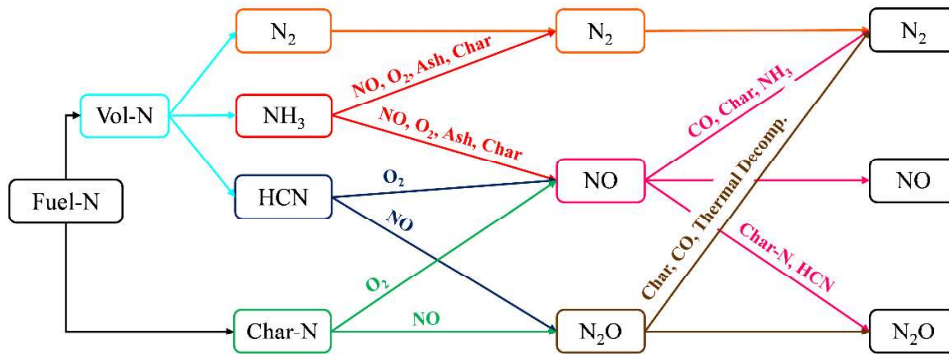
Figure 3.3. The reaction path of the fuel nitrogen

The partitioning of fuel nitrogen into char nitrogen and volatile nitrogenous products such as HCN, NH₃ and N₂ are determined based on experimental data [142,159] (elemental analysis and TGA-FTIR) and literature data [160,161] within the scope of a previous thesis study [159]. Figure 3.3 illustrates the partitioning of the nitrogen within the fuel into char nitrogen and volatile gases.
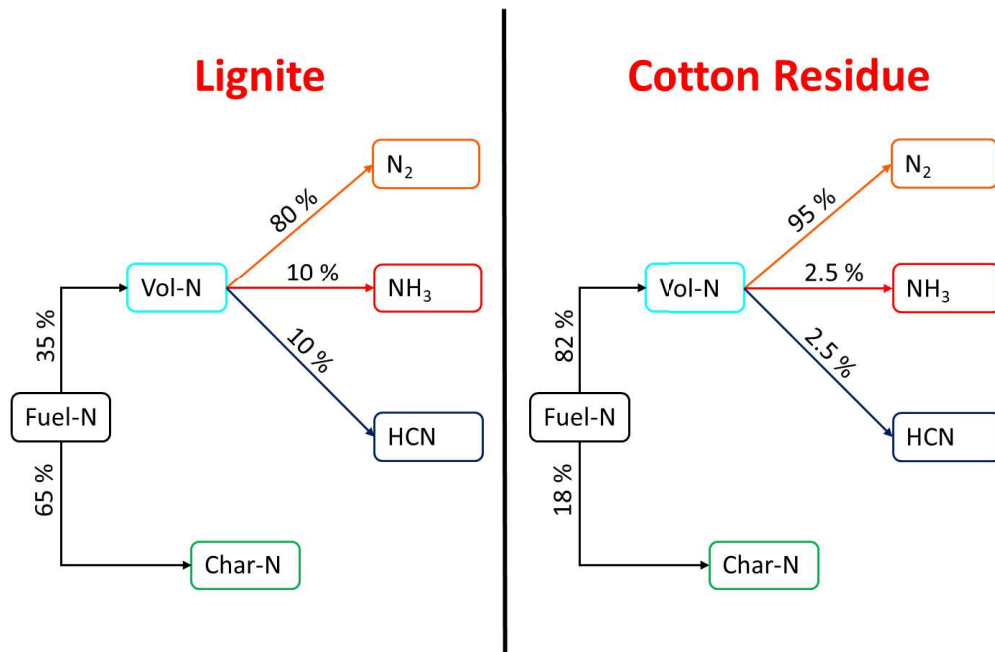
Figure 3.4. The partitioning of nitrogen within the fuel into char nitrogen and volatile gases

Once devolatilization is complete, those products undergo 16 concurrent chemical reactions. The reactions catalyzed by CaO are omitted based on the previous findings stating the negligible influence of limestone on N_2O formation [162,163]. Furthermore, heterogeneous reactions are only taken into account in the bed section due to low particle load in the freeboard of BFBCs. In the formation and reductions reactions of NO and N_2O external mass transfer effects are discarded as Johnsson and Dam-Johansen [164] observed no external mass transfer limitations up to particles of 5 mm for solid catalyzed reactions which is larger than the majority of the particles in this study. Further details of the formation and reduction of NO and N_2O are given elsewhere [142,159].

3.2.7   Mass Conservation Equations

By treating the emulsion phase as well-mixed and bubble phase and freeboard as plug flow, spatial variation of species concentrations is described by the conservation

equations for chemical species in the bubble phase, emulsion phase, and freeboard section:

$$\frac{dn_{j,b}}{dz} = A_{bed}\delta\left[\Re_{j,b} + K_{be}\left(C_{j,e} - C_{j,b}\right)\right] \tag{3.26}$$

$$0 = n_{j,e}\big|_{z=0} - n_{j,e} + V_{bed}\delta\left[\frac{1-\delta}{\delta}\varepsilon_{mf}\Re_{j,e} - K_{be}\left(C_{j,e} - \bar{C}_{j,b}\right)\right] \tag{3.27}$$

$$\frac{dn_{j,f}}{dz} = A_f\left(1 - \varepsilon_p\right)\Re_{j,f} \tag{3.28}$$

These equations are subject to the following boundary conditions:

$$@z = 0 \qquad n_{j,b} = y_{j,b}\frac{n_a}{1 + \dfrac{u_e}{u_b}\dfrac{1-\delta}{\delta}\varepsilon_{mf}} \tag{3.29}$$

$$@z = 0 \qquad n_{j,e} = y_{j,e}\frac{n_a}{1 + \dfrac{u_b}{u_e}\dfrac{\delta}{(1-\delta)\varepsilon_{mf}}} \tag{3.30}$$

$$@ z = H_{bed} \qquad n_{j,f} = n_{j,e} + n_{j,b} \tag{3.31}$$

The expressions for the species generation or depletion terms appearing in Eqs. (3.26), (3.27), and (3.28), $\Re_{j,b}$, $\Re_{j,e}$ and $\Re_{j,f}$, are determined using the reaction rates. The details of the species generation or depletion terms and the rate of chemical reaction considered in the model are given elsewhere [159].

3.2.8   Energy Conservation Equations

3.2.8.1   Energy Balance in Bed

Based on the assumption that the gas and the inert particles are at the same temperature and that the mass of combustion gases and char particles are negligible compared to the mass of inerts, a combined gas/solid phase energy balance for bed can be written as;

$$n_a \int_{T_r}^{T_a} c_{p,a} dT - \alpha \frac{A_T}{L_T} \int_0^{L_T} U_{cw}(T_{bed} - T_{cw}) dx$$

$$-A_{bw} h_{bw}(T_{bed} - T_{bw,s}) - m_{CO} c_{p,i}(T_{bed} - T_r)$$

$$-m_{bd} c_{p,i}(T_{bed} - T_{ref}) - n_g \sum_{j=1}^n y_j \int_{T_r}^{T_{bed}} c_{p,g_j} dT$$

$$-(m_{coal} x_{H_2O} + m_{bio} x_{H_2O}) \lambda^0 + Q_p + Q_{rxn} = 0 \tag{3.32}$$

where Q_{rxn} is heat generated from chemical reactions and Q_p is energy transferred from burning char particles. Energy loss through the bed walls is taken into account by making a one-dimensional heat transfer analysis.

In order to account for the energy absorbed by the in-bed heat exchanger, a separate energy balance is performed on the cooling water:

$$\frac{m_{cw}}{\pi} \frac{dT_{cw}}{dx} - \frac{d_{T,o}}{c_{p,cw}} h_{cw}(T_{bed} - T_w) = 0 \tag{3.33}$$

Surface temperature of the tube wall, T_w, is calculated by solving a surface energy balance:

$$h_{cw} d_{T,o}(T_{bed} - T_w) - h_i d_{T,i}(T_w - T_{cw}) = 0 \tag{3.34}$$

3.2.8.2 Energy Balance in Freeboard

By resolving an energy conservation equation that takes convective transport, and heat generation and loss into account, the freeboard gas temperature profile is determined;

$$\frac{dT_f}{dz_f} = \frac{A_f}{n_f C_{p,g}} [R(1 - \varepsilon_p) - \nabla \cdot \boldsymbol{q}_r] \tag{3.35}$$

with the following boundary condition:

$$@ \ z_f = 0 \qquad T_f = T_{bed} \tag{3.36}$$

The R term of Eq. (3.35) stands for the heat generation and loss rate per unit freeboard volume which is the summation of heat generation due to chemical reaction (R_{rxn}), heat loss from freeboard walls (R_{fw}), and heat exchange between solid particles and the gaseous medium (R_p);

$$R = R_{rxn} + R_{fw} + R_p \tag{3.37}$$

The term stands for the heat exchange between solid particles and the gaseous medium (R_p) can be expressed using the following equation:

$$
\begin{aligned}
R_p = {} & \frac{3F_{CO}}{A_{bed}\rho_d} \int_{r_{min}}^{r_{maxe}} \frac{P_{z,d}(r)}{ru_p(r)} \big[h_p(T_d - T_f)\big] dr \\
& + 3\varepsilon_d \int_{r_{maxe}}^{r_{min}} \frac{P_{z,d}(r)}{r} \big[h_p(T_d - T_f)\big] dr \\
& + 3\varepsilon_i \int_{r_{maxe}}^{r_{max}} \frac{P_{z,i}(r)}{r} \big[h_p(T_i - T_f)\big] dr
\end{aligned}
\tag{3.38}
$$

The term $\nabla \cdot q_r$ of Eq. (3.35) represents the radiative ST that is taken from the radiation model once RTE is solved.

The axial temperature profile of freeboard side walls can be calculated by solving an energy balance considering that the summation of radiative and convective heat transfer rates between freeboard and side walls is equal to heat transfer through the walls via conduction:

$$h_{fw}(T_f - T_{fw}) + q_{r,w} - \frac{(T_{fw} - T_{fw,o})}{R_w} = 0 \tag{3.39}$$

where $q_{r,w}$ is the net wall radiative HF obtained by the solution of RTE and h_{fw} is estimated by the following approach adopted from Kunii and Levenspiel [165]:

$$\frac{h_{fw} - h_g}{h_{z_f=0} - h_g} = exp(-az_f/2) \tag{3.40}$$

The term a in Eq. (3.40) refers to the decay constant of the particles along the freeboard and is estimated by using the correlation of Choi et al. [148] as given by Eq. (3.8). The term h_g stands for the gas component which can be estimated utilizing the correlation suggested by Gnielinski [166];

$$h_g = \frac{k_g}{d_{bed}} \left[\frac{(f/8)(Re - 1000)Pr}{1 + 12.7(f/8)^{0.5}(Pr^{2/3} - 1)} \right] \tag{3.41}$$

Considering convective and RHT from particles to the freeboard and walls and char combustion, energy balance equations for char and fly ash particles can be written as in Eqs. (3.42) and (3.43), respectively. The detailed derivation of the freeboard particle energy balance is given in Appendix F.

$$\rho_d \varepsilon_d u_0 C_{p,d} \frac{dT_d}{dz_f} = - \int_{r_{max,e}}^{r_{max}} \frac{3\varepsilon_d P_{z,d}}{r_c} h_p(T_d - T_f) dr - \int_{r_{min}}^{r_{max,e}} \frac{3F_{CO,d}P_{z,d}(r)}{r_d u_0 A_f \rho_d} h_p(T_d - T_f) dr$$

$$- \nabla \cdot q_{r,d} + \frac{x_{FC}}{x_{FC} + x_{ash}} \int_{r_{max,e}}^{r_{max}} \frac{3\varepsilon_d P_{z,d}(r)}{r_d} \Re_{C,f} \Delta H_{rxn}^o dr$$

$$+ \frac{x_{FC}}{x_{FC} + x_{ash}} \int_{r_{min}}^{r_{max,e}} \frac{3F_{CO,d}P_{z,d}(r)}{r_d u_0 A_f \rho_d} \Re_{C,f} \Delta H_{rxn}^o dr \tag{3.42}$$

$$\rho_i \varepsilon_i u_0 C_{p,i} \frac{dT_i}{dz_f} = - \int_{r_{max,e}}^{r_{max}} \frac{3\varepsilon_i P_{z,i}(r)}{r_i} h_p(T_i - T_f) dr$$

$$- \int_{r_{min}}^{r_{max,e}} \frac{3F_{CO,i}P_{z,i}(r)}{r_i u_0 A_f \rho_i} h_p(T_i - T_f) dr - \nabla \cdot q_{r,i} \tag{3.43}$$

Similarly, Eqs. (3.42) and (3.43) are subjected to the following boundary conditions:

$$@ z_f = 0 \qquad T_d = T_{d,bed}; \quad T_i = T_{i,bed} \tag{3.44}$$

96

The performance of the FBC system model coupled with the radiation model will be tested against the same FBC system model without coupling it with the radiation model. For the FBC system model without radiation model, freeboard gas temperature profiles can be obtained using Eq. (3.35) by omitting the radiative ST, $\nabla \cdot \boldsymbol{q}_r$.

$$\frac{dT_f}{dz_f} = \frac{A_f}{n_f C_{p,g}} \left[R(1 - \varepsilon_p) \right] \tag{3.45}$$

where $\boldsymbol{R}$ is the heat generation and loss rate per unit freeboard volume which is defined as:

$$R = R_{rxn} + R_{fw} + R_p \tag{3.46}$$

In the FBC system model without radiation model, RHT is simply accounted for by utilizing the Stefan-Boltzmann law for radiative heat exchange between particles and gases:

$$\boldsymbol{R}_p = \frac{3F_{CO}}{A_{bed}\rho_d} \int_{r_{min}}^{r_{maxe}} \frac{P_{z,d}(r)}{r u_p(r)} \left[h_p(T_d - T_f) + \varepsilon_d \sigma(T_d^4 - T_f^4) \right] dr$$

$$+ 3\varepsilon_d \int_{r_{maxe}}^{r_{min}} \frac{P_{z,d}(r)}{r} \left[h_p(T_d - T_f) + \varepsilon_d \sigma(T_d^4 - T_f^4) \right] dr$$

$$+ 3\varepsilon_i \int_{r_{maxe}}^{r_{max}} \frac{P_{z,i}(r)}{r} \left[h_p(T_i - T_f) + \varepsilon_i \sigma(T_i^4 - T_f^4) \right] dr \tag{3.47}$$

The emissivity of fly ash particles, ϵ_i, is estimated noting that it is equal to their absorption efficiency [167] that can be calculated utilizing Mie theory and their d_{32}. For the estimation of the emissivity of freeboard char particles, ϵ_d, however, the empirical correlation of Schiemann et al. [167] is adopted. Using the above-mentioned relations, the emissivities of freeboard char and fly ash particles are determined as 0.58 and 0.24, respectively.

The wall temperature profile is calculated by solving the energy balance given in Eq. (3.39) by omitting the net wall radiative HF term, $\boldsymbol{q}_{r,w}$.

97

$$h_{fw}(T_f - T_{fw}) + \mathbf{q_{r,w}} - \frac{(T_{fw} - T_{fw,o})}{R_w} = 0 \qquad (3.48)$$

RHT is taken into consideration by utilizing a RHT coefficient, h_r, in Eq. (3.49);

$$\frac{h_{fw} - (h_r + h_g)}{h_{z_f=0} - (h_r + h_g)} = exp\left(-az_f/2\right) \qquad (3.49)$$

where h_r stands for the radiative component which can be estimated by:

$$h_r = \varepsilon_{fw}\sigma(T_f + T_{fw})(T_f^2 + T_{fw}^2) \qquad (3.50)$$

For the FBC model without freeboard particle energy balance, the freeboard char particle temperatures are assumed to be equal to the freeboard gas temperature where temperatures of freeboard ash particles are taken to be their temperature in the bed section.

3.3   Solution Procedure

3.3.1   Coupling between System Model and Radiation Model

Solution domains for the test rig utilized in the 1-D steady state FBC system model for co-combustion of lignite and CR and radiation model are schematically illustrated in Figure 3.5. The boundary at the top of the freeboard is considered to be an equivalent gray surface with an emissivity of 0.87 calculated based on area-weighted average emissivity of the tubes and the gases. On the other hand, the boundary at the bottom of the freeboard is taken to be black surface due to Hohlraum effect [168].
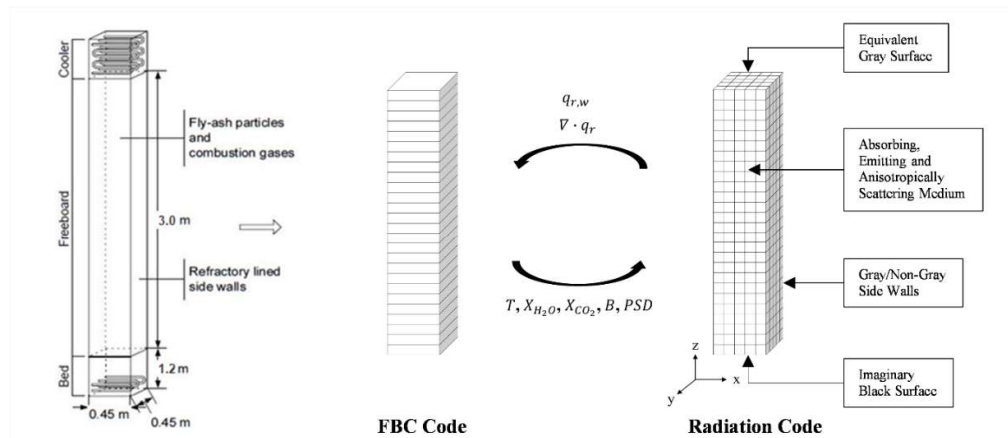
Figure 3.5. Solution domains for the test rig utilized in the 1-D steady state FBC system model for co-combustion of lignite and CR and radiation model

The algorithm of the coupling of the FBC system model with the radiation model is illustrated in Figure 3.6. The coupling algorithm for the radiation and FBC system models is initiated by the specification of initial data for both models. Coupling between the radiation and FBC system models is carried out by regular transfer of temperature and CO_2 and H_2O concentration profiles, particle loads, and PSDs from the FBC model to the radiation model. The radiation model then provides radiative ST and HF fields for the freeboard energy balance equations as the solution propagates in time until a steady-state solution is found.
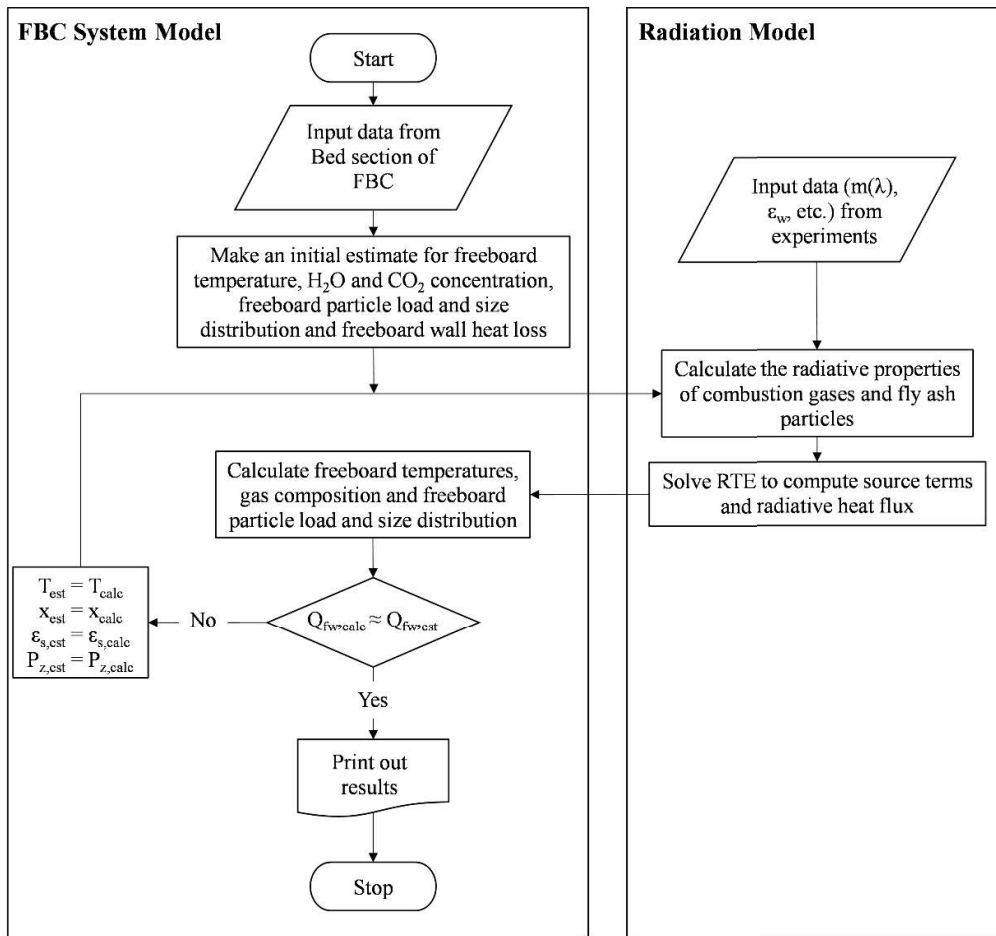
Figure 3.6. Algorithm of the coupling of 1-D steady-state FBC system model for co-combustion of lignite and CR with radiation model

3.3.2   Algorithm of the Coupled Code

Application of the model necessitates empirical and semi-empirical correlations for heat and mass transfer coefficients, combustion kinetics, elutriation, entrainment rates, etc.

In the application of the model, direct use of the elutriation rate constant and particle hold-up distribution of Choi et al. [148] yielded higher carry-over flow rates and incorrect particle loads at the combustor exit. To match the measured carry-over flow rates, the elutriation rate constant is multiplied by 0.20. On the other hand, the decay

constant of the inert ash hold-up expression of Choi et al. [148] is multiplied by 0.24 to match the predicted and measured particle loads at the freeboard exit.

The kinetic expression suggested by Hottel et al. [153] predicts CO concentrations approximately one order of magnitude lower compared to the measurements. To match the measured and predicted CO concentrations, this expression is just simply multiplied with 0.3.

Figures 3.7 to 3.9 show the algorithm of the steady state model code in compact form. The solution starts with defining initial conditions as calculated by the steady-state code for the same test rig. The details of the steady-state model can be found elsewhere [154]. The coupled transient FBC system model is mainly based on the regular transfer of temperature and species concentration fields solved by the FBC system model and ST field and wall radiative HFs solved by the radiation model at each time step.

The ODE system is integrated using a readily available solver ROWMAP utilizing implicit Runge-Kutta methods. The solution of non-linear algebraic equation systems, on the other hand, is achieved by utilizing the subroutine ZERO. Detailed solution procedure of steady-state and transient codes for lignite combustion can be found elsewhere [154].

In the application of the model, direct use of the elutriation rate constant and particle hold-up distribution of Choi et al. [148] yielded higher carry-over flow rates and incorrect particle loads at the combustor exit. To match the measured carry-over flow rates, the elutriation rate constant of char particles is multiplied by 0.45, and the elutriation rate constant of ash particles is multiplied by 0.10. Fine-tuning for the carry-over flow rate at the cyclone exit was the simplest approach since the carry-over flow rate was only a function of elutriation. On the other hand, the decay constant of the inert ash hold-up expression of Choi et al. [148] is multiplied by 4.2 to match the predicted and measured particle loads at the freeboard exit.

The kinetic expression suggested by Hottel et al. [153] predicts CO concentrations approximately one order of magnitude lower compared to the measurements. To match the measured and predicted CO concentrations, this expression is just simply multiplied with 0.1.

Figures 3.7 to 3.9 show the algorithm of the steady state model code in compact form. The solution starts with making initial guesses for T_{bed}, $\bar{y}_{O_2,e}$, $M_{d,coal}$, $M_{d,bio}$, F_a, $T_{bw,o}$ and $f_{3,bio}/f_3$. Then, $\bar{\bar{T}}_d$ values are calculated using the estimated parameters. There exists seven loops in the model for convergence of $M_{d,coal}$, $M_{d,bio}$, F_a, $\bar{y}_{O_2,e}$, $\bar{T}_{d,coal}$, $\bar{T}_{d,bio}$ and T_{bed}.

The ODE system is integrated using a readily available solver LSODES utilizing implicit Backward-Differentiation Formula (BDF) method. The solution of non-linear algebraic equation systems, on the other hand, is achieved by utilizing the subroutine ZERO and HYBRID. Detailed solution procedure of steady-state code for lignite combustion can be found elsewhere [154].

102
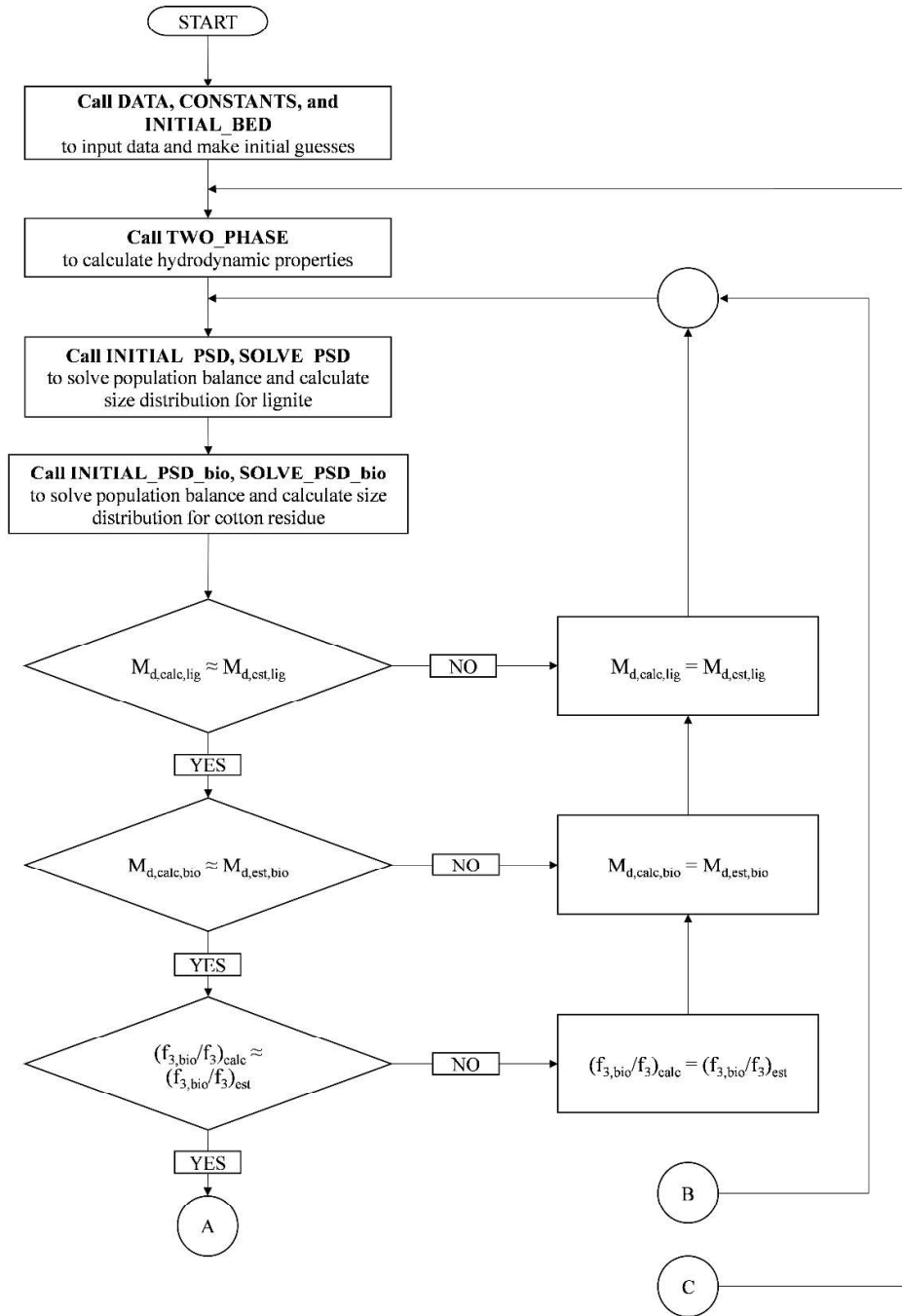
Figure 3.7. Flowchart for the steady state code for bed section
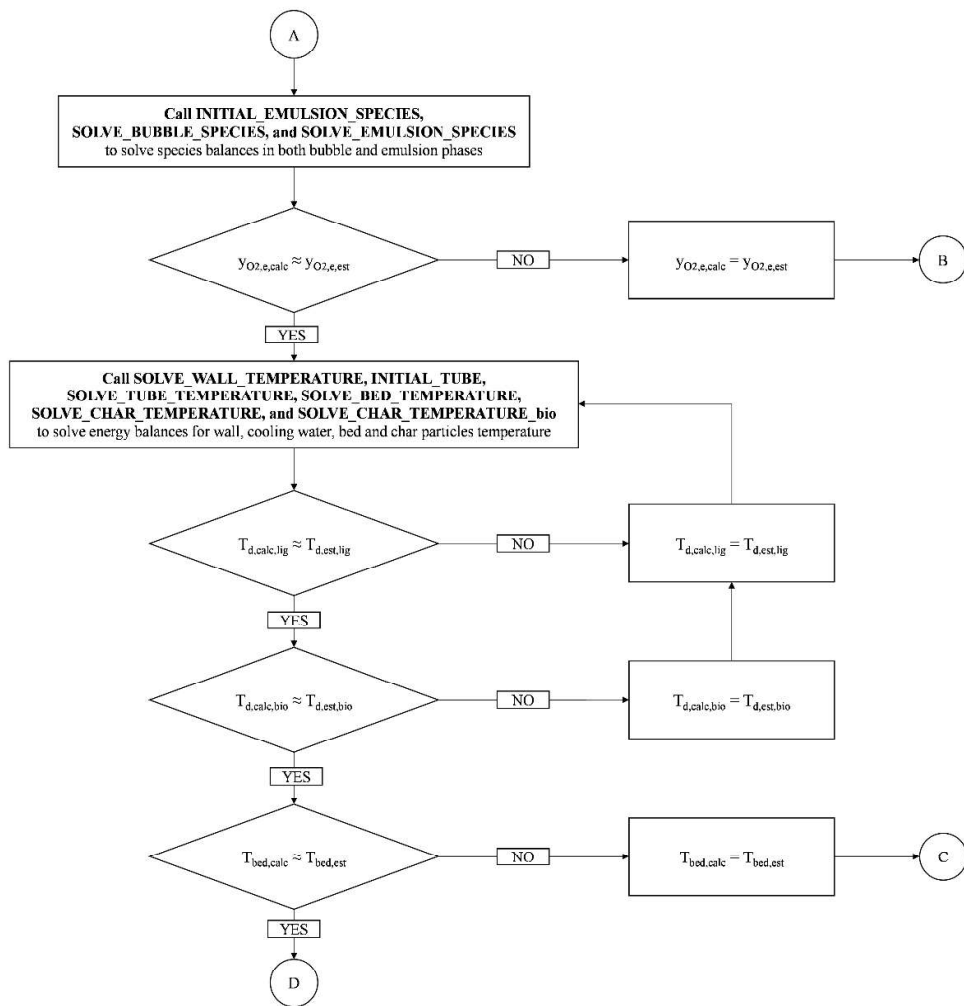
Figure 3.8. Flowchart for the steady state code for bed section
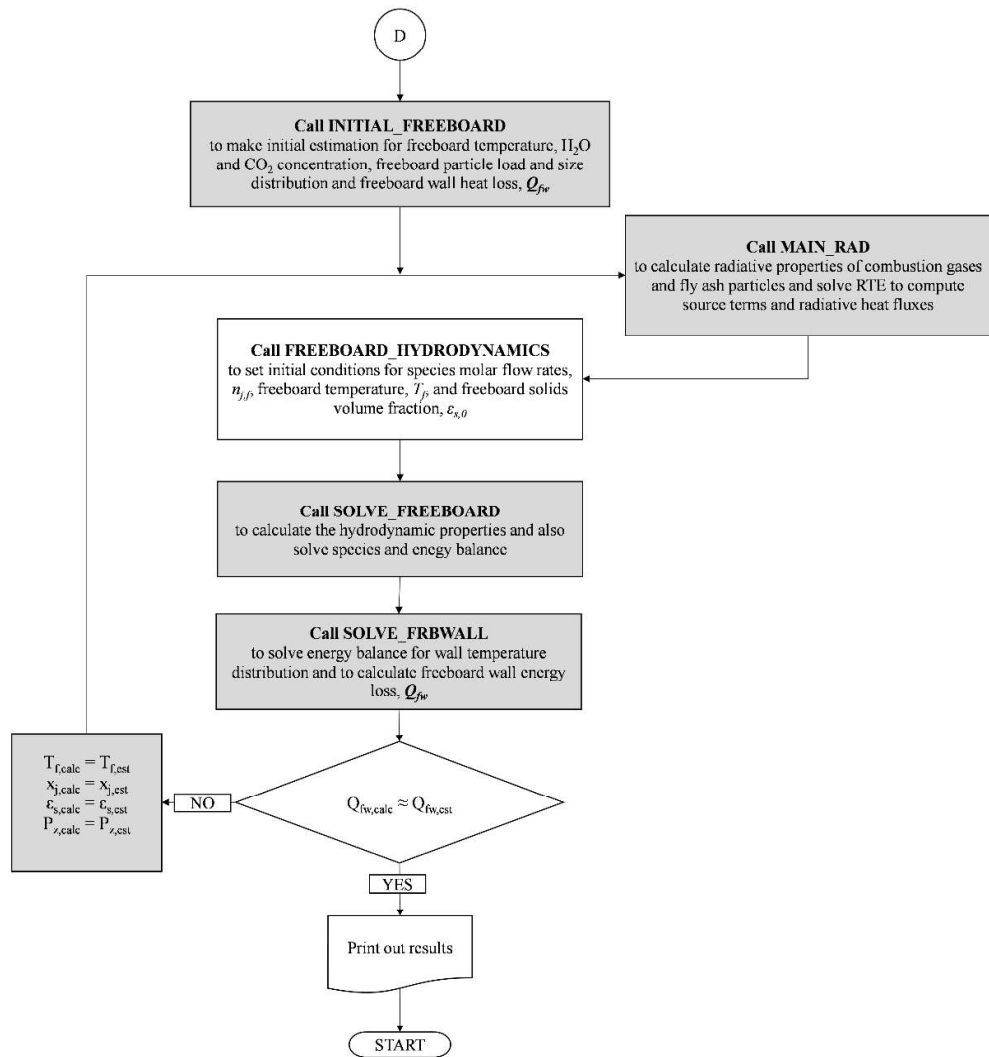
Figure 3.9. Flowchart for the steady state code for freeboard section (The shaded areas show the modified sections of this study)

CHAPTER 4

1-D TRANSIENT SYSTEM MODEL FOR ABFBC FIRING LIGNITE

4.1   General

The 1-D transient system model for the combustion of lignite in the 0.3 MW_t ABFBC test rig is originally developed by Selcuk and Degirmenci [28,154]. The transient system model for the combustion of lignite is based on energy and species conservation equations in both bed and freeboard regions. The model involves several subroutines for modeling bed and freeboard hydrodynamics, volatile release and combustion, char particles combustion and size distribution, and heat transfer. The model includes a sufficiently detailed reaction scheme and seven gaseous species, which are, O_2, CO, CO_2, H_2O, SO_2, CH_4, and N_2.

The main assumptions for the present model are illustrated in Figure 4.1 and Figure 4.2 for bed and freeboard sections, respectively. In the present model, volatiles, not released to the bed, are assumed to be released with a linear distribution to the freeboard i.e., volatiles are taken to be released uniformly to the freeboard section.
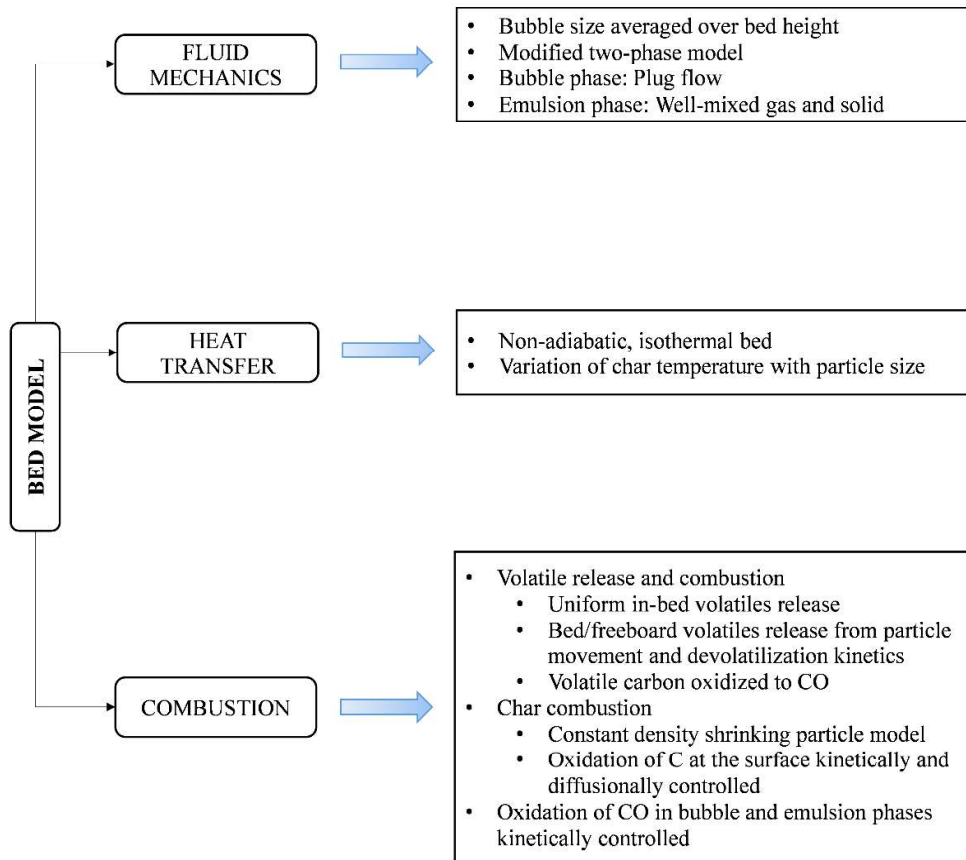
Figure 4.1. An overview of the transient bed model assumptions
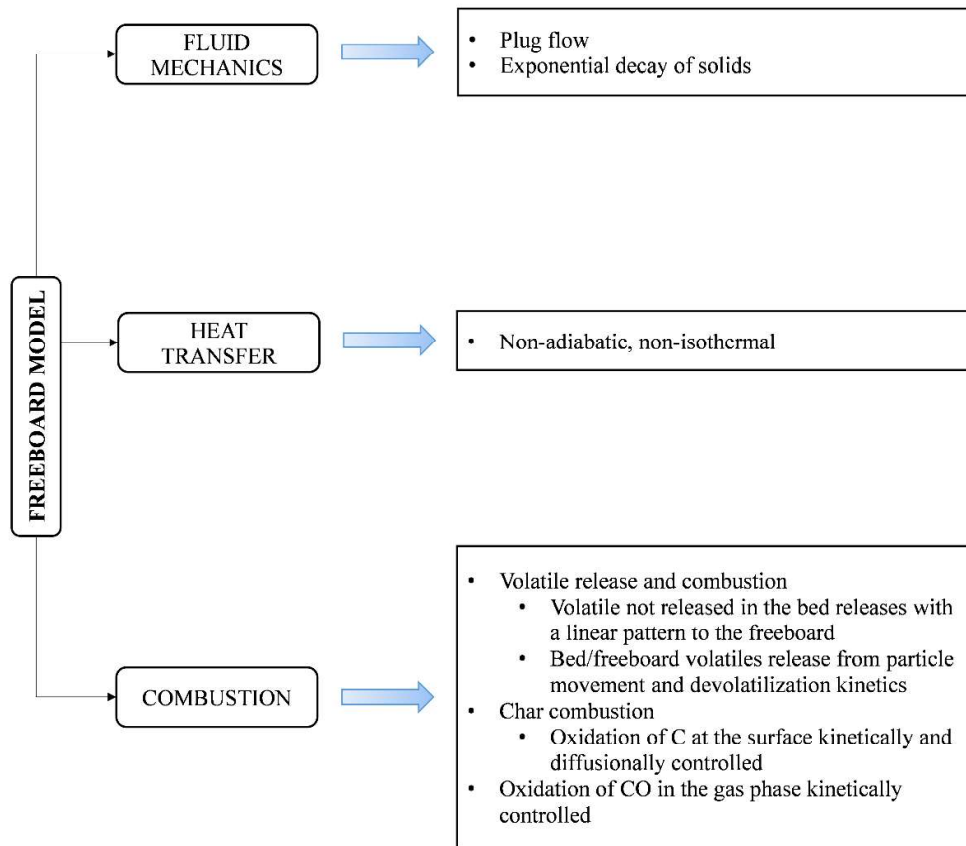
Figure 4.2. An overview of the transient freeboard model assumptions

Details of the model and model equations are described elsewhere [28]. In the present study, the radiation model is applied only to the freeboard section of METU 0.3 MW_t ABFBC test rig. In the following sections, only the components that are related to the coupling of the FBC model with the radiation code will be described. However, a brief description of the sub-models included in the overall system model will also be provided for the sake of integrity.

4.2   ABFBC Model Description

4.2.1   Bed and Freeboard Hydrodynamics

The motion of particles and gas in the bubbling bed is represented with the modified two-phase theory of Grace and Clift [143] and model of Gogolek and Becker [145]. The emulsion phase is taken to be well-mixed ~~mixed~~ whereas the solid-free bubbles rise in plug flow. An average bubble size calculated by integrating bubble size distribution along the bed from the expression proposed by Mori and Wen [147] is used.

The gases in the emulsion and bubble phases are assumed to mix instantaneously at the entrance of the freeboard and rise in plug flow. The hold-up of freeboard particles, consisting of char and ash, is assumed to decay exponentially as a function of height in the freeboard with the decay constant suggested by Choi et al. [148]. A more detailed description, involving some model equations, is provided in section 3.2.1 and further details of the bed and freeboard hydrodynamics are given in [154].

4.2.2   Volatile Release and Combustion

Volatile matter released during the devolatilization of lignite is assumed to be released instantaneously and uniformly distributed to the emulsion phase. The ratio of the volatiles released to the bed section to the total amount of volatiles (X_{vl}) is estimated using the volatiles release model suggested by Stubington et al. [151] together with the parallel independent reaction model suggested by Anthony and Howard [152]. Regarding the volatile combustion, volatile carbon, hydrogen, and sulfur species are taken to burn rapidly to produce CO, H_2O, and SO_2, respectively. The kinetics of CO oxidation occurring both in the bubbles and emulsion is described by the expression of Hottel et al. [153]. Further information regarding the volatiles release sub-model can be found elsewhere [92,154].

4.2.3   Char Combustion

CO is assumed to be the sole product of char particles' combustion considering the typical FBC opeating conditions. The combustion of char is taken into consideration by utilizing the shrinking particle model which accounts for both film mass transfer and kinetic resistances. The film mass transfer coefficient is obtained from the relation of Jung and La Nauze [155]. Combustion kinetics of lignite chars are represented by the kinetic law of Field et al. [156]. The char particle temperature in the bed section is determined from the solution of energy balance eqaution for a spherical shape having uniform temperature profile:

$$\frac{dT_d}{dt} = \frac{3x_{fc}\Delta H_{R1}^0\,\Re(r)}{rM_C C_{p,d}(x_{fc} + x_a)} - \frac{3}{r\rho_d C_{p,d}}\left[h_p(T_d - T_{bed}) + \sigma\varepsilon(T_d^4 - T_{bed}^4)\right] \tag{4.1}$$

Further details of the char combustion model are given in section 3.2.3 and Ref. [154].

4.2.4   Particle Size Distribution

Char PSD for lignite in the bubbling bed is determined by making the population balance of Levenspiel et al. [165];

$$\frac{dW(r)}{dt} = F_0 P_0(r) - F_{bd}\frac{W(r)}{M_d} - W(r)E(r) + \frac{d}{dr}[W(r)\Re(r)]$$
$$- \frac{3}{r}W(r)\Re(r) \tag{4.2}$$

which is then solved by direct integration procedure suggested by Selçuk et al. [169]. Eq. (4.2) is subjected to the following boundary condition:

$$@ \quad r = r_{max} \quad\quad W(r) = 0 \tag{4.3}$$

The term, $\Re(r)$, in Eq. (4.2) is the rate of shrinkage which is calculated by Eq. (3.17).

The attrition of lignite particles is neglected based on the previous findings of Gogebakan and Selcuk [93] where an assessment study is carried out in the same test rig. Moreover, it is assumed that the size distribution of inerts in the bed is taken to be equal to the size distribution of char particles. Further details of the PSD can be found in section 3.2.4 and Ref. [93,94].

4.2.5   Mass Conservation Equations

By treating the emulsion phase as well-mixed and the bubble phase and freeboard as plug flow, temporal variation of species concentrations is determined by solving the chemical species balances in the bubble phase, emulsion phase, and freeboard section:

$$\frac{dn_{j,b}}{dt} = \frac{RT_{bed}n_b}{PA_{bed}\delta}\left[A_{bed}\delta\Re_{j,b} + A_{bed}\delta K_{be}\left(C_{j,e} - C_{j,b}\right) - \frac{dn_{j,b}}{dz}\right] + \frac{n_{j,b}}{T_{bed}}\frac{dT_{bed}}{dt}$$
$$+ \frac{n_{j,b}}{n_b}\frac{dn_b}{dt} \tag{4.4}$$

$$\frac{dn_{j,e}}{dt} = \frac{RT_{bed}n_e}{PV_{bed}(1-\delta)\varepsilon_{mf}}\left[V_{bed}(1-\delta)\varepsilon_{mf}\Re_{j,e} - V_{bed}\delta K_{be}\left(C_{j,e} - \bar{C}_{j,b}\right) - n_{j,e}\right.$$
$$\left. - n_{j,e}\Big|_{z=0}\right] + \frac{n_{j,e}}{T_{bed}}\frac{dT_{bed}}{dt} + \frac{n_{j,e}}{n_e}\frac{dn_e}{dt} \tag{4.5}$$

$$\frac{dn_{j,f}}{dz} = \frac{RT_f n_b}{PA_f\left(1-\varepsilon_p\right)}\left[A_f\left(1-\varepsilon_p\right)\Re_{j,f} - \frac{dn_{j,f}}{dz}\right] + \frac{n_{j,f}}{T_f}\frac{dT_f}{dt} + \frac{n_{j,f}}{n_f}\frac{dn_f}{dt} \tag{4.6}$$

These equations are solved by applying the following boundary conditions:

$$@z = 0 \qquad n_{j,b} = y_{j,b}\frac{n_a}{1 + \dfrac{u_e}{u_b}\dfrac{1-\delta}{\delta}\varepsilon_{mf}} \tag{4.7}$$

$$@z = 0 \qquad n_{j,e} = y_{j,e}\frac{n_a}{1 + \dfrac{u_b}{u_e}\dfrac{\delta}{(1-\delta)\varepsilon_{mf}}} \tag{4.8}$$

$$@ z = H_{bed} \qquad n_{j,f} = n_{j,e} + n_{j,b} \tag{4.9}$$

The expressions for the species generation or depletion terms appearing in Eqs. (4.4), (4.5), and (4.6), $\mathfrak{R}_{j,b}, \mathfrak{R}_{j,e}$ and $\mathfrak{R}_{j,f}$, are determined using the reaction rates. The details of the species generation or depletion terms and the rate of chemical reaction considered in the model are given elsewhere [28,154].

4.2.6   Energy Conservation Equations

4.2.6.1   Energy Balance in Bed

Energy balance on the bed is formulated by assuming that the gas and the inert particles are at the same temperature and that the mass of combustion gases and char particles are negligible compared to the mass of inerts;

$$\frac{dT_{bed}}{dt} = \frac{1}{c_{p,i}M_i}\left\{ n_a \int_{T_r}^{T_a} c_{p,a} dT \right.$$

$$- \alpha d_{T,o} \int_0^{L_T} U_{cw}(T_{bed} - T_{cw})dx - A_{bw}h_{bw}(T_{bed} - T_{bw,s})$$

$$- (n_e + n_b)\sum_{j=1}^{n} y_j \int_{T_r}^{T_{bed}} c_{p,g_j}dT - m_{CO}c_{p,i}(T_{bed} - T_r)$$

$$\left. - m_{bd}c_{p,i}(T_{bed} - T_r) - (m_{coal}x_{H_2O})\lambda^0 + Q_p + Q_{rxn}\right\} \qquad (4.10)$$

where Q_{rxn} is heat generated from chemical reactions and Q_p is energy transferred from burning char particles. The details of energy loss through the bed walls can be found elsewhere [28,154].

Neglecting the heat transfer resistance of the tubes, the spatial variation of the temperature of the cooling water is given by the following equation:

$$\frac{dT_{cw}}{dt} = \frac{4d_{T,o}}{d_{T,i}^2\rho_{cw}c_{p,cw}}h_{cw}(T_{bed} - T_w) - \frac{4m_{cw}}{\pi d_{T,i}^2\rho_{cw}}\frac{dT_{cw}}{dx} \qquad (4.11)$$

The surface temperature of the tube wall, T_w, is calculated by solving a surface energy balance:

$$h_{cw}d_{T,o}(T_{bed} - T_w) - h_i d_{T,i}(T_w - T_{cw}) = 0 \qquad (4.12)$$

The overall bed-to-tube surface heat transfer coefficient, h_{cw}, consists of three modes gas convective, particle convective, and RHT.

$$h_{cw} = h_g + h_p + h_r \qquad (4.13)$$

In the model, gas convective, h_g, and particle convective, h_p, heat transfer coefficients are calculated by adopting the correlations proposed by Denloye and Botterill [170]:

$$h_r = \varepsilon_w \sigma (T_{bed} + T_w)\left(T_{bed}^2 + T_w^2\right) \qquad (4.14)$$

4.2.6.2 Energy Balance in Freeboard

In the transient coupled model, the energy conservation equation for the freeboard section can be written by including the radiative ST to the freeboard energy balance in the original FBC model developed by Selcuk and Degirmenci [28] which considers the gas convective transport, and heat loss and generation:

$$\frac{\partial T_f}{\partial t} = \frac{RT_f^2 n_f}{A_f(1-\varepsilon_p)PT_r}\frac{\partial T_f}{\partial z_f} + \frac{RT_f^2}{PM_g T_r C_{p,g}}\left(R - \frac{\nabla \cdot \boldsymbol{q}_r}{(1-\varepsilon_p)}\right)$$
$$- \frac{RT_f^2(T_f - T_r)}{A_f(1-\varepsilon_p)PT_r}\frac{\partial n_f}{\partial z_f} \qquad (4.15)$$

Eq. (4.15) is subjected to the following boundary condition:

$$@ \; z_f = 0 \qquad T_f = T_{bed} \qquad (4.16)$$

In Eq. (1), the term $\boldsymbol{R}$ is the heat generation and loss rate per unit volume, which is the summation of heat loss/generation via chemical reaction ($\boldsymbol{R_{rxn}}$), heat loss through the freeboard walls ($\boldsymbol{R_w}$) and convective heat transport from fly ash and char

114

particles to the gaseous medium (R_p) and the term $\nabla \cdot q_r$ is the radiative ST, which can be obtained from the solution of the RTE. The heat generation due to convective heat transport from the particles to the gaseous medium (R_p) is determined by the following expression, which considers only convective transport between the particles and the gaseous medium:

$$R_p = \frac{3F_{CO}}{A_{bed}\rho_d} \int_{r_{min}}^{r_{maxe}} \frac{P_{z,d}(r)}{r u_p(r)} \left[h_p(T_d - T_f) \right] dr$$

$$+ 3\varepsilon_d \int_{r_{maxe}}^{r_{min}} \frac{P_{z,d}(r)}{r} \left[h_p(T_d - T_f) \right] dr$$

$$+ 3\varepsilon_i \int_{r_{maxe}}^{r_{max}} \frac{P_{z,i}(r)}{r} \left[h_p(T_i - T_f) \right] dr \tag{4.17}$$

Noting that the rate of energy transferred from freeboard to wall by radiation and convection must be equal to the rate of energy transferred through the walls, an energy balance at the freeboard side wall surfaces can be formulated to obtain the freeboard wall temperature profile;

$$h_{fw}(T_f - T_{fw}) + q_{r,w} - \frac{(T_{fw} - T_{fw,o})}{R_w} = 0 \tag{4.18}$$

where $q_{r,w}$ is the net wall radiative HF obtained from the radiation model and h_{fw} can be estimated using the approach suggested by Kunii and Levenspiel [165]:

$$\frac{h_{fw} - h_g}{h_{z_f=0} - h_g} = exp(-az_f/2) \tag{4.19}$$

where $h_{z_f=0}$ is the heat transfer coefficient at the freeboard entrance which is taken as the heat transfer coefficient between bed and wall. The term a in Eq. (4.19) refers to the decay constant of the particles along the freeboard and is estimated by using the correlation of Choi et al. [148] as given by Eq. (3.8). The term h_g stands for the gas component which can be estimated utilizing the correlation suggested by Gnielinski [166];

$$h_g = \frac{k_g}{d_{bed}} \left[\frac{(f/8)(Re - 1000)Pr}{1 + 12.7(f/8)^{0.5}(Pr^{2/3} - 1)} \right] \tag{4.20}$$

For the investigation of the influence of coupling a detailed RHT model to the FBC system model, predictions of the coupled models are compared with the FBC system model without radiation model [28] where Stefan-Boltzmann law and an empirical correlation for the RHT coefficient, h_r, are employed in Eqs. (4.17) and (4.19), respectively, to account for RHT instead of solving RTE.

For the FBC system model without radiation model, freeboard gas temperature profiles can be obtained using Eq. (4.15) by omitting the radiative ST, $\nabla \cdot \boldsymbol{q}_r$.

$$\frac{\partial T_f}{\partial t} = \frac{RT_f^2 n_f}{A_f(1 - \varepsilon_p)PT_r} \frac{\partial T_f}{\partial z_f} + \frac{RT_f^2 \boldsymbol{R}}{PM_g T_r C_{p,g}}$$
$$- \frac{RT_f^2 (T_f - T_r)}{A_f(1 - \varepsilon_p)PT_r} \frac{\partial n_f}{\partial z_f} \tag{4.21}$$

where $\boldsymbol{R}$ is the heat generation and loss rate per unit freeboard volume which is defined as:

$$\boldsymbol{R} = \boldsymbol{R}_{rxn} + \boldsymbol{R}_{fw} + \boldsymbol{R}_p \tag{4.22}$$

The term, $\boldsymbol{R}_p$, can be rearranged by simply utilizing the Stefan-Boltzmann law for radiative heat exchange between particles and gases:

$$\boldsymbol{R}_p = \frac{3F_{CO}}{A_{bed}\rho_d} \int_{r_{min}}^{r_{maxe}} \frac{P_{z,d}(r)}{r u_p(r)} \left[h_p(T_d - T_f) + \epsilon_d \sigma(T_d^4 - T_f^4) \right] dr$$

$$+ 3\varepsilon_d \int_{r_{maxe}}^{r_{min}} \frac{P_{z,d}(r)}{r} \left[h_p(T_d - T_f) + \epsilon_d \sigma(T_d^4 - T_f^4) \right] dr$$

$$+ 3\varepsilon_i \int_{r_{maxe}}^{r_{max}} \frac{P_{z,i}(r)}{r} \left[h_p(T_i - T_f) + \epsilon_i \sigma(T_i^4 - T_f^4) \right] dr \tag{4.23}$$

The emissivity of fly ash particles, ϵ_i, is estimated noting that it is equal to their absorption efficiency [167] that can be calculated utilizing Mie theory and their d_{32}.

For the estimation of the emissivity of freeboard char particles, ϵ_d, however, the empirical correlation of Schiemann et al. [167] is adopted. Using the above-mentioned relations, the emissivities of freeboard char and fly ash particles are determined as 0.59 and 0.29, respectively.

The wall temperature profile can be obtained from the energy conservation equation given in Eq. (4.18) by omitting the net wall radiative HF term, $\boldsymbol{q_{r,w}}$:

$$h_{fw}(T_f - T_{fw}) + \boldsymbol{q_{r,w}} - \frac{(T_{fw} - T_{fw,o})}{R_w} = 0 \tag{4.24}$$

RHT is taken into consideration by utilizing a RHT coefficient, h_r, in Eq. (4.25);

$$\frac{h_{fw} - (h_r + h_g)}{h_{z_f=0} - (h_r + h_g)} = ex\, p(-az_f/2) \tag{4.25}$$

where h_r stands for the radiative component which can be estimated by:

$$h_r = \varepsilon_{fw}\sigma(T_f + T_{fw})(T_f^2 + T_{fw}^2) \tag{4.26}$$

4.3   Solution Procedure

4.3.1   Coupling between System Model and Radiation Model

Solution domains for the freeboard of the test rig utilized in the 1-D transient FBC system model for combustion of lignite and radiation model are schematically represented in Figure 4.3. The emissivities of the boundaries with the cooler at the top and with the bed section at the bottom are taken as 0.87 and 1.0 based on a previous study of Kozan and Selcuk [168].
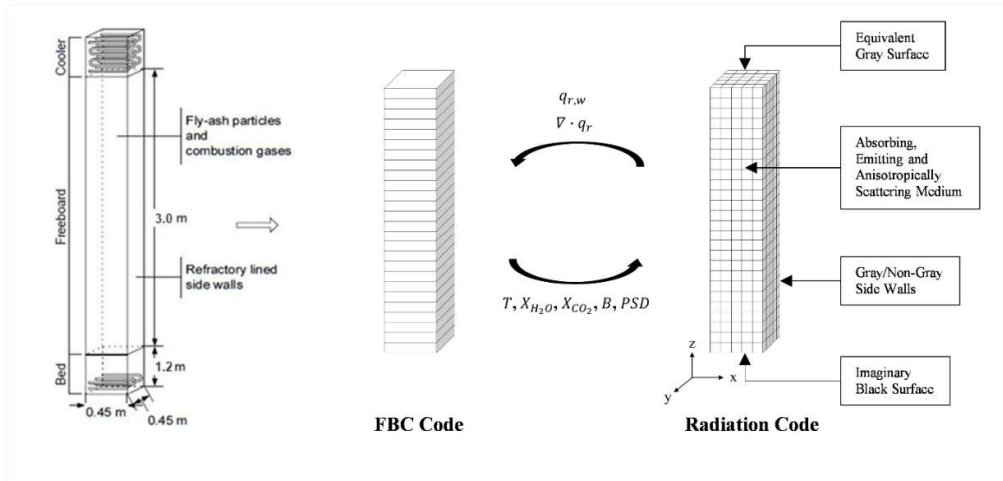
Figure 4.3. Solution domains for the test rig utilized in the 1-D transient FBC system model for combustion of lignite and radiation model

The algorithm of the coupling of the transient FBC system model with the radiation model is illustrated in Figure 4.4. Coupling between the transient FBC system model and radiation model is mainly based on regular transfer of temperature and species concentration fields solved by the FBC system model to the radiation model, which in turn provides ST field and wall radiative HFs for the energy conservation equations of freeboard as solution advances in time.

The algorithm starts with the specification of the initial conditions obtained from the steady-state model and grid resolution for the numerical solution. Utilizing the initial conditions, the radiation model advances one time step (t_p), and estimates the radiative properties of medium involving combustion gases and fly ash particles, and thus determines radiative energy STs and HFs at all grid locations along x-, y- and z-directions. Then, these STs are averaged over x- and y-coordinates at each grid location along the z-direction, and net wall HFs for grids in the z-direction are calculated. With these averaged radiative STs and net wall HFs, the transient FBC code marches to the next time step and makes concentration and temperature profiles, particle load profiles, and PSD for the radiation model available in the next time step. Upon the next call, the radiation model initiates the solution of RTE for the next time step by utilizing the radiative intensities determined from the previous

118

call to converge faster. The user-defined time step t_p for the exchange of necessary information between the FBC and radiation codes is selected as 1 second. This user-defined t_p is further divided into smaller internal time steps by the ODE solver. The ODE solver ROWMAP, which uses a time adaptive method, chooses the time steps in such a way that maintains the accuracy and stability of the evolving solution.
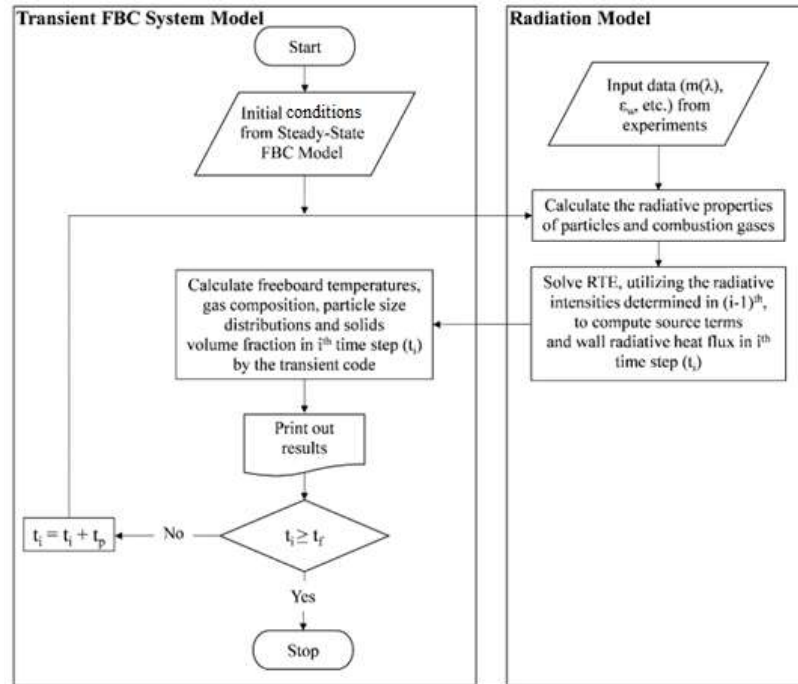
Figure 4.4. Algorithm of the coupling of transient FBC system model with the radiation model

4.3.2 Algorithm of the Coupled Code

In the application of the model, direct use of the elutriation rate constant and particle hold-up distribution of Choi et al. [148] yielded higher carry-over flow rates and incorrect particle loads at the combustor exit. To match the measured carry-over flow rates, the elutriation rate constant is multiplied by 0.20. On the other hand, the decay constant of the inert ash hold-up expression of Choi et al. [148] is multiplied by 0.24 to match the predicted and measured particle loads at the freeboard exit.

The kinetic expression suggested by Hottel et al. [153] predicts CO concentrations approximately one order of magnitude lower compared to the measurements. To match the measured and predicted CO concentrations, this expression is just simply multiplied with 0.3.

Figures 3.7 to 3.9 show the algorithm of the steady state model code in compact form. The solution starts with defining initial conditions as calculated by the steady-state code for the same test rig. The details of the steady-state model can be found elsewhere [154]. The coupled transient FBC system model is mainly based on the regular transfer of temperature and species concentration fields solved by the FBC system model and ST field and wall radiative HFs solved by the radiation model at each time step.

The ODE system is integrated using a readily available solver ROWMAP utilizing implicit Runge-Kutta methods. The solution of non-linear algebraic equation systems, on the other hand, is achieved by utilizing the subroutine ZERO. Detailed solution procedure of steady-state and transient codes for lignite combustion can be found elsewhere [154].

Figure 4.5. Flowchart for the transient code (The shaded areas show the modified sections of this study)
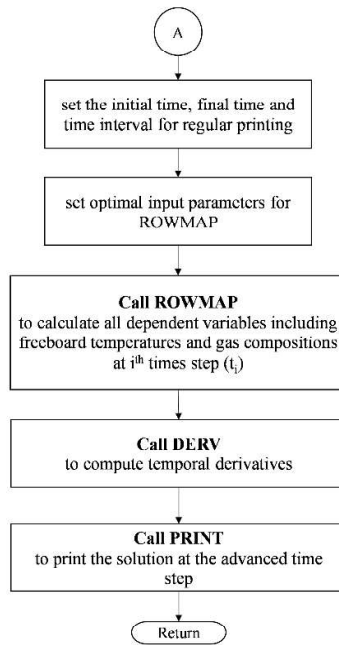
Figure 4.6. Flowchart for the transient code

122

CHAPTER 5

2-D COMPUTATIONAL FLUID DYNAMICS (CFD) MODEL FOR ABFBC FIRING LIGNITE

5.1   General

In this section, the details of the 2-D computational fluid dynamics (CFD) model of the 0.3 MW_t ABFBC test rig firing lignite only, developed within the scope of this thesis study, are described. The CFD model is developed using commercial CFD software, ANSYS Fluent 2020 R1 [98]. The model accounts for multiphase gas-solid flow, turbulence, drying, devolatilization and char combustion of lignite, combustion of gaseous species, species transport, and convective and RHT. The complex multiphase flow in the test rig is represented as two Eulerian and one Lagrangian phase for combustion gases, inert bed material (which is ash) and lignite, respectively. The hydrodynamics of the gas phase is described by the k-ε turbulence model whereas the kinetic theory of granular flow (KTGF) is utilized to represent the hydrodynamics of the inert phase. The RTE is solved by the DOM together with some user-defined functions (UDFs) written to estimate the radiative properties of combustion gases and particles. Moreover, for the lignite phase, a dense discrete phase model (DDPM) embedded in ANSYS Fluent is utilized to consider the interaction between the lignite phase with each Eulerian phase. The CFD model presented in this study involves a reaction scheme with two heterogeneous and three homogeneous chemical reactions, 8 gaseous species; O_2, CO_2, CO, H_2, H_2O, Volatile, SO_2, and N_2 and two solid species; inert bed material (ash), and lignite, are utilized. The details of conservation equations and sub-models utilized in the 2-D CFD model will be described in the following sections.

5.2   CFD Model Description

The 2-D CFD model for ABFBC firing lignite can be described in terms of multiphase gas-solid flow, turbulence, chemical reaction, and radiation.

5.2.1   Modeling of Multiphase Gas-Solid Flow

As described earlier, the complex multiphase flow in the 0.3 MW$_t$ ABFBC test rig is represented by two Eulerian and one Lagrangian phase for combustion gases, inert bed material, and lignite, respectively. In the Eulerian phase, the particles are treated as a continuum where the collision between particles is treated using KTGF. In the Lagrangian phase, on the other hand, instead of solving Navier-Stokes equations, each group of particles is tracked according to Newton's second law of motion. The following subsections summarize the governing equations for each phase under investigation within the scope of this study.

5.2.1.1   Gas Phase

The gas phase mass conservation equation can be written as;

$$\frac{\partial}{\partial t}\left(\alpha_g \rho_g\right) + \nabla \cdot \left(\alpha_g \rho_g \boldsymbol{u_g}\right) = \sum_{p=1}^{N_p}\left(\dot{m}_{pg} - \dot{m}_{gp}\right) + S_g \tag{5.1}$$

where α_g is the volume fraction of the gas phase, ρ_g is the gas phase density, $\boldsymbol{u_g}$ is the gas phase velocity, $\dot{m}$ is the mass transfer between phases, S_g is the ST due to heterogeneous reactions, p is the phase index and N_p is the total number of phases. The density of the gas phase (ρ_g) is calculated by the ideal gas equation of state.

To calculate the species concentration distribution, the following generalized species conservation equation is solved for each gas phase species;

$$\frac{\partial}{\partial t}\left(\alpha_g \rho_g Y_{g,j}\right) + \nabla \cdot \left(\alpha_g \rho_g \boldsymbol{u_g} Y_{g,j}\right)$$

$$= -\nabla \cdot \alpha_g \boldsymbol{J_{g,j}} + \alpha_g r_{g,j} + \sum_{p=1}^{N_p}\left(\dot{m}_{j,pg} - \dot{m}_{j,gp}\right) + \mathcal{R} \qquad (5.2)$$

where $Y_{g,j}$ is the mass fraction of the gaseous species j, $R_{g,j}$ is the rate of homogeneous reactions, $\mathcal{R}$ is the rate of heterogeneous reactions and $\boldsymbol{J_{g,j}}$ is the diffuse flux which can be defined as;

$$\boldsymbol{J_{g,j}} = -\left(\rho_g D_j + \frac{\mu_t}{Sc_t}\right)\nabla Y_{g,j} - D_{T,i}\frac{\nabla T}{T} \qquad (5.3)$$

where D_j diffusivity of the species j in the gas phase, μ_t is the turbulent viscosity, Sc_t is the turbulent Schmidt number and $D_{T,i}$ is the thermal (Soret) diffusion coefficient. The gas phase momentum conservation equation can be written as;

$$\frac{\partial}{\partial t}\left(\alpha_g \rho_g \boldsymbol{u_g}\right) + \nabla \cdot \left(\alpha_g \rho_g \boldsymbol{u_g} \boldsymbol{u_g}\right)$$

$$= -\alpha_g \nabla P_g + \nabla \cdot \bar{\bar{\tau}}_g + \alpha_g \rho_g g$$

$$+ \sum_{p=1}^{N_p} K_{pg}\left(\boldsymbol{u_p} - \boldsymbol{u_g}\right)\left(\dot{m}_{pg}\boldsymbol{u_{pg}} - \dot{m}_{gp}\boldsymbol{u_{gp}}\right) + \left(\boldsymbol{F_{ext,g}} + \boldsymbol{F_{td,g}}\right) \;(5.4)$$

where P_g is the gas pressure, $\bar{\bar{\tau}}_g$ is the stress tensor, K is the momentum exchange coefficient between phases, $\boldsymbol{F_{ext,g}}$ is the external body forces, and $\boldsymbol{F_{td,g}}$ is the turbulent dispersion force. The first three terms of the RHS of Eq. (5.4) denote pressure force, shear force, and gravity, respectively. The fourth term denotes the momentum exchange between phases, and the last term is the forces applied to the gas phase. The stress tensor for the gas phase is given by the following expression;

$$\bar{\bar{\tau}}_g = \alpha_g \mu_g \left(\frac{\partial \boldsymbol{u_{g,i}}}{\partial x_j} + \frac{\partial \boldsymbol{u_{g,j}}}{\partial x_i}\right) - \frac{2}{3}\mu_g \delta_{ij}\frac{\partial \boldsymbol{u_{g,k}}}{\partial x_k} \qquad (5.5)$$

where μ is the dynamic viscosity and δ_{ij} is the Kronecker delta.

Finally, the energy conservation equation for the gas phase in the enthalpy form is written as;

$$\frac{\partial}{\partial t}(\alpha_g \rho_g h_g) + \nabla \cdot (\alpha_g \rho_g \boldsymbol{u_g} h_g)$$

$$= -\alpha_g \frac{\partial P_g}{\partial t} + \bar{\bar{\tau}}_g : \nabla \boldsymbol{u_g} - \nabla \cdot \boldsymbol{q_g} + S_g$$

$$+ \sum_{p=1}^{N_p} Q_{pg}\left(\dot{m}_{pg} h_{pg} - \dot{m}_{gp} h_{gp}\right) \tag{5.6}$$

where h_g is the specific enthalpy of the gas phase, $\boldsymbol{q_g}$ is the HF, S_g is the ST due to chemical reaction and radiation, and Q is the intensity of heat exchange between phases. The first three terms of the RHS of Eq. (5.6) denote work done by pressure forces, work done by viscous forces, and rate of heat conduction, respectively.

5.2.1.2   Inert Phase

Similar to the gas phase, the mass and momentum conservation equation for inert bed material particles are written as follows;

$$\frac{\partial}{\partial t}(\alpha_i \rho_i) + \nabla \cdot (\alpha_i \rho_i \boldsymbol{u_i}) = \sum_{p=1}^{N_p}\left(\dot{m}_{pi} - \dot{m}_{gi}\right) + S_i \tag{5.7}$$

$$\frac{\partial}{\partial t}(\alpha_i \rho_i \boldsymbol{u_i}) + \nabla \cdot (\alpha_i \rho_i \boldsymbol{u_i} \boldsymbol{u_i})$$

$$= -\alpha_i \nabla P_i + \nabla \cdot \bar{\bar{\tau}}_i + \alpha_i \rho_i g + \sum_{p=1}^{N_p} K_{pi}\left(\boldsymbol{u_p} - \boldsymbol{u_i}\right)\left(\dot{m}_{pi} \boldsymbol{u_{pi}} - \dot{m}_{ip} \boldsymbol{u_{ip}}\right)$$

$$+ \left(\boldsymbol{F}_{ext,i} + \boldsymbol{F}_{td,i}\right) \tag{5.8}$$

where α_i, ρ_i, and $\boldsymbol{u_i}$ are the volume fraction, density, and velocity of the inert phase and $\bar{\bar{\tau}}_i$ is the stress tensor of the inert phase which can be written as;

126

$$\bar{\bar{\tau}}_i = \alpha_i \mu_i \left(\frac{\partial \boldsymbol{u}_{i,i}}{\partial x_j} + \frac{\partial \boldsymbol{u}_{i,j}}{\partial x_i} \right) - \frac{2}{3} \mu_i \delta_{ij} \frac{\partial \boldsymbol{u}_{i,k}}{\partial x_k} + \lambda_i \frac{\partial \boldsymbol{u}_{i,k}}{\partial x_k} \tag{5.9}$$

where λ_i is the bulk viscosity term, which is negligible for the gas phase as given in Eq. (5.5). As can be seen from Eq. (5.8), the terms solid pressure (P_i) and solid viscosity (μ_i) arises in the momentum conservation equation for the inert phase which are often described by the KTGF. The solid pressure is described by the expression of Lun et al. [171] which contains a kinetic term and a particle collision term;

$$P_i = \alpha_i \rho_i \Theta_i + 2\rho_i (1 + e_{ii}) \alpha_i{}^2 g_{0,ii} \Theta_i \tag{5.10}$$

where Θ_i is the granular temperature, e_{ii} is the restitution coefficient for the collision of inert particles, and $g_{0,ii}$ is the radial distribution function which is determined by the following expression;

$$g_{0,ii} = \left[1 - \left(\frac{\alpha_i}{\alpha_{i,max}} \right)^{1/3} \right]^{-1} \tag{5.11}$$

where $\alpha_{i,max}$ is the maximum packing limit for the inert phase which is defined as 0.63 as suggested by ANSYS Fluent [172]. The bulk viscosity (λ_i) in Eq. (5.9) for the inert phase is given by [171]:

$$\lambda_i = \frac{4}{3} \alpha_i{}^2 \rho_i d_i g_{0,ii} (1 + e_{ii}) \left(\frac{\Theta_i}{\pi} \right)^{1/2} \tag{5.12}$$

The term solid viscosity (μ_i), on the other hand, is defined by the summation of collisional, kinetic, and frictional viscosities:

$$\mu_i = \mu_{i,col} + \mu_{i,kin} + \mu_{i,fr} \tag{5.13}$$

It should be noted at this point that the frictional viscosity ($\mu_{i,fr}$) becomes important when the volume fraction of inerts is close to the maximum packing limit as in the case investigated in this study. Therefore, it is included in the calculation of solid viscosity. For the collisional, kinetic, and frictional viscosities of the inert phase, the

expressions developed by Gidaspow et al. [173], Syamlal et al. [174] and Schaeffer [175], respectively, are utilized;

$$\mu_{i,col} = \frac{4}{5}\alpha_i{}^2\rho_i d_i g_{0,ii}(1 + e_{ii})\left(\frac{\Theta_i}{\pi}\right)^{1/2} \tag{5.14}$$

$$\mu_{i,kin} = \frac{\alpha_i \rho_i d_i \sqrt{\Theta_i \pi}}{96\alpha_i(1 + e_{ii})g_{0,ii}}\left[1 + \frac{4}{5}g_{0,ii}\alpha_i(1 + e_{ii})\right]^2 \alpha_i \tag{5.15}$$

$$\mu_{i,fr} = \frac{P_i sin\varphi}{2\sqrt{I_{2D}}} \tag{5.16}$$

where φ is the angle of internal friction which is 30º as suggested by ANSYS Fluent [172], and I_{2D} is the second invariant of the deviatoric stress tensor.

The granular temperature of the inert phase (Θ) is proportional to the kinetic energy of the inert particles as given by the formal expression below;

$$\Theta_i = \frac{1}{3}\boldsymbol{u'_i}\boldsymbol{u'_i} \tag{5.17}$$

where $\boldsymbol{u'_i}$ is the fluctuating inert phase velocity. The granular temperature is generally calculated from the granular energy transport equation derived from KTGF which takes the following form;

$$\frac{3}{2}\left[\frac{\partial}{\partial t}(\alpha_i\rho_i\Theta_i) + \nabla \cdot (\alpha_i\rho_i\boldsymbol{u_i}\Theta_i)\right]$$
$$= \left(-P_i\bar{\bar{I}} + \bar{\bar{\tau}}_i\right):\nabla\boldsymbol{u_i} + \nabla \cdot \left(k_{\Theta_i}\nabla\Theta_i\right) - \gamma_{\Theta_i} + \varphi_{pi} \tag{5.18}$$

where $\left(P_i\bar{\bar{I}} + \bar{\bar{\tau}}_i\right):\nabla\boldsymbol{u_i}$ is the granular energy generation due to stress tensor, $k_{\Theta_i}\nabla\Theta_i$ is the diffusion transport, γ_{Θ_i} is the collisional granular energy dissipation and φ_{pi} is the energy exchange between phases ($= -3K_{pi}\Theta_i$). Rather than solving the partial differential equation given by Eq. (5.18), convection and diffusion transport terms can be neglected assuming granular energy is in steady-state and dissipates locally:

$$0 = \left(-P_i\bar{\bar{I}} + \bar{\bar{\tau}}_i\right):\nabla\boldsymbol{u_i} - \gamma_{\Theta_i} + \varphi_{pi} \tag{5.19}$$

The algebraic form of the granular energy transport equation has been shown to provide reasonable predictions in fluidized beds [176]. Therefore, in this study, the granular temperature of the inert phase is estimated using Eq. (5.19). The collisional energy term in Eq. (5.19) is estimated using the expression of Lun et al. [171].

Finally, for the determination of the temperature of the inert phase, the following energy conservation equation can be solved;

$$\frac{\partial}{\partial t}(\alpha_i \rho_i h_i) + \nabla \cdot (\alpha_i \rho_i \boldsymbol{u_i} h_i)$$
$$= -\alpha_i \frac{\partial P_i}{\partial t} + \bar{\bar{\tau}}_i : \nabla \boldsymbol{u_i} - \nabla \cdot \boldsymbol{q_i} + S_i$$
$$+ \sum_{p=1}^{N_p} Q_{pi}(\dot{m}_{pi} h_{pi} - \dot{m}_{ip} h_{ip}) \tag{5.20}$$

5.2.1.3   Lignite Phase

Unlike the Eulerian approach for the solid phase in which the solid particles are treated as a continuum, the DPM treats the solid phase as dispersed particles by tracking them according to Newton's 2nd law. However, in its original form, the discrete phase is not taken into consideration when solving the equation for the continuous phase equations as it assumes the volume fraction of the discrete particles is very low [100]. To alleviate this problem, the DDPM, in which the interactions between discrete and continuous phases are considered, is utilized.

The discrete lignite particles are tracked by solving Newton's 2nd law in the following form;

$$\frac{\partial \boldsymbol{u_l}}{\partial t} = F_D(\boldsymbol{u} - \boldsymbol{u_l}) + \frac{g(\rho_l - \rho)}{\rho_l} + \boldsymbol{F}_{vm,l} + \boldsymbol{F}_{interaction} \tag{5.21}$$

where $\boldsymbol{F}_{vm,l}$ is the virtual mass force and F_D is the drag per unit mass;

$$F_D = \frac{18\mu}{\rho_l d_l{}^2} \frac{C_D Re}{24} \tag{5.22}$$

where C_D is the drag coefficient and Re is the particle Reynold's number ($=$ $\rho d_l |u - u_l|/\mu$). Finally, the term $\boldsymbol{F_{interaction}}$ denotes the interparticle interactions and is determined by the following expression;

$$\boldsymbol{F_{interaction}} = -\frac{1}{\rho_l} \nabla \cdot \bar{\bar{\tau}}_l \tag{5.23}$$

where $\bar{\bar{\tau}}_l$ is the stress tensor for the lignite phase which is determined by the KTGF similar to the inert phase.

The mass conservation equation for the DDPM can be written by noting that the mass loss of lignite particles is solely due to drying, devolatilization, and char combustion:

$$\frac{\partial m_l}{\partial t} = \left(\frac{\partial m_l}{\partial t}\right)_{dry} + \left(\frac{\partial m_l}{\partial t}\right)_{devol} + \left(\frac{\partial m_l}{\partial t}\right)_{char} \tag{5.24}$$

The terms on the RHS stand for mass losses to the gas phase by drying, devolatilization, and char combustion, respectively. The rates of drying, devolatilization, and char combustion will be described in the following sections.

The energy balance for the DDPM can be written as follows;

$$m_l C_{p,l} \frac{dT_l}{dt} = hA_l(T_\infty - T_l) + A_l \varepsilon_l \sigma\left(\theta_R{}^4 - T_l{}^4\right) - f_h \left(\frac{\partial m_l}{\partial t}\right)_{char} H_{rxn}$$
$$- \left(\frac{\partial m_l}{\partial t}\right)_{devol} h_{fg,v} \tag{5.25}$$

where A_l, ε_l, and $C_{p,l}$ are surface area, emissivity, and specific heat capacity of particles, H_{rxn} is the reaction enthalpy of char combustion, $h_{fg,v}$ is the enthalpy of devolatilization, σ is the Stefan-Boltzmann constant, θ_R is the radiation temperature [$= (G/4\sigma)^{0.25}$] and f_h is the fraction of heat released absorbed by char particles which is recommended as 1.0 if the char burnout product is CO only [172]. The terms on the RHS of the equation are convective heat transfer, RHT, and heat

generation/consumption due to char combustion and devolatilization, respectively. The heat transfer coefficient h can be calculated by the expression of Ranz and Marshall [177]:

$$h = \frac{k_g}{d_l}\left(2.0 + 0.6Re_l^{1/2}Pr_g^{1/3}\right)$$ (5.26)

5.2.1.4 Phase Interactions

The momentum exchange coefficients (K) in Eqs. (5.4) and (5.8) are determined by the expression of Gidaspow [173] which is a combination of Wen and Yu model [178] and Ergun equation [179]. To account for the interphase turbulent momentum transfer, the model of Lopez de Bertodano [180] is applied between the gas and inert phases. On the other hand, the dispersion of discrete phase particles due to turbulence in continuous phases is taken into account by the discrete random walk model. The restitution coefficient for the collision of lignite and inert particles (e_{il}) is taken as 0.9. Finally, the interfacial area between phases (A_i) is estimated by the following expression:

$$A_i = \frac{6\alpha_p}{d_p}$$ (5.27)

where α_p and d_p are the volume fraction and diameter of inert or lignite particles.

5.2.2 Modeling of Turbulence

Turbulence is of significant importance in combusting systems as it has an obvious impact on heat and mass transfer. However, modeling of turbulent flow is not straightforward as it, originally, requires the 3-D transient solution of Navier-Stokes equations with the utilization of very small grid sizes to take the small-scale eddies into consideration. This approach is referred to as the direct numerical simulation (DNS) and is the most accurate treatment of turbulent flows. Nevertheless, it requires

high CPU time, which makes it affordable for only a few fundamental or academic problems with very low Reynolds numbers. For practical applications, generally operated with high Reynolds numbers, more computationally efficient methods were developed by time-averaging the governing equations and introducing a new property called 'turbulent (eddy) viscosity' to represent the Reynolds stress tensor arising from time-averaging the governing equations. In the literature, these approaches are referred to as Reynolds averaged Navier-Stokes (RANS) models. The major concern of RANS models is to accurately represent the Reynolds stress tensor or turbulent viscosity. For this purpose, many variations of RANS models have been developed including mixing length theory, Spalart-Allramas model, k-ε model, k-ω model, etc.

In the present work, the realizable k-ε model is utilized to treat the turbulent flow as it is a sufficiently robust and commonly used model in FBC applications. In this model, the turbulent viscosity is estimated by the solution of two transport equations: one is for turbulent kinetic energy (k) and the other for its dissipation rate (ε). The transport equations are given by the following expressions;

$$\frac{\partial}{\partial t}\left(\alpha_g \rho_g k\right) + \nabla \cdot \left(\alpha_g \rho_g \boldsymbol{u_g} k\right)$$
$$= \nabla \cdot \alpha_g \left(\mu_g + \frac{\mu_{g,t}}{\sigma_k} \nabla \cdot k\right) + \alpha_g (G_k + G_b - \rho_g \varepsilon - Y_M) \qquad (5.28)$$

$$\frac{\partial}{\partial t}\left(\alpha_g \rho_g \varepsilon\right) + \nabla \cdot \left(\alpha_g \rho_g \boldsymbol{u_g} \varepsilon\right)$$
$$= \nabla \cdot \alpha_g \left(\mu_g + \frac{\mu_{g,t}}{\sigma_\varepsilon} \nabla \cdot \varepsilon\right)$$
$$+ \alpha_g \left(\rho_g C_1 S\varepsilon - \rho_g C_2 \frac{\varepsilon^2}{k + \sqrt{\upsilon\varepsilon}} C_{1\varepsilon} \frac{\varepsilon}{k} C_{3\varepsilon} G_b\right) \qquad (5.29)$$

132

where;

$$C_1 = max\left[0.43, \frac{\eta}{\eta + 5}\right], \qquad \eta = S\frac{\varepsilon}{k}, \qquad S = \sqrt{2S_{i,j}S_{i,j}},$$

$$S_{i,j} = \frac{1}{2}\left(\frac{\partial \boldsymbol{u}_{g,i}}{\partial x_j} + \frac{\partial \boldsymbol{u}_{g,j}}{\partial x_i}\right) \tag{5.30}$$

In Eqs. (5.28) and (5.29), G_k is the turbulent kinetic energy due to the mean velocity gradient, G_b is the turbulent kinetic energy due to buoyancy, Y_M is the contribution of the fluctuating dilatation in compressible turbulence to the overall dissipation rate, and σ_k and σ_ε are turbulent Prandtl numbers for k and ε. The constants $C_{1\varepsilon}$, C_2, σ_k and σ_ε are selected as 1.44, 1.9, 1.0, and 1.2, respectively.

The terms G_k, G_b and Y_M are determined by the following expressions:

$$G_k = \mu_{g,t}S^2, \qquad S = \sqrt{2S_{i,j}S_{i,j}}, \qquad S_{i,j} = \frac{1}{2}\left(\frac{\partial \boldsymbol{u}_{g,i}}{\partial x_j} + \frac{\partial \boldsymbol{u}_{g,j}}{\partial x_i}\right) \tag{5.31}$$

$$G_b = -g_i\frac{\mu_{g,t}}{\rho_g Pr_t}\frac{\partial \rho}{\partial x_i} \tag{5.32}$$

$$Y_M = 2\rho_g\varepsilon Ma_t^2 \tag{5.33}$$

where Ma_t is the turbulent Mach number $(= \sqrt{k/a^2})$ where a is the speed of sound. The $C_{3\varepsilon}$ in Eqs. (5.28) and (5.29) can be calculated by the following expression;

$$C_{3\varepsilon} = tanh\left|\frac{v}{u}\right| \tag{5.34}$$

where v is the component of the flow velocity parallel to the gravitational vector and u is the component of the flow velocity perpendicular to the gravitational vector.

Once the transport equations for k and ε are solved, the turbulent viscosity $(\mu_{g,t})$ is expressed as follows;

$$\mu_{g,t} = \rho_g C_\mu \frac{k^2}{\varepsilon} \tag{5.35}$$

133

where C_μ is a variable as a function of mean strain and rotation rates, the angular velocity of the system rotation, and the turbulence fields (k and ε). The details of the realizable k-ε model can be found elsewhere [172].

Another challenging aspect of modeling turbulent flow is the treatment of the near-wall region where large gradients of solution variables occur. This region is basically subdivided into three regions which are the viscous sublayer, buffer layer, and fully-turbulent region. In the viscous sublayer, the momentum transport is derived by the molecular transport whereas turbulence dominates the fully-turbulent region. Since the near-wall region has a significant impact on turbulence, its accurate representation is of significant importance. Generally, there are two approaches for the treatment of the near-wall region when dealing with turbulent flow. One of them is to fully resolve the near-wall region by utilizing sufficiently small grid sizes such that all the subdivisions of the near-wall region, including the viscous sublayer, are taken into consideration. However, this approach requires smaller grid sizes, and hence, leads to higher CPU requirements. In the other alternative method, the near-wall region is treated by using semi-empirical methods called 'wall functions' instead to link the wall and fully-turbulent region. In the present work, the near-wall region is treated by the use of scalable wall functions which is the extension of the wall function of Launder and Spalding [181] for fine grids.

5.2.3   Modeling of Chemical Reactions

During the operation of fluidized bed combustors, lignite particles undergo drying, devolatilization, and char combustion. In the present work, these processes are taken to occur consecutively.

When coal particles are fed to a fluidized bed combustor, they first release their moisture content which is called drying. In this study, the drying process is assumed to be controlled by diffusion only. After all the moisture content is released, devolatilization starts to take place. Char particles start burning after devolatilization.

134

The products of devolatilization and char combustion then undergo concurrent gas phase reactions. The details of devolatilization, char combustion, and gas phase combustion are given in the following sub-sections.

5.2.3.1   Devolatilization Model

The devolatilization is taken into account by the following reaction in the 2-D simulation of the 0.3 MWt ABFBC test rig.

$$Coal \rightarrow Char + Volatiles \tag{R5.1}$$

The products of devolatilization are taken to be released into the gas phase. The rate of devolatilization is represented by the two-competing-reaction model of Kobayashi et al. [182]. According to the devolatilization model of Kobayashi et al., the primary decomposition of coal to its intermediate products is governed by two competing reactions as shown in Figure 5.1.
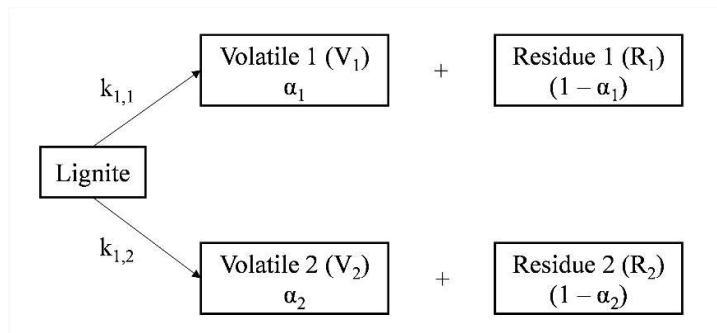
Figure 5.1. The schematic representation of the two-competing-reaction model of Kobayashi et al. [182]

In Figure 5.1, α_1 and α_2 stand for the mass stoichiometric coefficients. The rate constant of each reaction is described by the Arrhenius equation:

$$k_{1,1} = A_{1,1}\, exp\left(-E_{1,1}/RT\right) \tag{5.36}$$

$$k_{1,2} = A_{1,2}\, ex\, p\left(-E_{1,2}/RT\right) \tag{5.37}$$

The first reaction is dominant at low temperatures whereas the second reaction is faster at high temperatures. In other words, the activation energy of the second reaction, $E_{1,2}$, needs to be higher than that of the first reaction, $E_{1,1}$. The overall weight loss of coal particles in dry and ash-free (d.a.f.) basis can then be evaluated using the following integral:

$$\Delta W = \frac{m_{V_1} + m_{V_2}}{m_{VM} + m_{Char}} = \int_0^t (\alpha_1 k_{1,1} + \alpha_2 k_{1,2}) \, exp\left(-\int_0^t (k_{1,1} + k_{1,2})dt \right) dt \quad (5.38)$$

The parameters for the devolatilization model of Kobayashi et al. [182] are taken from Ubhayakar et al. [183] as they are stated to be applicable for high volatile content coals such as lignite and bituminous coal [184]. Table 5.1 summarizes the parameters for the devolatilization model of Kobayashi et al. [182]. The mass stoichiometric coefficients (α_1 and α_2) are selected as 0.54 and 1.0, respectively, based on recommendations of ANSYS Fluent [172].

Table 5.1 The kinetic parameters for the devolatilization model [183]

α_1	0.54	$A_{1,1}$ (1/s)	3.75 x 10^5	$E_{1,1}$ (J/kmol)	7.37 x 10^7
α_2	1.00	$A_{1,2}$ (1/s)	1.40 x 10^{13}	$E_{1,2}$ (J/kmol)	2.51 x 10^8

5.2.3.2   Char Combustion Model

CO is taken to be the sole product of char combustion under typical fluidized bed combustion temperatures:

$$C_{(s)} + 0.5 \, O_2 \rightarrow CO \quad\quad\quad\quad\quad\quad (R5.2)$$

The rate of char combustion is represented with the intrinsic combustion model embedded in ANSYS Fluent software. In the intrinsic combustion model, both bulk diffusion and chemical reaction are taken into considerations;

$$-\frac{dm_l}{dt} = A_l \frac{\rho R T_\infty Y_{g,O_2}}{MW_{O_2}} \frac{D_0 \Re}{D_0 + \Re} \qquad (5.39)$$

where D_0 is the diffusion rate coefficient, which can be estimated by:

$$D_0 = C_1 \frac{[(T_l + T_\infty)/2]^{0.75}}{d_l} \qquad (5.40)$$

The term, $\Re$, is expressed in terms of intrinsic kinetic rate and pore diffusion rate;

$$\Re = \eta \frac{d_l}{6} \rho_l A_l k_2 \qquad (5.41)$$

where η is the effectiveness factor as a function of Thiele modulus, ρ_l is the lignite particle density, A_l is the specific internal surface area of the lignite char particle and k_2 is the intrinsic reactivity, which is of Arrhenius form:

$$k_2 = A_2 \, exp(-E_2/RT_l) \qquad (5.42)$$

The pre-exponential factor, A_2, and the activation energy, E_2, for the char combustion are taken as 0.859 kg/m^2.s.Pa and 1.49 x 10^8 J/kmol from Field et al. [156]. The parameters for the intrinsic char combustion model, which are mass diffusion rate constant, C_1, char porosity, mean pore radius, tortuosity, and specific internal surface area are taken as 1.0 x 10^{-11} kg/m^2.s.Pa [185], 0.50 [186], 3.73 nm [187], 1.414 [172], and 197 m^2/g [187], respectively.

5.2.3.3   Gas Phase Reactions

The gaseous products of devolatilization and char combustion are combined in the gas phase and undergo concurrent reactions to form CO_2 and H_2O as final products. In the present work, the gas mixture consists of lignite volatiles, H_2, H_2O, CO, CO_2, SO_2, O_2, and N_2. The species, lignite volatiles, released during the devolatilization

of lignite is represented by the chemical formula of $C_aH_bN_cS_dO_e$ where a, b, c, d, and e are determined based on the proximate and ultimate analyses of the lignite. Assuming that volatile C, H, N, and S are converted into CO, H_2, N_2, and SO_2 during volatile combustion, the gas phase volatile combustion reaction can be defined in the 2-D simulation of the test rig as;

$$Volatiles + E\ O_2 \rightarrow A\ CO + B\ H_2 + CN_2 + D\ SO_2 \tag{R5.3}$$
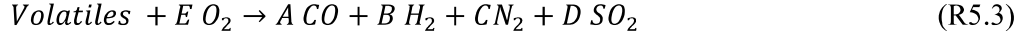
where stoichiometric coefficients, A, B, C, D, and E, are determined based on the proximate and ultimate analyses of the lignite. The rate of volatile combustion is represented by an Arrhenius rate expression taken from Heikkinen et al. [188].

$$-r_3 = 3.8 \cdot 10^7\ exp\left(-0.555 \cdot 10^8 / RT_g\right) C_{g,vol} C_{g,O_2} \tag{5.43}$$

The rate of CO and H_2 combustion in the gas phase are represented by an Arrhenius rate expression taken from Wu et al. [185] and Xie et al. [189], respectively.

$$CO + 0.5O_2 \rightarrow CO_2 \tag{R5.4}$$

$$H_2 + 0.5O_2 \rightarrow H_2O \tag{R5.5}$$

$$-r_4 = 1.3 \cdot 10^{11}\ exp\left(-1.33 \cdot 10^8 / RT_g\right) C_{g,CO} C_{g,O_2}{}^{0.5} \tag{5.44}$$

$$-r_5 = 5.159 \cdot 10^{15} \cdot T_g{}^{-1.5}\ exp\left(-2.85 \cdot 10^7 / RT_g\right) C_{g,H_2}{}^{1.5} C_{g,O_2} \tag{5.45}$$

For the calculation of gas phase reactions, the finite-rate/eddy-dissipation model is utilized in order to take turbulence-chemistry interaction into consideration. In this model, the gas phase reaction rate is determined as the slower one between the finite rate and the eddy dissipation rates;

$$r_{g,i} = min\left(r_{g,i,A}, r_{g,i,e}\right) \tag{5.46}$$

where $r_{g,i,A}$ is the reaction rate based on the finite rate model which is determined by the Eqs. (5.43) − (5.45), and $r_{g,i,e}$ is the reaction rate based on the eddy-dissipation model;

$$r_{g,i,e} = \gamma_{g,i} MW_i A \rho_g \frac{\varepsilon}{k} min \left(min_R \left(\frac{Y_R}{\gamma_{g,R} MW_R} \right), B \frac{\sum_P Y_P}{\sum_j^{N_{sp}} \gamma_{g,j} MW_j} \right) \tag{5.47}$$

where A and B are empirical constants which are 4.0 and 0.5, respectively, $\gamma_{g,i}$ is the energy dissipation per unit volume, the subscript R denotes reactant, and the subscript P denotes product.

5.2.4 Modeling of Radiation

The RHT is taken into consideration by using the DOM where the continuous angular domain is represented by a finite number of discrete solid angles. Then, the DOM representation of the RTE in a certain position r and direction Ω for a spectral medium bounded by gray-diffuse walls takes the following form:

$$\nabla \cdot \left(I_j(r, \Omega) \Omega \right)$$
$$= \left(\kappa_{g,j} + \kappa_l \right) I_{b,j} + E_{p,j} - \left(\kappa_{g,j} + \kappa_l + \sigma_l \right) I_j(r, \Omega)$$
$$+ \frac{\sigma_l}{4\pi} \int_0^{4\pi} I_j(r, \Omega') \Phi(\Omega, \Omega') d\Omega' \tag{5.48}$$

where I_j is the radiation intensity in the jth band, $\kappa_{g,j}$ is the gas absorption coefficient in the jth band, $I_{b,j}$ is the blackbody intensity in the jth band and Φ is the scattering phase function. The terms $E_{p,j}$, κ_l and σ_l are the particle emissive power, particle absorption coefficient, and particle scattering coefficient, respectively, and calculated by the following expressions:

$$E_p = \lim_{V \to 0} \sum_{n=1}^{N_p} \varepsilon_{l,n} A_{l,n} \frac{\sigma T_{l,n}^4}{\pi V} \tag{5.49}$$

$$\kappa_l = \lim_{V \to 0} \sum_{n=1}^{N_p} \varepsilon_{l,n} \frac{A_{l,n}}{V} \tag{5.50}$$

$$\sigma_l = \lim_{V \to 0} \sum_{n=1}^{N_p} (1 - f_{l,n})(1 - \varepsilon_{l,n}) \frac{A_{l,n}}{V} \tag{5.51}$$

where $\varepsilon_{l,n}$ is the particle emissivity, $f_{l,n}$ is the scattering factor equivalent to the ratio of forwardly scattered radiation to the total scattered radiation, $A_{l,n}$ is the projectile area of particles. Noting that the walls are gray and diffuse, Eq. (48) is subjected to the following boundary condition;

$$q_{out} = (1 - \varepsilon_w) \int\limits_{\boldsymbol{\Omega} \cdot \boldsymbol{n} > 0} I_j(\boldsymbol{r}, \boldsymbol{\Omega})(\boldsymbol{\Omega} \cdot \boldsymbol{n}) d\boldsymbol{\Omega} + \varepsilon_w I_{b,w,j} \tag{5.52}$$

where ε_w is the wall emissivity and $I_{b,w,j}$ is the blackbody intensity in the jth band at the wall temperature.

Each octant of the angular space is discretized into 4 x 4 finite solid angles over θ and φ angles, respectively. Furthermore, the pixel resolution (N_{θ_p} and N_{φ_p}) is selected as 1 x 1.

It should be noted that ANSYS Fluent discards scattering due to continuous phases (gas phase and inert phase) when the interaction between discrete particles and radiation is activated [172], i.e., the scattering inert phase is automatically discarded in the RHT calculations. Fortunately, it was shown that the share of RHT in the bed section, where most of the inert particles exist, does not exceed 15 % [190]. Therefore, absorption and scattering of thermal radiation by inert particles are neglected by simply taking their absorption and scattering coefficients as zero.

In this study, four different gas radiative property models are decided to be utilized to test the effect of gas radiation on the predictions of 2-D CFD simulation for the test rig. The gas radiative property models are the WSGG model of Bordbar et al. [113], the WSGG model of Smith et al. [115], Bordbar's 10 band model [61] and domain-based WSGG. Among them, the domain-based WSGG model is already embedded in ANSYS Fluent software whereas all other gas radiative property models are incorporated into the software via user-defined function (UDF) within

the scope of this study. The details of the gas radiative property models under consideration are described in sections 2.2.3 and 2.2.8.

The input data for the particle radiative properties are the emissivity and scattering factor for the lignite phase particles. Lignite particles in the system are taken to be completely burned based on the carbon content of the fly ashes collected from the cyclone and bag filter during experiments. The emissivity and scattering factor for the lignite phase particles can be determined by the following expressions:

$$\varepsilon_l = Q_{abs,l} \tag{5.52}$$

$$f_l = g_l \tag{5.53}$$

where $Q_{abs,l}$ and g_l are absorption efficiency and asymmetry factor of the lignite phase particles which can be determined using Mie theory [46] by utilizing the RI of the size distribution of particles. The RI of particles can be determined using Ebert's model [124] as a function of ash composition. Since the particles in the system are treated as gray, the Planck mean Mie solutions are used as gray properties.

5.3   Simulation Set-up

5.3.1   Solution Domain and Mesh Structure

The schematic representation and the mesh structure for the 2-D CFD model of the test rig firing lignite only are shown in Figure 5.2. As illustrated by the figure, the meshes are finer around the cooler tubes. Furthermore, there are 67054 triangular elements in the whole geometry as further increase in the mesh number does not signifincantly influence the accuracy.
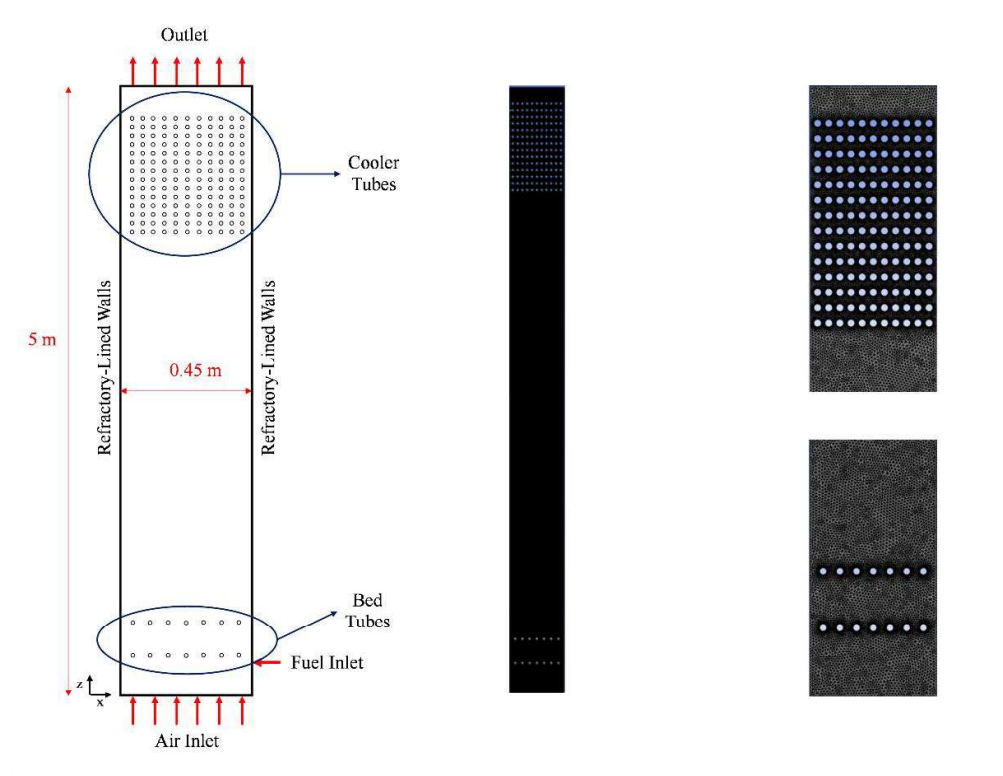
Figure 5.2. The schematic representation and the mesh structure for the 2-D CFD model of METU 0.3 MW$_t$ ABFBC test rig firing lignite only

The shape of the cells also has a significant impact on the accuracy of the numerical solution. Therefore, some important parameters regarding the shape of the cells, such as aspect ratio and skewness, are listed in Table 5.2. Skewness shows how the shape of the cell is close to a perfect geometric shape such as an equilateral triangle, square, etc. It ranges from 0 to 1 where the former means perfect shape and the latter indicates high deviation from the perfect shape. Highly skewed cells can decrease accuracy and destabilize the solution. A general rule is that the maximum skewness for a triangular/tetrahedral mesh in most flows should be kept below 0.95, with an average value that is less than 0.33 [172]. As can be seen from Table 5.2, skewness for the meshes under consideration is acceptable. Furthermore, the aspect ratio can be briefly defined as the ratio of the longest face of a cell to the shortest one. Generally, it is suggested to avoid aspect ratios above 5:1 in the bulk flow (away

142

from the walls). The aspect ratios of the cells are also within the acceptable limit as shown in Table 5.2.

Table 5.2 Mesh properties

	Aspect ratio	Skewness
Average	1.204	0.056
Maximum	2.441	0.539

5.3.2   Boundary Conditions

The boundary conditions are given based on input data obtained from the combustion test carried out in the test rig. The original test rig is equipped with a distributor plate (probably at the same temperature as the bed material) at the bottom of the bed. However, due to its complicated geometry, it is discarded from the 2-D model of the test rig, and the inlet cold air is taken to be uniformly distributed at the entrance of the system. However, this approach leads to the overcooling of the bed due to the direct RHT between the bed and cold inlet air. To eliminate the overcooling of the bed section by the cold inlet air stream, the inlet boundary is simply discarded in the RHT calculations by setting its emissivity to zero.

The 2-D model requires heat transfer coefficients of the cooling tubes located in the bed and cooler modules of the test rig, which are shown in Figure 5.2. The overall bed-to-tube surface heat transfer coefficient (h_{bt}) consists of three modes; gas convection, particle convection, and RHT:

$$h_{bt} = h_g + h_i + h_r \tag{5.54}$$

In the model, gas and particle convective heat transfer coefficients are calculated by following the empirical correlation suggested by Denloye and Botterill [170];

$$h_g = \frac{k_g}{d_i^{0.5}} 0.86 Ar^{0.39} \tag{5.55}$$

$$h_i = \frac{k_g}{d_i} 0.843 Ar^{0.15} \tag{5.56}$$

where k_g is the thermal conductivity of the gas, d_i is the diameter of bed material (inert phase particles) and Ar is the Archimedes number ($= gL^3 \rho_g (\rho_p - \rho_g)/\mu^2$). Since the effect of radiation is already taken into account by a more accurate representation, RHT (h_r) contribution of the overall bed to tube surface heat transfer coefficient (h_{bt}) is omitted in this study.

The heat transfer coefficient between the freeboard and cooler tubes, on the other hand, is calculated by the following expression which is deduced for the heat transfer between a fluid flowing through a bank of tubes [166];

$$h_{ct} = \frac{k_g}{d_{ct}} C_2 C_1 Re_{D,max}{}^m Pr^{0.6} \left(\frac{Pr}{Pr_s}\right)^{0.25} \tag{5.57}$$

where C_2 is 0.97 for 11 tube rows, C_1 and m are 0.27 and 0.63, respectively for the system under investigation, $Re_{D,max}$ is the maximum Reynold's number across the tubes ($= u_{g,max} d_{ct} \rho_g / \mu_g$), Pr is the Prandtl number calculated using the average temperature around the tube bank, Pr_s is the Prandtl number calculated using the outlet temperature of the tube bank, and d_{ct} is the tube diameter.

The heat transfer through the combustor wall is taken into consideration by conduction using an effective thermal conductivity calculated from the thermal conductivities of 6 cm refractory and 20 cm insulation bricks. For the heat transfer from the outside surface of the walls to the atmosphere, only the free convection heat transfer is considered using the heat transfer coefficient ($h_{w,o}$) estimated from the following expression [166]:

$$h_{w,o} = \frac{k_{air}}{L_w} \left\{ 0.825 + \frac{0.387 Ra_L{}^{1/6}}{[1 + (0.492/Pr)^{9/16}]^{8/27}} \right\}^2 \tag{5.58}$$

The emissivities of the bed and cooler tube surfaces are taken from measurements of Jo et al. [140] whereas that of the inner surface of refractory walls is from the measurements of Jackson and Yen [139].

Table 5.3 lists the injection properties of the fuel inlet. Lignite particles are taken to be injected into the bed section through the fuel inlet stream. The inlet temperature of the lignite particles is taken to be 100 °C. The size of lignite particles is represented with the Rosin-Rammler size distribution function given as:

$$Y_d = \exp\left(- d_l/\overline{d_l}\right)^n \tag{5.58}$$

where d_l is the diameter of lignite particles, Y_d is the mass fraction of particles with a diameter greater than d, n is the size distribution parameter and $\overline{d_l}$ is the mean particle diameter, which corresponds to the diameter where $Y_d = e^{-1} \approx 0.368$. The estimation of size parameters $\overline{d_l}$ and n is given in Appendix G.

Table 5.3 Lignite injection properties for the 2-D CFD model of the METU 0.3 MWt ABFBC test rig firing lignite

Parameter	
Injection type	Surface
Particle type	Combusting
Inlet temperature (°C)	100
Number of diameters	25
Drag law	Gidaspow

5.3.3 Numerical Methods

Initially, the bed is patched with inert ash with a height of 0.7 m from the bottom, a volume fraction of 0.6, and a temperature of 1200 K. Then, transient simulations are performed for 30 s to obtain a quasi-steady state, and then for another 10 s for collecting the time-averaged data. The time-step size is set as 0.01 s which is found

to be acceptable by Adamczyk et al. [191] and Farid et al. [192]. An additional time step size can be defined for particle tracking which is taken to be the same as the fluid time step size in the simulations to ensure convergence. Besides, the phase-coupled SIMPLE, first-order upwind spatial discretization, and first-order implicit transient discretization schemes are adopted.

CHAPTER 6

DESCRIPTION OF THE TEST CASES

6.1   0.3 MW$_t$ Atmospheric Bubbling Fluidized Bed Combustor Test Rig

Experimental work was carried out by Degirmenci et al. [28,154], Harmandar et al. [193,194] and Gogebakan et al. [8,195–198] in former studies on a 0.3 MW$_t$ ABFBC Test Rig. The test rig was constructed and operated for the investigation of combustion, in-situ desulfurization, and NO$_x$ emission characteristics of low-quality Turkish lignites and Turkish lignite/biomass blends. The test rig is schematically illustrated in Figure 6.1. As illustrated in the figure, the test rig basically consists of a forced draft (FD) fan, a windbox with an ash removal system, a modular combustor, a cyclone with recycle leg, a baghouse filter, an induced draft (ID) fan, and a fuel and limestone feeding system.
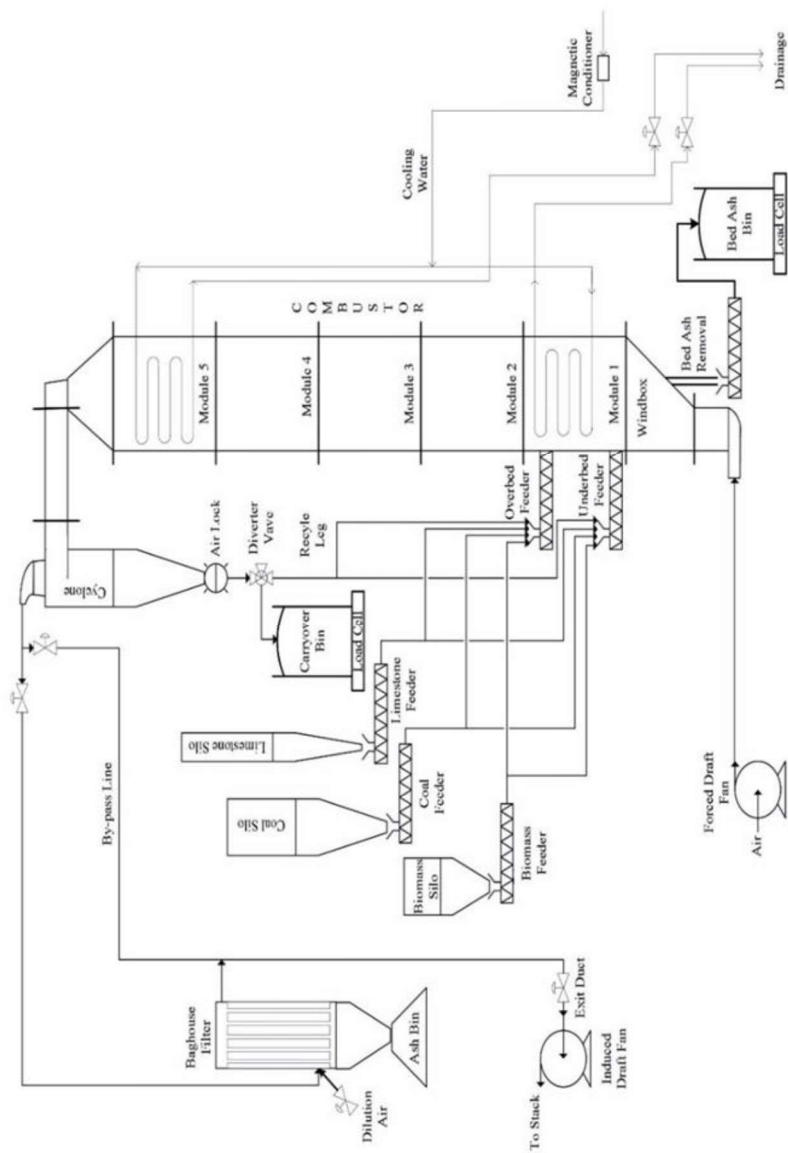
Figure 6.1. Schematic representation of METU 0.3 MW$_t$ ABFBC test rig

148

6.1.1   The Combustor

The main body of the ABFBC test rig is a modular combustor formed by five modules with an internal cross-section of 0.45 m × 0.45 m and a height of 1 m. The modular combustor is insulated by a combination of 6-cm refractory bricks and 20-cm insulation bricks.

The first and fifth modules from the bottom are referred to as bed and cooler, respectively, and the ones in between are referred to as freeboard modules. In the be module, there exists 7 water-cooled U-tubes (25 mm OD, stainless steel) 5 ports for thermocouples, 4 ports for gas sampling probes, one port for LPG distributor, one port for ignitor and two ports for feeding fuel/limestone mixture. There is two feeding ports; one is 22 cm and the other is 85 cm above the distributor plate. The cooler module contains a water-cooled tube bundle involving 11 tubes (26.7 mm OD, carbon steel) with 14 passes installed across the cross-section of the cooler module to cool down the stack gases.

The fluidizing air fed by an FD fan enters the bottom of the windbox through a pipe of 6.5 m long and 7.8 cm ID on which a manual gate valve, an automatic butterfly valve, and a vortex flowmeter are installed. Air supplied to the windbox by means of the pipe of 7.8 cm ID diverges to the full cross-section of the combustor at the distributor plate located 1.4 m above the entrance port. Sieve type distributor plate contains 412 holes, each 4.5 mm in diameter, arranged in a triangular pattern. Flue gases pass through the cooler module before they enter the cyclone. They then enter the baghouse filter to leave the elutriated particles before passing through an ID fan to exit from the stack.

6.1.2   Solids Handling System

Lignite, biomass, and limestone are contained in different silos and fed to the system by pre-calibrated volumetric feeders under each silo. The mixture of lignite, biomass and limestone is fed to the bubbling bed water-cooled screw feeders either 22 cm or

85 cm above the distributor plate. Bed ash is withdrawn from the bed through a 5 cm ID, 1.1 m long water-cooled ash removal pipe.

The elutriable fines leaving the combustor first arrive the cyclone where majority of them are captured. Particles collected by cyclone are either discharged from the system or recycled to the combustor. To collect fine particles that cannot be captured by the cyclone, a pulse-jet type baghouse filter with a 100 % collection efficiency for particles greater than 1 μm is utilized.

6.1.3 Cooling Water System

Cooling water required for the test rig is divided into two streams, one for the in-bed tube bundles, the other for the tube bundle in the cooler module. The heat transfer area of the tube bundles in the bed and cooler modules are 0.30 m^2 and 4.3 m^2, respectively. The cooling water sent to the cooler module provides a counter current flow.

6.1.4 Gas Sampling and Analysis System

For the measurement of the concentrations and emissions of the gaseous species in the combustor and at the exit of the combustor, 10 gas sampling probes are located in the positions given in Table 6.1. The online continuous gas analyzers with which the test rig is equipped are listed in Table 6.2. Among them, the measurement of temporal variation of O_2 and CO at the combustor exit is carried out by a zirconium oxide sensor which is Bailey SMA 90. On the other hand, dry concentrations of O_2, CO, CO_2, SO_2, NO and N_2O along the combustor are measured by ABB Advanced Optima 2000 and Siemens Ultramat 6 connected in series. There are two modules of ABB Advanced Optima 2000 analyzer which are Magnos 106 (a magnetochemical analyzer for the O_2 concentration) and Uras 14 (infrared analyzer for CO, CO_2, NO and N_2O concentrations). Finally, Siemens Ultramat 6 measures SO_2 concentrations based on non-dispersive infrared (NDIR) method.

Table 6.1 Relative positions of gas sampling probes

Probe No	Distance above the distributor plate, cm
P10	26
P9	56
P8	69
P7	85
P6	123
P5	183
P4	291
P3	344
P2	419
P1	500

Table 6.2 On-line gas analyzers

Instrument	Gas Species
Bailey SMA 90	O_2, CO
Siemens Ultramat 6	SO_2
ABB Advanced Optima 2000 (Magnos 106)	O_2
ABB Advanced Optima 2000 (Uras 14)	CO, CO_2, NO, N_2O

6.1.5   Instrumentation and Control Systems

The test rig is extensively equipped with instrumentation and control systems for research purposes. These systems can be divided into the following categories:

- Data acquisition and control system

- Solid flow control and monitoring

- Air and gas flow control and monitoring

- Cooling-water flow control and monitoring

- On-line continuous gas analyzers

- Pressure sensors

- Temperature sensors

The process values along the combustor are logged to a PC by a data acquisition and control system (Bailey INFI 90).

K type thermocouples (Chromel-Alumel) with grounded junctions are located in various positions along the combustors to measure spatial and temporal variations of gas temperatures and to minimize their response time. The tips of the thermocouples are located on the symmetry axis of the combustor. The axial positions of thermocouples are given in Table 6.3. The temperature of air feed at the downstream of vortex flow meter and temperatures of cooling water at the exits of bed and cooler bundles are measured by resistance thermocouples of type Pt-100. Further information regarding the test rig and its operation procedures such as procedures before cold start-up, during runs, after shut down is provided elsewhere [195].

Table 6.3 Relative positions of thermocouples

Thermocouple No	Distance above the distributor plate, cm
TC1	25
TC2	44
TC3	73
TC4	73
TC5	97
TC6	133
TC7	154
TC8	226
TC9	257
TC10	285
TC11	330
TC12	361
TC13	425
TC14	500

Radiative HFs incident on the refractory side walls of the freeboard are measured by water-cooled Medtherm 48P-20-22K HF transducer during the steady-state operation of the test rig. The transducer is a Gardon gage with a diameter of 19 mm. Design HF range of the transducer is 0-227 kW/m^2. The certified calibration of the transducer is accurate to $\pm$ 0.5% for most ranges. ZnSe window attachment was installed to the transducer to eliminate the convective mode of heat transfer, thus making the basic transducer a radiative HF transducer, or a radiometer. The sensor absorptance is in the spectral range of 0.5-22 μm, covering most of the thermal radiation spectrum. The view angle of the transducer is 150° with the ZnSe window.

6.2 Experimental Conditions

In the following sub-sections, the experimental conditions including operation parameters, measurements of temperatures, concentrations and solid flowrates, fuel, sorbent, and ash analyses, etc. are summarized for the combustion tests carried out by Degirmenci et al. [28,154], Harmandar et al. [193,194] and Gogebakan et al. [8,195–198].

6.2.1 Steady State and Transient Coal Combustion Tests

Results of a steady-state and transient combustion test which was carried out in a previous study [28] are utilized as input data for application and validation of the 1-D transient system model described in Chapter 4. These steady-state and transient combustion tests are referred to as Test 1 in the rest of this thesis study.

Operation conditions of the steady-state and transient combustion tests are listed in Table 6.4. In the combustion test, low-quality lignite, namely Aydın lignite, is fired in its own ash owing to its high ash content.

Table 6.4 Operating conditions of the steady state combustion test (Test 1) [28]

Operation parameter	
Coal flow rate, kg/h	89.6
Bed drain flow rate, kg/h	1.2
Carryover ash flow rate, kg/h	21.4
Air flow rate, kmol/h	22.8
Excess air, %	47
Superficial velocity, m/s	3.1
Average bed temperature, ℃	853
Average freeboard temperature, ℃	870
Combustion efficiency, %	95
Bed cooling water flow rate, kg/h	1368
OHTC in bed, W/m^2.K	238
OHTC in freeboard, W/m^2.K	59
Bed height, m	1.2

The results of proximate and ultimate analyses of Aydın lignite used in Test 1 are summarized in Table 6.5. As shown in the table, lignite used in the experiments is characterized by its high VM/FC ratio (~1.5), high ash content (~28 %), low combustible sulfur content (~0.5 %), and low nitrogen content (~ 1.3 %).

Table 6.5 Fuel analyses of Test 1 [28]

	Lignite
Proximate analysis (as received basis, wt. %)	
Moisture	17.0
Ash	28.0
VM	33.0
FC	22.0
ρ_{bulk} (kg/m^3)	1140
d_{32} (mm)	0.87
Ultimate analysis (dry basis, wt. %)	
Carbon	46.6
Hydrogen	3.5
Nitrogen	1.3
Oxygen	14.4
Combustible sulfur	0.5
HHV, MJ/kg (as received basis, wt. %)	17.1

Ash constituents of Aydın lignite are listed in Table 6.6. With regard to ash compositions, lignite ash is mainly composed of acidic oxides.

Table 6.6 Fuel ash compositions of Aydın lignite burned in Test 1 [28]

	Aydın lignite (wt. %)
Silica, SiO_2	44.1
Aluminum, Al_2O_3	45.5
Ferric, Fe_2O_3	5.9
Calcium, CaO	0.1
Magnesium, MgO	0.5
Sulfur, SO_3	1.9
Sodium, Na_2O	1.9
Potassium, K_2O	2.5

Particle load (B) is calculated as the average of carry over flow rates as follows:

$$B = \frac{F_{cyclone} + F_{bagfilter}}{u_0 A_c} \qquad (6.1)$$

The dynamic performance of the test rig is tested through a combustion test where step changes are imposed on the air flow rate and coal flow rate by keeping all other parameters constant. The transient responses of temperatures, O_2, and CO concentrations at the freeboard exit on the step changes are investigated. Step changes in air and coal flow rates and durations are depicted in Figure 6.2. In addition to that, the magnitudes and durations of the step changes are listed in Table 6.7.
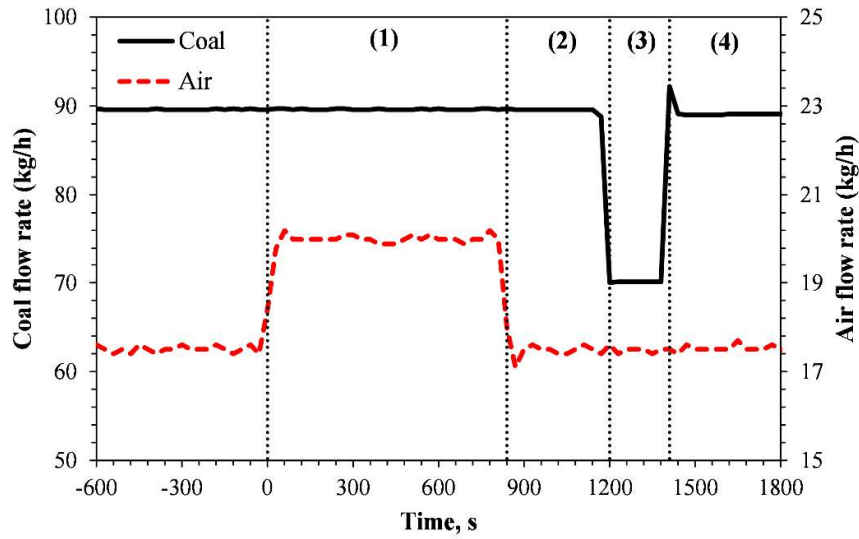
Figure 6.2. Step changes imposed on coal and air feed rates during transient combustion test (Test 1) [28]

Table 6.7 Magnitudes and durations of the step changes imposed on coal and air flow rates during transient combustion test (Test 1) [28]

	1	2	3	4
Δm_f (%)	0	0	-22	27
Δn_a (%)	14	-12	0	0
Δt (s)	840	360	210	∞

6.2.2 Coal Combustion Tests with and without Fly Ash Recycling

Results of two steady-state combustion tests which were carried out in a previous study [194] are utilized as input data for application and validation of the particle and gas radiative property models described in Chapter 2. In this section, measurements were carried out for two combustion tests utilizing low calorific value and high ash content Turkish lignite, namely Beypazarı lignite, one without recycle (Test 2) and the other with recycle of particles collected in the cyclone (Test 3). It

158

should be highlighted at this point that these combustion tests are used to model the RHT within the freeboard as radiative HF measurements are available for these tests. Operation conditions of Test 2 and Test 3 are listed in Table 6.8.

Table 6.8 Operating conditions of Tests 2 and 3 [194]

Operation parameter	Test 2	Test 3
Coal flow rate (kg/h)	101	101
Bed drain flow rate (kg/h)	7	11
Cyclone ash flow rate (kg/h)	22.6	239.2
Baghouse filter ash flow rate (kg/h)	1.1	3.4
Carryover flow rate (kg/h)	23.7	242.7
Recycle ratio (-)	0	2.37
Excess air (%)	43	36
Superficial velocity (m/s)	3.0	2.8
Average bed temperature (℃)	875	846
Average freeboard temperature (℃)	871	890
Average side wall temperature (℃)	830	837
Equivalent top surface temperature (℃)	635	667
Average H_2O concentration (%)	10	10
Average CO_2 concentration (%)	10	11
Bed height (m)	0.9	0.9

The characteristics and ash constituents of Beypazarı lignite used in Tests 2 and 3 are summarized in Table 6.9 and Table 6.10. Lignite burned in these combustion tests is characterized by its high VM/FC ratio (~1.9), high ash content (~36 %), high combustible sulfur content (~2.7 %), and low nitrogen content (~ 1.4 %).

Table 6.9 Fuel analyses of Tests 2 and 3 [194]

	Lignite
Proximate analysis (as received basis, wt. %)	
Moisture	13.7
Ash	36.4
VM	32.7
FC	17.2
ρ_{bulk} (kg/m^3)	905
d$_{32}$ (mm)	1.47
Ultimate analysis (dry basis, wt. %)	
Carbon	38.1
Hydrogen	3.2
Nitrogen	1.4
Oxygen	12.4
Combustible sulfur	2.7
Total sulfur	4.5
HHV, MJ/kg (as received basis, wt. %)	13.2

Table 6.10 Fuel ash compositions of Beypazarı lignite burned in Tests 2 and 3 [194]

	Beypazarı lignite (wt. %)
Silica, SiO_2	36.6
Aluminum, Al_2O_3	12.5
Ferric, Fe_2O_3	9.4
Calcium, CaO	0.7
Magnesium, MgO	1.1
Sulfur, SO_3	27.4
Sodium, Na_2O	6.5
Potassium, K_2O	1.3
Titanium, TiO_2	3.0

For the application of the 3-D spectral radiation code to the freeboard of the test rig, the profiles of medium and wall temperatures, CO_2 and H_2O concentrations, size distributions, and chemical compositions of fly ash particles including bag filter and cyclone ashes, and spectral wall emissivities must be provided as input data.

Freeboard medium and wall temperature profiles are plotted in Figure 6.3 whereas their fitted polynomial coefficients, fitted to the freeboard temperature measurements obtained during steady-state operation, are listed in Table 6.11. On the other hand, H_2O and CO_2 concentrations in the freeboard are taken to be uniform as given in Table 6.8, owing to rapid combustion of indigenous lignite with a high VM/FC ratio.
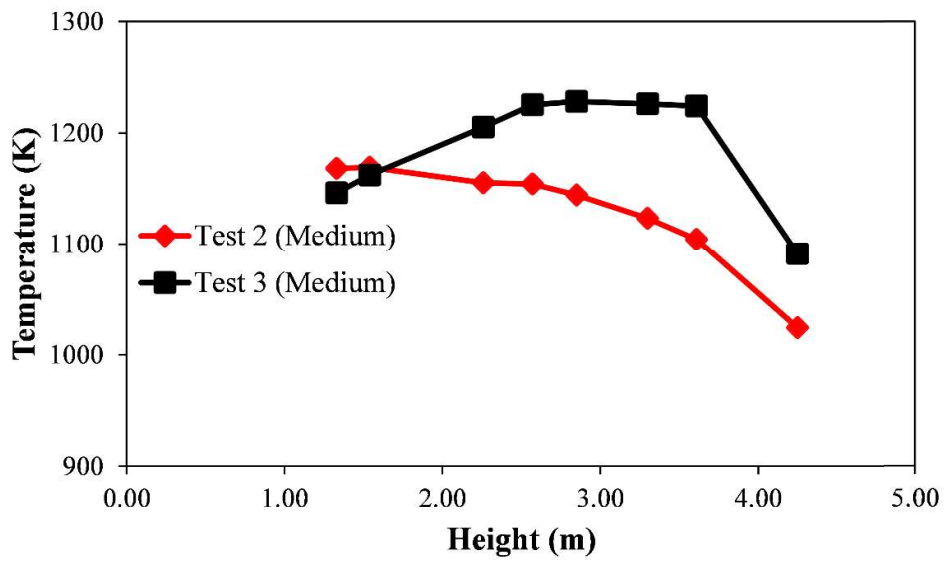
Figure 6.3. Profiles of measured medium temperatures for Test 2 and Test 3 [194]

Table 6.11 Polynomials for temperature profiles of Test 2 and Test 3

	Test 2	Test 3
Medium temperature profile, K $T_m(z)=\sum_{i=0}^{6} a_i z^i$		
a_0	1149.66	1106.52
a_1	-15.50	16.62
a_2	-1.35	-90.85
a_3	42.65	116.33
a_4	-30.56	-50.22
a_5	7.84	9.59
a_6	-0.71	-0.73
Wall temperature profile, K $T_w(z)=\sum_{i=0}^{6} b_i z^i$		
b_0	1146.50	1110.440
b_1	40.50	61.590
b_2	-129.23	-226.770
b_3	137.01	246.250
b_4	-62.89	-106.200
b_5	13.14	20.580
b_6	-1.04	-1.52

Measurements of the size distributions of particles collected from both cyclone and baghouse filter for all combustion tests under investigation are conducted by sieve analysis and laser light scattering technique, respectively. PSDs of particles are illustrated in Figure 6.4. Furthermore, the physical properties and chemical compositions of the fly ash particles collected by cyclone and bag house filter are tabulated in Tables 6.12 and 6.13, respectively. It is worth noting at this point that the fly ash particles in the freeboard involve particles collected by cyclone and baghouse filter.
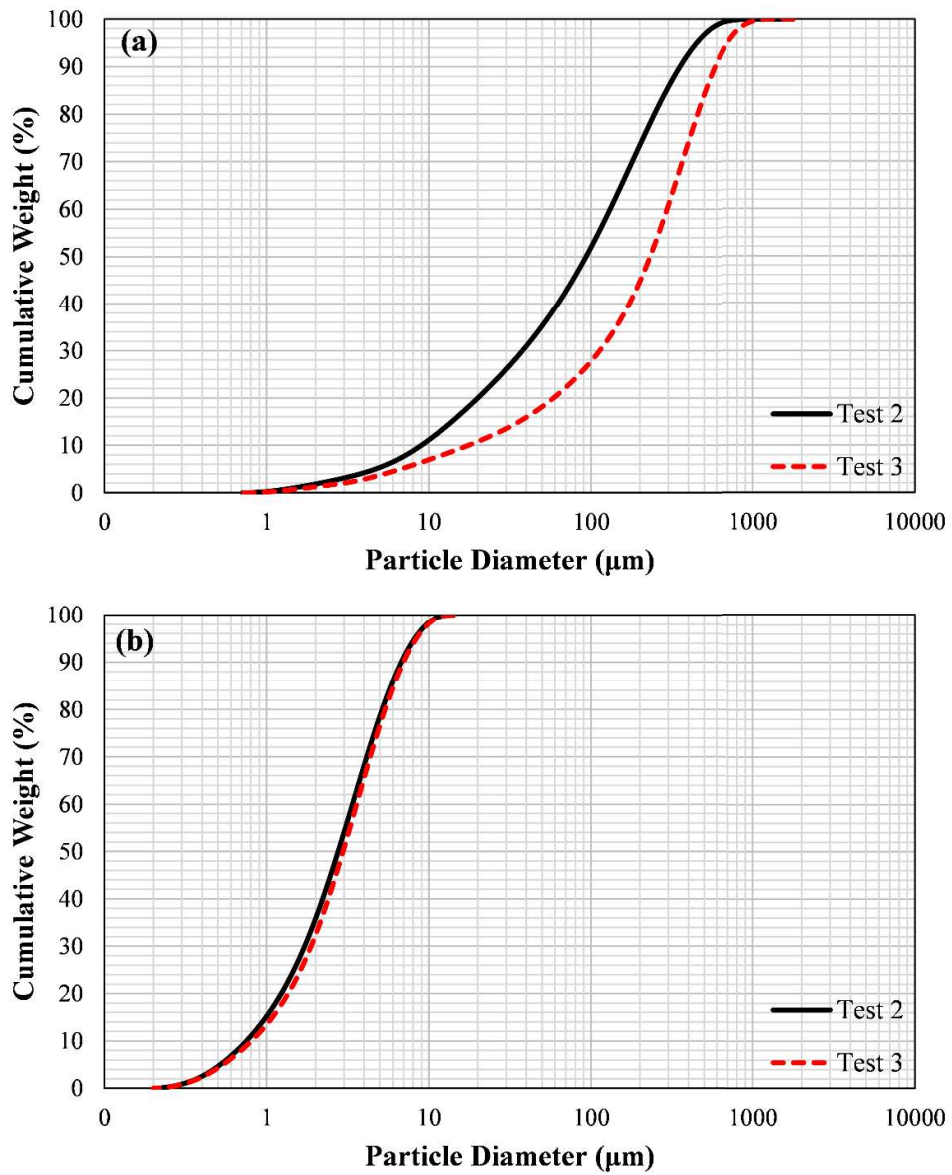
Figure 6.4. Cumulative PSDs of particles collected by (a) cyclone and (b) baghouse filter for Test 2 and Test 3 [194]

Table 6.12 Physical and chemical properties of the particles collected from cyclone and bag filter [194]

	Test 2		Test 3	
	Cyclone	Bag Filter	Cyclone	Bag Filter
Physical properties				
Particle Load (g/m^3)	11		131	
Particle Density (kg/m^3)	1029	610	931	690
d_{32} (µm)	32.7	1.7	20.5	1.8
d_{50} (µm)	231.7	2.8	93.2	3.0
d_{90} (µm)	587.4	6.8	353.9	7.0
Chemical compositions (dry basis, wt%)				
SiO_2	46.52	28.37	47.40	36.41
Al_2O_3	16.58	13.00	16.92	12.97
CaO	0.37	1.16	0.41	2.37
Fe_2O_3	12.98	23.80	13.08	18.82
MgO	0.99	1.20	1.01	0.99
TiO_2	4.92	8.05	3.58	7.29
Na_2O	6.92	4.73	7.07	3.99
K_2O	2.28	1.52	1.90	1.32
SO_3	8.44	18.16	8.63	15.85

6.2.3 Coal Combustion Tests with Limestone and Biomass Addition

Results of five combustion and co-combustion tests carried out in an earlier study [195] were used within the scope of this study to validate the radiation models coupled with and without FBC system models. The operation conditions of the combustion tests are listed in Table 6.13. In Test 4, lignite was burned without limestone and biomass addition whereas in Test 5, lignite was burned with limestone addition. In Tests 6, 7, and 8, lignite was co-fired with OR, HS, and CR with a share

of 49, 42, and 41 % on a weight basis, respectively, and with limestone addition. In all the runs, the lignite was burned in its own ash due to its high ash content. The feed point location was 0.22 m above the distributor plate for all runs.

Table 6.13 Operating conditions of Tests 4 – 8 [8,196]

	Test 4	Test 5	Test 6	Test 7	Test 8
Coal flow rate (kg/h)	76.5	68.7	30.2	32.4	35.7
Biomass flow rate (kg/h)	0.0	0.0	28.8	23.3	25.2
Biomass share (mass basis) (%)	0	0	49	42	41
Biomass share (thermal basis) (%)	0	0	55	50	48
Limestone flow rate (kg/h)	0.0	22.4	11.2	13.9	12.9
Ca/S molar ratio	0.0	2.7	3.3	3.3	2.7
Bed drain ash flow rate (kg/h)	6.9	8.3	1.5	2.2	0.0
Cyclone ash flow rate (kg/h)	14.2	19.4	11	12.1	18.0
Bag filter ash flow rate (kg/h)	0.4	1.2	1.7	1.9	0.0
Carry over ash flow rate (kg/h)	14.6	20.6	12.7	14.0	18.0
Superficial velocity (m/s)	2.2	1.9	1.9	1.9	2.0
Average bed temperature (°C)	894	848	852	854	857
Average frb. temperature (°C)	866	817	849	835	843
Bottom surface temperature (°C)	*	851	859	859	*
Top surface temperature (°C)	*	564	602	584	*
Bed height (m)	1.02	1.12	1.10	1.10	1.15
Average H_2O concentration (%)	*	14.43	20.31	19.08	*
Average CO_2 concentration (%)	*	13.75	12.46	12.91	*
Bed cooling water flow rate, kg/h	3629	2842	3165	4073	4802
Frb. cooling water flow rate, kg/h	1792	2767	2691	2423	3170

*these values are required as input data for the radiation model without coupling with FBC system model. Since Tests 4 and 8 are only used in FBC system models, these values are neither calculated nor reported for these tests

In Tests 4 – 8, Çan lignite is fired. The characteristics and ash constituents of Çan lignite and biomass (OR, HS, and CR) burned in the combustion tests are summarized in Tables 6.14 and 6.15. Lignite used in the experiments is characterized by its high VM/FC ratio (~1.2), high ash content (~26 %), high total sulfur content (~4.1 %), and low nitrogen content (~ 1.1 %). On the other hand, all biomass almost contains no ash and sulfur. Their VM/FC (~5.2) ratio is very high compared to lignite. The nitrogen content of CR (~ 4.1 %) is much higher than that of lignite and other biomass. Regarding ash compositions, lignite ash is mainly composed of acidic oxides whereas biomass ash is mainly composed of basic oxides.

Table 6.14 Lignite analyses of Tests 4 – 8 [8,196]

	Test 4	Test 5	Test 6	Test 7	Test 8
Proximate analysis (as received basis, wt%)					
Moisture	16.35	16.48	16.75	17.14	17.47
Ash	28.78	26.74	23.89	27.46	24.29
VM	29.79	31.05	32.04	30.36	31.44
FC	25.17	25.74	27.33	25.04	26.80
ρ_{bulk} (kg/m^3)	905	905	905	905	905
d_{32} (mm)	0.44	0.58	0.59	0.47	0.48
Ultimate analysis (dry basis, wt%)					
Carbon	44.60	44.93	44.83	41.92	40.04
Hydrogen	3.95	4.09	4.00	4.01	3.84
Nitrogen	1.09	1.14	1.20	0.96	0.98
Oxygen	11.97	13.96	17.66	15.64	21.42
Combustible Sulphur	3.98	3.86	3.61	4.33	4.29
Ash	34.41	32.02	28.70	33.14	29.43
Total Sulphur	4.17	4.07	3.66	4.33	4.35
Calorific Value					
LHV, MJ/kg	12.3	13.3	14.0	12.5	17.4
Ash Compositions (%)					
Silica, SiO_2	57.29	56.56	52.70	51.91	50.11
Aluminum, Al_2O_3	19.67	17.49	19.14	21.82	22.57
Ferric, Fe_2O_3	12.05	10.99	11.26	12.15	11.46
Calcium, CaO	4.85	9.21	7.78	7.92	7.79
Magnesium, MgO	0.82	0.57	0.52	0.58	0.55
Sulfur, SO_3	2.00	2.05	5.23	2.31	4.24
Sodium, Na_2O	1.58	1.45	1.62	1.60	1.51
Potassium, K_2O	0.21	0.31	0.21	0.33	0.18
Titanium, TiO_2	1.53	1.38	1.54	1.37	1.58

Table 6.15 Biomass analyses of Tests 4 – 8 [8,196]

	OR	HS	CR
Proximate analysis (as received basis, wt%)			
Moisture	6.07	7.62	6.93
Ash	4.24	1.46	5.38
VM	75.69	73.04	75.57
FC	14.00	17.89	12.14
ρ_{bulk} (kg/m^3)	591	320	364
d_{32} (mm)	0.36	4.86	1.45
Ultimate analysis (dry basis, wt%)			
Carbon	50.22	49.77	46.79
Hydrogen	6.38	5.86	6.48
Nitrogen	1.72	0.56	4.40
Oxygen	37.03	42.15	36.23
Combustible Sulphur	0.14	0.08	0.32
Ash	4.51	1.58	5.78
Total Sulphur	0.14	0.11	0.32
Calorific Value			
LHV (MJ/kg)	18.1	17.5	17.4
Ash Compositions (%)			
Silica, SiO_2	31.19	2.28	0.00
Aluminum, Al_2O_3	5.29	2.59	0.81
Ferric, Fe_2O_3	5.17	7.11	4.95
Calcium, CaO	17.52	38.84	10.83
Magnesium, MgO	2.51	6.60	14.77
Sulfur, SO_3	2.64	5.50	0.00
Sodium, Na_2O	5.21	7.40	10.29
Potassium, K_2O	27.95	27.86	57.51
Titanium, TiO_2	2.52	1.81	0.85

For the tests with limestone additions, limestone with physicochemical properties shown in Table 6.16 was utilized.

Table 6.16 Characteristics of Beypazarı limestone

Size Distribution		Chemical Analysis (wet)	
Size (mm)	Weight (%)	Component	Weight (%)
1.180 - 1.000	14.80	Moisture	0.69
1.000 - 0.850	5.29	$CaCO_3$	88.92
0.850 - 0.710	6.26	$MgCO_3$	6.44
0.710 - 0.600	10.66	SiO_2	2.91
0.600 - 0.500	3.84	Na_2O	0.15
0.500 - 0.425	9.74	K_2O	0.08
0.425 - 0.355	6.14	Al_2O_3	0.39
0.355 - 0.180	15.06	Fe_2O_3	0.43
0.180 - 0.106	10.49	LOI	42.43
0.106 - 0.000	17.75	d_{50}: 0.43 mm	

For the application of the 3-D spectral radiation code to the freeboard of the test rig, the profiles of medium and wall temperatures, CO_2 and H_2O concentrations, size distributions, and chemical compositions of fly ash particles including bag filter and cyclone ashes, and spectral wall emissivities must be provided as input data.

The freeboard medium temperature profile, which is plotted in Figure 6.5, is represented as a 4th order polynomial. The polynomial coefficients fitted to the freeboard temperature measurements obtained during steady-state operation are listed in Table 6.17. Wall temperatures, on the other hand, are taken to be 15 K lower than the medium temperatures based on the previous measurements conducted in the same system [199]. CO_2 and H_2O concentrations are taken to be uniform in the freeboard, as given in Table 1, due to the rapid combustion of lignite and biomasses with a high VM/FC ratio.

170
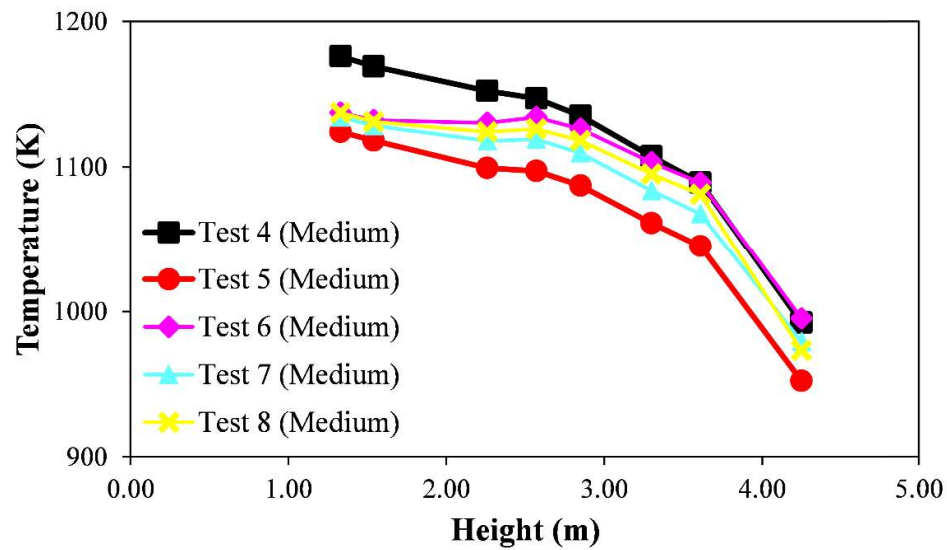
Figure 6.5. Profiles of measured medium temperatures for Tests 4 – 8 [8,196]

Table 6.17 Polynomials for temperature profiles of Tests 5 – 7 [8,196]

	Test 5	Test 6	Test 7
Medium temperature profile, K $T_m(z)=\sum_{i=0}^{4} a_i z^i$			
a_0	1054.754	1084.888	1098.314
a_1	162.522	97.155	79.561
a_2	-128.329	-71.881	-64.496
a_3	39.535	24.416	21.444
a_4	-4.629	-3.305	-2.876

the polynomial coefficients are used as input data for RHT model without coupling FBC system model. Since Tests 4 and 8 are only used in FBC system models, the polynomial coefficients are neither calculated nor reported for these tests

Measurements of the size distributions of particles collected from both cyclone and baghouse filter for all combustion tests under investigation are conducted by sieve analysis and laser light scattering technique, respectively. PSDs of particles are illustrated in Figure 6.6.
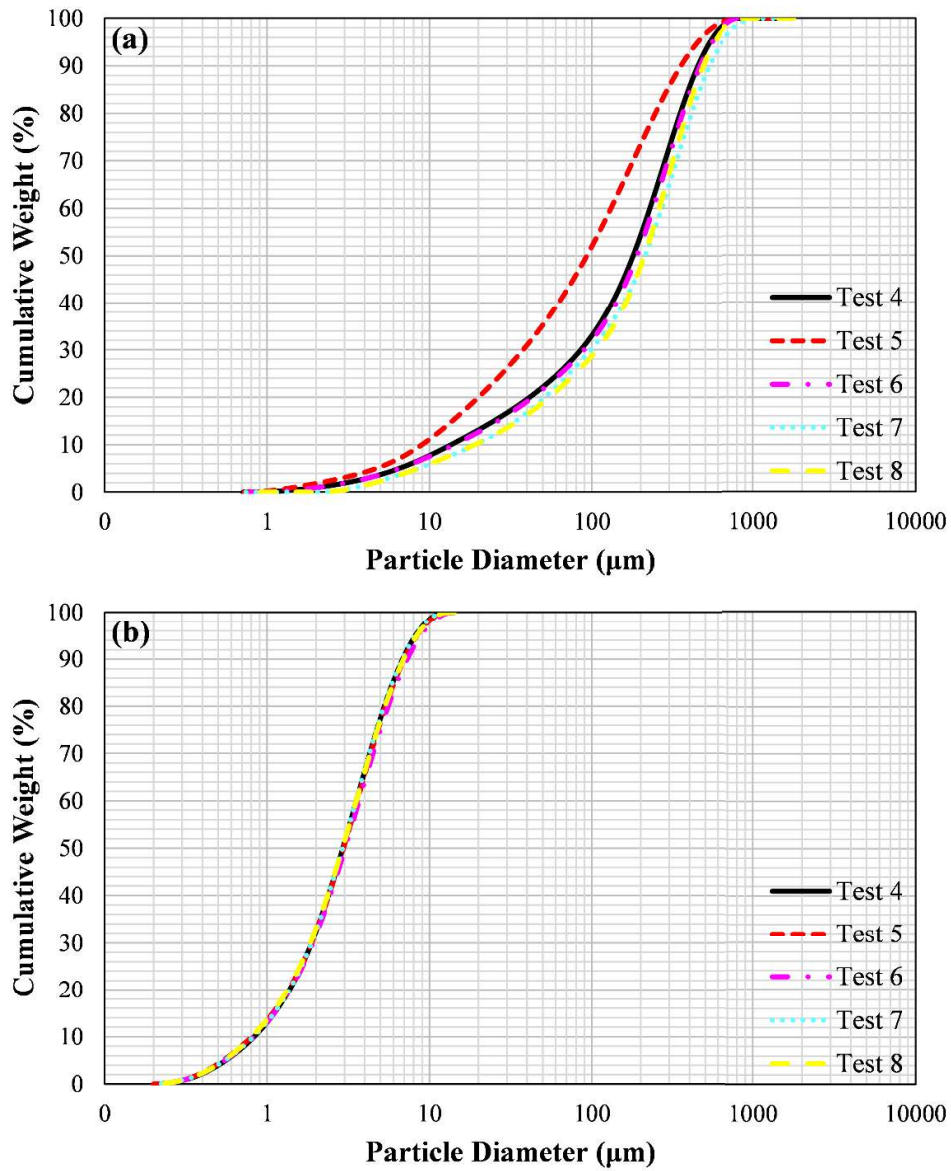
Figure 6.6. Cumulative PSDs of particles collected by (a) cyclone and (b) baghouse filter for Tests 4 – 8 [8,196]

The physical properties and chemical compositions of the particles collected from cyclone and baghouse filter for Test 4 – 8 are listed in Tables 6.18 and 6.19, respectively. As shown by the tables, addition of limestone from Test 4 to Test 5 decreases size distribution of the cyclone particles due to small size of limestone

172

particles. On the other hand, the size distribution of the cyclone particles increases with the addition of biomass due to (i) low bulk density of biomass (see Tables 6.14 and 6.15) which leads to elutriation of less dense coarse particles and (ii) low limestone flowrate in the co-firing tests owing to the low sulfur content of biomass (see Tables 6.13 to 6.15). However, as shown by Table 6.19, the bag filter PSD is not significantly affected by the addition of biomass and limestone. Except CR, the addition of biomass increases the fraction of fine bag filter particles by increasing their flowrates while reducing the flowrate of cyclone particles (see Table 6.13). The tendency of biomass to form finer ash particles was also highlighted in a previous study [200]. In the co-firing tests, the projected surface area of cyclone particles remarkably decreases whereas that of bag filter particles slightly increases. This effect is attributed to higher bag filter particle fraction in fly ash during co-firing.

Table 6.18 Physical and chemical properties of the particles collected from cyclone for Tests 4 – 8 [8,196]

	Test 4	Test 5	Test 6	Test 7	Test 8
Physical properties					
Particle Load (g/m^3)	8.9	14.0	7.9	8.7	12.3
Particle Density (kg/m^3)	1202	1247	1356	1319	1247
d_{32} (µm)	31.2	20.6	32.0	45.5	46.0
d_{50} (µm)	157.9	98.9	189.7	212.9	210.7
d_{90} (µm)	451.2	375.5	467.7	535.2	487.7
Projected Surface Area (m^2/m^3)	0.38	0.87	0.29	0.24	0.33
Chemical compositions (dry basis, wt%)					
SiO_2	51.61	23.27	19.58	31.51	17.52
Al_2O_3	20.92	8.04	7.51	7.96	2.45
CaO	7.41	39.96	45.10	31.48	53.10
Fe_2O_3	10.48	7.40	6.67	6.98	6.89
MgO	0.69	4.61	4.63	2.06	1.89
TiO_2	1.73	0.91	0.83	1.30	0.76
Na_2O	2.34	1.36	1.60	1.46	0.36
K_2O	0.77	0.97	1.43	1.31	1.10
SO_3	4.05	13.47	12.65	15.94	15.93

Table 6.19 Physical and chemical properties of the particles collected from bag house filter for Tests 4 – 8 [8,196]

	Test 4	Test 5	Test 6	Test 7	Test 8*
Physical properties					
Particle Load (g/m^3)	0.2	0.9	1.2	1.4	0.0
Particle Density (kg/m^3)	1202	818	890	865	
d_{32} (μm)	1.8	1.8	1.8	1.8	
d_{50} (μm)	2.9	3.0	3.0	2.9	
d_{90} (μm)	6.9	7.0	7.3	6.8	
Projected Surface Area (m^2/m^3)	0.72	0.94	1.19	0.96	
Chemical compositions (dry basis, wt%)					
SiO_2	45.82	23.27	19.58	31.51	32.16
Al_2O_3	14.68	8.04	7.51	7.96	5.98
CaO	9.49	39.96	45.10	31.48	22.91
Fe_2O_3	17.36	7.40	6.67	6.98	17.52
MgO	0.80	4.61	4.63	2.06	1.54
TiO_2	1.88	0.91	0.83	1.30	1.05
Na_2O	1.57	1.36	1.60	1.46	1.97
K_2O	0.47	0.97	1.43	1.31	1.07
SO_3	7.93	13.47	12.65	15.94	15.81

*since the baghouse filter ash flow rate of Test 8 is measured as 0.0, physical properties of bag filter ashes of Test 8 are not included in the table

CHAPTER 7

RESULTS AND DISCUSSIONS

7.1   Assessment of Spectral Gas Radiative Property Models in Bubbling Fluidized Bed Combustors

The main goal of this thesis study is to couple comprehensive system models for the 0.3 MWt ABFBC test rig with 3-D radiation models based on MOL of DOM or DOM using both sufficiently accurate and computationally efficient methods for the estimation of spectral radiative properties of combustion gases, particles, and walls. However, regarding the solution of RTE, one of the most challenging part is the estimation of spectral radiative properties of molecular gases as they oscillate wildly throughout the entire thermal spectrum. For this reason, the effect of spectral properties of combustion gases, particles, and walls and the accuracy and computational efficiency of the estimation techniques for those properties are assessed first with the 3-D spectral radiation model in isolation from the BFBC system model prior to coupling.

Therefore, one of the objectives of this study is to test the accuracies of two spectral gas radiative property models, Bordbar's 10 band model and banded SLW-1 model, in isolation from the FBC system models in the presence of spectral particles and walls for BFBCs by comparing their predictions with experimental measurements and benchmark solutions. The following sub-sections summarize the major findings of this assessment study.

7.1.1   Assessment of Bordbar's 10 Band Model

Bordbar's 10 band model is first coupled with the 3-D radiation model under investigation within the scope of this study for modeling of RHT in the freeboard of METU 0.3 MW_t ABFBC test rig. The RTE is solved by using MOL solution of DOM. The model is applied to the combustion tests where Beypazarı lignite is fired with (Test 2) and without (Test 3) fly ash recycling. The assessment of the accuracy and computational efficiency of Bordbar's 10 band model is achieved by comparing its predictions with measurements and benchmark solutions.

The RTE is solved separately from the FBC system model. S_N angular discretization method suggested by Carlson and Lathrop [101] is selected for the MOL solution of DOM. The system of ODEs obtained after angular and spatial discretization is solved by the readily available ROWMAP code which utilizes ROW-methods of order 4 and uses Krylov techniques for the solution of linear systems [105]. All tests are performed on a computer with Intel® Core™ i7-2600 CPU 3.40 GHz processor having 16.00 GB of RAM.

7.1.1.1   Benchmarking in a 1-D Test Problem

The predictive accuracies of the spectral gas radiative property models, Bordbar's 10 band model, and banded SLW, are first tested on a 1D benchmark problem [61]. The system under investigation, which is shown in Figure 7.1, consists of a slab between two infinitely long parallel plates. The slab has a thickness of 1.0 m and contains an isothermal binary gas mixture of H_2O and CO_2 with uniform mole fractions of $\chi_{H_2O} = 0.2$ and $\chi_{CO_2} = 0.1$ at 1000 K. The slab is bounded by black walls at 300 K from both sides. In this study, predictions of banded SLW and Bordbar's 10 band model coupled with MOL solution of DOM are validated against the LBL solutions available for the same 1D benchmark problem [61]. Both gas models are coupled with a 1D radiation model utilizing MOL of DOM by employing 100 uniform grid structure, S_8 angular discretization method, and two-point upwind

differencing scheme (DSS012). Furthermore, banded SLW approach is represented by 5 x 5 gray gas mixtures.

$$L = 1.0 \text{ m}$$

$$T_{med} = 1000 \text{ K}$$
$$y_{H2O} = 0.2$$
$$y_{CO2} = 0.1$$

x

$$T_{wall} = 300 \text{ K}$$
$$\varepsilon_{wall} = 1.0$$
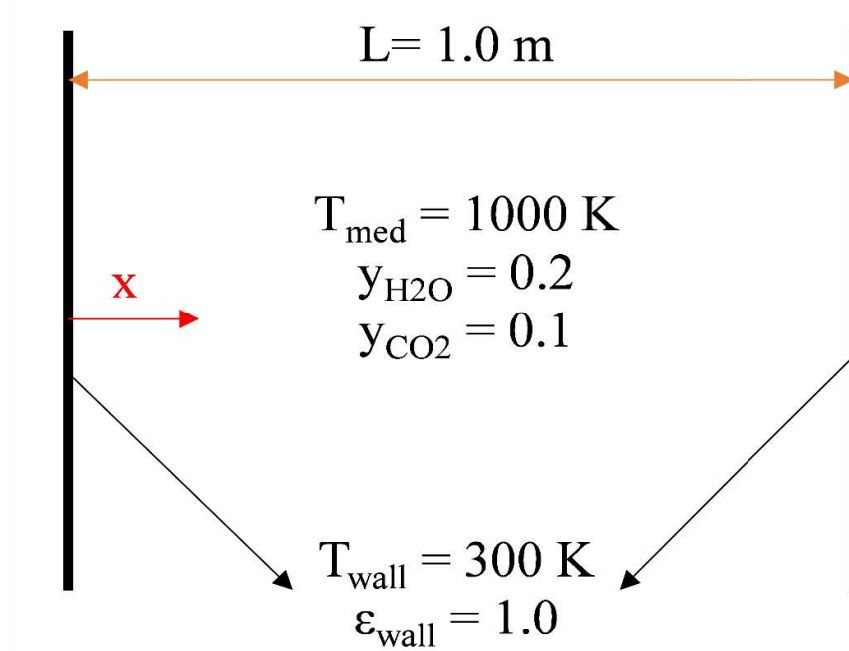
Figure 7.1. 1D slab benchmark problem of Bordbar et al. [61]

The comparisons of net wall HF and ST profiles of banded SLW, Bordbar's 10 band model, and LBL are shown in Figure 7.2. As shown by the figure, predictions with banded SLW and Bordbar's 10 band model are in good agreement with the reference solution. Furthermore, mean absolute error percentages are summarized in Table 7.1. As can be seen from the table, mean absolute error percentages between RHT predictions of banded SLW and LBL and those of Bordbar's 10 band model and LBL are almost the same. In other words, predictions of banded SLW and Bordbar's 10 band model agree well with the benchmark solutions obtained in this 1D benchmark problem.

Table 7.1 Mean absolute error percentages in net wall HFs (q_w) and STs (∇q) for 1D benchmark problem

	1D Benchmark Problem		
	Bordbar's 10 Band Model	**Banded SLW**	**LBL**
Error in q_w (%)	18.59	19.76	Reference
Error in ∇q* (%)	21.84	19.04	Reference

* Error in STs = $[\sum_i^N \left(\frac{|\nabla q_{,i} - \nabla q_{LBL,i}|}{\nabla q_{LBL,i}} \right) \times 100]/N$
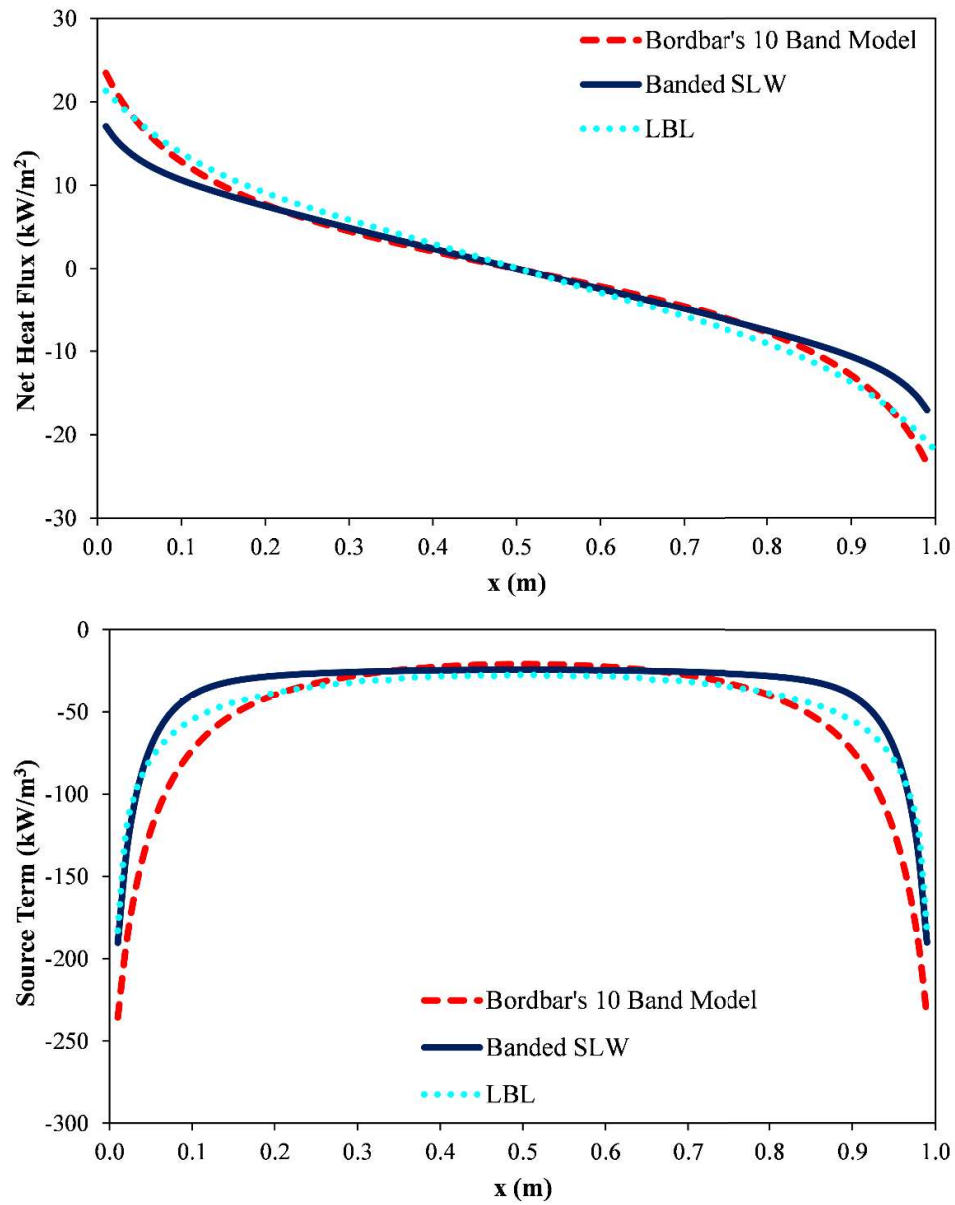
Figure 7.2. Net wall HF and ST predictions of Bordbar's 10 band model [61], banded SLW [52] and LBL [61] for 1D benchmark problem

7.1.1.2 ABFBC Test Rig

In this section, the RHT in the freeboard of METU 0.3 MW_t ABFBC test rig is simulated by using 3-D radiation code under investigation. The RTE is solved by applying MOL of DOM. In the combustion tests, Beypazarı lignite is burned with (Test 2) and without (Test 3) fly ash recycling. In the application of the model, a uniform structure of $11 \times 11 \times 81$ grids, the S_6 angular discretization method [199] and three-point upwind differencing scheme (DSS014) [201] are utilized. The CPU time requirements of the test are estimated from the beginning of the calculation till the steady state solutions providing an error tolerance of 0.1 [Eq. (2.19)].

The data for the application of the models are taken from the measurements (given in section 6.1.2) obtained during two air-fired combustion tests, one without (Test 2 Air-Fired) and the other with recycle of cyclone particles (Test 3 Air-Fired). In this section, the influence of gas composition on RHT is also tested. For this purpose, the 3-D radiation code coupled with Bordbar's 10 band model is also applied to Test 2 and Test 3 by using gas compositions corresponding to oxy-fired combustion (85 % CO_2 and 10 % H_2O based on the 3D oxy-fired benchmark of Bordbar et al. [61]) which are labeled as Test 2 Oxy-Fired and Test 3 Oxy-Fired, respectively. The rest of the input parameters are taken to be the same with the corresponding air-fired combustion tests.

To adopt Bordbar's 10 band, 15 wavelength intervals (9 active bands and 6 windows) presented in Table 2.12 are utilized. Furthermore, pressure (P) and spectrally averaged mean beam length ($L = 3.6 \ x \ Volume/Surface \ area$) are taken to be 1 atm and 0.38 m, respectively. On the other hand, for banded SLW model, the gas absorption coefficients are estimated using correlations deduced from HITRAN 1992 database [44,202]. The nongray gas mixture in banded SLW is represented as mixture of 5×5 gray gases whose absorption cross-sections is ranging between 3×10^{-5} and 60 ($m^2 \ mol^{-1}$) for H_2O and 3×10^{-5} and 120 ($m^2 \ mol^{-1}$) for CO_2.

182

For the estimation of particle radiative properties, on the other hand, a uniform particle load of 0.01 and 0.13 (kg m^{-3}) for Test 2 and Test 3, respectively, is used as input data based on the pressure drops and carry over flowrate measurements of the combustion tests [194]. The single particle properties which are absorption efficiency and scattering efficiency are estimated using Mie theory for 34 discrete particle size and 147 wavelengths. Finally, the RI of particles are estimated using Goodwin's model [123] and fly ash compositions of Test 2 and Test 3 for 147 wavelengths. Banded particle, gas, and wall properties are calculated based on the band dividing scheme shown in Table 2.12 in which, the thermal spectrum is divided into 15 wide bands. Alumina-silicate refractory (70 % Al_2O_3 and 26 % SiO_2) side walls are taken as non-gray, diffuse walls. Spectral wall emissivity of refractory-lined walls is taken from a previous experimental study carried out by Jackson and Yen [139].

The RTE is solved for each wide band so that intensity distribution can be evaluated at each wide band separately, from which total intensity distribution can be found by simple summation rule. Banded representations of particle absorption and scattering coefficients, asymmetry factors, and side wall emissivities are illustrated in Figure 7.3.
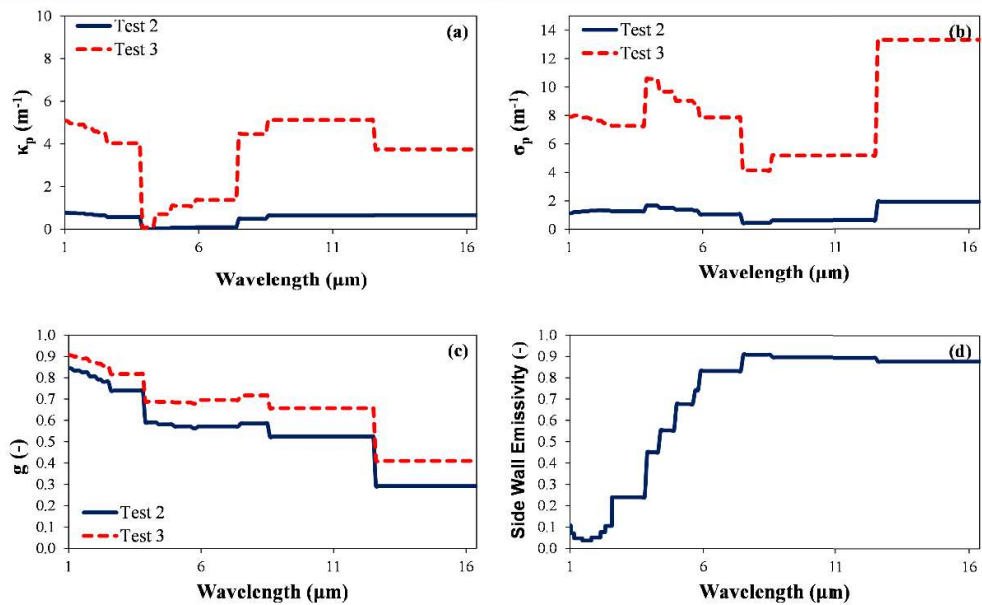
Figure 7.3. Banded representations of (a) particle absorption coefficients (b) particle scattering coefficients (c) asymmetry factors (d) side wall emissivities for all combustion tests

The performance of Bordbar's 10 band model at low particle load (B = 0.01 kg/m^3) is first tested by comparing its incident wall HF and center line ST predictions with those of banded SLW for Test 2 Air-Fired without recycle. In addition to that, the assessment of accuracies of both Bordbar's 10 band model and banded SLW is evaluated by comparing their incident wall HF predictions with the measurements obtained from the freeboard of METU 0.3 MW$_t$ ABFBC test rig. RHT predictions of Bordbar's 10 band model and banded SLW are compared for Test 2 Air-Fired in Figure 7.4. Mean absolute error percentages in RHT predictions with corresponding CPU times are shown in Table 7.2. As Table 7.2 and Figure 7.4 illustrate, incident wall HF predictions of Bordbar's 10 band model and banded SLW is found to be in acceptable agreement. However, Bordbar's 10 band model remarkably overestimates ST profiles at the centerline. This is considered to be due to the difference in total gas emissivities calculated by Bordbar's 10 band model and banded SLW which are 0.29 and 0.13, respectively.
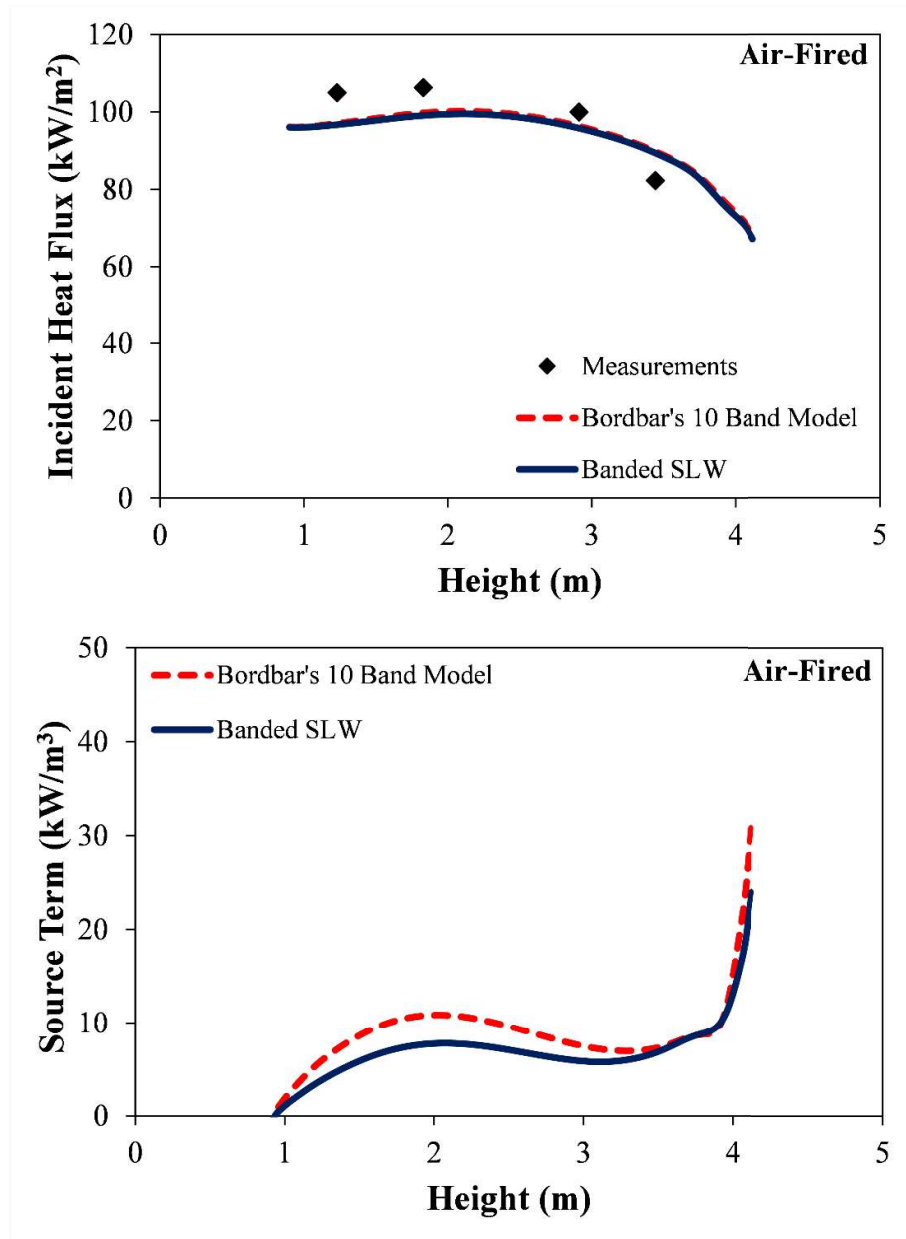
Figure 7.4. Incident wall HF and ST predictions of Bordbar's 10 band model and banded SLW for Test 2 Air-Fired for non-gray walls

Table 7.2 Mean absolute error percentages between incident HFs (q_w) and ST along the centerline (∇q) predictions of Bordbar's 10 band model and banded SLW for Test 2 Air-Fired for non-gray walls

	Test 2 Air-Fired	
	Bordbar's 10 Band Model	**Banded SLW**
Error in q_w (%)	0.59	Reference
Error in ∇q* (%)	30.51	Reference
CPU Time, s	568	27595
CPU Ratio, -	0.02	1.00

* Error in STs = $[\sum_i^N \left(\frac{|\nabla q_{Bordbar,i} - \nabla q_{Banded\ SLW,i}|}{\nabla q_{Banded\ SLW,avg}} \right) \times 100]/N$

To demonstrate the influence of gas composition on the performance of Bordbar's 10 band model, assessment of the accuracy of the model is also tested by using gas compositions representing the oxy-fired combustion systems and are presented in Figure 7.5 and Table 7.3. As Figure 7.5 and Table 7.3 indicate, incident HF predictions of Bordbar's 10 band model perfectly agree with those of banded SLW for Test 2 Oxy-Fired. The change in gas composition results in significant improvement in the accuracy of ST predictions (from 30.51 % to 6.99 %). This may be due to the exact agreement between the gas emissivities which are predicted to be 0.19 by the two models.

With regard to CPU efficiency of the two models, Bordbar's 10 band model requires around 50 times less CPU than that of banded SLW which is attributed to the solution of 15 RTE (15 bands x 1 gray gas mixture) for Bordbar's banded model compared to 375 RTE solutions (15 bands x 25 gray gas mixtures) for banded SLW for each grid and ordinate. Although Bordbar's 10 band model is found to be CPU efficient,

186

the predictive accuracies reveal that it should be preferred in oxy-fired rather than air-fired applications.
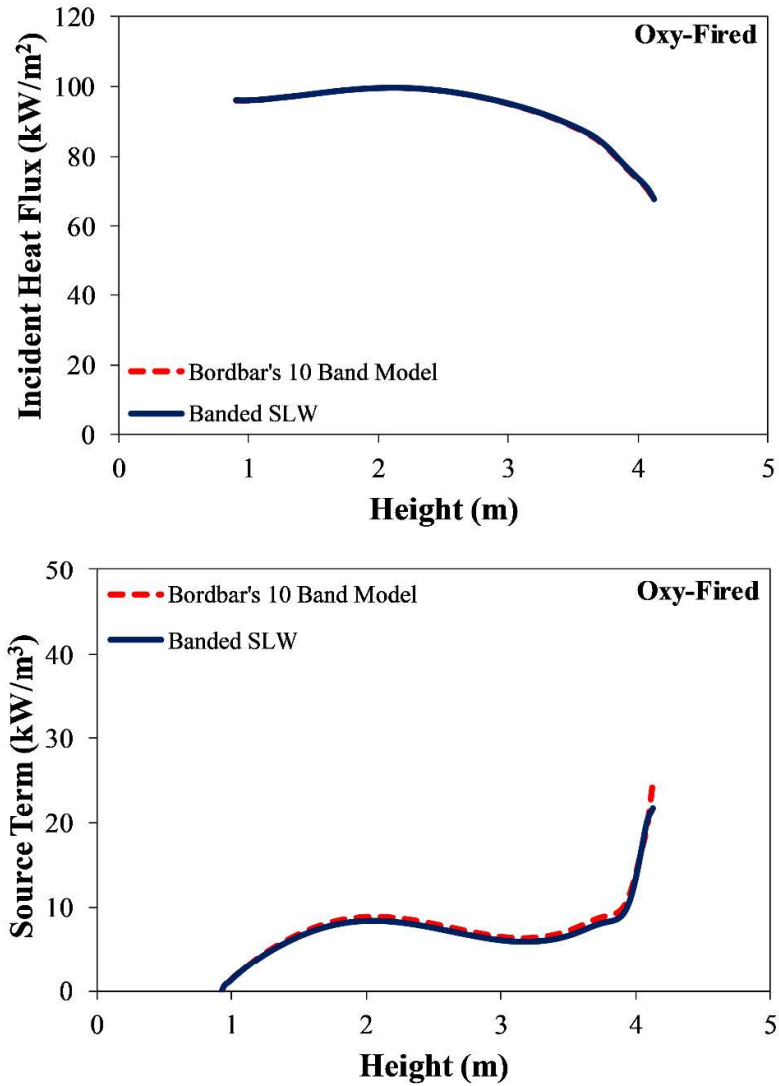
Figure 7.5. Incident wall HF and ST predictions of Bordbar's 10 band model and banded SLW for oxy-fired case of Test 2 Oxy-Fired

Table 7.3 Mean absolute error percentages in incident HFs (q_w) and STs along the centerline (∇q) predictions of Bordbar's 10 band model and banded SLW for Test 2 Oxy-Fired for non-gray walls

	Test 2 Oxy-Fired	
	Bordbar's 10 Band Model	**Banded SLW**
Error in q_w (%)	0.17	Reference
Error in ∇q* (%)	6.99	Reference
CPU Time, s	624	33126
CPU Ratio, -	0.02	1.00

* Error in STs = $[\sum_{i}^{N} \left(\frac{\left| \nabla q_{Bordbar,i} - \nabla q_{Banded\ SLW,i} \right|}{\nabla q_{Banded\ SLW,avg}} \right) \times 100]/N$

In the next part of this section, the assessment of predictive accuracy and CPU efficiency of Bordbar's 10 band model is tested in Test 3 Air-Fired with recycle where particle load is high (B = 0.13 kg/m³). Figure 7.6 illustrates the profiles of wall HF and STs along the center line predicted by Bordbar's 10 band model and banded SLW for Test 3 Air-Fired. The mean absolute error percentages and corresponding CPU times of both models are given in Table 7.4. As can be seen from the figure and table, incident HF profiles of Bordbar's 10 band model and banded SLW overlap and both are found to be in reasonable agreement with measurements. Furthermore, an order of magnitude increase in particle load from Test 2 (B = 0.01 kg/m³) to Test 3 (B = 0.13 kg/m³) results in significant improvement in the accuracy of ST predictions. This improvement is considered to be due to the dominance of particle radiation in Test 3 Air-Fired when particle load is increased by an order of magnitude. In order to support this finding, the individual contributions of gas and particle radiation to total radiation is evaluated by running the same radiation codes by neglecting particle radiation. For this purpose, particle

188

radiative properties of Test 2 and 3 in air and oxy-fired conditions are taken as zero by keeping all other input parameters the same. Banded SLW is utilized as gas radiative property model. The contribution of gas radiation is estimated by dividing the ST predicted by neglecting particle radiation to the ST predicted by considering both particle and gas radiation. The contribution of particle radiation is also calculated by subtracting the ratio of gas radiation to total radiation from 1. The ratio of gas and particle radiation to total radiation calculated for Test 2 and 3 in air-fired conditions are tabulated in Table 7.5. As can be seen in the table, the contribution of particle radiation increases with the increase in particle load.

Table 7.4 Mean absolute error percentages in incident HFs (q_w) and STs along the centerline (∇q) predictions of Bordbar's 10 model and banded SLW for Test 3 Air-Fired for non-gray walls

	Test 3 Air-Fired	
	Bordbar's 10 Band Model	**Banded SLW**
Error in q_w (%)	0.30	Reference
Error in ∇q* (%)	2.61	Reference
CPU Time, s	299	14368
CPU Ratio, -	0.02	1.00

* Error in STs = $[\sum_i^N \left(\frac{|\nabla q_{Bordbar,i} - \nabla q_{Banded\ SLW,i}|}{\nabla q_{Banded\ SLW,avg}} \right) \times 100]/N$
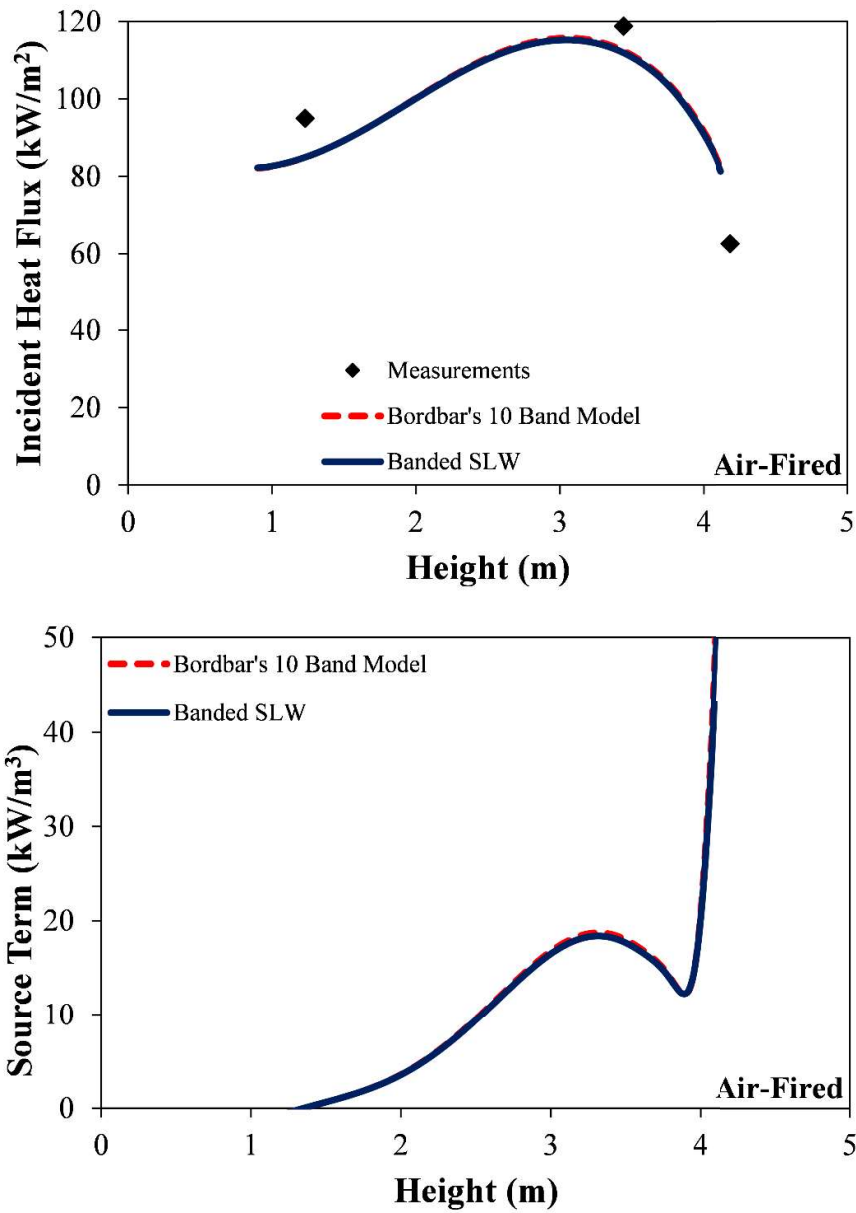
Figure 7.6. Incident wall HF and ST predictions of Bordbar's 10 band model and banded SLW for Test 3 Air-Fired for non-gray walls

Table 7.5 Contribution of gas radiation to total radiation in Test 2 and 3 in air-fired condition

	Ratio of gas radiation to total radiation	Ratio of particle radiation to total radiation
Test 2 Air-Fired	0.36	0.64
Test 3 Air-Fired	0.29	0.71

The influence of gas composition on the performance of Bordbar's 10 band model is also investigated in Test 3 where particle load is high (B = 0.13 kg/m^3) by utilizing gas compositions representing the oxy-fired combustors. Comparisons of incident HF and ST profiles of Bordbar's 10 band model and banded SLW for Test 3 Oxy-Fired are shown in Figure 7.7, and mean absolute error percentages and corresponding CPU times are tabulated in Table 7.6. As demonstrated in Figure 7.7 and Table 7.6, Bordbar's 10 band model provides similar incident HF and ST solutions to those of banded SLW with much less CPU time requirements. The ratio of gas and particle radiation to total radiation calculated for Test 2 and 3 in oxy-fired conditions are listed in Table 7.7. As shown by the table, the contribution of gas radiation is considerable in both Test 2 and Test 3. The results indicate that accurate gas radiative property models are also necessary for oxy-fired conditions even in cases with high particle loads as in freeboards of BFBCs with recycle.
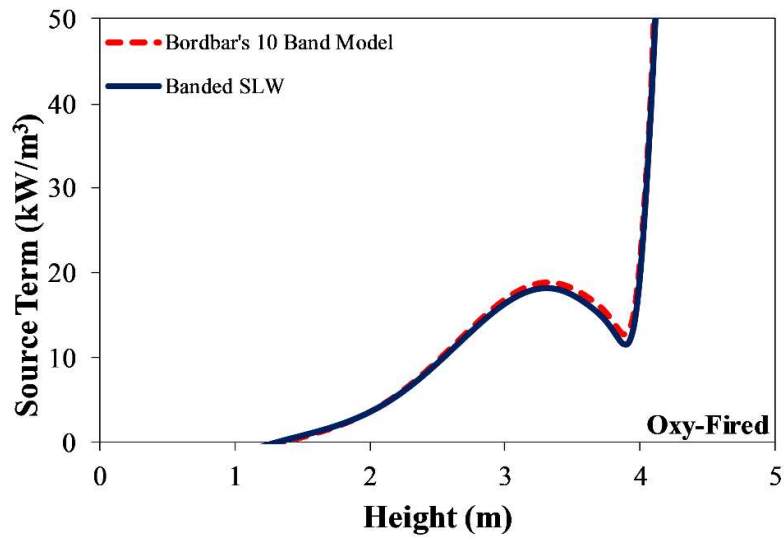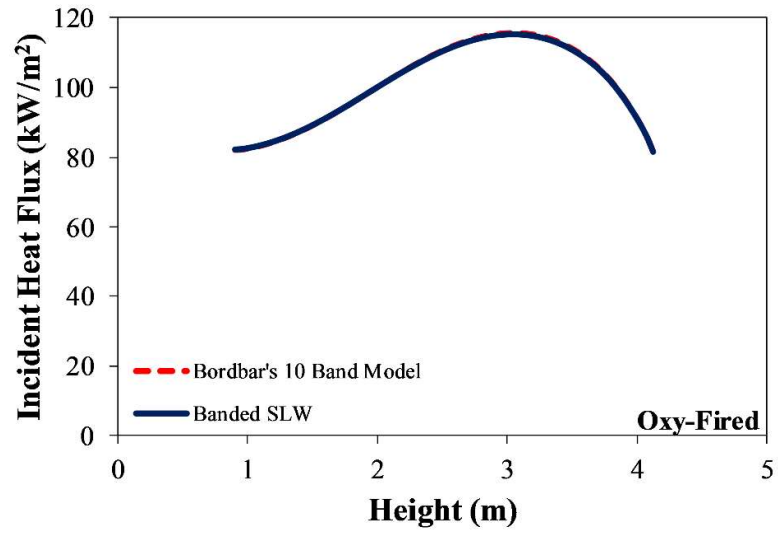
Figure 7.7. Incident wall HF and ST predictions of Bordbar's 10 band model and banded SLW for Test 3 Oxy-Fired for non-gray walls

Table 7.6 Mean absolute error percentages in incident HFs (q_w) and STs along the centerline (∇q) predictions of Bordbar's 10 band model and banded SLW for Test 3 Oxy-Fired for non-gray walls

	Test 3 Oxy-Fired	
	Bordbar's 10 Band Model	Banded SLW
Error in q_w (%)	0.20	Reference
Error in ∇q* (%)	5.74	Reference
CPU Time, s	315	17062
CPU Ratio, -	0.02	1.00

* Error in STs = $[\sum_{i}^{N} \left(\frac{|\nabla q_{Bordbar,i} - \nabla q_{Banded\ SLW,i}|}{\nabla q_{Banded\ SLW,avg}} \right) \times 100]/N$

Table 7.7 Contribution of gas radiation to total radiation in Test 2 and 3 in oxy-fired condition

	Ratio of gas radiation to total radiation	Ratio of particle radiation to total radiation
Test 2 Oxy-Fired	0.46	0.54
Test 3 Oxy-Fired	0.38	0.62

7.1.2 Assessment of Banded SLW-1

Assessment of the performance of banded SLW-1 is investigated by the application of the model to the freeboard of METU 0.3 MW_t ABFBC test rig firing Beypazarı

lignite with (Test 2) and without (Test 3) fly ash recycling. In this section, the 3-D radiation model utilizing MOL of DOM with banded SLW-1 model is implemented without coupling with the FBC system model. In the following sub-sections, the major findings obtained from the application of banded SLW-1 to the freeboard of METU 0.3 MW_t ABFBC test rig and their comparison against the measurements and benchmark solution obtained by banded SLW, are provided.

S_N angular discretization method suggested by Carlson and Lathrop [101] is selected for the MOL solution of DOM. The system of ODEs obtained after angular and spatial discretization is solved by the readily available ROWMAP code which utilizes ROW-methods of order 4 and uses Krylov techniques for the solution of linear systems [105]. All tests are performed on a computer with Intel® Core™ i7-2600 CPU 3.40 GHz processor having 16.00 GB of RAM. In the application of the model, a uniform structure of $11 \times 11 \times 81$ grids, the S_6 angular discretization method [199] which were shown to provide an accurate and CPU-efficient solutions in the assessment study carried out by Ates et al. [28], are utilized. The CPU time requirements of the test are estimated from the beginning of the calculation till the steady state solutions providing an error tolerance of 0.1 [Eq. (2.19)].

The data for the application of the models are taken from the measurements (given in section 6.1.2) obtained during two air-fired combustion tests, one without (Test 2 Air-Fired) and the other with recycle of cyclone particles (Test 3 Air-Fired). In this section, the influence of gas composition on RHT is also tested. For this purpose, the 3-D radiation code coupled with Bordbar's 10 band model is also applied to Test 2 and Test 3 by using gas compositions corresponding to oxy-fired combustion (85 % CO_2 and 10 % H_2O based on the 3D oxy-fired benchmark of Bordbar et al. [61]) which are labeled as Test 2 Oxy-Fired and Test 3 Oxy-Fired, respectively. The rest of the input parameters are taken to be the same with the corresponding air-fired combustion tests.

In banded SLW model which is the benchmark solution in the following sections, the non-gray mixture of combustion gases is represented by 5×5 gray gas mixtures whose absorption cross-sections is ranging between 3×10^{-5} and 60 (m^2 mol^{-1}) for H_2O and 3×10^{-5} and 120 (m^2 mol^{-1}) for CO_2, which were found to provide sufficiently accurate predictions in a previous assessment study [199]. The gas absorption coefficients are estimated using correlations deduced from HITRAN 1992 database [44,202] due to absence of correlations gathered from HITEMP 2010 [114]. Fortunately, it was shown that the predicted absorption coefficients of the combustion gases by using HITRAN and HITEMP databases are in reasonable agreement under the conditions of FBCs by the previous study of Ates et al. [44].

For the estimation of particle radiative properties, on the other hand, a uniform particle load of 0.01 and 0.13 (kg m^{-3}) for Test 2 and Test 3, respectively, is used as input data based on the pressure drops and carry over flowrate measurements of the combustion tests [194]. The single particle properties which are absorption efficiency and scattering efficiency are estimated using Mie theory for 34 discrete particle size and 147 wavelengths. Finally, the RI of particles are estimated using Goodwin's model [123] and fly ash compositions of Test 2 and Test 3 for 147 wavelengths. Banded particle, gas, and wall properties are calculated based on the band dividing scheme shown in Table 2.12 in which, the thermal spectrum is divided into 15 wide bands. Alumina-silicate refractory (70 % Al_2O_3 and 26 % SiO_2) side walls are taken as non-gray, diffuse walls. Spectral wall emissivity of refractory-lined walls is taken from a previous experimental study carried out by Jackson and Yen [139].

Banded particle, gas, and wall properties are calculated based on the band dividing scheme shown in Table 7.8 in which, the thermal spectrum is divided into 8 wide bands. The RTE is solved for each wide band so that intensity distribution can be evaluated at each wide band separately, from which total intensity distribution can be found by simple summation rule. Banded representations of particle absorption

and scattering coefficients, asymmetry factors, and side wall emissivities are illustrated in Figure 7.8.

Table 7.8 Band dividing scheme utilized in this study and corresponding fraction of blackbody emissive power for Test 2 and Test 3

Band No.	Start (μm)	End (μm)	Δf (Test 2)	Δf (Test 3)
1	0.0	2.4	0.20	0.20
2	2.4	3.1	0.19	0.19
3	3.1	4.1	0.20	0.20
4	4.1	4.8	0.09	0.09
5	4.8	6.3	0.13	0.13
6	6.3	8.9	0.10	0.10
7	8.9	12.1	0.04	0.04
8	12.1	20.0	0.03	0.03
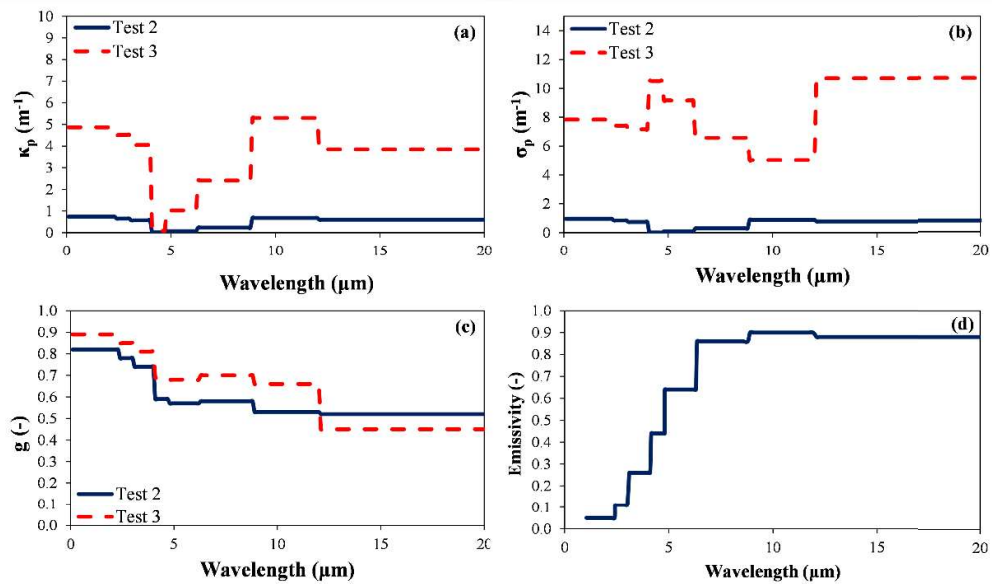
Figure 7.8. Banded representations of (a) particle absorption coefficients (b) particle scattering coefficients (c) asymmetry factors (d) side wall emissivities for all combustion tests

7.1.2.1 Effect of Path Lengths on the Predictive Accuracy of Banded SLW-1

Effect of path length selection on the predictive accuracy of banded SLW-1 for Test 2 Air-Fired with non-gray particles and walls is investigated in this section. Figure 7.9 displays the comparison between incident wall HF and ST profiles of banded SLW-1 utilizing 0.5 and 1.25 times the freeboard height, spectrally averaged mean beam length and spectrally dependent mean beam lengths as L_1 and L_2, respectively and banded SLW for Test 2 Air-Fired. Furthermore, mean absolute error percentages with corresponding CPU times are summarized in Table 7.9. It should be noted that banded SLW model is used as the benchmark solution for the calculation of errors in STs and HFs since SLW model was reported to theoretically approach to line-by-line solution in isothermal and homogeneous media if sufficient number of gray gases is utilized [64]. As shown by the table, all radiation models including banded

197

SLW deviate from the measurements about 6 %. The incident HF predictions of all L_1 and L_2 values utilized in banded SLW-1 agree well with benchmark solutions and measurements. On the other hand, the band-wise estimation of L_1 and L_2 using spectrally dependent mean beam length gives the ST predictions with the highest accuracy. Therefore, band-wise estimation of L_1 and L_2 using spectrally dependent mean beam length is utilized in the rest of the present study.
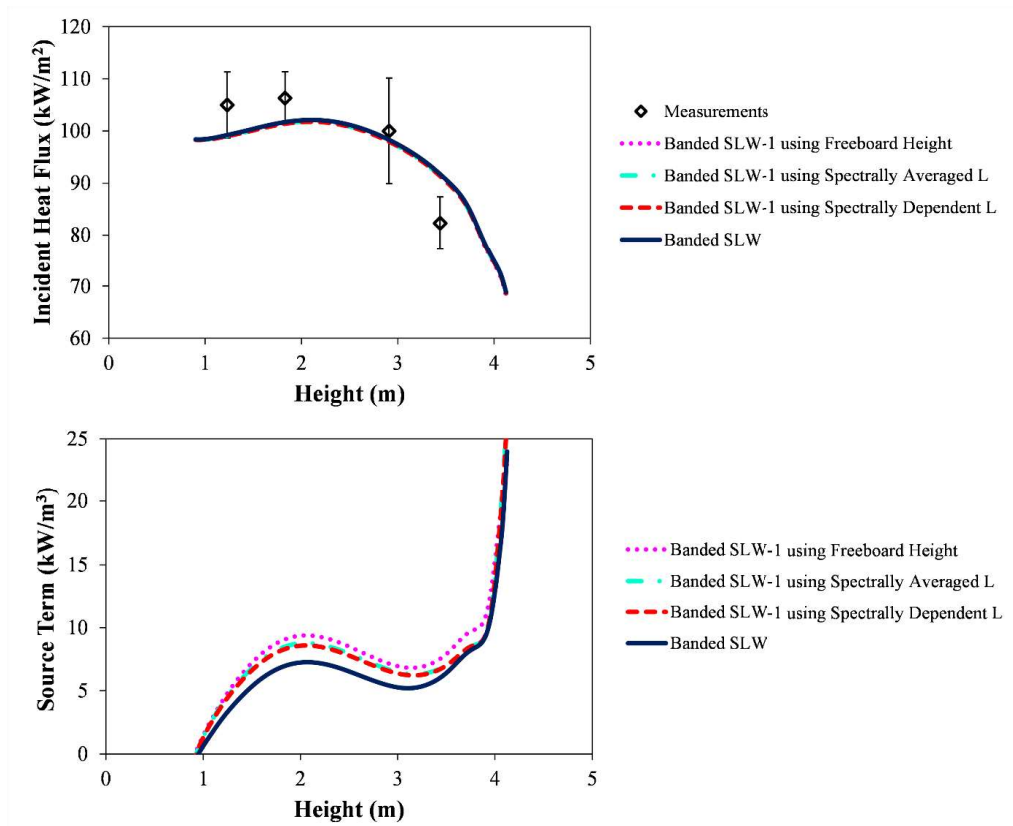
Figure 7.9. Incident wall HF and ST predictions of banded SLW-1 and banded SLW for Test 2 Air-Fired in the presence of non-gray particles and walls

Table 7.9 Mean absolute error percentages of incident HFs (q_w) and STs along the centerline (∇q) predictions of banded SLW-1 and banded SLW for Test 2 Air-Fired in the presence of non-gray particles and walls

	Test 2 Air-Fired			
	Banded SLW-1			Banded SLW
	Freeboard Height	Spectrally Averaged L	Spectrally Dependent L	
Comparison with Measurements				
Error in q_w* (%)	5.76	5.76	5.77	5.67
Comparison with Reference Solution				
Error in q_w (%)	0.33	0.31	0.33	Reference
Error in ∇q** (%)	27.02	18.60	16.49	Reference
Computational Requirements				
CPU Time, s	677	728	742	15717
CPU Ratio, -	0.04	0.05	0.05	1.00

* Error $= [\sum_i^N \left(\frac{|q_{w,measured,i} - q_{w,predicted,i}|}{q_{w,measured,i}} \right) \times 100]/N$ where i is the index for the port location

** Error $= [\sum_i^N \left(\frac{|\nabla q_{Banded\ SLW-1,i} - \nabla q_{Banded\ SLW,i}|}{\nabla q_{Banded\ SLW,avg}} \right) \times 100]/N$ where i is the computational grid

Performance of banded SLW-1 using three different path lengths for Test 2 Air-Fired in the existence of non-gray particles and walls are also tested by comparing the ST predictions of banded SLW-1 in each band with those of banded SLW. Comparison of ST predictions of banded SLW-1 and banded SLW in each band for Test 2 Air-Fired is shown in Table 7.10. As shown by Table 7.10, accuracy of ST predictions

of banded SLW-1 is not uniform throughout the bands, and error in ST predictions is the highest in the 4th band (4.1 – 4.8 μm) where the gas absorption coefficient is the highest. However, the error in ST predictions of banded SLW-1 in the 4th band decreases significantly when utilizing spectrally dependent mean beam length in the calculation of L_1 and L_2 instead of freeboard height or spectrally averaged mean beam length.

Table 7.10 Mean absolute error percentages between ST predictions of banded SLW-1 and banded SLW for each band for Test 2 Air-Fired in the presence of non-gray particles and walls

Band No.	Band Interval (μm)	Test 2 Air-Fired			
		Banded SLW-1			Banded SLW
		Freeboard Height	Spectrally Averaged L	Spectrally Dependent L	
1	1 – 2.4	27.2	26.6	26.6	Reference
2	2.4 – 3.1	21.0	16.6	16.3	Reference
3	3.1 – 4.1	33.2	13.8	15.7	Reference
4	4.1 – 4.8	235.6	99.8	69.9	Reference
5	4.8 – 6.3	26.6	21.9	21.9	Reference
6	6.3 – 8.9	17.7	18.1	17.5	Reference
7	8.9 – 12.1	1.5	2.3	2.5	Reference
8	12.1 – 20.0	20.5	18.6	15.3	Reference

As the optimum values of path length, L_1 and L_2, are sensitive to the test problem under consideration, a sensitivity analysis of the path length values on the accuracy of HF and ST predictions for Test 2 under air-fired conditions is carried out to select

an optimum pair of L_1 and L_2. The sensitivity of incident HF and ST predictions to L_1 and L_2 values for Test 2 is shown in Table 7.11. As can be seen from the table, L_1 and L_2 values do not significantly influence the accuracy of incident wall HF predictions. However, decreasing L_1 and L_2 leads to considerable improvement in the accuracy of ST predictions, and $L_1 = 0.10$ x L_e and $L_2 = 1.10$ x L_e provide the most accurate ST predictions for Test 2 in the existence of non-gray particles and walls. Therefore, $L_1 = 0.10$ x L_e and $L_2 = 1.10$ x L_e are utilized for the banded SLW-1 in the rest of this section.

Table 7.11 Sensitivity of incident HF and ST predictions to L_1 and L_2 values for Test 2 in the presence of non-gray particles and walls

L_1	L_2	Error in q_w* (%)	Error in ∇q* (%)	CPU Time, s
0.50 x L_e	1.10 x L_e	0.34	15.69	771
0.50 x L_e	1.25 x L_e	0.33	16.49	780
0.50 x L_e	1.50 x L_e	0.31	17.67	771
0.50 x L_e	2.00 x L_e	0.28	19.58	677
0.10 x L_e	1.25 x L_e	0.36	9.33	794
0.25 x L_e	1.25 x L_e	0.34	13.09	761
0.50 x L_e	1.25 x L_e	0.33	16.49	677
0.80 x L_e	1.25 x L_e	0.31	18.90	780
0.10 x L_e	**1.10 x L_e**	**0.38**	**8.63**	**775**

Error values are calculated with respect to Banded SLW

201

7.1.2.2 ABFBC Test with Low Particle Load

In this section, the assessment of the performance of banded SLW-1 at low particle load (B = 0.01 kg/m^3) is tested by comparing its incident wall HF and centerline ST predictions with those of banded SLW for Test 2 under air-fired and oxy-fired conditions. Figure 7.10 illustrates incident HF and ST profiles of banded SLW-1 and banded SLW for both Test 2 Air-Fired and Test 2 Oxy-Fired. Moreover, the mean absolute error percantages in HF and ST predictions with corresponding CPU times are tabulated in Table 7.12. As demonstrated by the figure and the table, RHT predictions of banded SLW-1 agree reasonably with those of banded SLW for Test 2 under both air-fired and oxy-fired conditions. It should be noted that the last measurement port located at 4.20 m is discarded from the error calculation as the radiation models do not provide accurate predictions for that location due to the very sharp temperature decrease provided by the cooling module. The underpredictions of incident HFs at the first two probe locations, at 1.23 m and 1.83 m, are due to the increased radiative emissions from particles of the splash zone which are not considered in the radiation model as mentioned previously. HFs at the last probe location, at 3.44 m, are overpredicted in all radiation models as the probe is located close to the cooling tubes starting from 4.25 m of the combustor. CPU requirements of banded SLW-1 are about 20-25 times lower than those of banded SLW due to the representation of the spectrum with two gas mixtures (one gray gas and one clear gas) instead of 5 x 5 gas mixtures. Moreover, the present banded SLW-1 model provides more accurate ST predictions with similar CPU requirements compared to Bordbar's 10 band model which was previously assessed in the same combustion test (see section 7.1.1). Therefore, it can be concluded that banded SLW-1 can be utilized to reduce CPU requirements in both air-fired and oxy-fired BFBCs.
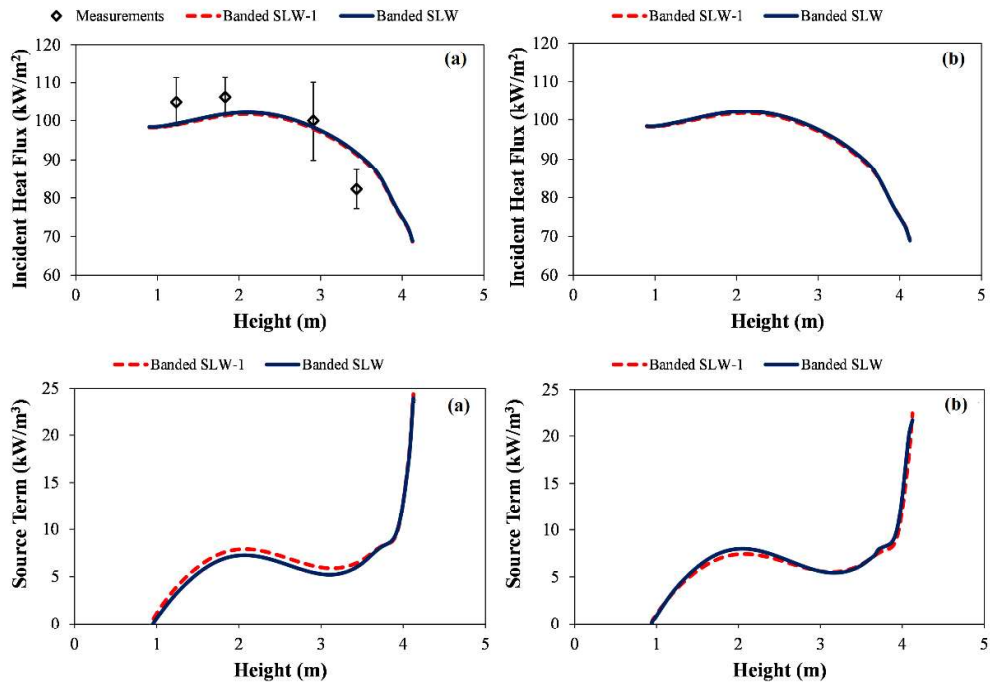
Figure 7.10. Incident wall HF and ST predictions of banded SLW-1 and banded SLW for (a) Test 2 Air-Fired and (b) Test 2 Oxy-Fired in the presence of non-gray particles and walls

Table 7.12 Mean absolute error percentages between incident HFs (q_w) and STs along the centerline (∇q) predictions of banded SLW-1 and banded SLW for Test 2 Air-Fired and Test 2 Oxy-Fired in the presence of non-gray particles and walls

	Test 2 Air-Fired		Test 2 Oxy-Fired	
	Banded SLW-1	**Banded SLW**	**Banded SLW-1**	**Banded SLW**
Comparison with Measurements				
Error in q_w* (%)	5.80	5.67	Not Applicable	Not Applicable
Comparison with Reference Solution				
Error in q_w (%)	0.38	Reference	0.37	Reference
Error in ∇q** (%)	8.63	Reference	5.29	Reference
Computational Requirements				
CPU Time, s	775	15717	742	20017
CPU Ratio, -	0.05	0.79	0.04	1.00

* Error $= [\sum_i^N \left(\frac{|q_{w,measured,i} - q_{w,predicted,i}|}{q_{w,measured,i}} \right) \times 100]/N$ where i is the index for the port location

** Error $= [\sum_i^N \left(\frac{|\nabla q_{Banded\ SLW-1,i} - \nabla q_{Banded\ SLW,i}|}{\nabla q_{Banded\ SLW,avg}} \right) \times 100]/N$ where i is the computational grid

7.1.2.3 ABFBC Test with High Particle Load

The accuracy and computational efficiency of banded SLW-1 model are tested at high particle load (B = 0.13 kg/m^3) by comparing its HF and ST predictions with

those of banded SLW for Test 3 under both air-fired and oxy-fired scenarios. Comparison of the HF and ST profiles of banded SLW-1 and banded SLW for Test 3 Air-Fired and Test 3 Oxy-Fired in the existence of non-gray particles and walls is demonstrated in Figure 7.11. Moreover, the mean absolute error percentages in incident HF and ST predictions and corresponding CPU times for Test 3 Air-Fired and Test 3 Oxy-Fired are listed in Table 7.13. As demonstrated by the figure and the table, banded SLW-1 provides sufficiently good accuracy in RHT predictions with much lower CPU requirement compared to banded SLW for Test 3 Air-Fired and Test 3 Oxy-Fired.
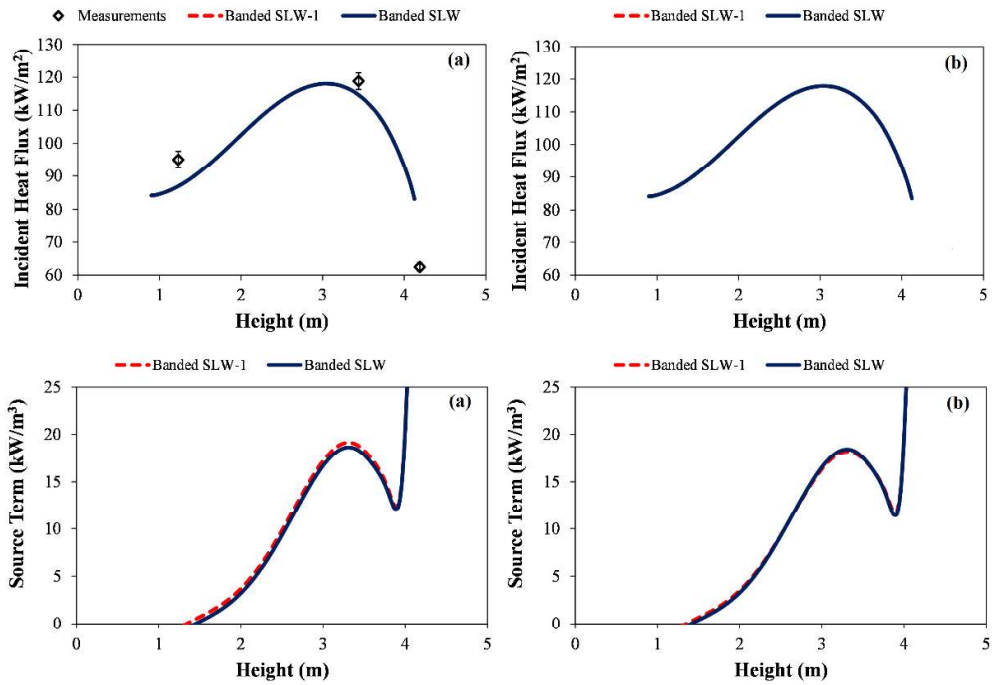
Figure 7.11. Incident wall HF and ST predictions of banded SLW-1 and banded SLW for (a) Test 3 Air-Fired and (b) Test 3 Oxy-Fired in the presence of non-gray particles and walls

Mean absolute error percantages in ST predictions shown in Tables 7.12 and 7.13 indicate that increasing particle load one order of magnitude from Test 2 to Test 3 leads to improvement in the accuracy of the ST predictions. This effect is considered to be due to the fact that particles become more dominant in RHT as particle load

205

increases. To test this hypothesis, the individual contributions of gas and particle radiation to total radiation are evaluated by running the same radiation codes by neglecting particle radiation. For this purpose, particle radiative properties of Test 2 and 3 under air and oxy-fired conditions are taken as zero by keeping all other input parameters the same. The contribution of gas radiation is estimated by dividing the ST predicted by neglecting particle radiation to the ST predicted by considering both particle and gas radiation. Banded SLW is utilized as a gas radiative property model in those calculations. Table 7.14 tabulates the individual contributions of gas and particle radiation for both Test 2 and Test 3 under air-fired and oxy-fired conditions. As can be seen from the table, the contribution of particle radiation is increased as the particle load increases from Test 2 to Test 3 for both air-fired and oxy-fired conditions. However, gas radiation is still considerable even in Test 3 Air-Fired where individual contribution of particle radiation is the highest. The results indicate that accurate gas radiative property models are necessary for the freeboard of bubbling fluidized bed combustors with or without recycle operating under air-fired or oxy-fired conditions.

Table 7.13 Mean absolute error percentages between incident HFs (q_w) and STs along the centerline (∇q) predictions of banded SLW-1 and banded SLW for Test 3 Air-Fired and Test 3 Oxy-Fired in the presence of non-gray particles and walls

	Test 3 Air-Fired		Test 3 Oxy-Fired	
	Banded SLW-1	**Banded SLW**	**Banded SLW-1**	**Banded SLW**
Comparison with Measurements				
Error in q_w* (%)	6.11	6.07	Not Applicable	Not Applicable
Comparison with Reference Solution				
Error in q_w (%)	0.04	Reference	0.04	Reference
Error in ∇q** (%)	4.66	Reference	2.33	Reference
Computational Requirements				
CPU Time, s	408	8687	422	10352
CPU Ratio, -	0.05	1.00	0.04	1.00

* Error $= [\sum_i^N \left(\frac{|q_{w,measured,i} - q_{w,predicted,i}|}{q_{w,measured,i}} \right) \times 100]/N$ where i is the index for the port location

** Error $= [\sum_i^N \left(\frac{|\nabla q_{Banded\ SLW-1,i} - \nabla q_{Banded\ SLW,i}|}{\nabla q_{Banded\ SLW,avg}} \right) \times 100]/N$ where i is the computational grid

Table 7.14 Contribution of gas radiation to total radiation in Test 2 and 3 under both air-fired and oxy-fired conditions

	Ratio of gas radiation to total radiation	Ratio of particle radiation to total radiation
Test 2 Air-Fired	0.34	0.66
Test 3 Air-Fired	0.26	0.74
Test 2 Oxy-Fired	0.45	0.55
Test 3 Oxy-Fired	0.35	0.65

7.1.3 Concluding Remarks for Assessment of Spectral Gas Radiative Property Models

In this section, the accuracy and computational efficiency of two gas radiative property models, namely Bordbar's 10 band model and banded SLW-1, are tested by comparing their RHT predictions with the measurements and benchmark solutions. In conclusion, it was found that Bordbar's 10 band model and banded SLW-1 require around 50 and 20 times less CPU than that of banded SLW, respectively. Therefore, Bordbar's 10 band model can be used to reduce CPU requirement of the spectral RTE solution for BFBCs with recycle or CFBCs where RHT is dominated by particles. Banded SLW-1 accurately predicts the RHT in BFBCs with and without recycle and reduces the CPU requirement of the spectral RTE solution in those systems.

7.2 Effect of Spectral Wall Radiative Properties on Radiative Heat Transfer in Bubbling Fluidized Bed Combustors

None of the studies in the literature investigated the influence of gray wall assumption in BFBCs. However, as mentioned before, the correct treatment of RHT in such systems requires the utilization of non-gray boundaries. Therefore, one of the objectives of this thesis study is to investigate the effect of gray and non-gray wall emissivities of different types of wall materials common in industry and utility boilers on RHT predictions. In the following sub-sections, the major finding obtained from the application of the 3-D radiation code based on MOL of DOM utilizing banded SLW-1 and Mie theory for the radiative properties of particle-laden combustion gases to the freeboard of METU 0.3 MW_t ABFBC test rig is presented. It should be noted at this point that the 3-D radiation model is solved without coupling it with the FBC system models.

S_N angular discretization method suggested by Carlson and Lathrop [101] is selected for the MOL solution of DOM. The system of ODEs obtained after angular and spatial discretization is solved by the readily available ROWMAP code which utilizes ROW-methods of order 4 and uses Krylov techniques for the solution of linear systems [105]. All tests are performed on a computer with Intel® Core™ i7-2600 CPU 3.40 GHz processor having 16.00 GB of RAM. In the application of the model, a uniform structure of $11 \times 11 \times 81$ grids, the S_6 angular discretization method [199] which were shown to provide accurate and CPU-efficient solutions in the assessment study carried out by Ates et al. [28], is utilized. The CPU time requirements of the test are estimated from the beginning of the calculation till the steady state solutions providing an error tolerance of 0.1 [Eq. (2.19)].

The data for the application of the models are taken from the measurements (given in section 6.1.2) obtained during two air-fired combustion tests, one without (Test 2 Air-Fired) and the other with recycle of cyclone particles (Test 3 Air-Fired). The details of the gas and particle readiative property models can be found in section 7.1.2. Alumina-silicate refractory (70 % Al_2O_3 and 26 % SiO_2) side walls are taken

as non-gray, diffuse walls. Spectral wall emissivity of refractory-lined walls is taken from a previous experimental study carried out by Jackson and Yen [139]. Moreover, in order to take into consideration the influence of wall material on RHT, parametric studies are conducted by using different type of wall materials common in industry and utility boilers instead of alumina-silicate refractory; cold water wall made up of thermally oxidized SA508 carbon steel and the same water wall covered by coal slag formed by fly ashes. Spectral wall emissivities of refractory-lined walls, water walls and slag-covered water walls are determined as described in section 2.4. Ebert's model of RI [124] is used to calculate spectral refractive and absorptive indices of coal slags covering water wall using fly ash compositions and wall temperatures of Test 2 and Test 3. In order to calculate the gray wall emissivities of each material, spectral emissivities are spectrally averaged (Planck mean) over the wavelength of interest. Spectral and gray representation of wall emissivities of refractory-lined walls, water walls and slag-covered water walls for Test 2 and Test 3 are plotted in Figure 7.12.
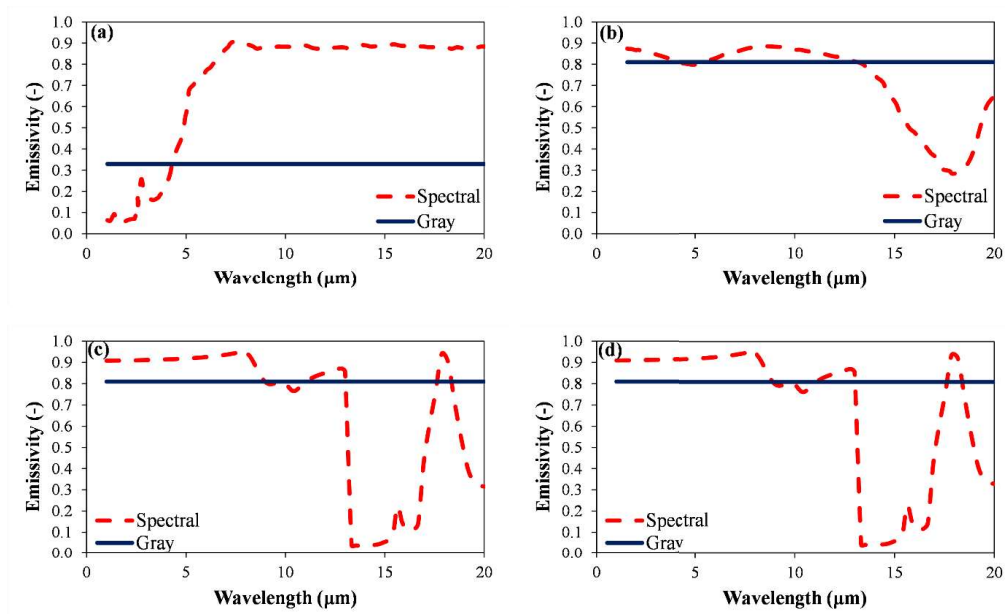
Figure 7.12. Spectral variation of side wall emissivities of (a) refractory-lined wall (b) water wall (c) slag covered water wall for Test 2 (d) slag covered water wall for Test 3

7.2.1 Influence of Gray and Non-Gray Hot Refractory-Lined Walls

In this section, the incident wall HFs and STs predicted by MOL of DOM with non-gray gas and particle properties utilizing gray and non-gray refractory-lined wall emissivities for Test 2 and Test 3 under air-fired conditions are compared and illustrated in Figure 7.13. Furthermore, the mean absolute error percantages in incident HF and ST predictions and corresponding CPU times for Test 2 Air-Fired and Test 3 Air-Fired are listed in Table 7.15. As can be seen from the figure and table, the deviations of incident HF predictions of both gray and nongray walls from the measurements are found to be approximately 6 % for both Test 2 and Test 3 under air-fired conditions. However, ST predictions of gray walls deviate up to 37 % from those of non-gray walls in the upper region of the freeboard where the temperature of the medium and the wall decreases due to the cooler module. However, an order of magnitude increase in the particle load from Test 2 to Test 3 leads to significant improvement in the accuracy of ST predictions.
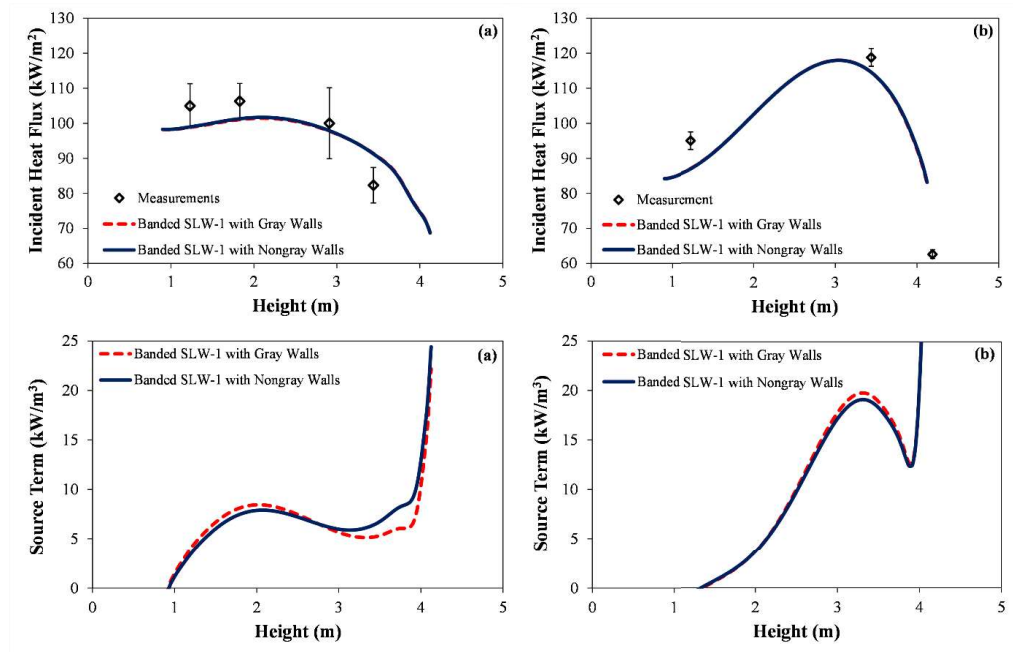
Figure 7.13. Incident wall HF and ST predictions of gray and non-gray refractory-lined wall emissivities for (a) Test 2 Air-Fired and (b) Test 3 Air-Fired

Table 7.15 Mean absolute error percentages in incident HFs (q_w) and STs along the centerline (∇q) for Test 2 and Test 3 with refractory-lined walls

	Test 2 Air-Fired		Test 3 Air-Fired	
	Banded SLW-1	**Banded SLW**	**Banded SLW-1**	**Banded SLW**
Comparison with Measurements				
Error in q_w* (%)	5.94	5.80	6.09	6.11
Comparison with Reference Solution				
Error in q_w (%)	0.16	Reference	0.10	Reference
Error in ∇q** (%)	12.05	Reference	2.69	Reference
Computational Requirements				
CPU Time, s	886	775	465	408
CPU Ratio, -	1.14	1.00	1.14	1.00

* Error $= [\sum_{i}^{N} \left(\frac{|q_{w,measured,i} - q_{w,predicted,i}|}{q_{w,measured,i}} \right) \times 100]/N$ where i is the index for the port location

** Error $= [\sum_{i}^{N} \left(\frac{|\nabla q_{Banded\ SLW-1,i} - \nabla q_{Banded\ SLW,i}|}{\nabla q_{Banded\ SLW,avg}} \right) \times 100]/N$ where i is the computational grid

7.2.2   Influence of Gray and Non-Gray Cold Water Walls

Table 7.16 illustrates the comparison of incident HF and ST predictions of MOL of DOM with non-gray gas and particle properties utilizing gray and non-gray water wall (537 K) emissivities for Test 2 and Test 3 under air-fired conditions. Visual comparisons between HF and ST predictions of gray and non-gray water wall

emissivities for Test 2 and Test 3 are also demonstrated in Figure 7.14. Introducing a gray wall emissivity instead of spectral wall emissivity into the radiation model does not significantly influence the HF and ST predictions in all the tests, as illustrated in Table 7.16 and Figure 7.14, unlike the results of the case with hot refractory-lined walls. This is considered to be due to; (i) the similarity of the gray and spectral emissivities between 0- 10 μm [Figure 7.12(b)] which covers 95 % of the thermal radiation in FBC temperatures, (ii) the dominance of thermal radiation by the medium rather than low-temperature water walls.
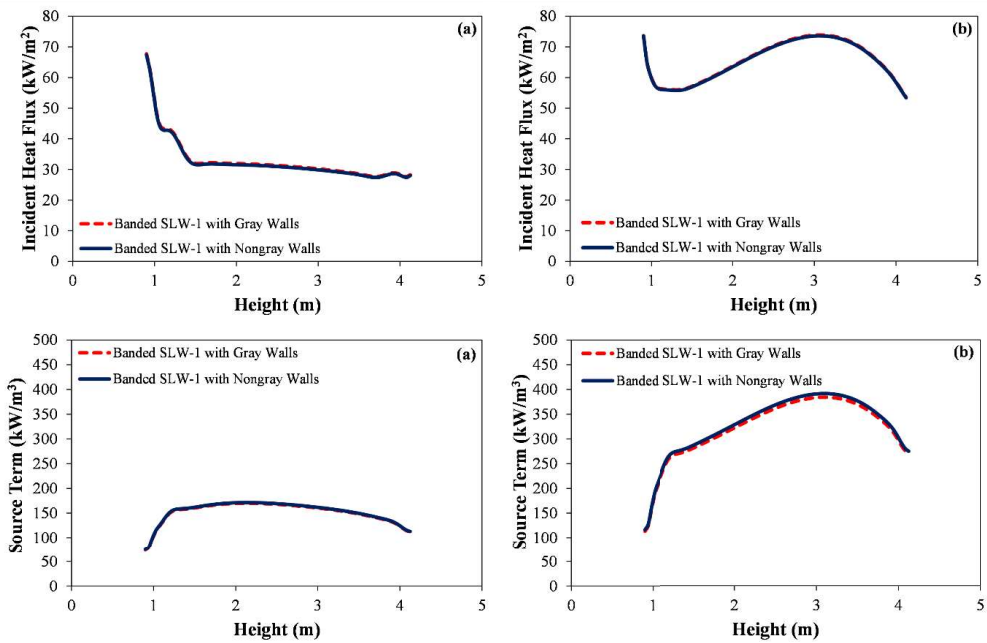
Figure 7.14. Incident wall HF and ST predictions of gray and non-gray water wall emissivities for (a) Test 2 Air-Fired and (b) Test 3 Air-Fired

Table 7.16 Mean absolute error percentages in incident HFs (q_w) and STs along the centerline (∇q) for Test 2 and Test 3 with water walls

	Test 2 Air-Fired		Test 3 Air-Fired	
	Gray Walls	**Non-Gray Walls**	**Gray Walls**	**Non-Gray Walls**
Comparison with Reference Solution				
Error in q_w	1.14	Reference	0.40	Reference
Error in ∇q*	0.91	Reference	1.96	Reference
Computational Requirements				
CPU Time, s	501	502	324	332
CPU Ratio, -	1.00	1.51	0.98	1.00

* Error in STs $= [\sum_i^N \left(\dfrac{\left| \nabla q_{Gray\ Wall,i} - \nabla q_{Non-gray\ Wall,i} \right|}{\nabla q_{Non-gray\ Wall,i}} \right) \times 100]/N$

7.2.3 Influence of Gray and Non-Gray Cold Slag Covered Water Walls

During the operation of industry or utility boilers, fly ash particles in the freeboard section become sticky due to high temperatures. These particles stick to cooler surfaces such as water walls building up an insulating layer of coal slag. This effect is investigated by conducting a parametric study where the side walls at 537 K are assumed to be covered by coal slag, with the compositions of fly ashes.

Comparison between HF and ST predictions of MOL solution of DOM with non-gray gases and particles properties using gray and non-gray slag covered water wall emissivities for Test 2 and Test 3 are demonstrated in Table 7.17 and Figure 7.15. Similar to the case with cold water walls, introducing a gray wall emissivity instead of spectral wall emissivity into radiation model does not significantly influence the

HF and ST predictions in all the tests, as illustrated in Table 7.17 and Figure 7.15. This is considered to be due to; (i) the similarity of the gray and spectral emissivities between 0 - 10 μm [Figures 7.12(c) and 7.12(d)] which covers 95 % of the thermal radiation in FBC temperatures, (ii) the dominance of thermal radiation by the medium rather than low-temperature water walls.

The error in ST predictions of gray and non-gray slag covered water wall emissivities, on the other hand, increases slightly with one order of magnitude increase in the particle load from Test 2 to Test 3. It should be noted that due to low wall temperatures of slag covered water walls, total radiative intensity leaving the wall [Eqs. (2.13) and (2.14)] is dominated by the reflected radiation incoming from the medium (2nd term in the RHS of Eqs. (2.13) and (2.14)). Therefore, wall intensities become sensitive to the medium intensities, and thus, medium properties. This is why the error in STs predicted by gray and non-gray slag covered water wall emissivities increases with increasing particle absorption and scattering coefficient from Test 2 to Test 3.
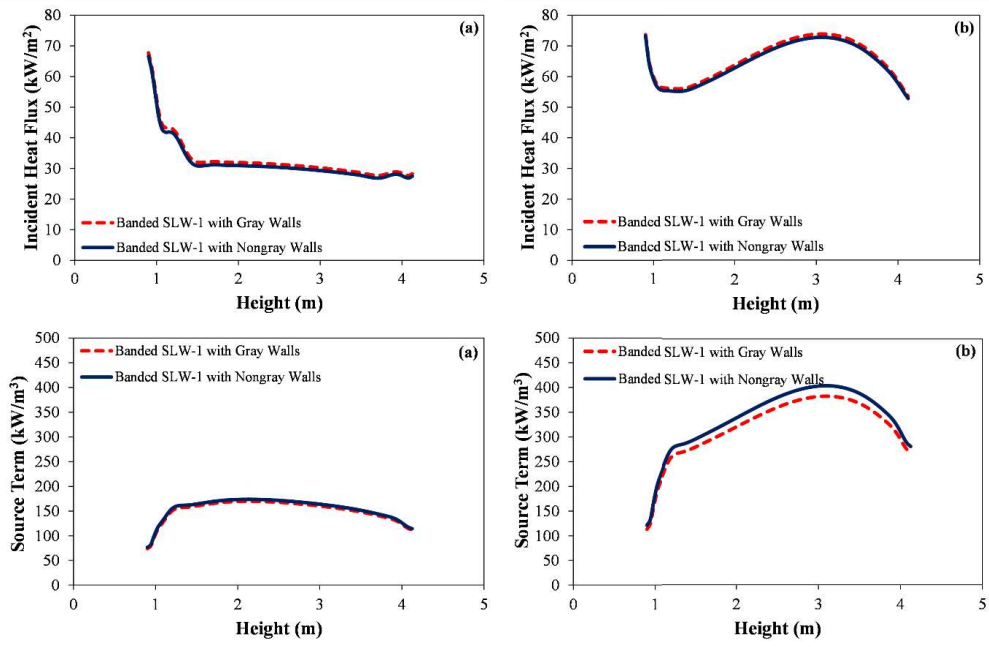
Figure 7.15. Incident wall HF and ST predictions of gray and non-gray slag covered water wall emissivities for (a) Test 2 Air-Fired and (b) Test 3 Air-Fired

Table 7.17 Mean absolute error percentages in incident HFs (q_w) and STs along the centerline (∇q) for Test 2 and Test 3 with slag covered water walls

	Test 2 Air-Fired		Test 3 Air-Fired	
	Gray Walls	Non-Gray Walls	Gray Walls	Non-Gray Walls
Comparison with Reference Solution				
Error in q_w	3.24	Reference	1.46	Reference
Error in ∇q*	2.44	Reference	5.30	Reference
Computational Requirements				
CPU Time, s	501	511	324	331
CPU Ratio, -	0.98	1.54	0.98	1.00

* Error in STs $= [\sum_i^N \left(\dfrac{\left| \nabla q_{Gray\ Wall,i} - \nabla q_{Non-gray\ Wall,i} \right|}{\nabla q_{Non-gray\ Wall,i}} \right) \times 100]/N$

7.2.4 Concluding Remarks for the Effect of Spectral Wall Radiative Properties

Based on the above-mentioned discussion regarding the influence of spectral wall radiative properties on RHT predictions of BFBCs, it can be concluded that using gray wall emissivity instead of spectral emissivity does not lead to significant error in incident wall HF predictions. On the other hand, utilizing gray wall emissivity for hot refractory-lined walls leads to significant inaccuracies in the ST predictions of the combustion tests where particle load is low due to higher share of wall radiation in the RHT. Discrepancies between the ST predictions of gray and non-gray cold water wall emissivities and those of gray and non-gray cold slag covered water wall emissivities which are common in industry and utility boilers are found to be

insignificant which is attributed to the combined effects of low wall temperatures and similar gray and non-gray water wall emissivities.

7.3   Effect of Type of Bag Filter Ash on Radiative Heat Transfer in Bubbling Fluidized Bed Combustors

As the contribution of thermal radiation to toal heat transfer in the freeboard of BFBCs is of remarkable importance because of the presence of radiating particles together with radiating gases, RHT characteristics of biomass and coal blends in FBCs require special attention. Nevertheless, a limited number of mathematical modeling studies exists in the literature that investigates the thermal radiation characteristics of BFBCs co-firing biomass/coal blends.

Ateş et al. [36] investigated the influence of adjusting the type of biomass on thermal radiation during co-combustion of Çan lignite with OR and HS and with limestone addition in a 0.3 MW_t ABFBC test rig with refractory lined walls at around 840 ℃ by applying a 3-D radiation code based on MOL of DOM utilizing gray gas, particle, and wall radiative properties. Based on their results, replacing OR with HS does not significantly affect the profiles of ST and HF along the combustor, however, when the wall material was taken to be a conventional panel tube wall at 264 ℃, both ST and HF predictions were found to increase by this replacement. This increase in the RHT predictions along the combustor was considered to be due to the increase in the number of fine particles when burning HS instead of OR. In another study for the investigation of the thermal radiation behavior of BFBCs, Ates et al. [37] applied the same radiation code coupled with gray gas, particle, and wall radiative properties to the freeboard of the same test rig where Çan lignite is co-fired with limestone and OR. Their results indicate that the addition of OR does not significantly affect the ST predictions although particle load in the freeboard is lower when OR is co-fired with lignite instead of firing lignite with limestone only. This effect can be related to the increasing number of fine particles during biomass combustion [200] leading to improved particle absorption and scattering. For this purpose, the contribution of fine

particles on the RHT during co-combustion of coal/biomass blends in BFBCs requires to be investigated to clarify the influence of co-firing on RHT. Moreover, this investigation has to be performed in the presence of spectral gas, particles, and walls since the utilization of spectral radiative properties is necessary in the accurate handling of RHT in these systems [203].

Therefore, one of the aim of this thesis study is to investigate the contribution of fine particles collected in bag filter on RHT in the freeboard of the 0.3 MWt ABFBC test rig where lignite (Test 5), lignite/ OR (Test 6), and lignite/ HS (Test 7) blends are fired with limestone addition by deploying a 3-D radiation code based on MOL of DOM coupled with spectral gas, particle, and wall radiative property models. The radiation code is executed by considering first the presence of combustion gases only, then combustion gases with fine particles only, and then combustion gases with all particles' radiation. The data for the radiation models and for their validations are provided from the measurements obtained during the same combustion test mentioned above (eee section 6.2.3).

S_N angular discretization method suggested by Carlson and Lathrop [101] is selected for the MOL solution of DOM. The system of ODEs obtained after angular and spatial discretization is solved by the readily available ROWMAP code which utilizes ROW-methods of order 4 and uses Krylov techniques for the solution of linear systems [105]. All tests are performed on a computer with Intel® Core™ i7-2600 CPU 3.40 GHz processor having 16.00 GB of RAM. In the application of the model, a uniform structure of $11 \times 11 \times 81$ grids, the S_6 angular discretization method [199] which were shown to provide an accurate and CPU-efficient solutions in the assessment study carried out by Ates et al. [28], is utilized.

For the results presented in the following section, the spectral gas radiative properties are estimated utilizing banded SLW-1 whereas the spectral radiative properties of particles are calculated using Mie theory due to the fact that the majority of particles considered in this study falls into the particle size range recommended for Mie

218

theory. The scattering of radiation is represented by the transport approximation as suggested in the previous assessment study [199].

Gray gas parameters of banded SLW-1 model ($\kappa_{j,1}$ and $a_{j,1}$) are estimated based on two emissivity approach where gray gas parameters are obtained by fitting total gas emissivities calculated at two different path lengths L_1 and L_2. In this study, total gas emissivities are estimated utilizing 10 x 10 (H_2O x CO_2) gray gas mixtures as 10 x 10 gray gas mixtures provide sufficient accuracy in RHT predictions. L_1 and L_2, on the other hand, are selected as 0.1 and 1.1 times spectrally dependent mean beam length.

Size distributions of cyclone and bag filter particles are taken from the measurements. Ebert's correlations [45,124] are used to determine the refractive indices of both cyclone and bag filter particles using the ash chemical compositions and temperatures of particles. The single particle properties are calculated by deploying Mie theory for 34 discrete sizes and 147 wavelengths. Spectral radiative properties (absorption and scattering coefficients and asymmetry factors) of the polydisperse particles with a discrete size distribution can be evaluated using the single particle properties. The thermal spectrum is represented with 8 spectral wavelength intervals $0 - 20$ μm which covers almost all thermal radiation under the temperatures of FBCs. Table 7.18 summarizes limits for each wide band and the corresponding fraction of blackbody emissive power (Δf) for all combustion tests.

Table 7.18 Band dividing scheme utilized in this study and corresponding fraction of blackbody emissive power (Δf) for all combustion tests

Band No.	Start (μm)	End (μm)	Δf (Test 1)	Δf (Test 2)	Δf (Test 3)
1	0.0	2.4	0.19	0.20	0.20
2	2.4	3.1	0.17	0.17	0.17
3	3.1	4.1	0.20	0.20	0.20
4	4.1	4.8	0.10	0.10	0.10
5	4.8	6.3	0.14	0.13	0.14
6	6.3	8.9	0.11	0.10	0.10
7	8.9	12.1	0.05	0.05	0.05
8	12.1	20.0	0.03	0.03	0.03

7.3.1 Radiative Properties of Cyclone and Bag Filter Particles

In this section, the radiative properties of both cyclone and bag filter particles for all combustion tests under consideration are compared to investigate the influence of co-firing on the RHT. Figure 7.16 illustrates the comparison of the spectral absorptive and refractive indices of cyclone and bag filter particles for all tests. Refractive indices of cyclone and bag filter particles are quite similar throughout the entire spectrum under investigation for all combustion tests with and without biomass co-firing. On the other hand, the absorptive indices of bag filter particles are considerably higher compared to those of cyclone particles in the wavelength range of $1 - 4$ μm, which covers approximately 55 % of the thermal radiation under fluidized bed combustion conditions. The reason behind the significant difference between the absorptive indices of cyclone and bag filter particles is considered to be

220

due to the significant difference in the iron content of the cyclone and bag filter ashes as shown in Tables 6.18 and 6.19.
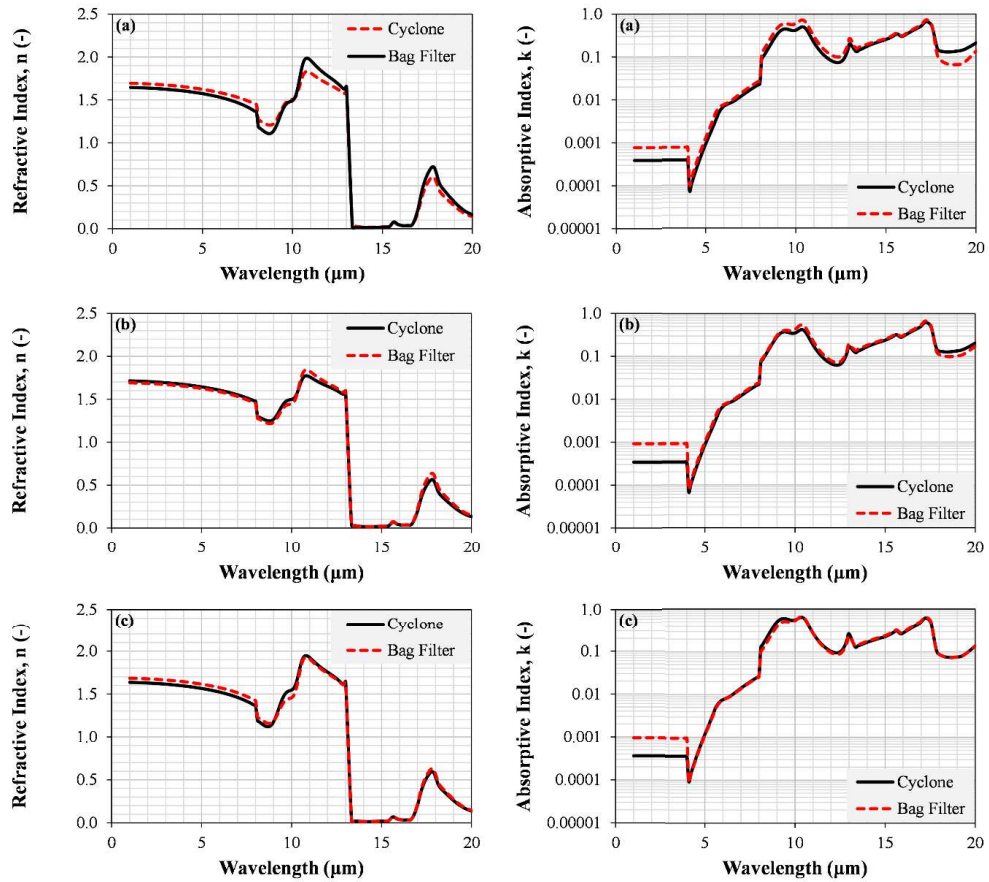
Figure 7.16. Refractive and absorptive indices of both cyclone and bag filter particles of (a) Test 5 (b) Test 6 and (c) Test 7

Predicted spectral radiative properties of bag filter (BF) and bag filter and cyclone ash particles (BF and Cyclone) for all tests are illustrated in Figures 7.17, 7.18, and 7.19. The radiative properties of fly ash particles are calculated for the wavelength range of 1-20 microns due to the lack of RI of particles between 0-1 microns. Fortunately, the interval between 0-1 microns covers only 0.1 % of the thermal radiation at the temperature of the system under consideration. As demonstrated by the figure, in Test 5 with the combustion of lignite only, bag filter particles contribute

221

to only a marginal part of absorption and scattering of radiation by fly ash particles. This effect is attributed to the significant amount of coarse particles produced by lignite combustion. With the addition of OR and HS in Test 6 and Test 7, on the other hand, bag filter particles dominate the particle absorption and scattering due to very high projected surface area of bag filter particles compared to cyclone particles. This is considered to be due to the tendency of biomass combustion to produce fine particles as reported before [200]. Asymmetry factors are not significantly influenced by biomass addition. Considering the similarity between refractive and absorptive indices of cyclone and bag filter particles except in the wavelength range of $1 - 4$ μm, the differences in absorption and scattering properties of cyclone and bag filter particles are considered to be due to the differences in particle load and particle size rather than the differences in refractive and absorptive indices.
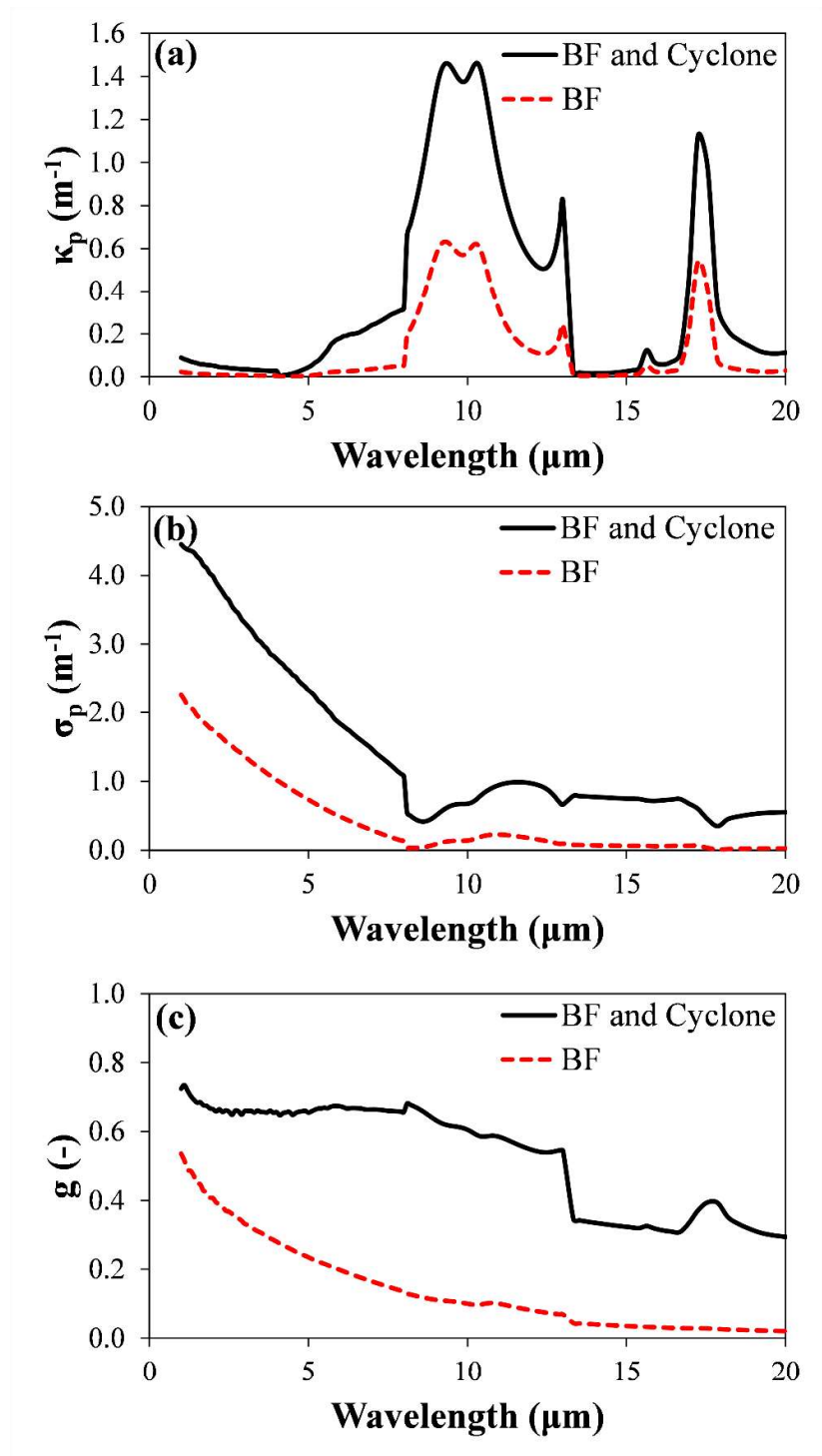
Figure 7.17. Spectral particle (a) absorption coefficients, (b) scattering coefficients and (c) asymmetry factors for Test 5
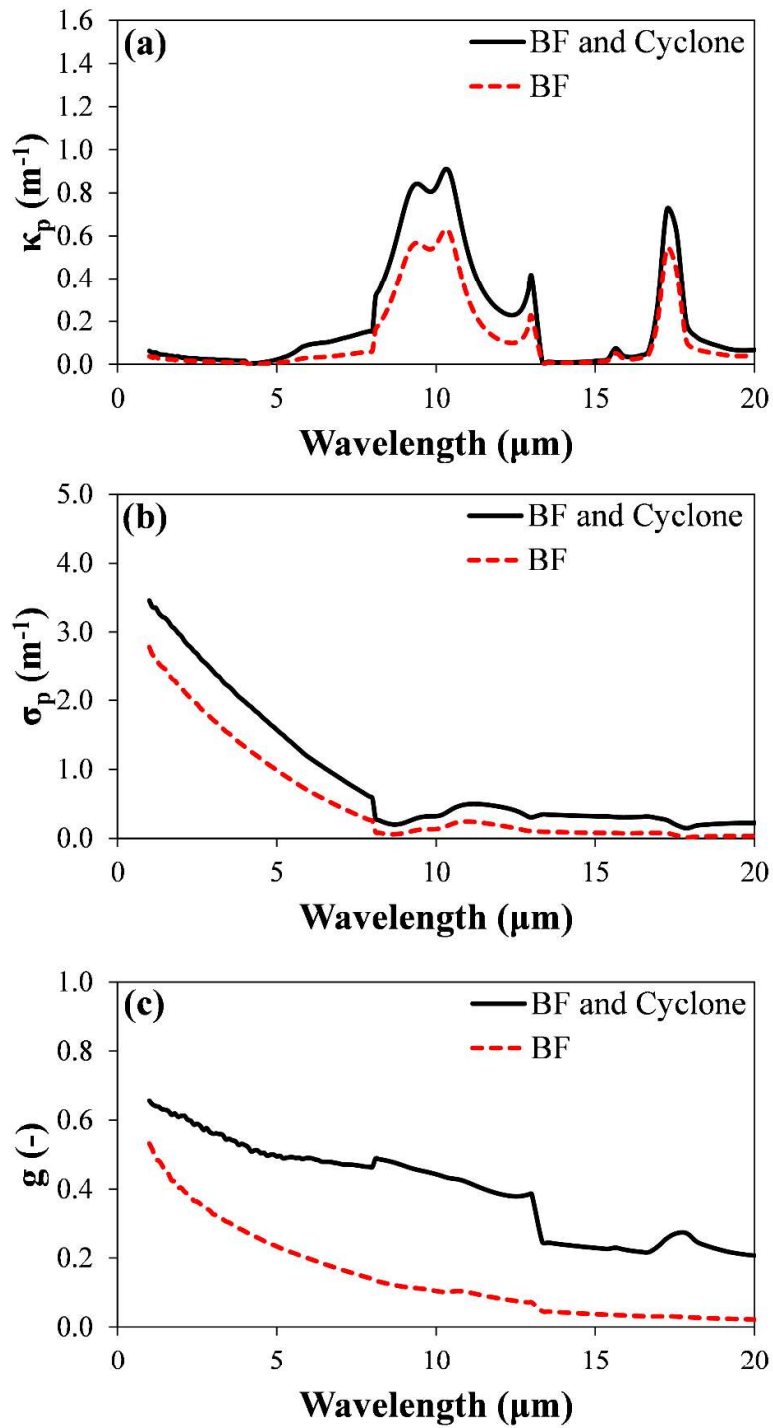
Figure 7.18. Spectral particle (a) absorption coefficients, (b) scattering coefficients and (c) asymmetry factors for Test 6
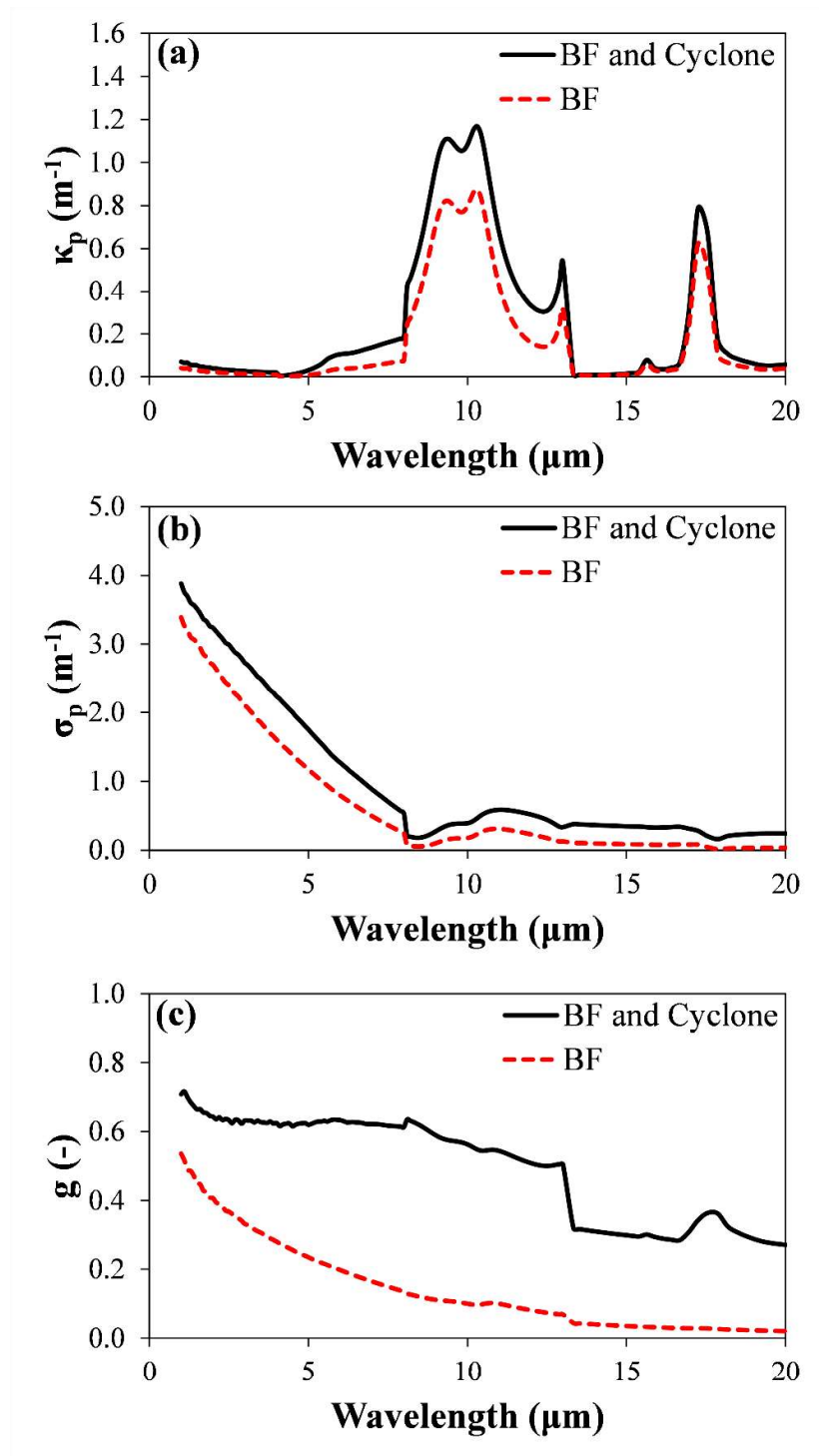
Figure 7.19. Spectral particle (a) absorption coefficients, (b) scattering coefficients and (c) asymmetry factors for Test 7

7.3.2 Influence of Cyclone and Bag Filter Particles and Combustion Gases on Radiative Heat Transfer

To assess the contribution of bag filter particles to spectral thermal radiation, ST and net wall HF predictions of spectral RHT models were evaluated without particles, only with bag filter particles, and with cyclone and bag filter particles for all combustion tests. However, before going through a detailed analysis, it should be pointed out that the existence of particles and combustion gases has not a noticeable impact on incident HFs due to the dominance of hot refractory-lined walls. Therefore, the comparison of incident HF profiles predicted by the RHT models is not included in the present work. The comparisons of the ST and net wall HF predictions without particles, with only bag filter particles, and with cyclone and bag filter particles for Tests 5, 6, and 7 are shown in Figure 7.20. As demonstrated by Figure 7.20, the net radiative wall HFs are positive in the lower part of the freeboard due to radiative heating by the bed surface whereas they are negative at the upper part which indicates radiative cooling by the cooler module at the end of the freeboard. Contribution of cyclone particles on the net HFs in Test 5 without co-firing is higher than that of bag filter particles. On the other hand, cyclone particles have a negligible effect on the net fluxes in the combustion tests with co-firing (Tests 6 and 7). Similar trends are also observed in the ST profiles. The sharp changes in the STs at the beginning and the end of the freeboard are considered to be due to the discontinuity between the medium temperature profile and the temperatures of the top and the bottom boundaries. This sharp difference in the ST profile is much higher at the top boundaries due to existence of the cooler module.
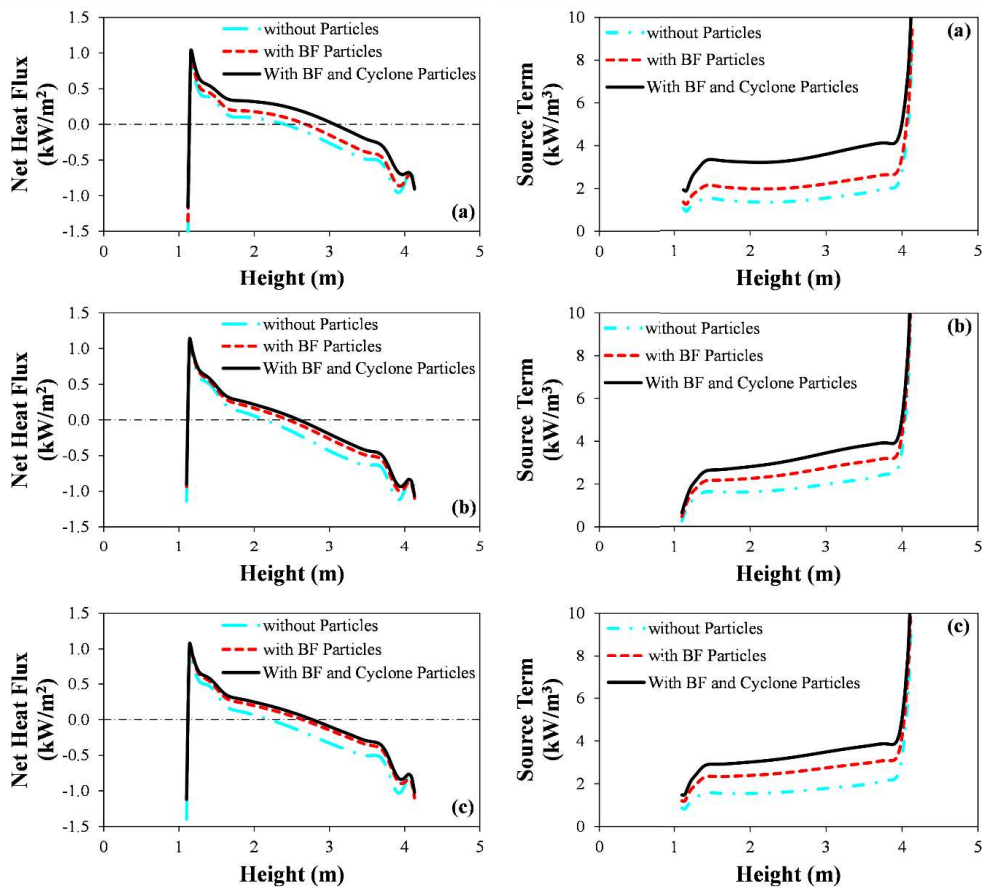
Figure 7.20. Net wall HF and ST profiles of radiative heat transfer models without particles (combustion gases only), only with bag filter particles, and with cyclone and bag filter particles for (a) Test 5, (b) Test 6, and (c) Test 7

Table 7.19 lists the average ST and net wall HF predictions of the RHT models without particles, only with bag filter particles, and with cyclone and bag filter particles for Tests 5, 6, and 7. As summarized in the table, the addition of biomass reduces the total net wall HF and ST predictions along the combustor. However, this decrease in the HF and the ST predictions is not significant despite the low ash content of biomass compared to lignite (see Tables 6.14 and 6.15) and low sulfur content of biomass leading to lower limestone flow rates in the co-firing tests (see Tables 6.13). The slight decrease in the HF and the ST predictions is considered to

be due to the fall in the contribution of cyclone particles to thermal radiation, which is compensated by the higher contribution of combustions gases and fine particles originating from biomass combustion.

Table 7.19 Average net wall HF and ST predictions without particles (combustion gases only), only with bag filter particles, and with cyclone and bag filter particles for Tests 5, 6, and 7

	Test 5	Test 6	Test 7
Average q_w (kW/m^2)			
With Cyclone and Bag Filter Particles	0.07	-0.07	-0.01
With Bag Filter Particles	-0.08	-0.12	-0.05
Without Particles	-0.17	-0.23	-0.19
Average ∇q (kW/m^3)			
With Cyclone and Bag Filter Particles	3.68	3.40	3.53
With Bag Filter Particles	2.35	2.79	2.84
Without Particles	1.72	2.11	1.97

In order to estimate the fractional contributions of combustion gases, bag filter particles, and cyclone particles to radiation, the radiation code is executed by considering first only combustion gases, then combustion gases with only bag filter particles, and then combustion gases with cyclone and bag filter particles radiation. Contributions of gas, bag filter, and cyclone particles to RHT are calculated as follows:

$$f_{gas} = \frac{\nabla q_{without\ particles}}{\nabla q_{with\ cyclone\ and\ bag\ filter\ particles}} \tag{7.1}$$

$$f_{BF} = \frac{\nabla q_{with\ BF\ particles} - \nabla q_{without\ particles}}{\nabla q_{with\ cyclone\ and\ bag\ filter\ particles}} \qquad (7.2)$$

$$f_{Cyclone} = 1 - f_{gas} - f_{BF} \qquad (7.3)$$

Estimated fractional contributions of combustions gases, bag filter particles, and cyclone particles for all tests are listed in Table 7.20. As can be seen from the table, the contribution of gas radiation to total RHT is slightly higher in co-firing tests due to (i) lower total freeboard (cyclone and bag filter) particle load due to low ash content of biomass (ii) high hydrogen content of the biomass fuel leading to higher water vapor concentration along the freeboard. Furthermore, the addition of OR and HS increases the contribution of bag filter particles on RHT and reduces the contribution of cyclone particles. This effect is considered to be due to the higher load of bag filter particles and the lower load of cyclone particles in the freeboard of the co-firing tests as can be seen from Table 6.18.

Table 7.20 Fractional contributions of combustions gases, bag filter particles, and cyclone particles to radiative heat transfer for all combustion tests

	Test 5	Test 6	Test 7
Combustion Gases	0.47	0.62	0.56
Bag Filter Particles	0.17	0.20	0.25
Cyclone Particles	0.36	0.18	0.19

The results of this study cannot be transferred directly to full-scale plants as the test rig with high surface to volume ratio (Surface area/Volume = 9.4) does not represent the commercial scale boilers. However, these results highlight the importance of bag filter and cyclone particle radiation in the modeling and design of commercial-scale bubbling FBCs co-firing lignite and biomass. Furthermore, these results also reveal that co-firing biomass in existing large-scale coal-fired bubbling FBCs may not

significantly deteriorate the RHT depending on the ash, hydrogen, and moisture content of the biomass.

7.3.3 Concluding Remarks for the Effect of Bag Filter and Cyclone Ashes

Based on the application of 3-D radiation code using MOL of DOM to the combustion and co-combustion tests carried out in METU 0.3 MW_t ABFBC test rig, it was found that while co-firing high ash content lignites with low ash content biomass in BFBCs, the contribution of cyclone particles to thermal radiation decreases. On the other hand, those of combustion gases and fine particles originated from biomass combustion increase. The contribution of gas radiation to total RHT in bubbling fluidized beds slightly increases with the addition of biomass due to (i) lower total freeboard (cyclone and bag filter) particle load due to low ash content of biomass and (ii) high hydrogen content of the biomass fuel leading to higher water vapor concentration along the freeboard. Finally, co-firing lignite and biomass in a coal-fired power plant instead of only lignite combustion may not deteriorate RHT in the freeboard depending on the ash, hydrogen, and moisture content of the biomass.

7.4 Effect of Soot on Radiative Heat Transfer in Bubbling Fluidized Bed Combustors

The solution of RTE becomes further complicated in the presence of spectral absorption, emission, and scattering properties of the medium. Studies involving thermal radiation in the FBCs have already taken into account the contributions of combustion gases (CO_2 and H_2O) [61,203–205] and fly ash particles [42,45] with reasonable accuracy and computational efficiency. However, there is no study in the literature investigating the influence of soot on RHT in the BFBCs.

Soot is formed during the operation of practical combustion devices especially the ones involving diffusion flames [206]. Previous experimental studies carried out in

BFBCs indicate the formation of flames in the bubbles [207] and just above the bubbling bed [207,208] during the combustion of different types of coal. Therefore, soot particles and aggregates are expected to form during the operation of BFBCs exclusively above the bubbling bed (i.e. splash zone) or in the bubbles which will eventually splash and mix with the gases in the splash zone. It is well known that soot is a strong absorber and emitter of infrared radiation in a continuous spectrum, which implies that it may contribute to thermal radiation significantly even at a very low volume fraction. Therefore, the radiative properties of soot should be considered together with combustion gases and particles for the modeling of thermal radiation in BFBCs.

Therefore, one of the aims of this study is to examine the influence of soot particles and aggregates on RHT in BFBCs. For this purpose, a radiative property model for soot particles and aggregates is first incorporated into an in-house developed 1-D radiation code to examine the influence of different parameters on soot radiative properties and RHT predictions. Then, spectral soot radiative property model is coupled with the 3-D radiation code utilizing MOL of DOM and spectral gas, fly ash particle, and wall radiative properties in order to investigate the influence of soot on thermal radiation in $0.3 \, MW_t$ ABFBC test rig, which represents the typical operation conditions of industrial BFBCs. In the following sections, details of this study and its major findings are presented.

S_N angular discretization method suggested by Carlson and Lathrop [101] is selected for the MOL solution of DOM. The system of ODEs obtained after angular and spatial discretization is solved by the readily available ROWMAP code which utilizes ROW-methods of order 4 and uses Krylov techniques for the solution of linear systems [105]. All tests are performed on a computer with Intel® Core™ i7-2600 CPU 3.40 GHz processor having 16.00 GB of RAM.

Gas radiative properties are estimated using SLW [51–53], banded SLW [52], banded SLW-1 [81,87,205]. Properties of fly ash particles, including bag filter and cyclone ashes, are estimated using Mie theory as the majority of fly ash utilized in

this study is too large for Rayleigh scattering theory yet too small for geometric optics approximation. Furthermore, the anisotropic scattering of fly ash particles is represented by using transport approximation [119]. For the radiative properties of soot particles and aggregates, Rayleigh scattering theory and electrostatic approximation (ESA) is utilized.

Gray gas parameters of banded SLW-1 model ($\kappa_{j,1}$ and $a_{j,1}$) are estimated based on two emissivity approach where gray gas parameters are obtained by fitting total gas emissivities calculated at two different path length L_1 and L_2. In this study, total gas emissivities are estimated utilizing 10 x 10 (H_2O x CO_2) gray gas mixtures as 10 x 10 gray gas mixtures provide sufficient accuracy in RHT predictions. L_1 and L_2, on the other hand, are selected as 0.1 and 1.1 times spectrally dependent mean beam length.

For the spectral solution of RTE, the thermal spectrum is divided into 8 spectral wide bands between $0 - 20$ μm which covers almost all thermal radiation under the temperatures of FBCs. The band dividing scheme is given in Table 7.21. For each wide band, intensity field is calculated individually by solving RTE utilizing banded properties of combustion gases, fly ash, and soot particles. Then, the total intensity field can directly be calculated by the addition of the intensities of each wide band.

Table 7.21 Band dividing scheme

Band No.	Start (μm)	End (μm)
1	0.0	2.4
2	2.4	3.1
3	3.1	4.1
4	4.1	4.8
5	4.8	6.3
6	6.3	8.9
7	8.9	12.1
8	12.1	20.0

7.4.1   1-D Test Problem

Before the application of the 3-D spectral radiation code, coupled with radiative property models for combustion gases, fly ash particles, and soot, to the 0.3 MW_t ABFBC test rig, the influence of soot on thermal radiation is first tested on a 1-D slab problem including combustion gases and soot. The effect of several parameters such as soot particle size, soot aggregate size, and utilization of gray soot properties, is tested in the 1-D slab problem.

The effect of soot on RHT is investigated on a 1-D slab problem adopted from Bordbar et al. [61] by using a developed 1-D radiation code utilizing the MOL of DOM coupled with SLW and banded SLW (band dividing scheme for banded SLW is presented in Table 7.21) model for gas radiative properties. The schematic representation of 1-D slab problem is illustrated in Figure 7.21. The system under investigation consists of two infinitely long parallel plates 1.0 m apart. The medium

bounded by two parallel plates originally consists of an isothermal and homogeneous mixture of H_2O and CO_2 at 1000 K and with 0.2 and 0.1 mole fractions, respectively. In this section, in order to assess the effect of soot on radiation, soot is also included in the medium with a volume fraction (f_v) of 3 x 10^{-6} based on the previous study of Butler et al. [209]. Both parallel plates are black surfaces at 300 K. In the solution of RTE for 1-D slab problem, a combination of 101 uniform grids (in the x-direction), two-point-upwind-differencing scheme (DSS012), and the S_8 angular quadrature scheme is used.
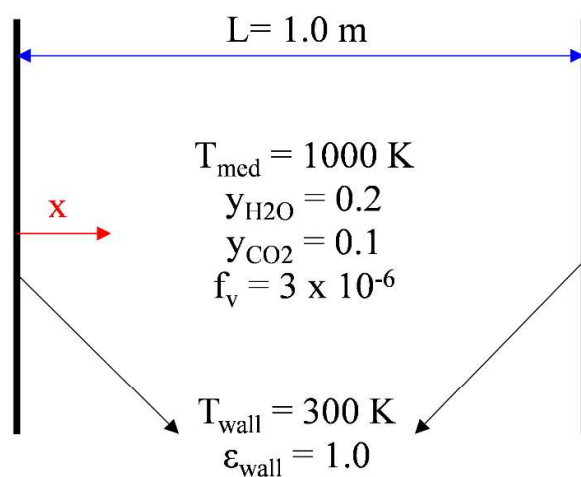
Figure 7.21. Schematic representation of 1-D slab problem

First of all, the effect of the number of gray gases on the predictive accuracy of SLW is tested for the 1-D slab problem in the absence of soot by comparing their net wall HF and ST predictions with those of reference solution. For this purpose, 5 x 5, 10 x 10, and 15 x 15 gray gases for H_2O and CO_2, respectively, are tested where predictions of 15 x 15 gray gases are taken as the reference solution. Comparison of RHT predictions of SLW model with different numbers of gray gases is illustrated in Figure 7.22. Errors in HFs and STs and CPU times are shown in Table 7.22. 10 x 10 number of gray gases for H_2O and CO_2 is found to provide the most satisfactory predictions. Therefore, 10x10 gray gases will be utilized for the 1-D slab problem.
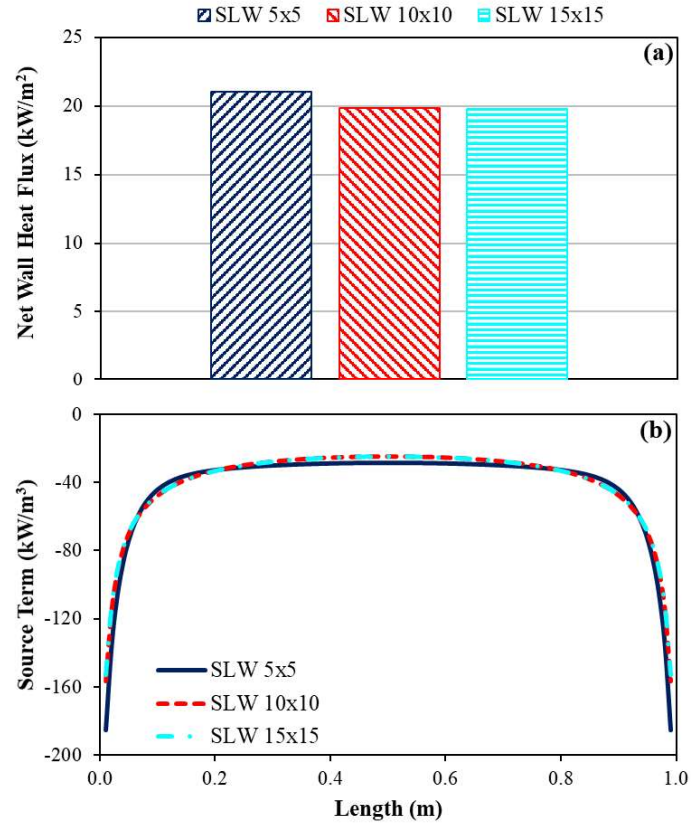
Figure 7.22. (a) Wall HF and (b) ST predictions of SLW model with 5 x 5, 10 x 10, and 15 x 15 number of gray gases for H_2O and CO_2 for 1-D slab problem

Table 7.22 Errors in HFs and STs and corresponding CPU times of SLW model with 5 x 5, 10 x 10, and 15 x 15 number of gray gases for H_2O and CO_2 for 1-D slab problem

	5 x 5	10 x 10	15 x 15
Error in q_w (%)	6.31	0.30	Reference
Error in ∇q* (%)	8.64	0.37	Reference
CPU Time, s	13	86	246

* Error $= [\sum_i^N \left(\dfrac{|\nabla q_i - \nabla q_{Reference,i}|}{\nabla q_{Reference,i}} \right) \times 100]/N$ where i is the computational grid

Before the assessment of the influence of soot on RHT, the performance of gray radiative properties of soot particles is tested by comparing its predictions with those of non-gray soot radiative properties for 1-D slab problem in the presence of 10 nm soot particles with a volume fraction of 3 x 10^{-6}. Figure 7.23 demonstrates net wall HF and ST predictions of banded SLW model with both gray and non-gray soot particle radiative properties. Moreover, errors in HF and ST predictions of gray soot properties are listed in Table 7.23. Gray radiative properties of soot particles provide sufficiently accurate RHT predictions (with less than 5 % errors), and thus, it will be employed for the 1-D slab problem in the rest of the study.
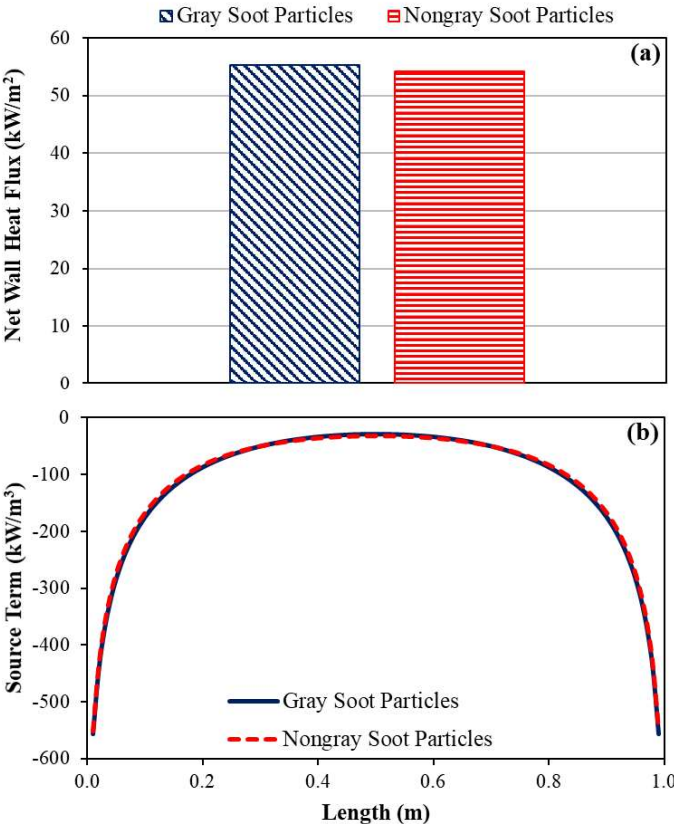
Figure 7.23. (a) Wall HF and (b) ST predictions of banded SLW model with gray and non-gray soot particle radiative properties for 1-D slab problem

Table 7.23 Error in HF and ST of banded SLW model with gray soot particle radiative properties for 1-D slab problem

	Gray Soot	**Non-Gray Soot**
Error in q_w (%)	1.75	Reference
Error in ∇q* (%)	4.67	Reference

* Error $= [\sum_i^N \left(\frac{|\nabla q_i - \nabla q_{Reference,i}|}{\nabla q_{Reference,i}} \right) \times 100]/N$ where i is the computational grid

The effect of soot particles and soot aggregates with different numbers of soot particles in an aggregate (N = 100, 250, 1000, and 10000) on RHT is investigated by applying 1-D radiation code using MOL of DOM with SLW model and gray radiative properties of soot particles and aggregates. This effect is tested using two different soot particle diameters ($d_{p,s}$ = 10 and 50 nm) in order to assess the influence of soot particle diameter on RHT as well. Comparison of scattering and absorption coefficients of the soot particles and soot aggregates is given in Table 7.24. Increasing the soot particle diameter and number of soot particles in an aggregate increases the scattering coefficient significantly while keeping the absorption coefficient of soot almost the same. It can be noted that the scattering coefficients of all aggregates are still very low (at least one order of magnitude) compared to the absorption coefficient. Net wall HF and ST predictions of the radiation models including soot particles and soot aggregates with different numbers of soot particles in an aggregate (N = 100, 250, 1000, and 10000) are illustrated in Figure 7.24. As demonstrated by the figure, addition of soot particles or aggregates significantly improves wall HFs and STs in the problem under consideration due to the high absorption and low scattering coefficient of soot as shown in Table 7.24. On the other hand, soot particle diameter and number of soot particles in an aggregate do not significantly influence the net wall HFs, and STs as absorption coefficient of soot is not significantly affected by those parameters.

Table 7.24 Absorption and scattering coefficients of soot particles and soot aggregates with different soot particle diameters ($d_p = 10$ and 50 nm) and numbers of soot particles in an aggregate (N = 100, 250, 1000, and 10000)

	$d_p = 10$ nm		$d_p = 50$ nm	
	κ_p (m^{-1})	σ_p (m^{-1})	κ_p (m^{-1})	σ_p (m^{-1})
Soot Particles	4.0799	0.00001	4.0967	0.0011
Soot Aggregates with N = 100	4.3210	0.0055	4.3388	0.1003
Soot Aggregates with N = 250	4.3232	0.0103	4.3410	0.1564
Soot Aggregates with N = 1000	4.3243	0.0211	4.3421	0.2599
Soot Aggregates with N = 10000	4.3246	0.0450	4.3425	0.4462
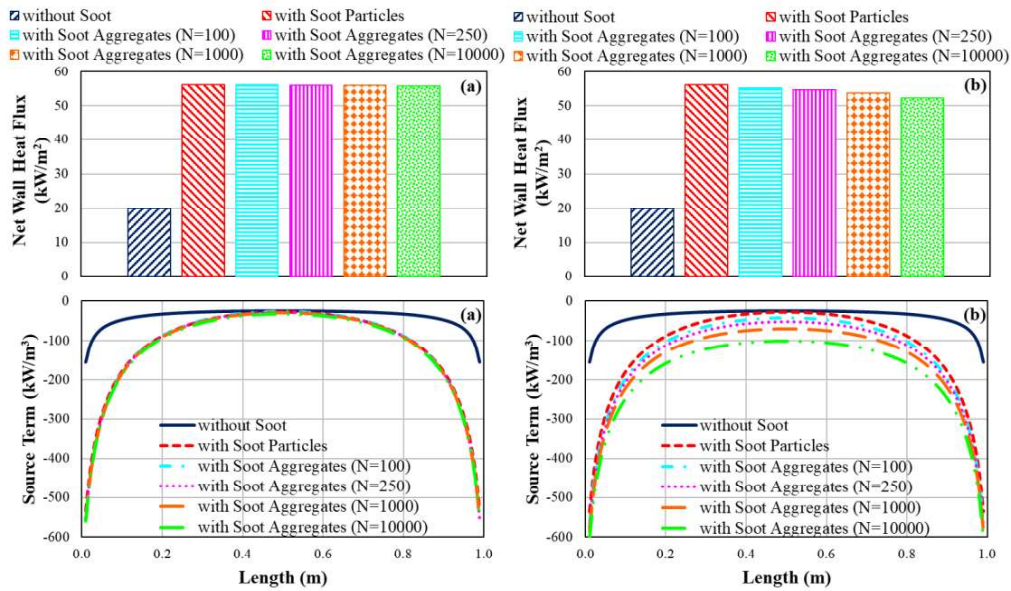
Figure 7.24. Net wall HF and ST predictions of SLW model with soot particles and soot aggregates with different numbers of soot particles in an aggregate (N = 100, 250, 1000, and 10000) for 1-D slab problem ((a) $d_p = 10$ nm, (b) $d_p = 50$ nm)

7.4.2   ABFBC Test Rig

After the application of radiation model to 1-D slab problem which shows remarkable impact of soot on RHT, the 3-D spectral radiation code is applied to the 0.3 MW_t ABFBC test rig. The freeboard of the test rig is originally bounded by hot refractory-lined walls. However, industrial-scale FBCs are generally bounded by cold water walls to extract the heat released during combustion. Therefore, a hypothetical study is performed where hot refractory-lined walls of the test rig are replaced with cold water walls, at 537 K and with spectral emissivity of thermally oxidized carbon steel (given in section 2.4), based on the experimental study of Andersson et al. [208] conducted in 16 MW_t FBC located at Chalmers University of Technology with similar freeboard temperatures. All parameters, except wall temperature and wall emissivity, are kept the same as those of the test rig firing indigenous lignite.

In this section, the effect of soot particles on RHT is studied by applying the 3-D spectral radiation code using MOL of DOM with banded SLW-1 for radiative properties of combustion gases, Mie theory for radiative properties of bag filter and cyclone ash particles, and Rayleigh scattering theory for soot particles in the freeboard of the test rig. Input data for the application of 3-D spectral radiation code is adapted from a previous experimental study conducted in the test rig firing indigenous lignite with limestone addition (Test 5).

Soot particles are assumed not to form aggregates as RHT predictions of soot particles and aggregates are quite similar as mentioned in section 7.4.1. Soot particles are taken to be uniformly released only in the splash zone of the 0.3 MW_t ABFBC test rig based on a previous study observing the formation of yellow diffusion flames at the bed surface [207]. The estimation of soot volume fraction and splash zone height is explained in detail in Appendix H. Based on the procedure given in Appendix H, the volume fraction of soot particles is calculated as 7.3 x 10^{-7} for Test 5 and taken to be uniform in the splash zone, which is estimated as 0.86 m from the

expanded bed height. The change of volume fraction of cyclone ash, bag filter ash, and soot particles along freeboard height for Test 5 is illustrated in Figure 7.25.
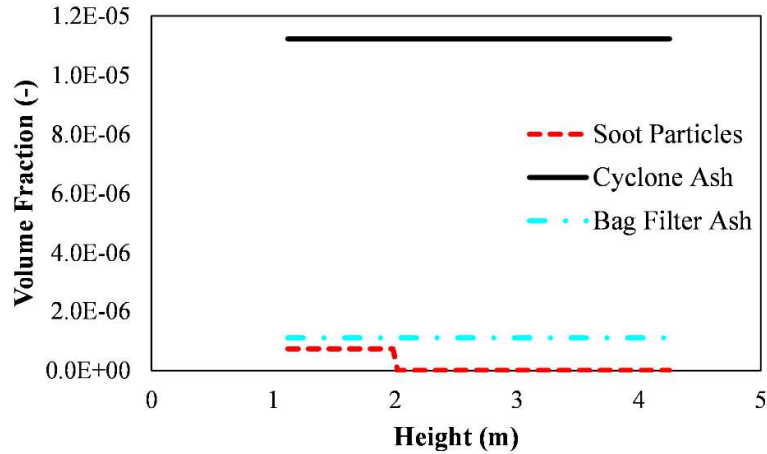
Figure 7.25. Volume fractions of cyclone ash, bag filter ash, and soot particles as a function of freeboard height for Test 5

For the solution of RTE for 3-D enclosure, S_6 angular discretization scheme, $11 \times 11 \times 81$ grid resolutions and three-point-upwind-differencing-scheme (DSS014) is utilized based on previous assessment studies [199,201]. It should be highlighted at this point that the sufficiency of such a low grid resolution (less than 10000 grid structure) to obtain converged solutions is considered to be due to almost isothermal temperature profile and uniform CO_2 and H_2O concentration and particle load along the freeboard of the test rig owing to rapid combustion of high VM/FC fuels under BFBC conditions. Under these circumstances, the intensity gradients in the RTE become smaller where coarser spatial discretization schemes are expected to become sufficient for the numerical solution of RTE.

Figure 7.26 demonstrates the comparison between the spectral refractive and absorptive indices of bag filter ashes, cyclone ashes, and soot particles existing in the test rig. As can be seen from the figure, refractive and absorptive indices of cyclone and bag filter ashes are quite similar in the whole thermal spectrum owing to similar chemical compositions as shown in Tables 6.18 and 6.19. On the other

240

hand, absorptive indices of soot are significantly greater than those of fly ash particles, especially in the wavelength range of 1 – 7 μm which stands for the 85 % of thermal radiation for the system under consideration. The difference between the refractive indices of soot particles and fly ash particles increases with increasing wavelength, especially when the wavelength becomes higher than 10 μm. However, those wavelengths do not contribute to the thermal radiation remarkably under the conditions of the test rig.
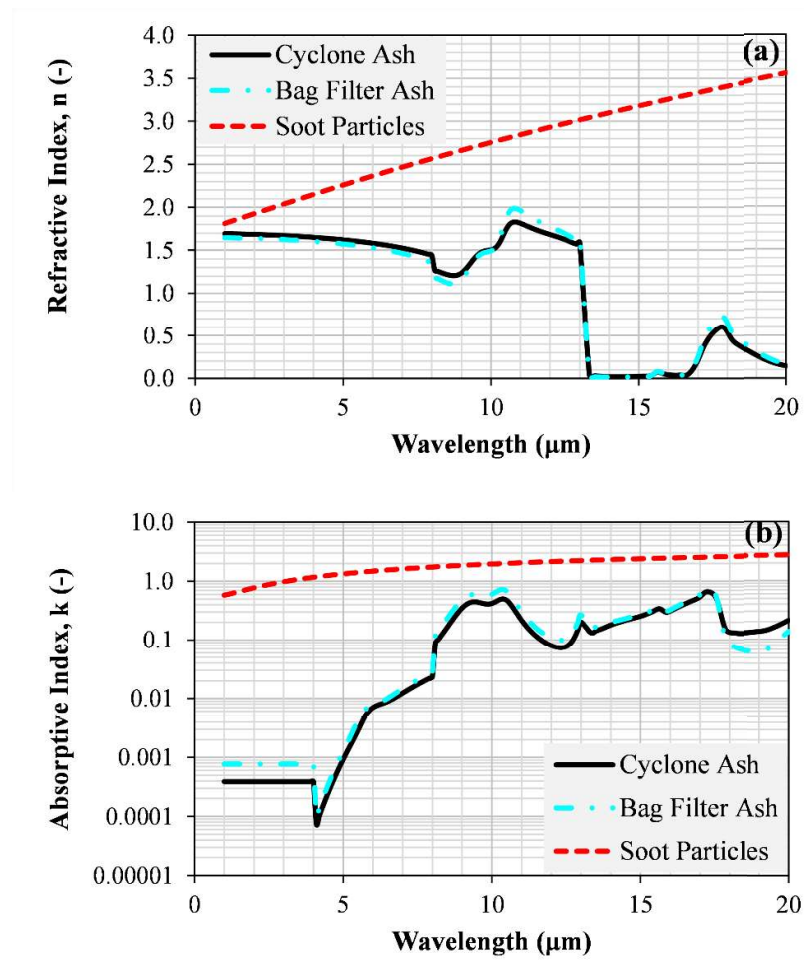
Figure 7.26. Spectral (a) refractive and (b) absorptive indices of bag filter ash, cyclone ash, and soot particles

Comparison of the absorption coefficient, scattering coefficient, and asymmetry factor of bag filter ashes, cyclone ashes, and soot particles is illustrated in Figures 7.27(a), 7.27(b), and 7.27(c), respectively. Absorption coefficient of soot particles is significantly greater than those of bag filter and cyclone ashes in the wavelength range of $1 - 7$ μm which covers almost 85 % of the thermal radiation of the system under investigation. This difference is attributed to the difference between the absorptive indices of soot and fly ash particles in the same wavelength range as highlighted in Figure 7.26(b). However, the scattering coefficient of the soot particles is negligible compared to those of bag filter and cyclone ashes.
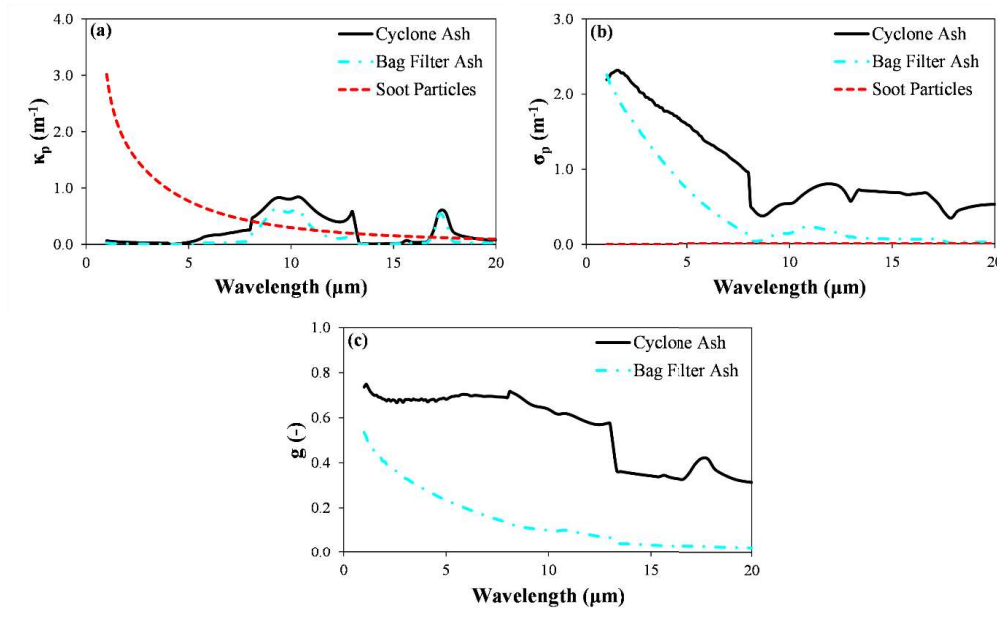
Figure 7.27. Spectral (a) absorption coefficient, (b) scattering coefficient, and (c) asymmetry factor of bag filter ash, cyclone ash, and soot particles

To assess the effects of combustion gases, bag filter particles, cyclone particles, and soot on RHT, 3-D spectral radiation code is executed by considering first presence of combustion gases only, then combustion gases with bag filter particles only, then combustion gases with cyclone and bag filter particles and then combustion gases with cyclone, bag filter, and soot particles. Incident wall HF and ST profiles of combustion test are demonstrated in Figures 7.28(a) and 7.28(b), respectively.

Presence of soot particles in the splash zone significantly improves both incident HF and STs. This effect is attributed to the combined effects of very high absorption coefficients of soot particles in the wavelength range of 1 – 7 μm (see Figure 7.27(a)) which covers almost 85 % of the thermal radiation of the system under investigation and negligible scattering coefficient throughout the entire spectrum.
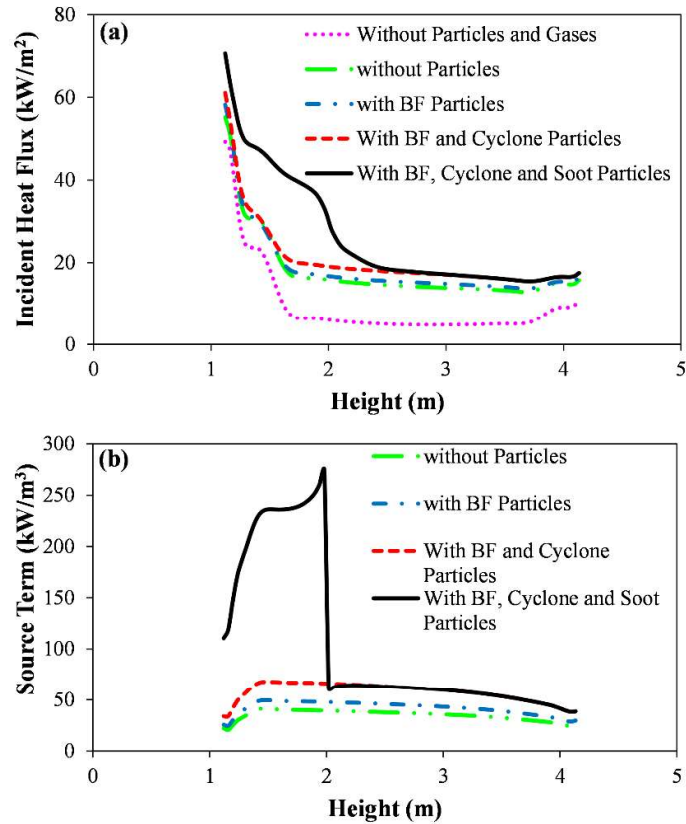
Figure 7.28. (a) Incident HF and (b) ST predictions of 3-D radiation code by considering the presence of only combustion gases, combustion gases with bag filter (BF) particles, combustion gases with cyclone and bag filter particles, and combustion gases with cyclone, bag filter, and soot particles

The fractional contribution of combustion gases, bag filter particles, cyclone particles, and soot to incident wall HFs and radiative STs in the splash zone and the whole freeboard of the test rig is estimated based on the ST and incident HF

243

predictions illustrated in Figures 7.28(a) and 7.28(b). The contributions of combustion gases, bag filter particles, cyclone particles, and soot to RHT in the splash zone and the whole freeboard are given in Table 7.25. As shown in the table, soot particles contribute significantly to RHT in both the splash zone and freeboard of the BFBC under investigation. The contribution of soot to RHT is higher in the splash zone compared to that in freeboard due to the absence of soot particles above the splash zone. Furthermore, the influence of wall on RHT is still important in both the splash zone and freeboard due to the existence of the hot boundary with the bed section. Apart from combustion gases (CO_2 and H_2O), fly ash particles, and soot, there exist some other gaseous species in the freeboard of the test rig such as CO, SO_2, NO, and N_2O which are discarded in the RHT calculations. However, their contribution to thermal radiation can roughly be estimated utilizing their Planck-mean absorption coefficients based on HITRAN and HITEMP databases reported by Modest [46] and concentration profiles of those gaseous species in the freeboard of the test rig reported in [196]. Based on the Planck-mean absorption coefficients, gaseous species, CO, SO_2, NO, and N_2O, contributes to less than 0.25 % of the gas radiation for the test rig under investigation which indicates neglecting those gaseous species in radiative transfer calculations does not lead to any remarkable error.

Table 7.25 Fractional contribution of combustion gases, bag filter particles, cyclone particles, and soot to incident wall HFs and radiative STs in the splash zone and the freeboard

| | Contribution to ST | | Contribution to HF | |
	Splash Zone	Freeboard	Splash Zone	Freeboard
Soot	0.72	0.44	0.36	0.21
Cyclone Ash	0.08	0.15	0.04	0.08
Bag filter Ash	0.03	0.07	0.02	0.03
Combustion Gases	0.17	0.34	0.18	0.32
Wall	-	-	0.40	0.36

In the present work, the soot volume fraction is estimated based on the assumptions which are (i) soot particles are uniformly distributed to the splash zone and (ii) all tar released during coal devolatilization is converted to soot. To understand the effect of these assumptions on the relative importance of soot on thermal radiation in BFBCs, a parametric study where different volume fractions of soot ($f_v = 7.0$ x 10^{-8}, 7.3 x 10^{-7}, and 4.0 x 10^{-6}) are utilized with 3-D radiation code by keeping all other parameters constant. Upper and lower limits are selected based on the range for soot volume fractions in small pool fires of diffusion flames reported by Bard and Pagni [210]. The intermediate soot volume fraction value ($f_v = 7.3$ x 10^{-7}) is the one utilized in the splash zone of the test rig firing indigenous lignite. Incident HF and ST profiles of the combustion test utilizing different soot volume fractions are illustrated in Figures 7.29(a) and 7.29(b), respectively. Furthermore, fractional contributions of soot to ST and HFs for different soot volume fractions are listed in Table 7.26. The contribution of soot to RHT is very sensitive to soot volume fraction which indicates experimental measurements of much more detailed models are necessary for the estimation of soot volume fractions. However, the findings obtained in this study

show that, even at the lowest volume fraction, soot particles have a noticeable impact on RHT in the splashing region of the freeboard. Therefore, it can be concluded that presence of soot should be taken into consideration in the radiative transfer calculations for BFBCs for accurate treatment of thermal radiation in those systems.
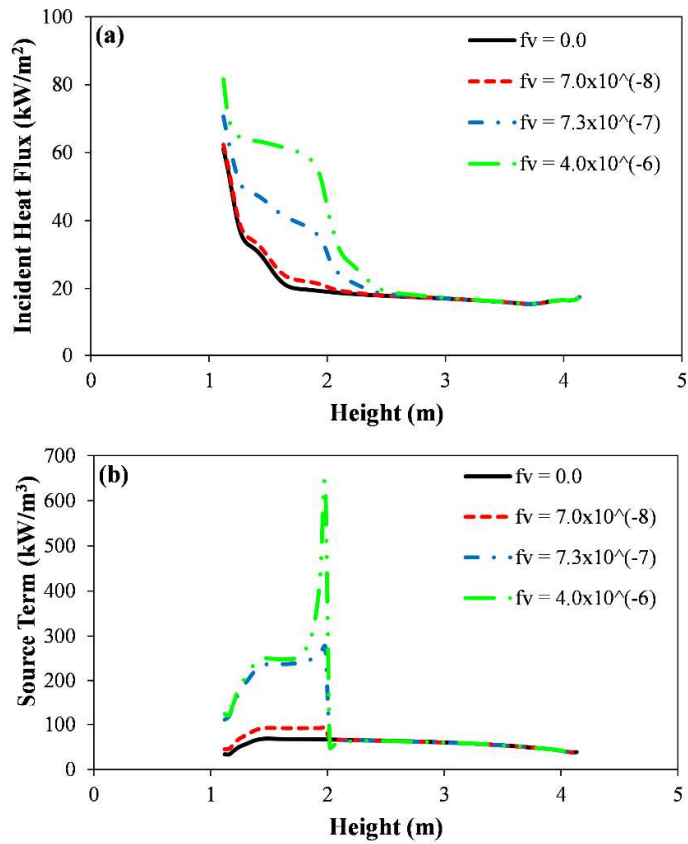
Figure 7.29. (a) Incident HF and (b) ST predictions of 3-D radiation code by utilizing different soot volume fractions

Table 7.26 Fractional contribution of soot particles to incident wall HFs and radiative sourve terms in the splash zone and the freeboard for different soot volume fractions

Soot Volume Fraction (f_v)	Contribution to ST		Contribution to HF	
	Splash Zone	Freeboard	Splash Zone	Freeboard
7.0×10^{-8}	0.26	0.10	0.07	0.03
7.3×10^{-7}	0.72	0.44	0.36	0.21
4.0×10^{-6}	0.76	0.50	0.53	0.35

Finally, RHT predictions of gray and non-gray radiative properties fly ash and soot particles are compared for the combustion tests carried out in the test rig where soot volume fraction is taken as 7.3×10^{-7}. Predicted HF and ST profiles using gray (Planck-mean) and non-gray radiative properties of fly ash and soot particles are illustrated in Figures 7.30(a) and 7.30(b), respectively. As shown by the figure and table, utilizing Planck-mean radiative properties for fly ash and soot particles instead of spectral properties does not produce any considerable error (1.93 % for incident HF and 4.85 % for ST) in RHT predictions for the test rig under investigation. For this purpose, it can be concluded that Planck-mean soot and fly ash radiative properties reduce CPU requirements of the solution of RTE for the test problem under consideration.
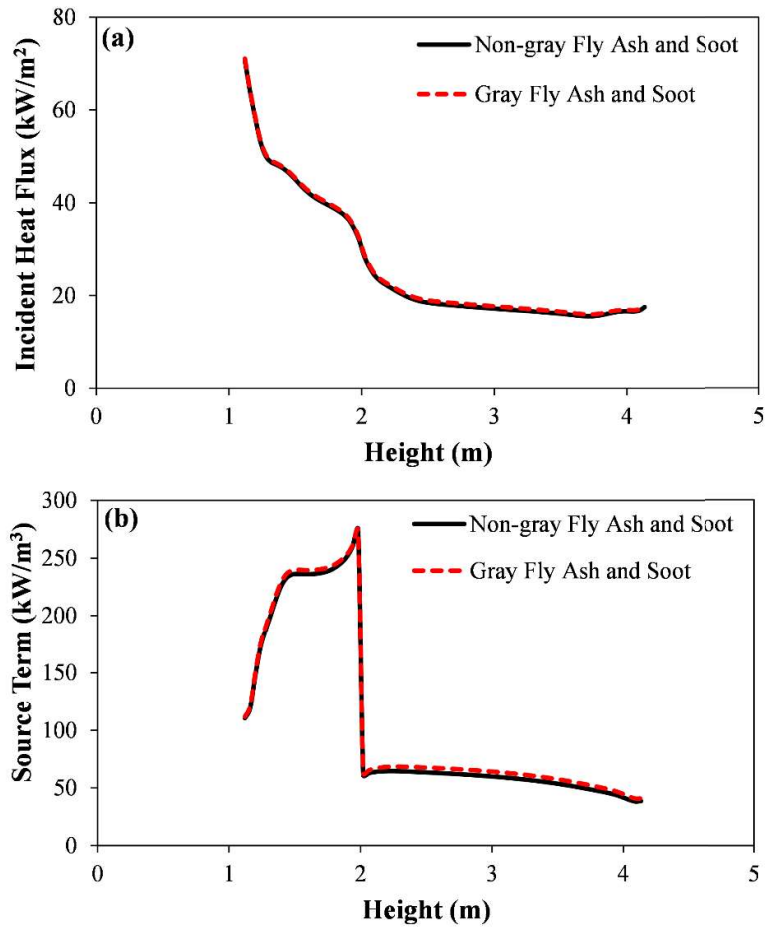
Figure 7.30. (a) Incident HF and (b) ST predictions of 3-D radiation code by utilizing gray (Planck-mean) and non-gray radiative properties fly ash and soot particles ($f_v = 7.3$ x 10^{-7})

7.4.3 Concluding Remarks for the Effect of Bag Filter and Cyclone Ashes

In this section, a parametric study carried out in a 1-D slab problem involving combustion gases and soot is carried out to reveal that soot particle diameter and number of soot particles in a soot aggregate do not significantly affect the net wall HF and ST predictions due to their insignificant effect on absorption coefficient. Later, the effect of soot on RHT is investigated in the freeboard of METU 0.3 MW_t

ABFBC test rig. It was found that the presence of soot particles in the splash zone of BFBCs significantly improves incident wall HFs and STs due to the combined effects of higher absorption coefficient of soot compared to fly ash particle in the wavelength range of 1 - 7 μm, which covers 85 % of the thermal radiation, and negligible scattering coefficient of soot throughout the entire thermal spectrum. Soot particles have been found to have a noticeable impact on RHT even at very low volume fractions based on a parametric study where different soot volume fractions, observed in different types of diffusion flames, are utilized. Planck-mean soot and fly ash particle properties are found to provide reasonably accurate RHT predictions for the freeboard of 0.3 MWt ABFBC test rig and can be used to improve the computational efficiency of the solution of RTE under these conditions.

7.5   Coupling of Radiation Model with the Transient System Model of ABFBC Firing Lignite

As mentioned before, none of the studies in the literature coupled a comprehensive transient system model for a BFBC with a sophisticated radiation model where RTE is explicitly solved in conjunction with conservation equations of other transport processes. BFBCs are characterized by the low particle load in the freeboard region. Furthermore, previous works regarding the heat transfer in FBCs state that RHT becomes significant when particle load is low [34,35]. Therefore, sufficiently accurate and computationally efficient-methods both for the solution of RTE and for the estimation of radiative properties of combustion gases, particles, and walls are necessary.

One aim of this thesis study is to couple a transient 1-D comprehensive system model for BFBC firing lignite with the 3-D radiation code using MOL solution of DOM coupled with robust radiative property models for combustion gases, particles, and walls. To accomplish such an objective, a comprehensive transient system model for METU 0.3 MW$_t$ ABFBC test rig, developed by Selcuk and Degirmenci [28] is chosen as basis. As the coupled BFBC system model requires input data obtained

249

from the steady-state BFBC system model, another objective of this study is to couple a steady-state 1-D system model for BFBC firing lignite with the same 3-D radiation code.

The performance of the coupled model is evaluated by comparing its predictions with the measurements of temperatures and concentrations of the species O_2, CO, and CO_2 along the combustor gathered from the test rig firing a typical Turkish lignite. Results of steady-state and transient combustion tests (Test 1) which were carried out in a previous study [28] are utilized as input data for application and validation of the model.

The details of the comprehensive transient 1-D BFBC system model are described in Chapter 4. In the solution of RTE, the S_6 scheme is used to discretize the angular domain whereas 11 x 11 x 80 grid points are employed to discretize the spatial domain. For the differencing of the spatial derivatives in MOL of DOM representation of RTE, three-point upwind differencing scheme, DSS014, is employed. The system of ODEs obtained after angular and spatial discretization is solved by the readily available ROWMAP code based on ROW-methods of order four (a class of linearly implicit Runge-Kutta methods) utilizing Krylov techniques for the solution of linear systems. All test are performed on a computer with Intel® Core™ i7-2600 CPU 3.40 GHz processor having 16.00 GB of RAM.

In the following sections, two different radiative property approaches are utilized in order to test the performances of different approaches. In the first approach which is labeled as 'present FBC model with spectral radiation model', gas radiative properties are determined using Bordbar's 10 band model [61] whereas spectral particle radiative properties are estimated by using Mie theory. On the other hand, in the second approach, 'present FBC model with SLW-1', spectral gas radiative properties are calculated using classical SLW-1 [81,82] whereas particle properties are taken to be gray. In both approaches, anisotropic scattering by particles is taken into account using transport approximation [119].

7.5.1 Results of the Combustion Test with Hot Refractory-Lined Walls

The predictive accuracy of the steady-state FBC system models coupled with and without radiation models is tested by comparing their temperature and gaseous emission predictions with the steady-state measurements obtained from a combustion test conducted in the test rig where Aydın lignite is fired. However, radiative HF predictions of the present model are not compared with the measurements as no measured radiative HF data is available for the combustion test under consideration. Fortunately, the spectral radiation models utilized in this study have already been validated against the incident HF measurements obtained in the same test rig where lignite is fired with and without fly ash recycling (see sections 7.1 and 7.2).

7.5.1.1 Validation Against Steady-State Measurements

Figure 7.31 compares the predictions and measurements of temperatures along the freeboard of the ABFBC test rig firing lignite. CPU requirements of FBC models with and without radiation models are shown in Table 7.27. As demonstrated by the figure, medium and wall temperature profiles predicted by all FBC models with and without radiation models are in reasonable agreement with the measurements. Using a sophisticated radiation code in conjunction with the system model of FBC does not significantly influence the temperature predictions for the combustion test under investigation. This insignificant difference in the temperature predictions of FBC models with and without radiation models is considered to be due to very low temperature difference between the medium and hot refractory-lined walls of the test rig which leads to low heat transfer rates in the freeboard section. However, RHT may become much more important in industrial and utility boilers where side walls are made up of cold membrane tube walls.

251
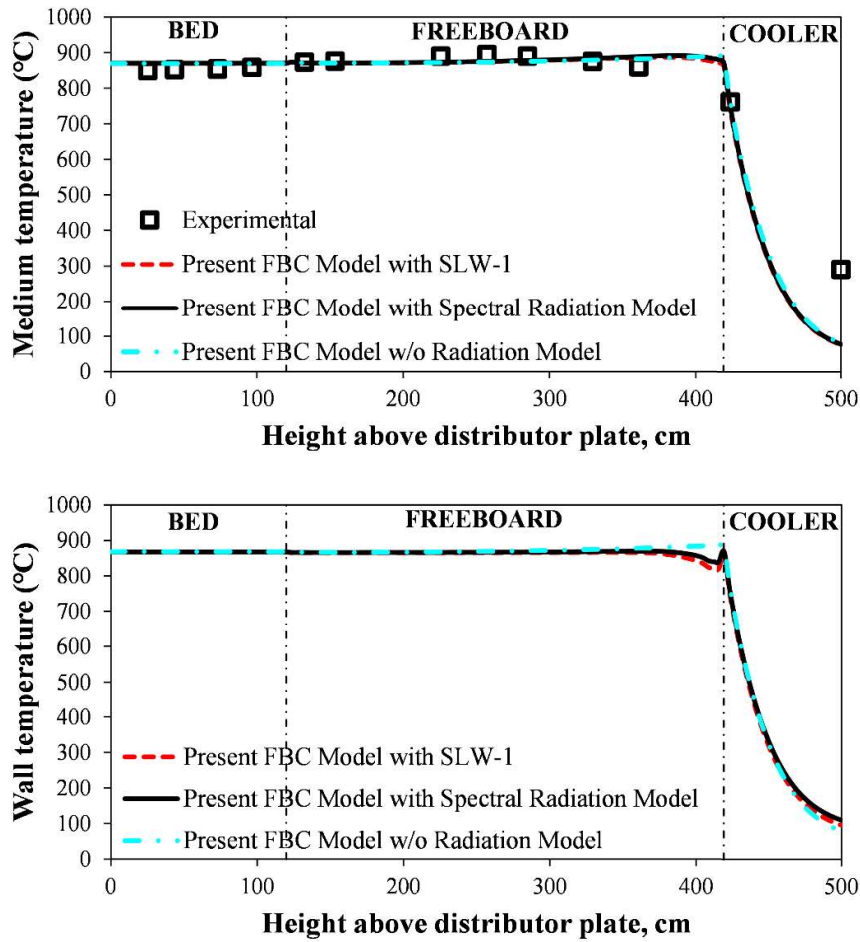
Figure 7.31. Medium and wall temperature profiles predicted by FBC models with and without radiation models under steady-state conditions

Table 7.27 CPU time requirements of the FBC models with and without radiation models under steady-state conditions

Present FBC model w/o radiation model	0.23 s
Present FBC model with SLW-1	2379 s
Present FBC model with spectral radiation model	13205 s

Figure 7.32 demonstrates the steady-state net HF, ST, emission term, and absorption term profiles along the freeboard predicted by FBC models with radiation model (note that ST = Emission − Absorption). As illustrated by the figure, net wall HF, centerline ST, centerline emission term, and centerline absorption term predictions of the present FBC model with spectral radiation model and present FBC model with SLW-1 are in reasonable agreement with each other. This is why temperature predictions of both coupled FBC models are quite similar as illustrated in Figure 7.31. Furthermore, freeboard centerline emission and absorption terms are similar in magnitude which indicates that re-absorption of thermal radiation is as significant as the emission for the test case under investigation. To conclude, SLW-1 model with gray particle and wall properties provides reasonable accuracy in the RHT predictions and thus in the temperature predictions along the freeboard of the test rig under investigation, and can be used to improve computational efficiency of the FBC models coupled with radiation models. Therefore, SLW-1 model with gray particle and wall properties will be utilized to estimate the radiative properties of particle-laden combustion gases in the freeboard of the test rig under investigation for the rest of this study.
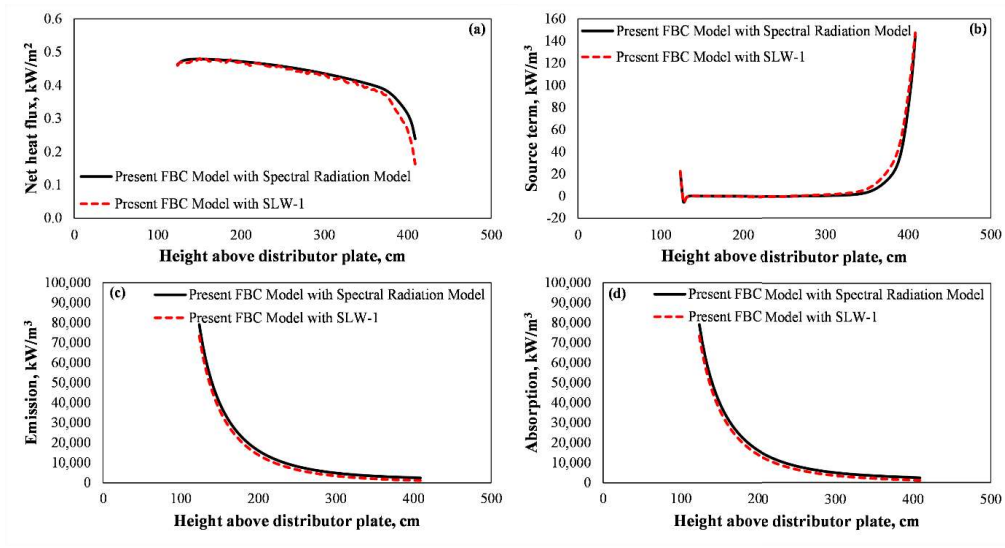
Figure 7.32. Predicted (a) net radiative HF, (b) centerline radiative ST, (c) centerline emission term and (d) centerline absorption term profiles under steady-state conditions for the combustion test where freeboard is bounded by hot refractory-lined walls (note that ST = Emission – Absorption)

Measurements and predictions of steady-state O_2, CO, and CO_2 concentrations along the combustor are illustrated in Figure 7.33. As demonstrated by the figure, measurements and predictions of the O_2, CO, and CO_2 concentrations for the combustion test under investigation are found to be in reasonable agreement. Utilization of a sophisticated radiation model coupled with a system model for FBC does not lead to any significant difference in the predictions of O_2, CO, and CO_2 emissions. This insignificant difference in the gaseous emission predictions is considered to be due to (i) insignificant deviations between the temperature profiles predicted by FBC models with and without radiation models (ii) combustion of the majority of the combustibles in the bed section.
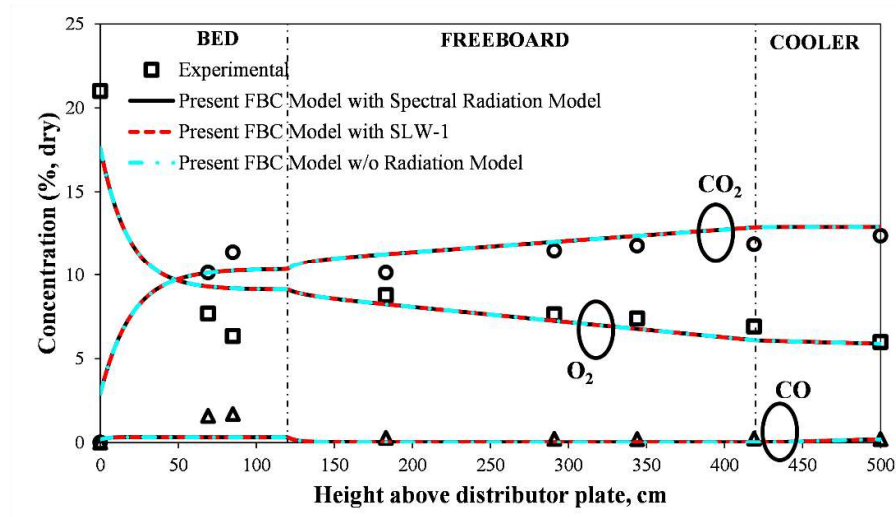
Figure 7.33. O_2, CO, and CO_2 concentration profiles predicted by FBC models with and without radiation models under steady-state conditions

7.5.1.2   Validation Against Transient Measurements

The dynamic performance of the test rig is tested through a combustion test where step changes are imposed on air flow rate and coal flow rate by keeping all other parameters constant (see Figure 6.2 and Table 6.7). The transient responses of temperatures, O_2 and CO concentrations at the freeboard exit on the step changes are investigated.

Figure 7.34 illustrates predicted and measured transient medium temperature profiles at the bed exit and at different freeboard heights (1.54 m, 2.57 m, 3.30 m, and 3.61 m). As demonstrated by the figure, all temperatures decrease until 840 s due to a step increase in the air flow rate between the time interval of 0 – 840 s (see Figure 6.2). Then, the air flow rate is suddenly reduced at 840 s, which leads to a gradual increase in the temperatures due to the introduction of less cold air into the system. At time is equal to 1200 s, a sudden decrease is imposed on the coal flow rate which results in a decrease in the temperatures due to low energy input to the system. Finally, the increase in the coal flow rate at 1400 s (see Figure 6.2) gradually increased the

temperature owing to the increase in the energy input to the system. It should be noted that the response of bed temperature and temperature at the beginning of the freeboard to step changes is more sluggish compared to that of freeboard temperature due to large thermal inertia of bed material and splashing particles at the beginning of the freeboard. Furthermore, the CPU times required for transient FBC model without radiation model and transient FBC model with SLW-1 for the test case under investigation are reported as 11061 s and 26640 s, respectively.
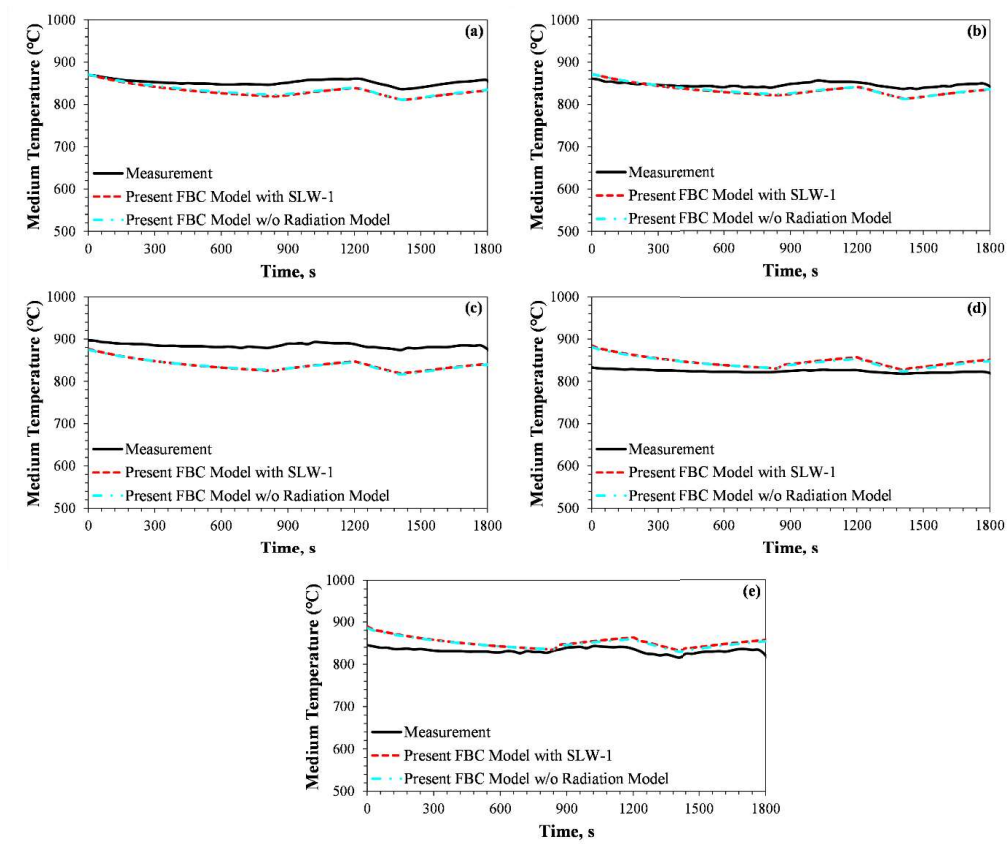
Figure 7.34. Predicted transient temperatures of (a) bed (b) freeboard at 1.54 m (c) freeboard at 2.57 m (d) freeboard at 3.30 and (e) freeboard at 3.61 m

Comparison of freeboard temperature predictions of FBC models with and without radiation model indicates that using a detailed radiation model does not significantly influence the temperature prediction in the test case under investigation. The reason behind the insignificant effect of using a detailed radiation model coupled with FBC

model on temperature predictions is that the freeboard of the test rig under investigation is bounded by hot refractory lined walls which makes the temperature difference and hence heat transfer in the freeboard insignificant.

Figures 7.35(a) and 7.35(b) demonstrate the individual contributions of radiation and convection in both freeboard wall and freeboard gas energy balances, respectively, for the combustion test where freeboard is bounded by hot refractory-lined walls. It should be noted that the terms in Figure 7.35 are taken as average along the freeboard height. As illustrated in Figure 7.35(a), radiative and convective HFs in the freeboard wall energy balance are similar in magnitude but opposite in direction which implies that radiation is as significant as convection in the wall energy balance. The opposite signs of convective and radiative HFs in wall energy balance are considered to be due to well-insulated freeboard side walls which consist of a combination of 6-cm-thick refractory bricks and 20-cm-thick insulation bricks and exposed to free convection from the outside. The heat transferred from the freeboard medium to the walls by convection is then transferred via radiation to colder bed surface, colder fly ash particles entrained from the bed and the cooling tubes at the exit of the freeboard. On the other hand, as demonstrated by Figure 7.35(b), convective heat transfer between particles and gases dominates the freeboard gas energy balance.
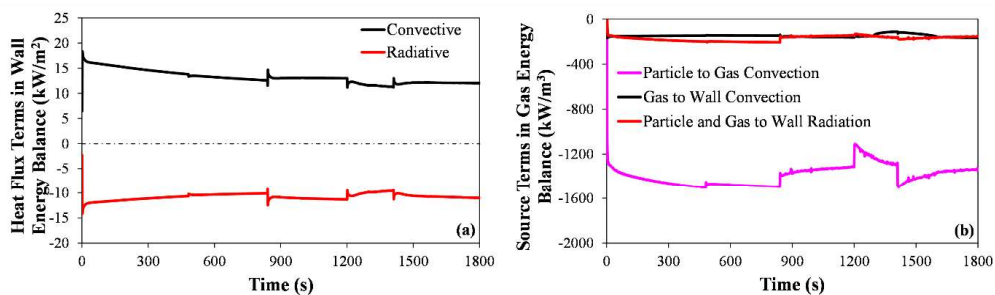
Figure 7.35. Individual contributions of radiation and convection in (a) freeboard wall and (b) freeboard gas energy balances

Predictions and measurements of transient O_2 concentrations at freeboard exit and CO concentrations at bed and freeboard exits for the combustion test under investigation are demonstrated by Figure 7.36. As can be noticed from the figure,

predictions of O_2 and CO concentrations agree reasonably with the measurements. On the other hand, utilization of a radiation model coupled with a system model for FBC does not lead to any significant difference in transient O_2 and CO concentrations. This insignificant difference in the concentration profiles is considered to be due to the fact that the majority of the combustibles are burned in the bed section owing to under bed feeding system of the test case under investigation.
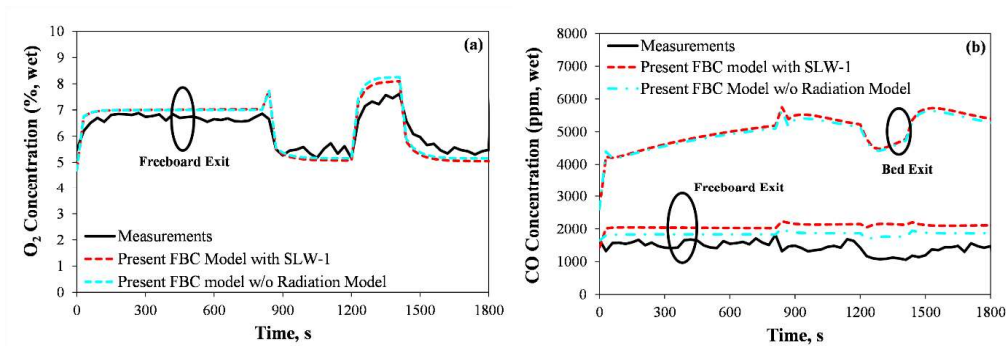
Figure 7.36. Predicted and measured transient (a) O_2 and (b) CO concentrations at freeboard exit

7.5.2   Results of the Combustion Test with Cold Water Walls

The findings reported in the previous section indicate that using a sophisticated radiation code in conjunction with the system model of the test rig, does not significantly influence the temperature predictions. This insignificant effect is due to the fact that the freeboard of the test rig is bounded by refractory-lined walls leading to very low temperature difference, and thus heat transfer rate between the surfaces and the medium. To test this hypothesis, a parametric study is carried out where hot refractory-lined side walls of the test rig are replaced with cold water walls at 537 K and with emissivity of thermally oxidized carbon steel as in utility or industrial boilers according to the experiments carried out in the 16 MW_t FBC in the Chalmers University of Technology [208,211]. Parameters, except the side wall temperatures

and side wall emissivities, are kept the same as those in Test 1. The results of this parametric study are summarized in the following sections.

7.5.2.1   Modeling of Steady-State Operation

Comparison of steady state medium temperature profiles predicted by FBC models with and without radiation models for the combustion test where freeboard is taken to be enclosed by cold water walls at 537 K is demonstrated by Figure 7.37. As illustrated by the figure, utilization of a sophisticated radiation model in conjunction with a BFBC system model significantly improves the accuracy of medium temperature predictions. On the other hand, temperature predictions of present FBC model with spectral radiation model and present FBC model with SLW-1 are in reasonable agreement with each other. Furthermore, CPU times recorded for all FBC models with and without radiation models, which is listed in Table 7.28, indicate that present FBC model with SLW-1 requires one order of magnitude less CPU time compared to FBC model with spectral radiation. Therefore, SLW-1 model with gray particle and wall properties provides reasonable accuracy in the temperature profiles along the freeboard of the test rig under investigation, and can be used to decrease CPU demands of the FBC models coupled with radiation models. For this purpose, SLW-1 model with gray particle and wall properties will be utilized to estimate the radiative properties of particles and combustion gases in the freeboard of the test rig under investigation for the rest of this study.
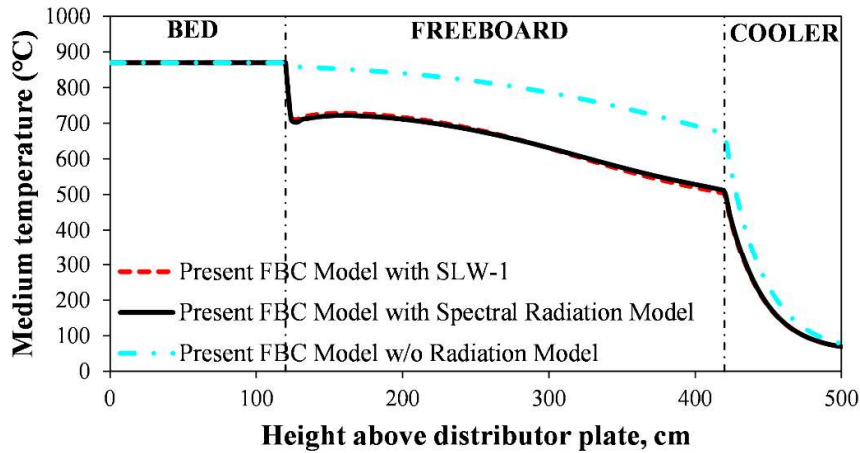
Figure 7.37. Medium temperature profiles predicted by FBC models with and without radiation models for the combustion test where freeboard is bounded by cold water walls at 537 K

Table 7.28 CPU time requirements of the FBC models with and without radiation models for the combustion test where freeboard is bounded by cold water walls at 537 K under steady-state conditions

Present FBC model w/o radiation model	0.23 s
Present FBC model with SLW-1	510 s
Present FBC model with spectral radiation model	3841 s

Figure 7.38 demonstrates the steady-state net HF, ST, emission term, and absorption term profiles along the freeboard predicted by FBC models with radiation model (note that ST = Emission − Absorption) for the combustion test where freeboard is bounded by cold water walls at 537 K. As the figure demonstrate, net wall HF, centerline ST, centerline emission term, and centerline absorption term predictions of present FBC model with SLW-1 reasonably agree with the those predicted by present FBC model with spectral radiation model. Similar to the results for the combustion test where freeboard is bounded by hot refractory-lined walls (see Figure

260

7.32), freeboard centerline emission and absorption terms are similar in magnitude. Therefore, SLW-1 model with gray particle and wall properties can also be utilized for the prediction of RHT in BFBCs bounded by cold water walls.
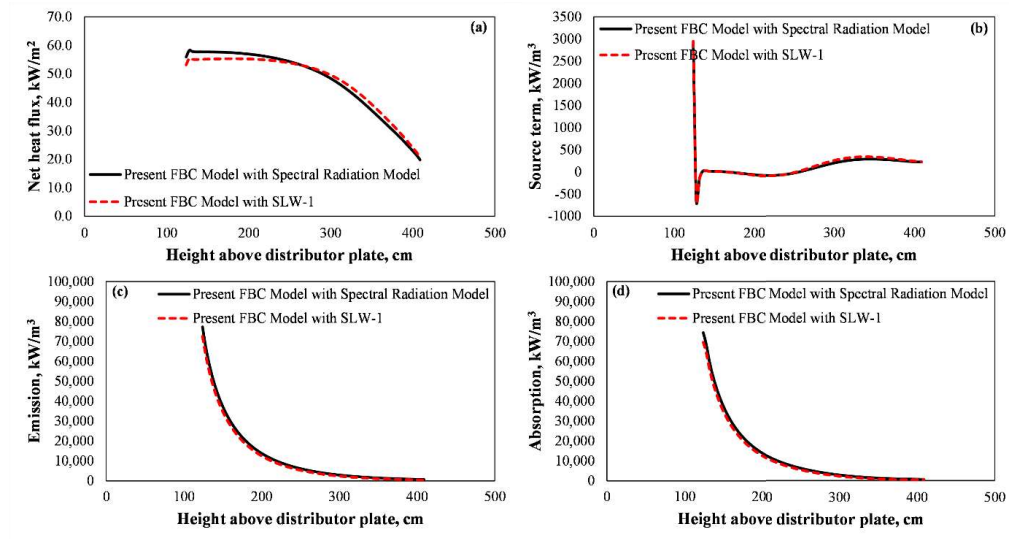
Figure 7.38. Predicted (a) net radiative HF, (b) centerline radiative ST, (c) centerline emission term and (d) centerline absorption term profiles under steady-state conditions for the combustion test where freeboard is bounded by cold water walls at 537 K (note that ST = Emission − Absorption)

Predicted steady-state O_2, CO, and CO_2 emissions of the combustor are shown in Table 7.29. As can be noticed from the table, reasonable agreement is achieved between the O_2, CO, and CO_2 emissions predictions of the FBC models with and without radiation models for the combustion test under investigation. Utilization of a sophisticated radiation model coupled with a system model for FBC does not lead to any significant difference in the predictions of O_2 and CO_2 emissions. This insignificant difference in the gaseous emission of O_2 and CO_2 is due to combustion of the majority of the combustibles in the bed section. However, the use of a radiation model remarkably increases CO emission as the present FBC model with SLW-1 predicts lower freeboard temperatures compared to the present FBC model without a radiation model leading to low CO oxidation rates in the freeboard. Furthermore, although the present FBC model does not consider nitrogen oxides formation and

reduction, nitrogen oxides chemistry in the FBC is known to be strongly dependent on the temperature, which indicates that difference in the temperature predictions of the FBC models with and without radiation models may lead to significant difference also in the nitrogen oxides emissions.

Table 7.29 Predicted gaseous emissions of the species O_2, CO_2 and CO for the combustion test where freeboard is bounded by cold water walls at 537 K

Species	Present FBC model w/o radiation model	Present FBC model with spectral radiation model	Present FBC model with SLW-1
O_2 (% wet)	5.39	5.47	5.47
CO_2 (% wet)	11.74	11.59	11.58
CO (% wet)	0.22	0.35	0.36

7.5.2.2   Modeling of Transient Operation

The dynamic response of the combustion test with cold water walls is also investigated on the combustion test where step changes imposed on coal and air flow rates as given in Figure 6.2. Figure 7.39 illustrates predicted transient medium temperature profiles at different freeboard heights (1.54 m, 2.57 m, 3.30 m, and 3.61 m) for the combustion test where freeboard is bounded by cold water walls at 537 K. As illustrated by the figure, bed temperatures decrease until 840 s due to a step increase in the air flow rate (see Figure 6.2). However, freeboard temperatures increase suddenly at the beginning due to an increase in the freeboard particle load (see Figure 7.40) caused by the higher superficial gas velocity. It should be noted that freeboard particles are assumed to be at their temperatures at the bed and thus heat the freeboard medium. Then, the freeboard temperature decreases gradually between the time interval of $0 - 840$ s. At 840 s, the air flow rate is suddenly reduced,

which leads to a gradual increase in the bed temperatures due to the introduction of less cold air into the system. The freeboard temperatures, on the other hand, decrease suddenly at 840 s due to a sharp decrease in the freeboard particle load as illustrated in Figure 7.40. After the sharp decrease, the freeboard temperatures start to increase gradually during the same time interval as bed temperature. After 1200 s, similar to the combustion test with hot refractory-lined walls, the bed and freeboard temperatures of the test with cold water walls first gradually decrease and then gradually increase due to the step changes imposed on the coal flowrates. Furthermore, the CPU times required for transient FBC model without radiation model and transient FBC model with SLW-1 for the combustion test where freeboard is bounded by cold water walls at 537 K are reported as 8830 s and 24846 s, respectively.
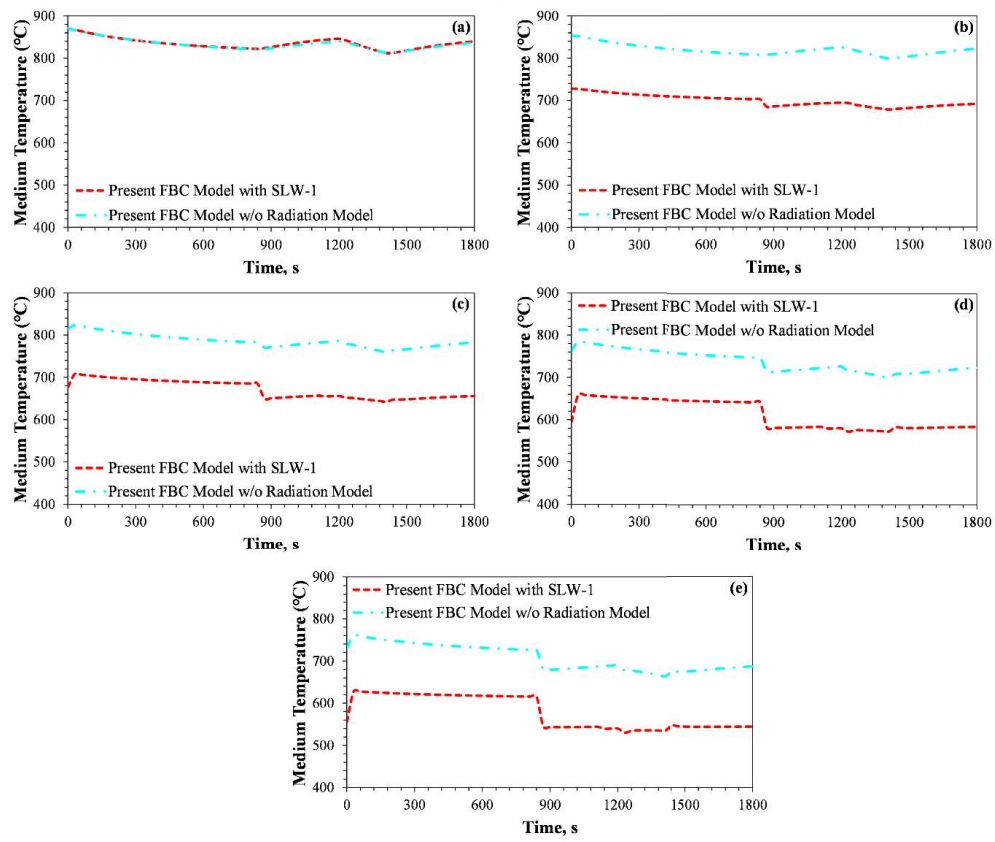
Figure 7.39. Predicted transient temperatures of (a) bed (b) freeboard at 1.54 m (c) freeboard at 2.57 m (d) freeboard at 3.30 and (e) freeboard at 3.61 m for the combustion test where freeboard is bounded by cold water walls at 537 K
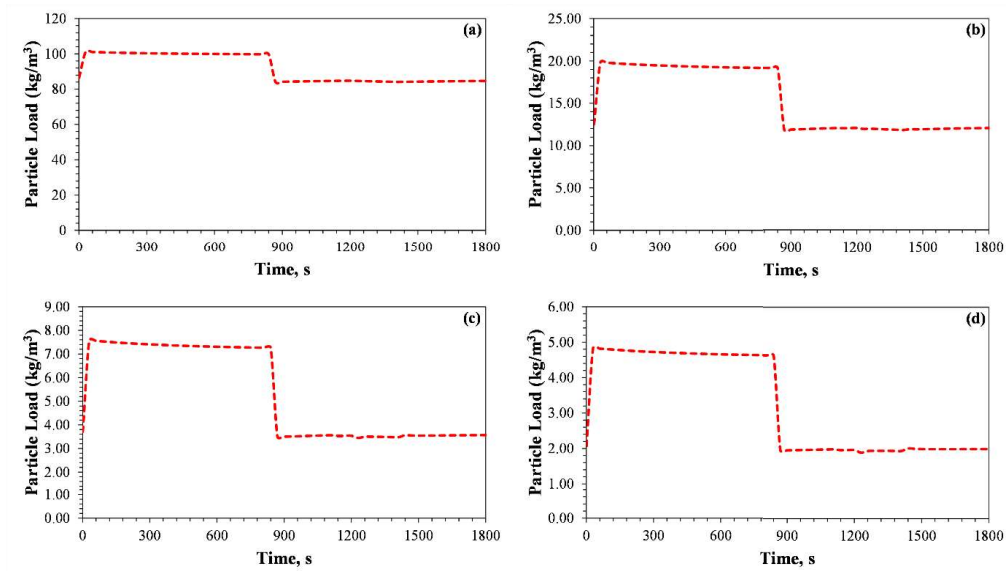
Figure 7.40. Predicted transient freeboard particle load (a) 1.54 m (b) 2.57 m (c) 3.30 m and (d) 3.61 m

The individual contributions of radiation and convection in freeboard gas energy balance for the combustion test with cold water walls are demonstrated by Figure 7.41. As demonstrated by the profiles, both convective and radiative heat transfer plays a significant role in freeboard heat transfer. To conclude, both accurate and computationally efficient models are necessary for modeling RHT in BFBCs. Unlike the results reported in Figure 7.35, convective heat transfer rate between the particles and gas is positive for the combustion test with cold water walls. This finding shows that the freeboard gas is heated by the hot particle leaving the bed at their temperatures in bed.
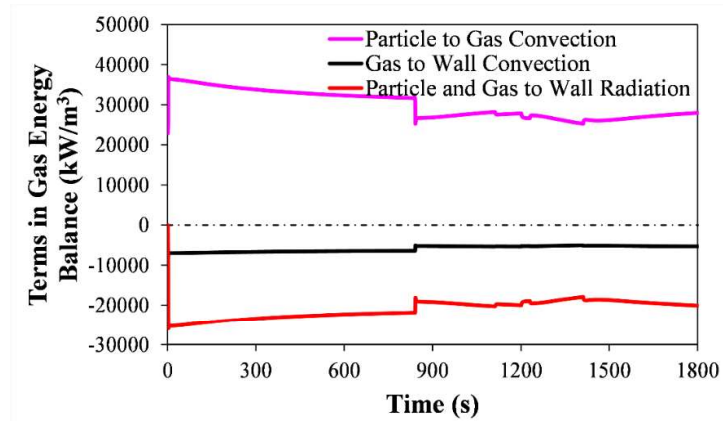
Figure 7.41. Individual contributions of radiation and convection in freeboard gas energy balance for the combustion test where freeboard is bounded by cold water walls at 537 K

Predicted transient O_2 and CO concentrations at freeboard exit for the combustion test under investigation are demonstrated by Figure 7.42. As demonstrated by the figure, using a sophisticated radiation significantly increases the CO concentrations.
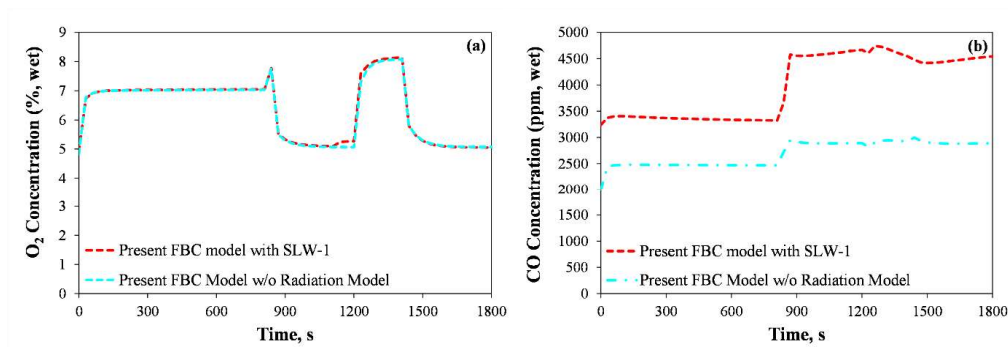
Figure 7.42. Predicted and measured transient (a) O_2 and (b) CO concentrations at freeboard exit for the combustion test where freeboard is bounded by cold water walls at 537 K

266

7.5.3 Concluding Remarks for the Coupling of Radiation Model with the Transient System Model

Utilization of a sophisticated radiation model, where RTE is explicitly solved in conjunction with the system model for 0.3 MW_t ABFBC test rig instead of using Stefan-Boltzmann law and an empirical correlation for the RHT coefficient, does not significantly influence the freeboard temperature predictions for the test case where freeboard is bounded by hot refractory-lined walls. This insignificant effect is considered to be due to the low temperature difference between the refractory-lined walls and the freeboard medium leading to low heat transfer rates in the freeboard. However, the deviation between the freeboard temperature predictions of the FBC models with and without a sophisticated radiation model is remarkable for the combustion test where freeboard is taken to be enclosed by cold water walls at 537 K. Based on the outcomes obtained from the coupled steady-state FBC system model and 3-D radiation model, a combination of SLW-1 for spectral gas properties, Mie theory for gray fly ash particle properties and gray wall properties provides sufficiently accurate HF, ST and freeboard temperature predictions with a significant saving in the CPU requirement in the coupled solution of RTE. Therefore, the combination of SLW-1 for spectral gas properties, Mie theory for gray fly ash particle properties and gray wall properties can be utilized to improve CPU efficiency of the coupled solution of RTE in BFBCs. O_2 and CO_2 emissions are not considerably affected by the use of radiation code in conjunction with the system model for BFBC for the combustion test under investigation as majority of the combustibles are burned in the bed section. However, CO emission predictions increase by the use of the radiation model coupled with BFBC model due to lower freeboard temperature predictions leading to low CO oxidation rates in the freeboard. The present transient FBC models coupled with the 3-D radiation model based on MOL of DOM utilizing SLW-1 model for combustion gases and gray radiative properties for particles and walls predicts accurately the transient responses of temperatures and O_2 and CO emissions on step changes imposed to coal and air flow

rates for the combustion test with hot refractory-lined walls and with cold water walls.

7.6 Coupling of Radiation Model with the Steady-State System Model of ABFBC Co-Firing Lignite with Cotton Residue

There is only a few number of BFBC studies coupling the solution of RTE with the solutions of other conservation equations. None of them couples a comprehensive BFBC system model with a radiation model utilizing spectral property estimation techniques for gases, particles, and walls. However, several studies involving radiation models in isolation from system models of FBCs indicate that [44,45,57,91] deployment of gray properties instead of spectral ones may lead to remarkable inaccuracies in the RHT predictions which directly influence temperature profiles. In the previous section, steady-state and transient BFBC models is coupled with a spectral radiation model for the combustion of lignite. However, when co-firing coal with biomass and limestone addition in fluidized beds, the number of fine particles in the freeboard increases [36,37]. Therefore, RHT may become more important in such cases as fine particles interact with radiation more than coarse particles owing to their high projected surface area. Moreover, coupled steady-state and transient BFBC models in the previous section do not consider the formation and reduction of NO and N_2O which is an important issue due to the high nitrogen content of CR [18].

Hence, another aim of this thesis study is to couple a 1-D comprehensive BFBC system model for co-firing lignite/CR blend with limestone addition with 3-D spectral and gray radiation models utilizing MOL of DOM and evaluate the performance of the coupled model against the original FBC model without coupling and measurements. To achieve this objective, a 1-D comprehensive model for METU 0.3 MW_t ABFBC test rig developed earlier by Selcuk and co-workers [18,92–97] is chosen as a basis.

The performance of the present coupled model is evaluated by comparing their predictions of temperature profiles and gaseous emissions (i) with those of the original FBC model without coupling and (ii) with in-situ measurements obtained from the test rig co-firing low-quality Turkish lignite, namely Çan lignite, with CR and limestone addition which is referred to as Test 8. The results of a co-combustion test (Test 8) that was conducted in an earlier study [8] are utilized for the application and validation of the system model.

The details of the comprehensive 1-D BFBC system model for co-firing of lignite and CR is described in Chapter 3. In the solution of RTE, S_6 scheme is used to discretize the angular domain whereas 11 x 11 x 82 grid points are employed to discretize the spatial domain. For the differencing of the spatial derivatives in MOL of DOM representation of RTE, three-point upwind differencing scheme, DSS014, is employed. The system of ODEs obtained after angular and spatial discretization is solved by the readily available ROWMAP code [105], based on ROW-methods of order four (a class of linearly implicit Runge-Kutta methods) utilizing Krylov techniques for the solution of linear systems. All tests are performed on a computer with Intel® Core™ i7-2600 CPU 3.40 GHz processor having 16.00 GB of RAM.

In the following sections, two different radiative property approaches are utilized in order to test the performances of different approaches. In the first approach which is labeled as 'FBC model with spectral radiation model', gas radiative properties are determined using Bordbar's 10 band model [61] whereas spectral particle radiative properties are estimated by using Mie theory. On the other hand, in the second approach, 'present FBC model with gray radiation model', gray gas radiative properties are calculated using gray wide band (GWB) model whereas Mie solution at $\lambda = 3$ μm are utilized as the gray particle radiative properties. In both approaches, anisotropic scattering by particles is taken into account using transport approximation [119].

The coupled FBC models are validated against experimental temperature profiles and gaseous emissions measured in a co-combustion test previously carried out in

the same test rig under consideration. Yet, the radiative HF field predicted by the FBC models is not validated against any experimental data since radiative HFs are not measured during the co-combustion test under investigation. However, validation of the spectral radiation model against measured incident HFs for the same test rig firing lignite is already available in sections 7.1 and 7.2.

Before comparing the temperature, RHT, and concentration predictions of the FBC models with the measurements, the particle load predictions of the present FBC model are compared to the particle load deduced from the experimental measurements carried out in the test rig as shown in Figure 7.43. As illustrated by the figure, experimental particle load data cannot be predicted by the FBC models without multiplying the decay constant expression of Choi et al. [148] [Eq. (3.8)] with 4.2. The reason behind the discrepancy between the experimental particle load and the particle load calculated by the original expression of Choi et al. [148] is considered to be due to the fact that the expression of Choi et al. [148] is originally developed for sand bed particles. However, in this study, the bed material is the ashes of lignite and CR.
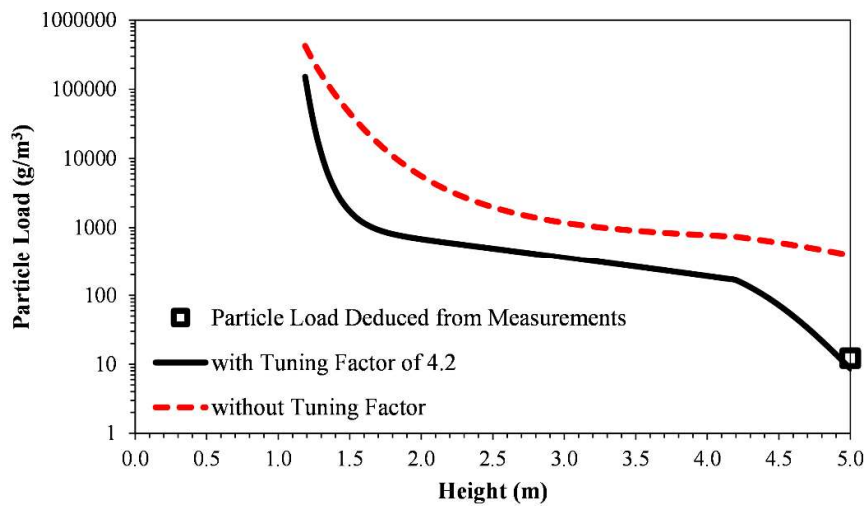
7.43. Particle load distribution along the combustor with and without multiplication of the decay constant [Eq. (3.8)] with a tuning factor of 4.2 for Test 8

Net wall HF and the centerline ST predictions of both gray and spectral models are compared in Figure 7.44. Gray radiation model underestimates the net wall HFs while ST predictions do not significantly deviate from those of the spectral radiation model.
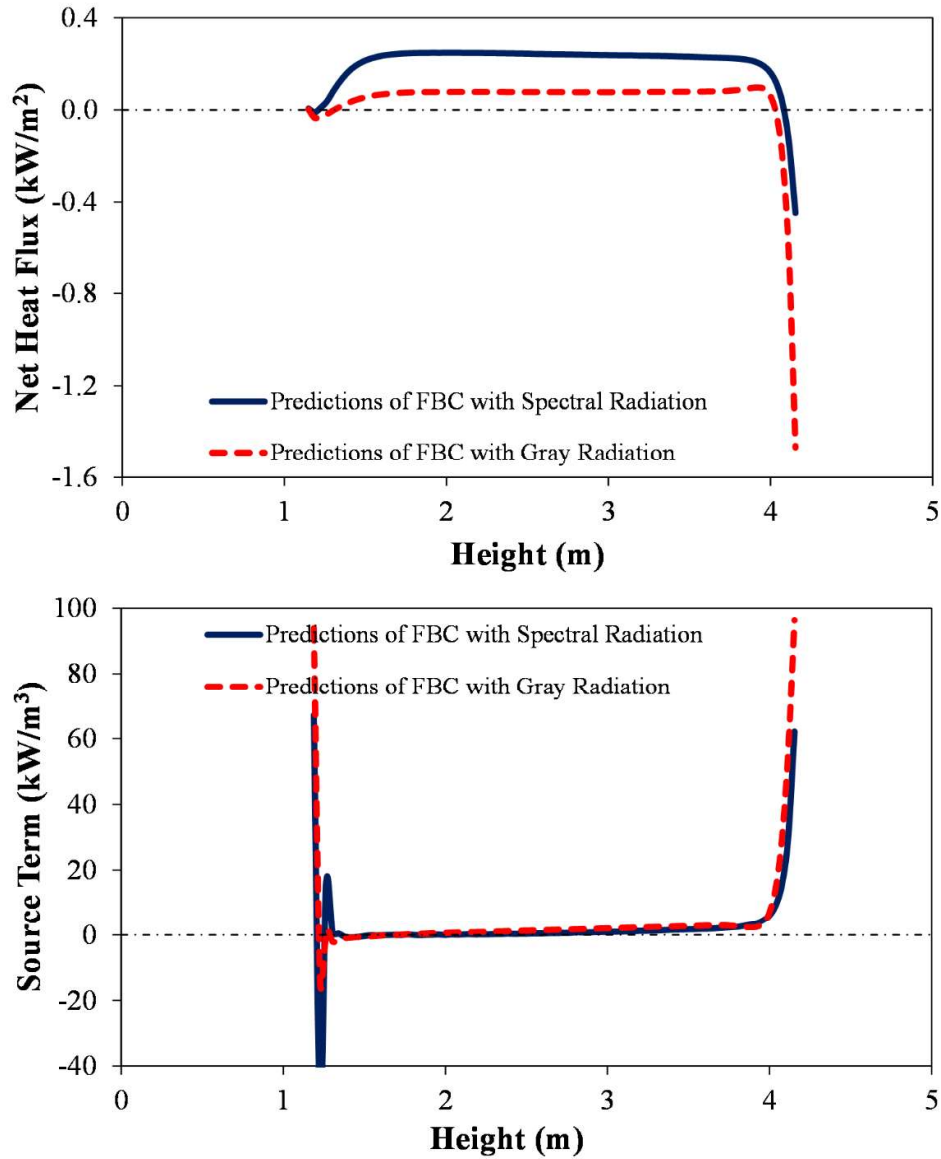
Figure 7.44. Net wall HF and the centerline ST predictions obtained by FBC system models coupled with gray and spectral radiation models for Test 8

Figure 7.45 shows the validation of temperature predictions of the FBC models against the measurements obtained from the test case under consideration. As shown by the figure, the deviation between the temperature profiles predicted by present and coupled FBC models is the highest at the end of the freeboard (up to 40 ℃ temperature difference) due to the existence of cooling surfaces at the end of the freeboard. FBC model coupled with spectral RTE model provides the most accurate freeboard temperature profiles with an average of 18.9 ℃ temperature difference from the measurements. The freeboard temperature predictions of the FBC model coupled with gray RTE model and the present FBC model deviate approximately 49.2 ℃ and 40.7 ℃ from the measurements, respectively. This slight difference between the accuracies of all FBC models with and without radiation model is due to the lower rate of freeboard heat transfer caused by a small temperature difference between the freeboard medium and enclosing side walls made up of refractory. Nevertheless, the effect of RHT on the temperature predictions of FBC models may be more crucial in industrial furnaces where freeboard side walls are cold membrane tube walls as can be seen in a previous work conducted on the same test rig [212]. The CPU requirement of the present FBC model is 185 s. On the other hand, the FBC model coupled with spectral and gray RTE models requires approximately 250 and 20 times higher CPU time than the present FBC model, respectively.
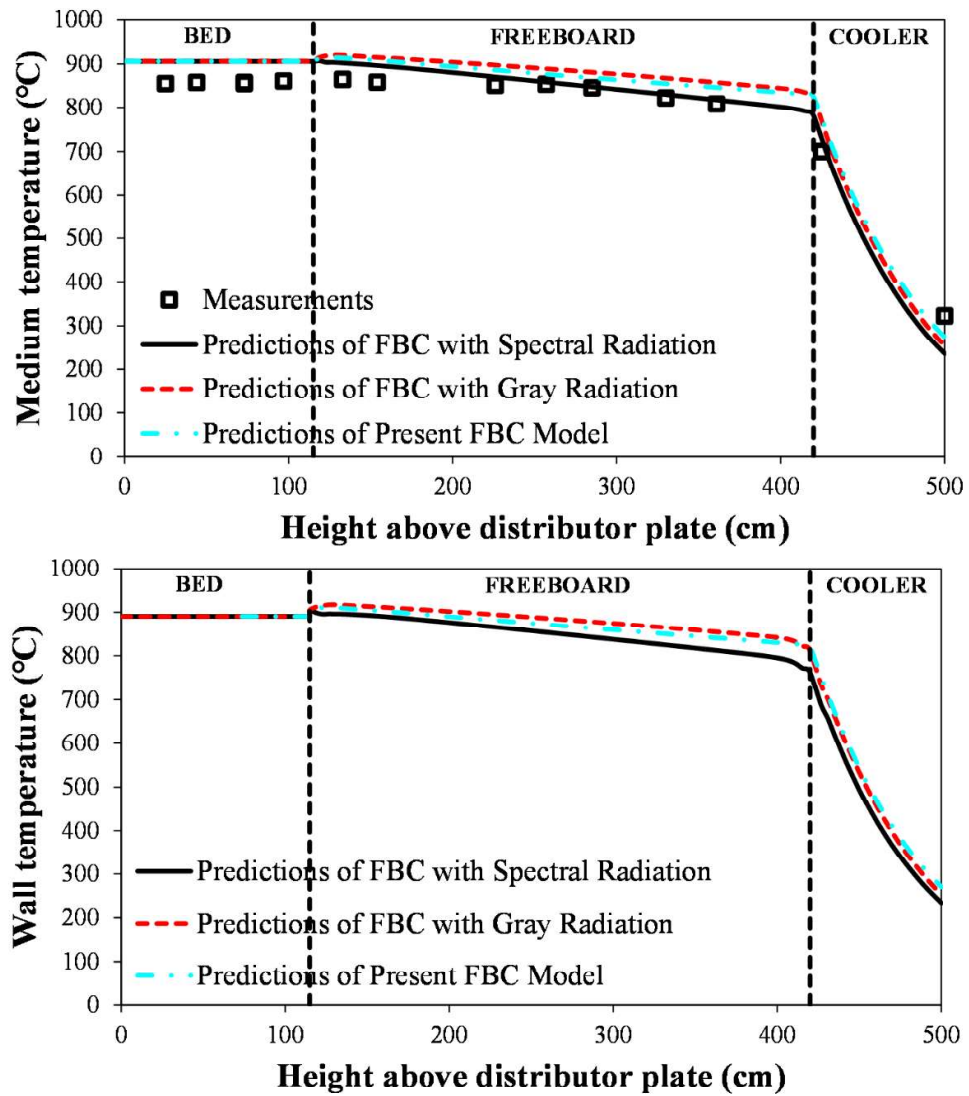
Figure 7.45. Medium and wall temperature predictions obtained by original FBC model and coupled FBC models for Test 8

Comparison between the radiative and convective STs and HFs and freeboard energy conservation equations for the test case under investigation is demonstrated in Figure 7.46. It should be highlighted at this point that ST and HF values for radiation and convection given in Figure 7.46 are obtained from the FBC model coupled with spectral radiation model. The negative values of ST profiles demonstrated in Figure 7.46(a) indicate that the direction of convective and radiative heat transfer is from the medium to the walls. Based on the comparison between the magnitudes of radiative and convective STs given in Figure 7.46(a), it can be concluded that the radiative ST is important at the beginning of freeboard due to the existence of splashing particles and the end of the freeboard due to existence of cooling module. Furthermore, the contribution of radiation to wall HFs is as significant as that of convection as shown in Figure 7.46(b). At the end of the freeboard, net wall radiative HFs (= incoming radiative HF to the side walls – outgoing radiative HF from the side walls) become negative. This effect is considered to be due to the existence of the cooling module at the end of the freeboard leading to higher outgoing radiative HFs from the side walls. In conclusion, significant contribution of radiative STs and wall HFs on freeboard heat transfer at the top of the freeboard due to cold surfaces provided by the cooling module indicates that radiation may have a significant contribution to freeboard heat transfer in industrial furnaces where freeboard is bounded by cold membrane tube walls instead of refractory.

Figure 7.46. Individual contributions of spectral radiation and convection in (a) freeboard gas (b) freeboard wall energy balances for Test 8

The influence of combustion gases and particles to total RHT in the test case under consideration are estimated by implementing the same spectral code without coupling it with the FBC model by discarding the effect of particles on radiation. Therefore, the radiative properties of the particles are taken to be zero whereas the rest of the parameters of the spectral radiation code are kept the same. Then, the individual contribution of gas radiation can simply be found by the ratio of STs without particles to the STs both with particles and combustion gases. The individual contributions of particles and gases to thermal radiation are calculated as 79 % and

21 %, respectively. The reason behind the high contribution of particles to the RHT in the freeboard is the existence of the splashing region where particle load is high due to bursting bubbles. However, in the upper part of the freeboard (between 2.5 m and 4.2 m), the individual contributions of particle and gas radiation are calculated as 26 % and 74 %, respectively. These findings indicate that both particles and combustion gases contribute to RHT in the co-combustion. Therefore, accurate methods for both particle and gas radiative properties are needed for co-combustion applications in BFBCs.

Measurements and predictions of the gaseous emissions for the co-combustion test are listed in Table 7.30. As shown by the table, all FBC models provide reasonable gaseous emission predictions. Implementation of spectral or gray RHT models to the FBC model under consideration does not significantly improve the accuracies in gaseous emission predictions. Furthermore, the slight difference between the gaseous emissions predicted by the FBC system models with and without radiation is caused by the burning of the majority of combustibles in the bubbling bed.

Table 7.30 Predicted and measured gaseous emissions for Test 8

Species	Present FBC model	FBC model with gray radiation	FBC model with spectral radiation	Measurement
O_2 (% dry)	5.2	5.2	5.3	5.1
CO_2 (% dry)	14.5	14.5	14.3	15.3
CO (% dry)	0.05	0.06	0.06	0.06
SO_2 (ppm dry)	603	603	606	486
NO (ppm dry)	289	289	290	285
N_2O (ppm dry)	84	82	92	60

7.6.1 Concluding Remarks for the Coupling of Radiation Model with the Steady-State System Model for Co-Combustion

After successfully coupling the 3-D radiation model using MOL of DOM with the steady-state system model for the bubbling fluidized bed co-combustion of lignite and CR, it was found that using a sophisticated radiation model coupled with FBC system model provides slightly more accurate temperature predictions for the freeboard of the ABFBC test rig where Çan lignite is co-fired with CR and limestone addition. The temperature predictions of FBC models coupled with spectral and gray radiation models do not significantly differ for the co-combustion test under investigation. This slight difference is considered to be due to low temperature difference between the medium and the hot refractory-lined walls leading to low heat transfer rate in the freeboard section. At the lower part of the freeboard, the radiation is dominated by particles due to splashing particles whereas radiation is dominated by combustion gases at the upper part of freeboard. Thus, accurate methods for the estimation of spectral radiative properties of both combustion gases and particles are needed. Utilization of a radiation model coupled with the system model for BFBC cofiring lignite with CR and limestone addition does not provide any further accuracy in the predictions of gaseous emission of the species O_2, CO_2, CO, SO_2, NO and N_2O for the co-combustion test under consideration due to combustion of the majority of combustibles in the bed section owing to under bed feeding system.

7.7 Effect of Freeboard Particle Energy Balance on the Coupled Steady-State Model of ABFBC Co-Firing Lignite with Cotton Residue

In this section, the predictions of comprehensive 1-D BFBC system model for co-combustion of lignite/CR blend by solving the freeboard particle energy balance equations are compared with the same model without solving the freeboard particle energy balance. The predictive performances of those models are evaluated by applying them to the test rig co-firing low-quality Turkish lignite, namely Çan

lignite, with CR and limestone addition which is referred to as Test 8. The results of a co-combustion test (Test 8) that was conducted in an earlier study [8] are utilized for the application and validation of the system model.

The details of the comprehensive 1-D BFBC system model for co-combustion of lignite/CR blend by solving the freeboard particle energy balance equations is described in Chapter 3. In the solution of RTE, S_6 scheme is used to discretize the angular domain whereas 11 x 11 x 82 grid points are employed to discretize the spatial domain. For the differencing of the spatial derivatives in MOL of DOM representation of RTE, three-point upwind differencing scheme, DSS014, is employed. The system of ODEs obtained after angular and spatial discretization is solved by the readily available ROWMAP code [105], based on ROW-methods of order four (a class of linearly implicit Runge-Kutta methods) utilizing Krylov techniques for the solution of linear systems. All test are performed on a computer with Intel® Core™ i7-2600 CPU 3.40 GHz processor having 16.00 GB of RAM.

In the following sections, two different radiative property approaches are utilized. In the first one which is the FBC model with spectral radiation model, gas radiative properties are determined using Bordbar's 10 band model [61] whereas spectral particle radiative properties are estimated by using Mie theory. On the other hand, in the second one, 'present FBC model with gray radiation model', gray gas radiative properties are calculated using gray wide band (GWB) model whereas Mie solution at $\lambda = 3$ μm are utilized as the gray particle radiative properties properties. In both approaches, anisotropic scattering by particles is taken into account using transport approximation [119].

7.7.1   Results of the Combustion Test with Hot Refractory-Lined Walls

The performance of the FBC system models by solving freeboard particle energy balance and in conjunction with the radiation models and is first tested by comparing their temperature and gaseous emission predictions with the measurements obtained

from a combustion test conducted in METU 0.3 MWt ABFBC test rig where Çan lignite is fired with CR and limestone addition where freeboard is bounded by hot refractory-lined walls.

Figure 7.47 illustrates radiative properties of combustion gases, fly ash, coal char and biomass char particles along the freeboard height predicted by FBC models with spectral and gray radiation models. It should be noted at this point that, the reported radiative properties predicted by FBC models with spectral radiation model are spectrally averaged values. As demonstrated by the figure, particle radiative properties predicted by FBC models with spectral (solid lines) and gray radiation (dashed lines) are in reasonable agreement whereas gray and spectral radiative properties of combustion gases are remarkably different. Furthermore, properties of fly ash particles are significantly higher than those of char particles as expected. Absorption coefficient of the combustion gases is higher than that of fly ash particles at the upper region of freeboard while fly ash particles dominate absorption of thermal radiation in the lower parts of the freeboard due to high concentration of splashing particles in this region.
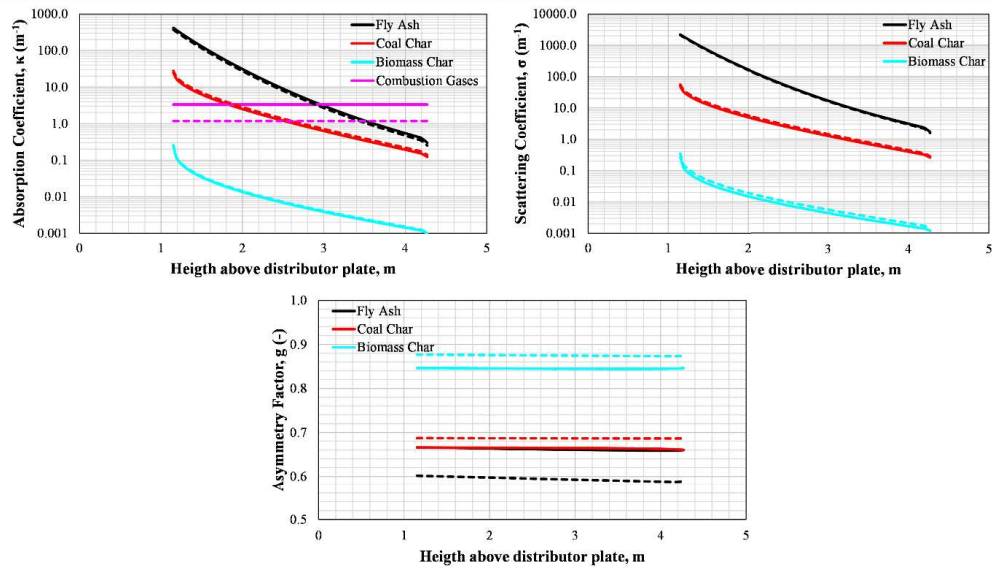
Figure 7.47. Radiative properties of combustion gases, fly ash, coal char and biomass char particles along the freeboard height predicted by FBC models with spectral and gray radiation models for Test 8 (solid lines: predictions of FBC models with spectral radiation; dashed lines: predictions of FBC models with gray radiation)

Figure 7.48 compares the predicted and measured gas, char, biomass char, ash, and wall temperatures along the combustor. Furthermore, predictions of the present FBC model without freeboard particle energy balance (labeled as 'Present FBC Model w/o FPEB) are also illustrated in Figure 7.48. It should be noted that present FBC model without FPEB assumes that ash particles' temperature is equal to their temperature in the bed whereas char particles' temperature is equal to freeboard temperature. As illustrated by the figure, all FBC models with and without radiation provide reasonable predictions for freeboard temperatures. Only char particle temperature predictions of the FBC system models with gray and spectral radiation models differ remarkably from those of the present FBC model without radiation. The difference in the temperature predictions along the cooler region is due to the fact that no radiation model is applied to the cooler region in the FBC system model

280

with gray radiation model. Finally, the present FBC model without FPEB provides reasonable temperature predictions as highlighted by the figure.
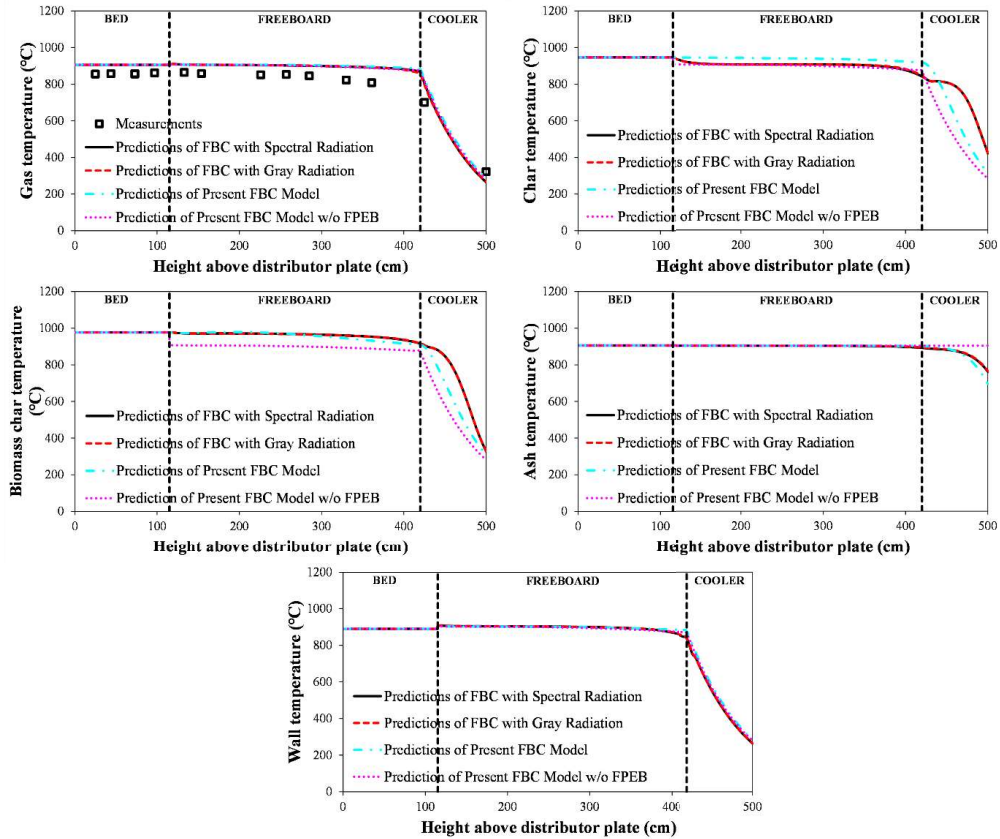
Figure 7.48. Gas, char, biomass char, ash, and wall temperature predictions obtained by the present FBC model and coupled FBC models for Test 8

CPU requirements of original and coupled FBC models are shown in Table 7.31. FBC model coupled with spectral RTE model requires approximately 230 and 15 times higher CPU time than the original FBC model and FBC model coupled with gray radiation model, respectively. As shown by the table, in the FBC model with spectral radiation, most of the CPU requirement is for the calculation of radiative properties as it requires the solution of Mie theory for 147 spectral points, 101 discrete particle sizes, 81 different freeboard height and 3 particle types (fly ash, coal char, and biomass char).

Table 7.31 CPU time requirements of the original FBC model and coupled FBC models for Test 8

	Present FBC model	FBC model with gray radiation	FBC model with spectral radiation
CPU Time for Bed (s)	18	18	18
CPU Time for Radiative Property Estimation (s)	-	707	31166
CPU Time for RTE Solution (s)	-	1745	11776
CPU Time for Freeboard Equations (s)	167	488	289
Total CPU Time (s)	185	2959	43246

Figure 7.49 demonstrates the individual contributions of radiation and convection in freeboard gas, coal char, biomass char, ash, and wall energy balances for the co-combustion test under investigation. It should be highlighted at this point that ST and HF values for radiation and convection given in Figure 7.49 are obtained from the FBC model coupled with spectral radiation model. As demonstrated by the ST profiles in Figure 7.49(a), radiative ST in gas energy balance is important at the end of the freeboard due to the existence of the cooling module. On the other hand, radiation dominates the heat transfer between the solid particles, including coal char, biomass char, and ash, and the medium especially at the end of freeboard as shown by Figures 7.49(b), 7.49(c), and 7.49(d). Furthermore, contribution of radiation to wall energy balance is as significant as that of convection as can be seen from Figure 7.49(e). The negative values of wall radiative HFs at the end of the freeboard indicate that side walls are cooled down directly by the cooling module via radiation. In

conclusion, the significant contribution of radiative STs and wall HFs to freeboard heat transfer at the end of the freeboard due to presence of cold surfaces provided by cooling module indicates that radiation may become much more important in the industrial and utility boilers where side walls are cold membrane tube walls instead of refractory.
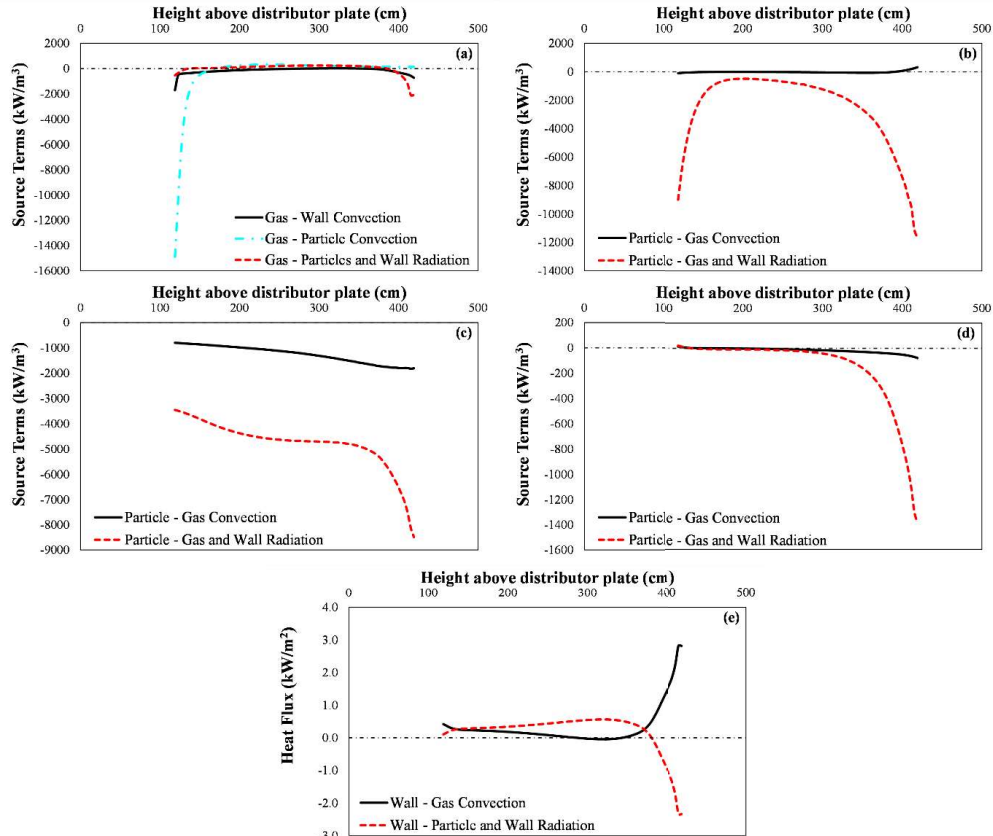
Figure 7.49. Individual contributions of spectral radiation and convection in (a) freeboard gas, (b) freeboard char, (c) freeboard biomass char, (d) freeboard ash, and (e) freeboard wall energy balances for Test 8

Measurements and predictions of gaseous emissions of O_2, CO_2, CO, SO_2, NO, and N_2O for the co-combustion test are shown in Table 7.32. As shown by the table, reasonable agreement is achieved between the measured and predicted emissions for the co-combustion test. Utilization of Stephan-Boltzmann law describes radiation in FBC leads to underprediction of O_2 and overprediction of CO_2. This is due to high

283

char particle temperature prediction of the present FBC model without radiation caused by disregarding the radiative heat exchange between particles and walls in the present FBC model. The difference between the SO_2, NO, and N_2O predictions of the FBC models with and without radiation models is insignificant. The insignificant difference between the SO_2 emission is due to the strong dependence of SO_2 to CaO load which is identical in all the models. The insignificant difference between the NO emission is due to the fact that (i) the majority of the combustibles are burned in the bed section owing to under bed feeding system and (ii) heterogeneous reactions of NO are discarded in the freeboard section. The insignificant difference between the N_2O emission is due to the insignificant difference in the gas temperature predictions of the FBC models with and without radiation. Finally, the present FBC model without FPEB provides reasonable gaseous emission predictions for the test case under investigation.

Table 7.32 Predicted and measured gaseous emissions of the species O_2, CO_2, CO, SO_2, NO, and N_2O for Test 8

Species	Present FBC model	Present FBC model w/o FPEB	FBC model with gray radiation	FBC model with spectral radiation	Exp.
O_2 (% dry)	4.6	5.0	4.9	4.9	5.1
CO_2 (% dry)	15.1	14.7	14.8	14.8	15.3
CO (% dry)	0.05	0.05	0.06	0.06	0.06
SO_2 (ppm dry)	586	586	586	586	486
NO (ppm dry)	290	290	290	290	285
N_2O (ppm dry)	74	76	76	76	60

7.7.2   Results of the Combustion Test with Cold Water Walls

The findings reported in the previous section indicate that using a sophisticated radiation code in conjunction with the system model of the test rig, does not significantly influence the temperature predictions. This insignificant effect is due to the fact that the freeboard of the test rig is bounded by hot refractory-lined walls leading to very low temperature difference, and thus lower heat transfer rate between the surfaces and the medium. To test this hypothesis, a parametric study is carried out where hot refractory-lined side walls of the test rig are replaced with cold water walls at 537 K and with emissivity of thermally oxidized carbon steel as in utility or industrial boilers according to the experiments carried out in the 16 MW$_t$ FBC in the Chalmers University of Technology [208,211]. Parameters, except the side wall temperatures and side wall emissivities, are kept the same as those in the combustions test. The results of this parametric study are summarized in the following sections.

Figure 7.50 compares the predicted and measured gas, coal char, biomass char, and ash temperatures along the combustor for the combustion test where freeboard is bounded by cold water walls at 537 K. Furthermore, predictions of the present FBC model without freeboard particle energy balance (labeled as 'Present FBC Model w/o FPEB) are also illustrated in Figure 7.50. It should be noted that present FBC model without FPEB assumes that ash particles' temperature is equal to their temperature in the bed whereas char particles' temperature is equal to freeboard gas temperature. As illustrated by the figure, char and ash temperature predictions of the coupled FBC models are significantly higher than those of present FBC model without radiation. This is due to consideration of direct heat exchange between the hot particles and cold walls via radiation in the coupled codes. The difference between the biomass char temperature predictions of the FBC models with and without radiation is not significant due to coarse particle size of biomass char particles (given in Figure 7.51(a)) owing to low particle density of CR. Temperatures of coal and biomass char particles reduce rapidly in the freeboard region compared

285

to that of ash particle due to low char density ($\rho_{d,l} = 770$ kg/m^3; $\rho_{d,bio} = 106$ kg/m^3) caused by drying and devolatilization. Finally, the present FBC model without FPEB provides reasonable gas and biomass char particle temperature predictions.
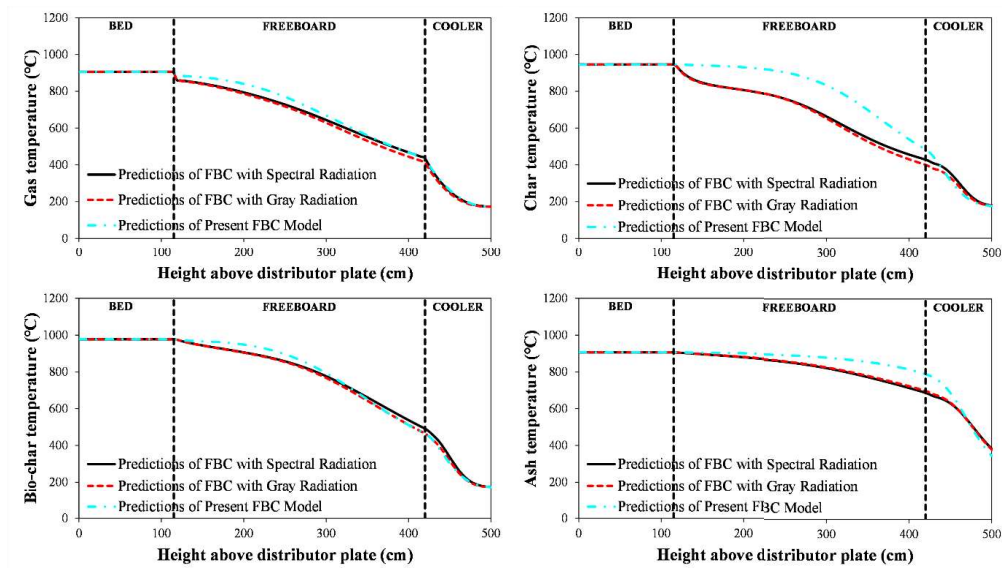
Figure 7.50. Gas, char, biomass char and ash temperature predictions obtained by present FBC model and coupled FBC models for Test 8 where freeboard is bounded by cold water walls at 537 K
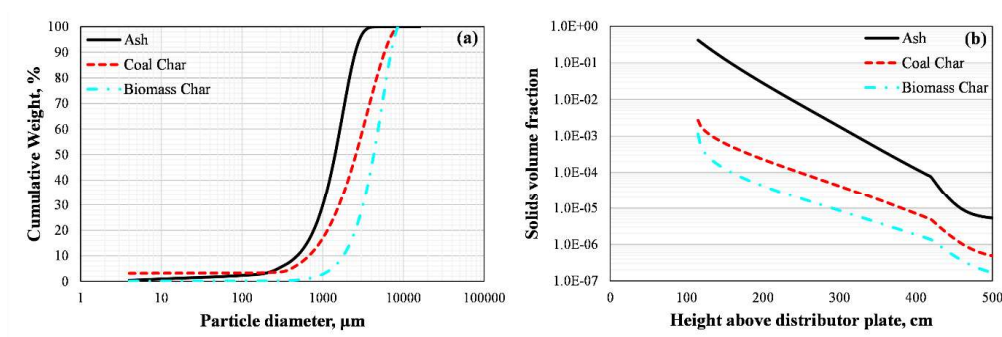
Figure 7.51. Freeboard entrained particles (a) load (b) size distribution at the center of freeboard for Test 8 where freeboard is bounded by cold water walls at 537 K

CPU requirements of original and coupled FBC models for the combustion test where freeboard is bounded by cold water walls at 537 K are shown in Table 7.33. FBC model coupled with spectral RTE model requires approximately 400 and 2

286

times higher CPU time than the original FBC model and FBC model coupled with gray radiation model, respectively.

Table 7.33 CPU time requirements of the original FBC model and coupled FBC models for Test 8 where freeboard is bounded by cold water walls at 537 K

	Present FBC model	**FBC model with gray radiation**	**FBC model with spectral radiation**
CPU Time for Bed (s)	18	18	18
CPU Time for Radiative Property Estimation (s)	-	6881	42372
CPU Time for RTE Solution (s)	-	14713	13948
CPU Time for Freeboard Equations (s)	98	4470	393
Total CPU Time (s)	116	26081	56731

Figure 7.52 demonstrates the individual contributions of radiation and convection in freeboard gas, char, biomass char, and ash energy balances for the combustion test where freeboard is bounded by cold water walls at 537 K. It should be highlighted at this point that ST and HF values for radiation and convection given in Figure 7.52 are obtained from the FBC model coupled with spectral radiation model. The contribution of radiation and convection in the freeboard heat transfer for the combustion test where freeboard is bounded by cold water walls at 537 K indicates that radiation is much more important than convection in the freeboard heat transfer for the test case under investigation.
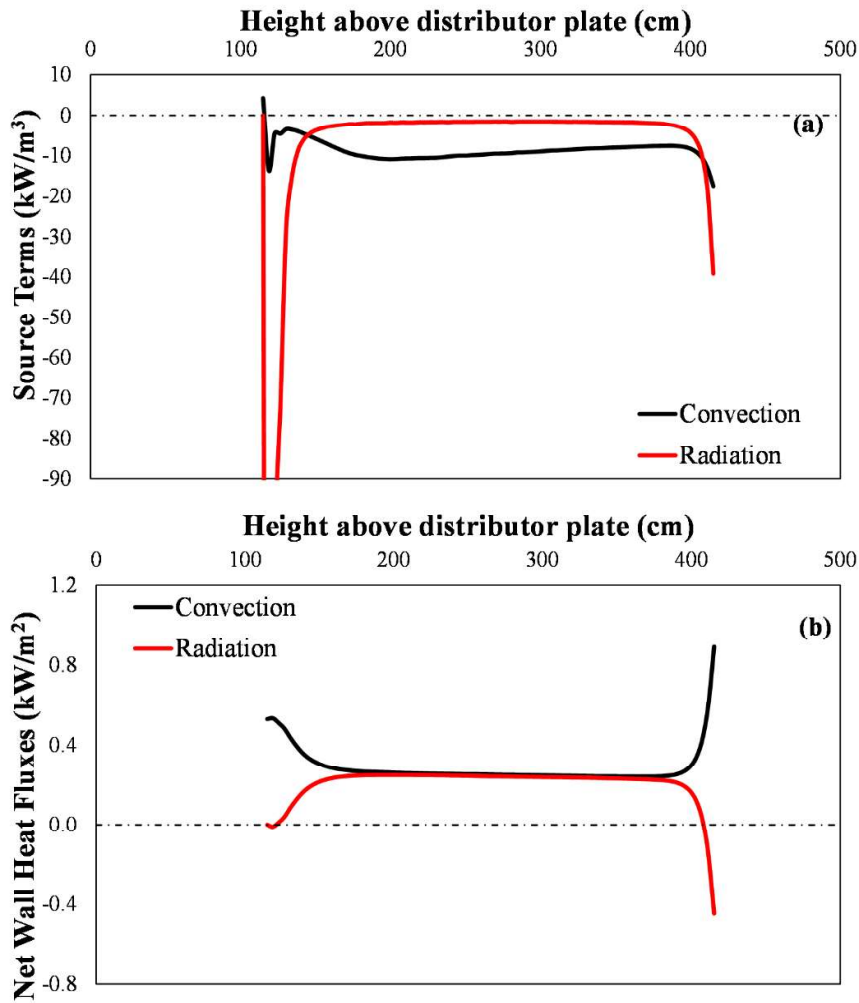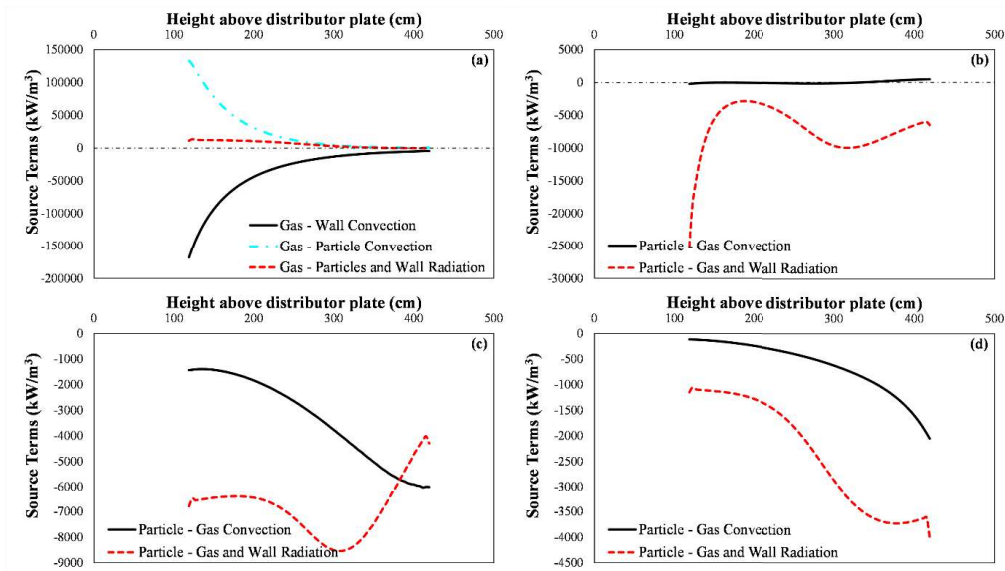
Figure 7.52. Individual contributions of spectral radiation and convection in (a) freeboard gas, (b) freeboard char, (c) freeboard biomass char, and (d) freeboard ash energy balances for the combustion test where freeboard is bounded by cold water walls at 537 K

Measurements and predictions of gaseous emissions of O_2, CO_2, CO, SO_2, NO, and N_2O for the combustion test where freeboard is bounded by cold water walls at 537 K are shown in Table 7.34. The predictions of the FBC models with and without radiation models for the combustion test where freeboard is bounded by cold water walls at 537 K are similar to those for the combustion test where freeboard is bounded by hot refractory-lined walls (see Table 7.32). The present FBC model without FPEB provides reasonable gaseous emission predictions for the test case under investigation.

Table 7.34 Predicted and measured gaseous emissions of the species O_2, CO_2, CO, SO_2, NO and N_2O for Test 8 where freeboard is bounded by cold water walls at 537 K

Species	Present FBC model	Present FBC model w/o FPEB	FBC model with gray radiation	FBC model with spectral radiation
O_2 (% dry)	5.0	5.4	5.4	5.4
CO_2 (% dry)	14.7	14.2	14.2	14.2
CO (% dry)	0.12	0.11	0.11	0.11
SO_2 (ppm dry)	601	601	604	604
NO (ppm dry)	294	294	295	295
N_2O (ppm dry)	103	103	107	107

7.8   Effect of Gas and Particle Radiative Property Models on the Predictions of CFD Model of ABFBC Firing Lignite

In this section, the predictions of a 2-D CFD model, developed within the scope of this thesis study, for a combustion test carried out in 0.3 MW_t test rig where Çan lignite is fired without limestone and biomass addition (Test 4) is compared with the experimental temperature and concentration profiles, pressures and gaseous emissions obtained from the in-situ measurements. The CFD model is developed using the commercial software ANSYS Fluent 2020 R1 [98]. The details of the model is provided in Chapter 5. Regarding the boundary conditions of the model, they are selected based on input data obtained from Test 4 carried out in the METU 0.3 MWt ABFBC test rig. The boundary conditions of the 2-D model are summarized in Table 7.35.

Table 7.35 Boundary conditions for the 2-D model of the METU 0.3 MWt ABFBC test rig

Parameter		Parameter	
Air Inlet		**Bed Tubes**	
Inlet gauge pressure (Pa)	5500	Wall thickness (m)	0.002
Inlet air velocity (m/s)	0.59	Wall roughness constant	0.5
Inlet air temperature (°C)	40.0	Heat transfer coefficient (W/m^2.K)	156.6
Turbulent intensity (%)	4.8	Free stream temperature (°C)	24.1
Internal emissivity	0.0	Internal emissivity	0.8
Outlet		**Cooler Tubes**	
Outlet gauge pressure (Pa)	0.0	Wall thickness (m)	0.003
Internal emissivity	1.0	Wall roughness constant	0.5
Walls		Heat transfer coefficient (W/m^2.K)	62.5
Wall thickness (m)	0.26	Free stream temperature (°C)	27.1
Wall roughness constant	0.5	Internal emissivity	0.8
Heat transfer coefficient (W/m^2.K)	3.58		
Free stream temperature (°C)	25.0		
Internal emissivity	0.33		

Before validating the predictions against the measurements, the transient wet CO_2 emissions at the combustor exit are investigated to show whether the simulation reaches to quasi-steady state after 30 s. Transient wet CO_2 emission predictions of the 2-D CFD model is illustrated in Figure 7.53. As illustrated by the figure, the wet CO_2 emissions between $30 - 40$ s remain constant, and the simulation reaches a steady state after 30 s. It should be noted at this point that the steady state predictions

presented in the following sections are obtained by time-averaging the data obtained between 30 – 40 s.
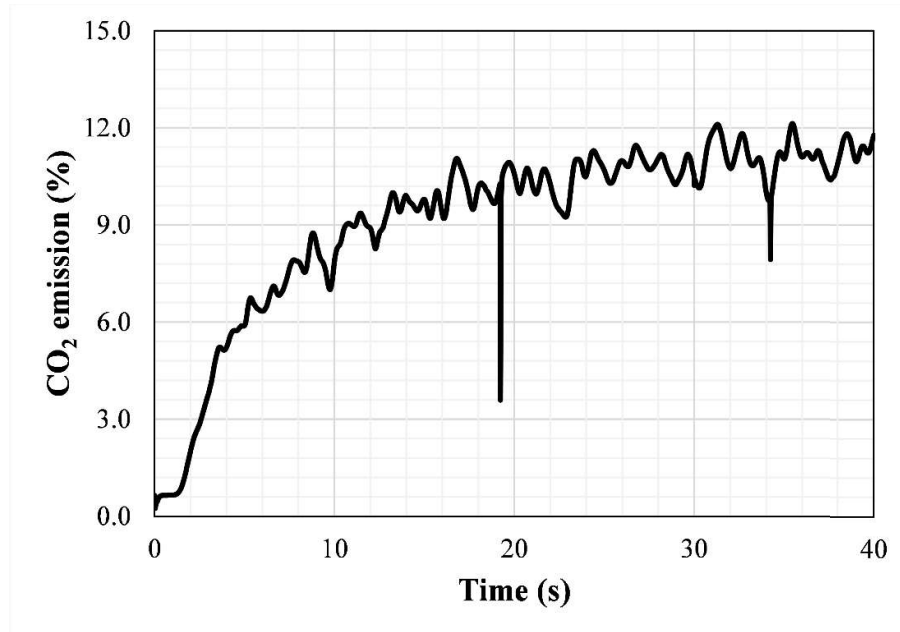
Figure 7.53. Transient wet CO_2 emissions predictions of the 2-D CFD simulation for Test 4

Figure 7.54 illustrates the predicted 2-D volume fraction field of inert bed materials and lignite particles' distribution at different simulation times. As shown by the figure 7.54(a), inert bed materials splash around 1.5 m with the combustion air. The bed seems to be in the bubbling regime as expected since no entrainment of bed material occurs. On the other hand, in Figure 7.54(b), the color bar indicates the temperature of the particles. This means green particles are hot lignite particles whereas blue particles are cold lignite particles. Fine lignite particles elutriate with the superficial gas velocity. The coarse lignite particles move in the bed section with bed materials.
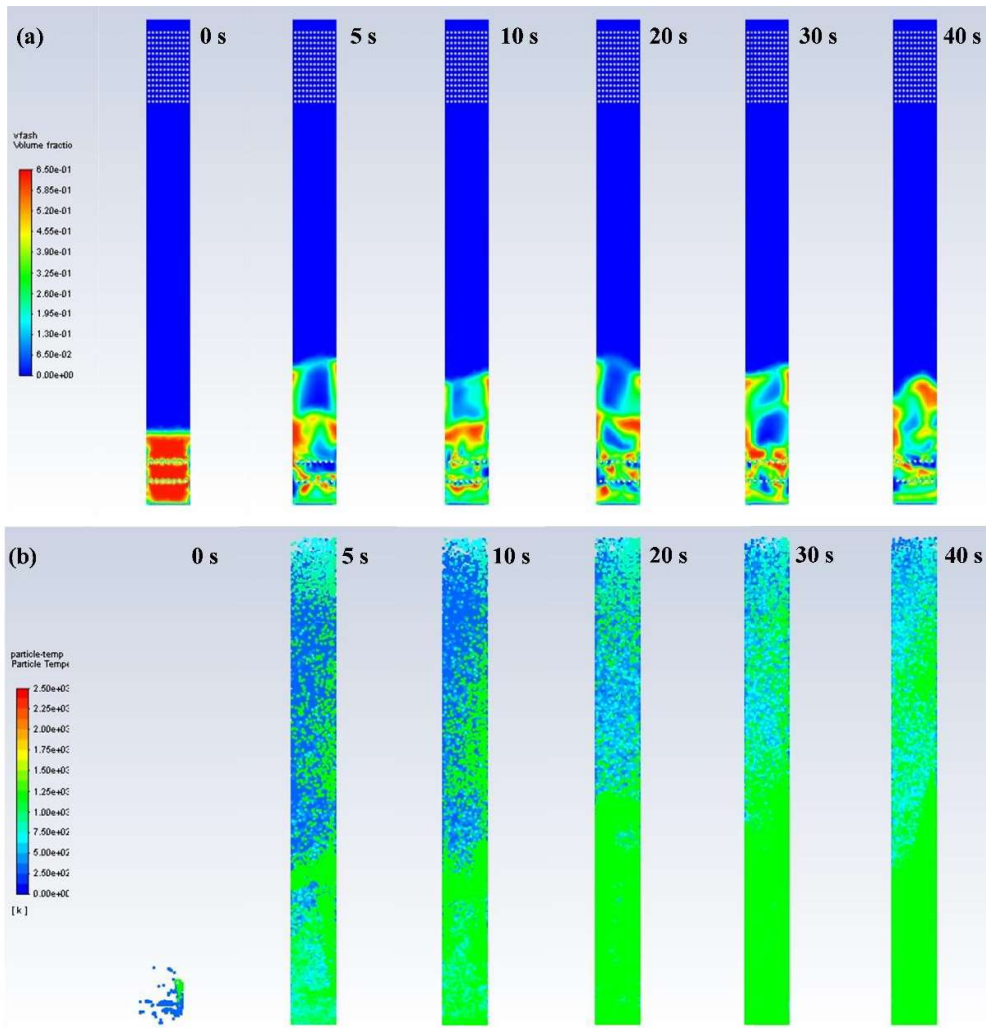
Figure 7.54. (a) the predicted 2-D volume fraction field of inert bed materials and (b) lignite particles' distribution at 0th, 5th, 10th, 20th, 30th and 40th minutes.

The centerline pressure profile and pressure gradient $(-\partial P/\partial z)$ predictions of the 2-D simulation and their comparison with the measurements are demonstrated by Figure 7.55. As demonstrated by the figure, the predicted and measured pressures are in reasonable agreement. The fluctuations of pressure gradient in the bed and cooler sections are considered to be due to the existence of tube banks which compress the gas mixture and lead to higher mechanical energy losses. Disregarding the fluctuations of pressure gradient due to bed tubes, the pressure gradient

292

$(-\,\partial P/\partial z)$ remains almost constant until 1 m, which indicates that the expanded bed height is approximately 1 m. This finding is also confirmed by the measured expanded bed height (1.02 m) as given in Table 6.13. Furthermore, the significant decrease in the pressure gradient between 1 – 1.5 m of the combustor suggests that the splash zone is located between 1 – 1.5 m. Therefore, the region between 0 – 1.5 m is referred to as bed and splash zone in the rest of the manuscript.
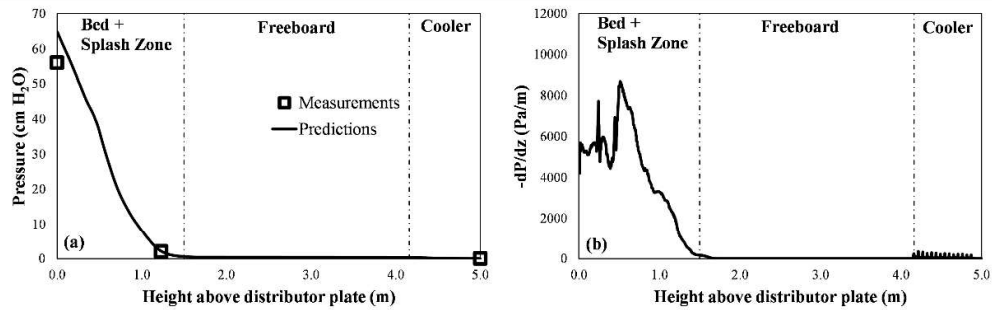
Figure 7.55. Centerline (a) pressure profile and (b) pressure gradient predictions of the 2-D CFD simulation and their comparison with the measurements for Test 4

The centerline gas temperature profile prediction of the 2-D simulations using WSGG – Smith, WSGG – Bordbar, Bordbar's 10 band model and DBWSGG and their comparison with the measurements are demonstrated by Figure 7.56. As shown by the figure, temperature predictions of both CFD simulations are very sensitive to the gas radiative property models for the test rig. DBWSGG model overestimates the temperatures at the end of the freeboard region whereas WSGG – Bordbar and Bordbar's 10 band model underestimates the temperatures for the test rig under investigation. The temperature predictions of WSGG – Smith agree reasonably with the measurements. The deviation between the predictions and measurements of gas temperatures at the bottom of the bed is probably due to the interaction between thermocouples and hot ash particles when measuring the bed temperatures during the combustion test.
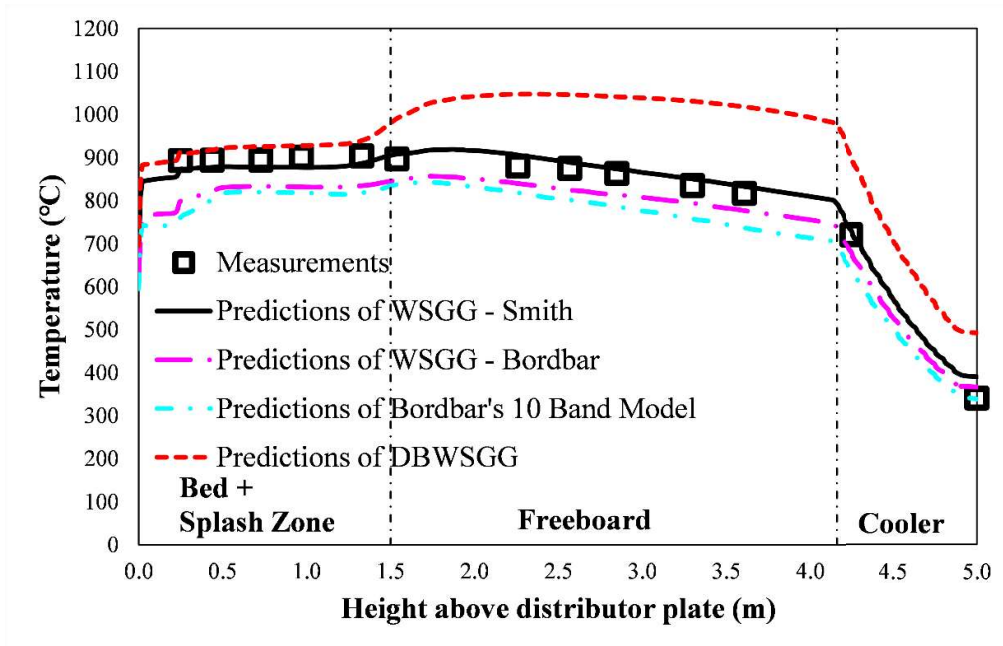
Figure 7.56. Centerline temperature profile predictions of the 2-D CFD simulation and its comparisons with the measurements for Test 4

Centerline dry O_2, CO_2, and CO concentration profile predictions of the 2-D simulation using different gas radiative property models and their comparisons with the measurements are shown by Figure 7.57. As demonstrated by the figure, CO predictions of all gas radiative property models reasonably agree with the measurements altough their temperature predictions differ significantly as highlighted in Figure 7.56. On the other hand, all CFD models slightly underestimate CO_2 concentrations.

294
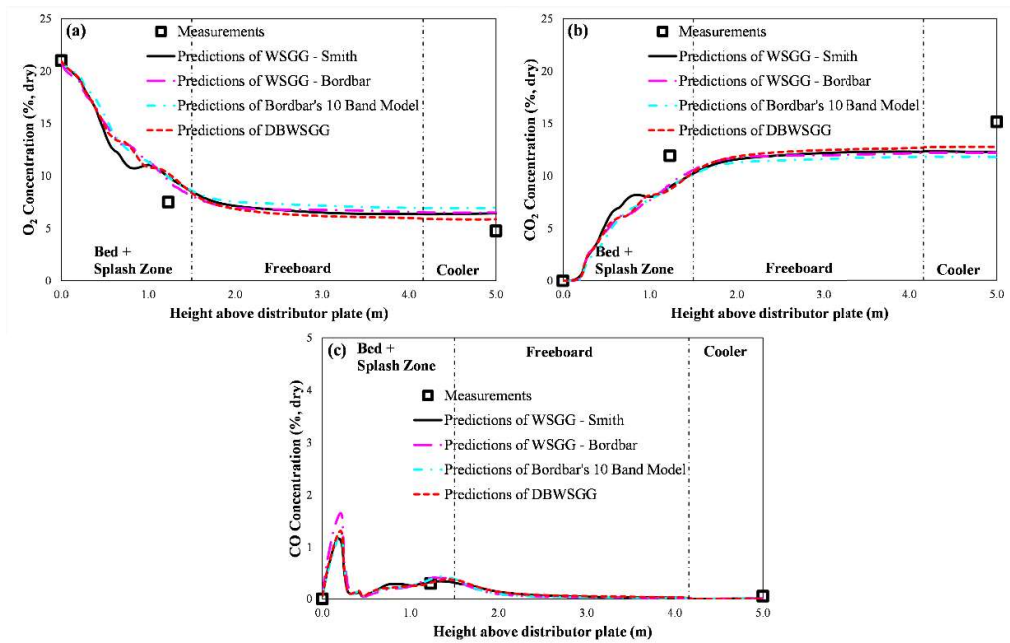
Figure 7.57. Centerline dry (a) O_2, (b) CO_2, and (c) CO concentration predictions of the 2-D CFD simulation and their comparisons with the measurements for Test 4

Comparison of predicted and measured gaseous emissions on dry basis are shown in Table 7.36. As can be seen from the figure, the CFD model with WSGG – Smith model slightly overestimates O_2 emissions and underestimates CO_2 emissions. The inaccuracy of the WSGG – Smith model, which is a more sophisticated representation of gas radiative properties compared to DBWSGG, is considered to be due to utilization of insufficiently accurate chemical kinetic models for the combustion of volatiles, char and gaseous species. Furthermore, CO emission predictions of both gas radiative property models deviate significantly from the measurement again for the same reason. However, the scope of this study is to test the performances of gas radiative property models, which are influenced by the temperature, CO_2 and H_2O and carry over flow rate (or particle load) predictions of 2-D CFD simulation. It was found that those predictions are sufficiently accurate to investigate the radiation in BFBCs. Therefore, utilization of sufficiently accurate chemical kinetic models is decided to be carried out in a future study.

295

Table 7.36 Predicted and measured gaseous emissions on a dry basis for Test 4

	DBWSGG	WSGG – Smith	WSGG – Bordbar	Bordbar's 10 Band Model	Measurements
O_2 (%, dry)	5.9	6.5	6.6	7.0	5.1
CO_2 (%, dry)	12.8	12.3	12.2	11.8	14.8
CO (%, dry)	0.002	0.006	0.004	0.007	0.050
Carry over flow rate (g/s)	11.6	9.2	9.0	8.7	4.1

The CPU time requirements of different gas radiative property models for the 2-D simulation of the test rig are compared in Table 7.37. The CPU times increase with the increasing complexity of the gas radiative property model due to the increase in the number of calculations for each cell, iteration and time step. WSGG – Smith can be considered as the optimal gas radiative property model owing to its accuracy and sufficiently high computational efficiency.

Table 7.37 CPU time requirements of different gas radiative property models for the 2-D simulation of Test 4

	DBWSGG	WSGG – Smith	WSGG – Bordbar	Bordbar's 10 Band Model
CPU Time per iteration (s)	0.611	0.602	0.893	0.628
Number of iteration	160000	160000	160000	160000

Finally, the centerline temperature profile predictions of two different particle radiative property approaches, one is the usage of Planck mean particle radiative

properties and the other is the utilization of particle radiative properties at 3 μm, are illustrated in Figure 7.58. Predictions with the Planck mean particle radiative properties are considered as the benchmark solution. As illustrated in the figure, using particle radiative properties at 3 μm instead of Planck mean particle radiative properties leads to significant deviations in temperature profile predictions for the test case under investigation.
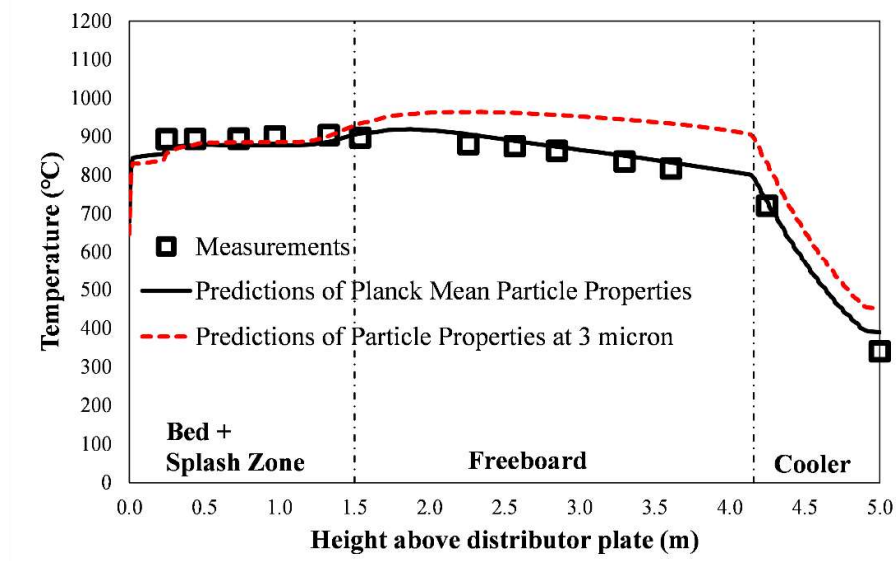
Figure 7.58. Centerline temperature profile prediction of the 2-D CFD simulation with different particle radiative property models and their comparisons with the measurements for Test 4

7.8.1 Concluding Remarks for the Computational Fluid Dynamics Model for Lignite Combustion

The findings obtained from the 2-D CFD simulations for the test rig under consideration reveal that temperature predictions of both CFD simulations are sensitive to the gas and particle radiative property models. Among the radiation models, the temperature predictions of WSGG – Smith for gas radiative properties and Planck Mean particle radiative properties agree reasonably with the

measurements. On the other hand, the deviation between concentration predictions of the radiation models is very small. This slight inaccuracy of the CFD models in the prediction of concentration profiles and gaseous emissions is considered to be due to utilization of insufficiently accurate chemical kinetic models for the combustion of volatiles char and gaseous species. However, the predictions of the CFD model is sufficiently accurate for the investigation of the predictive performances of gas radiative property models, which are influenced by the temperature, CO_2 and H_2O concentrations and carry over flow rate (or particle load) predictions of 2-D CFD simulation.

7.9 Effect of Particle Size Distribution and Complex Refraction Index of Alumina on Infrared Rocket Plume Signatures

After successfully coupling the 3-D radiation model with system models of FBC, the 3-D radiation model will be applied to a test case representing the typical conditions of solid rocket motor exhaust plumes to investigate RHT in solid rocket plumes where radiation is an important mechanism of heat transfer. Solid rocket propellants such as aluminized propellants are commonly used on ballistic missiles, space launchers, and tactical missiles. The addition of alumina to the propellant stabilizes the combustion process due to the micron size of aluminum particles and greatly raises the thrust level. Nevertheless, exhaust plumes of such systems are characterized by high infrared emission owing to the presence of alumina which makes them prone to be detected by infrared space or airborne surveillance sensors. As the design, operation, and optimization of these sensors are based on signatures of realistic rocket exhaust plumes, infrared signatures of solid rocket exhaust plumes have been investigated widely over decades. Among them, modeling studies have growing attention as the experimental works require expansive facilities.

There are several studies in the literature for modeling infrared signatures of solid motor rocket plumes [129,213–227]; however, none of them carries out a parametric study where the effect of using some simplifying assumptions such as using gray

optical properties, Sauter-mean/mass-mean diameters, temperature-independent optical properties, etc. in modeling of infrared plume signature, investigated under solid motor rocket plume conditions. Such assumptions, on the other hand, are of significant importance as they improve the computational efficiency of coupled problems by reducing the computational time required for the solution of Mie theory for each particle size, location, time, and wavelength under investigation. Therefore, the final objective of this study is to investigate the influence of using (i) mean diameters such as Sauter-mean diameter or mass-mean diameter instead of a PSD, (ii) optical properties for different phases and crystal structures of Al_2O_3 such as liquid Al_2O_3, α-Al_2O_3, and γ-Al_2O_3, (iii) temperature-independent optical properties for those phases and crystal structures of Al_2O_3, and (iv) gray optical properties of Al_2O_3 particles instead of spectral ones on the RHT predictions under rocket plume conditions. For this purpose, a previously developed [228] 3-D radiation code using DOM coupled with SNBCK for gas radiative properties and Mie theory for particle radiative properties is utilized. For the application and validation of this model, the 3-D rectangular test case of Liu et al. [112] representing the typical operating conditions of solid rocket plumes is selected.

RHT in rocket plumes is investigated in a hypothetical test case of Liu et al. [112] representing typical conditions of rocket plumes as represented by Figure 7.59. The test problem is a 2 x 2 x 8 m^3 rectangular plume involving 20 % H_2O and 80 % N_2 together with alumina particles bounded by cold black walls. The system includes 2 x 10^9 m^{-3} alumina particles with a particle diameter of 11.6 μm. The plume temperature is taken as symmetrical about the centerline of the plume and is specified as;
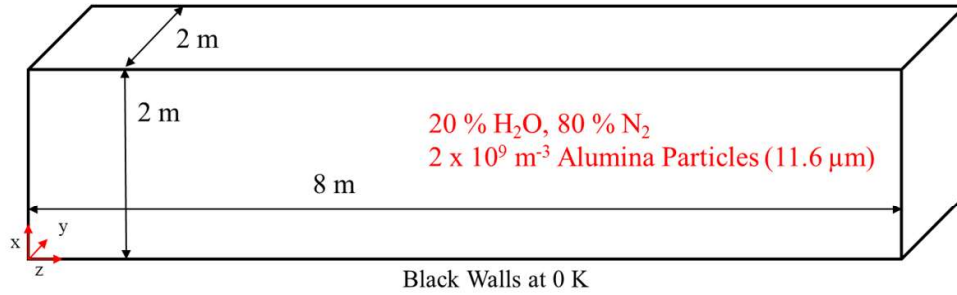
Figure 7.59. Schematic representation of the hypothetical test case of Liu et al. [112] representing typical conditions of rocket plumes

$$T = (T_c - T_e)f(r/R) + T_e \qquad (7.4)$$

where T_c is the centerline plume temperature and T_e is the temperature at exit ($z = 8$ m). The radial varition of the temperature profile is represented by the following expression;

$$f(r/R) = 1 - 3(r/R)^2 + 2(r/R)^3 \qquad (7.5)$$

where r is the distance from the plume centerline and R is the radius of the circular region. The plume temperature outside the circular region is assumed to be uniform and at the value of the exit temperature. The centerline temperature is assumed to increase linearly from 400 K at the inlet ($z = 0$) to 2400 K at $z = 0.75$ m and then decrease linearly to 800 K at the exit.

In this section, the 3-D radiation code is solved using DOM approach. Angular discretization is carried out based on the T4 scheme whereas the 11 x 11 x 120 spatial grid points in x-, y-, and z-directions are used to discretize the spatial domain. The wavelength range is taken as 2000-4000 cm^{-1} to predict the infrared signature of the plume. The reason behind the selection of this wavenumber range is that the previous study of Liu et al. [112], where the original test case is taken from, focuses on this wavenumber interval during their radiative transfer calculation. Therefore, the authors preferred not to change the conditions of the test case in the present work. Furthermore, this wavenumber range $2000 - 4000$ cm^{-1} is the focus of surveillance

sensors applications. This wavenumber range is the middle wave infrared region (MWIR) which is preferred in solid rocket motor surveillance applications owing to its high atmospheric transmission in most climates. The system of ODEs obtained after angular and spatial discretization is solved by the readily available ROWMAP code, based on the ROW-methods of order 4 and uses Krylov techniques for the solution of linear systems [105]. All tests are performed on a computer with Intel® Core™ i7-2600 CPU 3.40 GHz processor having 16.00 GB of RAM.

In the present work, radiative properties of gases are estimated using SNBCK model based on seven-point Gauss-Labatto quadrature. On the other hand, the spectral properties of particle clouds are estimated using Mie theory. Radiative properties of particles depend on their size distribution. For this purpose, a PSD is calculated according to the procedure given in Hermsen [229]. Based on this procedure, a mean diameter is first calculated as a function of nozzle throat diameter, Al_2O_3 concentration in the chamber, chamber pressure, and average chamber residence time;

$$d = 3.6304 D_t^{0.2932}[1 - \exp(-0.0008163 \zeta_c P_c \tau)] \tag{7.6}$$

where D_t is the nozzle throat diameter in inches, ζ_c is Al_2O_3 concentration in the chamber in g-mol/100 g, P_c is the chamber pressure in psia and τ is the average chamber residence in msec. Nozzle throat diameter, Al_2O_3 concentration in the chamber, chamber pressure, and average chamber residence time are selected as 52.7 in., 0.262 g-mol/100 g, 880 psia, and 350 ms based on Sambamurthi [230]. Using the mean diameter calculated by Eq. (7.6) and assuming that the standard deviation is 0.298 Hermsen [229], a PSD for alumina is described as a monomodal log-normal distribution;

$$f(d_p) = \frac{1}{d_p \sigma \sqrt{2\pi}} exp\left[-\frac{1}{2}\left(\frac{ln(d_p) - ln(\mu)}{\sigma}\right)^2\right] \tag{7.7}$$

where σ is the standard deviation, μ the mean diameter and $f(d_p)$ is the size distribution function. The PSD of alumina calculated by using the procedure described above is illustrated in Figure 7.60.
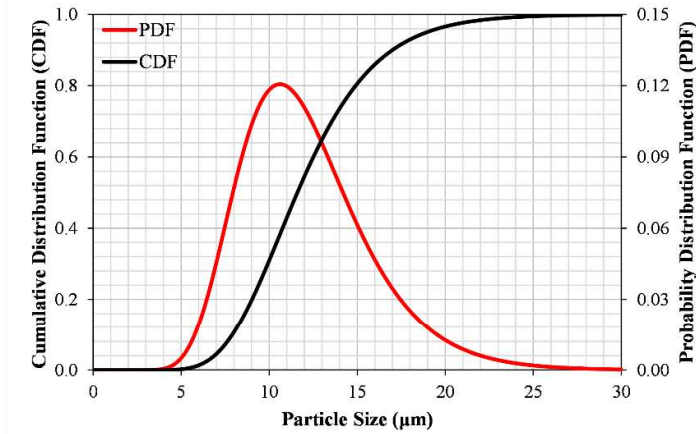
Figure 7.60. Estimated size distribution of alumina particles inside system under investigation

To test the influence of using PSD of alumina instead of using an average diameter on the predictions of RHT in rocket plumes, three different mean diameters, which are d_{43}, d_{32}, and 11.6 μm Liu et al. [112], are utilized. The mass mean diameter, d_{43}, is commonly used in rocket plume studies owing to its performance in predicting two-phase flow losses (Hermsen [229]) and is calculated as follows;

$$d_{43} = \sum_i \frac{n_i D_i^4}{n_i D_i^3} \tag{7.8}$$

where D_i is the diameter of the particles in i^{th} class and n_i is the number of particles in i^{th} class.

Sauter-mean diameter, d_{32}, is the diameter that has the same volume/surface area ratio of the particles cluster of interest. It is important for cases where the surface area of the particles affects significantly the phenomena such as chemical reaction, RHT, etc. Sauter-mean diameter can be calculated as follows;

$$d_{32} = 1 \bigg/ \sum_i \frac{f_i}{D_i} \qquad\qquad (7.9)$$

where f_i is the mass fraction of particles in i^{th} class. Using Eqs. (7.8) and (7.9), d_{43} and d_{32} are calculated as 12.1 μm and 11.1 μm, respectively.

Finally, an average diameter of 11.6 μm is also selected as it is used in the original test case under investigation developed by Liu et al. [112].

It is known that the radiative properties of alumina particles depend on their RI. For this purpose, influence of optical properties of different phases and crystal structures of alumina on RHT is tested under rocket plume conditions using different RI data for different phases as described in section 2.3.5.3. Another objective of this study is to compare the predictions of the model with absorbing-emitting gas and absorbing-emitting-scattering particles and those of the absorbing-emitting gas and non-absorbing-non-emitting-scattering particles. For the medium including absorbing-emitting gas and non-absorbing-non-emitting-scattering particles, the refractive index of alumina particles is taken as 1.74 by Liu et al. [112] whereas the absorption index is taken to be zero.

The 3-D radiation code using DOM coupled with SNBCK for gas radiative properties and Mie theory for particle radiative properties used in this study is benchmarked against the predictions obtained in the previous study of Liu et al. [112] for the same test case. Comparison of the narrow-band integrated radiation intensity distribution predictions of this study and those of Liu et al. [112] is illustrated in Figure 7.61. Narrow-band radiation intensity predictions of the present study agree well with those of Liu et al. [112].
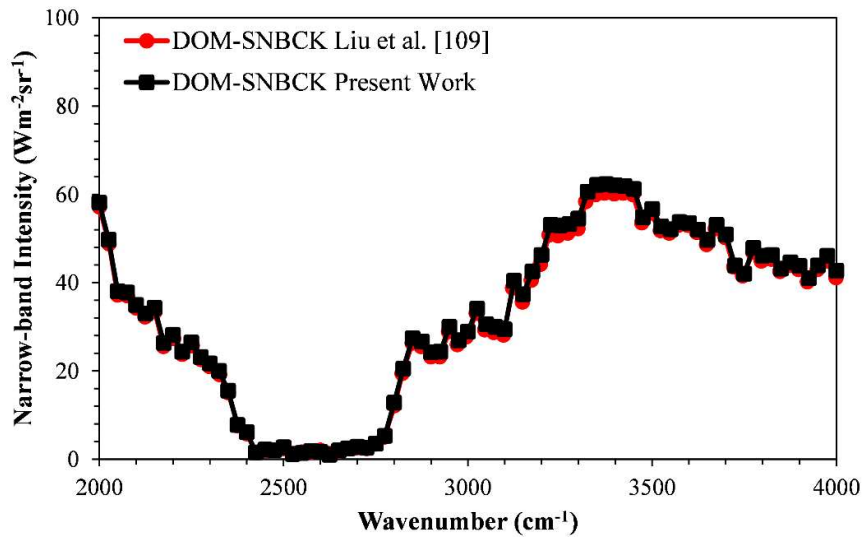
Figure 7.61. Narrow-band integrated radiation intensity distributions at x = 1 m, y = 1 m, and z = 7.9 m and along the direction of 0.0990147, 0.0990147, and 0.990147 predictions of this study and those of Liu et al. [112] between 2000 – 4000 cm^{-1}

The effect of considering absorption and emission of particles to RHT under rocket plume conditions is also investigated. Radiative properties of the particle cloud, which are absorption coefficients, scattering coefficients, and asymmetry factors, are calculated using the refractive and absorption indices γ-Al$_2$O$_3$, α-Al$_2$O$_3$, and liquid alumina given in Figure 2.10. The comparison of the radiative properties of γ-Al$_2$O$_3$, α-Al$_2$O$_3$, and liquid alumina is demonstrated by Figure 7.62. As demonstrated by the figure, the absorption coefficient of the γ-Al$_2$O$_3$ is the highest whereas that of liquid alumina is the lowest. The order of scattering coefficients of γ-Al$_2$O$_3$, α-Al$_2$O$_3$, and liquid alumina is exactly the opposite.
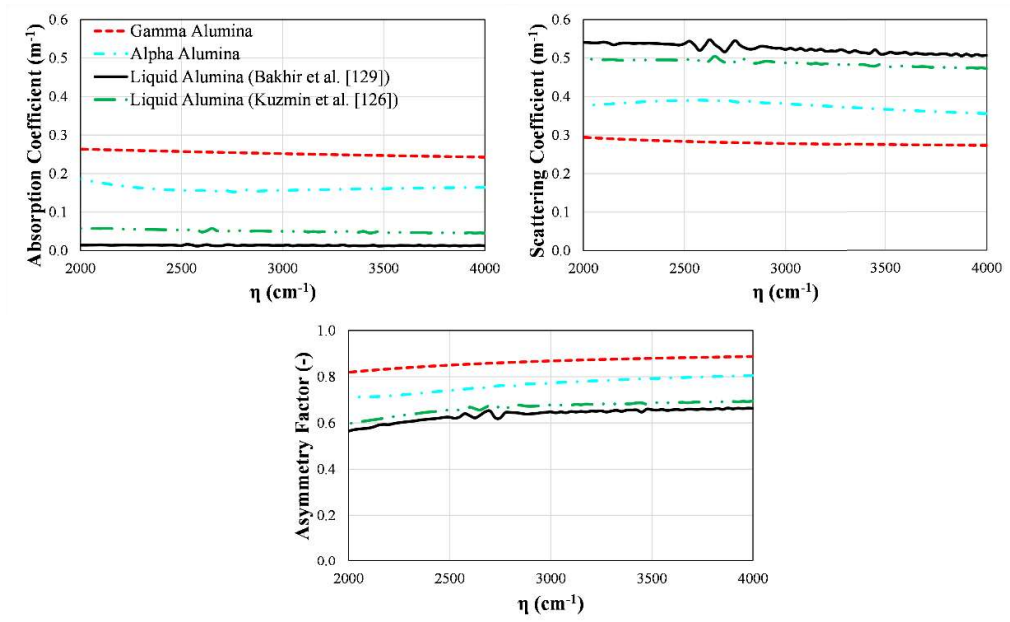
Figure 7.62. Predicted (a) absorption coefficients, (b) scattering coefficients and (c) asymmetry factors by using different alumina refractive and absorption indices

Comparison of the narrow-band integrated radiation intensity distributions predicted by using radiative properties of γ-Al$_2$O$_3$, α-Al$_2$O$_3$, and liquid alumina and predicted by neglecting absorption and emission of thermal radiation by alumina is shown in Figure 7.63. As demonstrated by the figure, absorption and emission of thermal radiation become important when γ-Al$_2$O$_3$ and α-Al$_2$O$_3$ are present in the system whereas it is not considerable for liquid alumina. This effect is considered to be due to low absorption indices and thus, absorption coefficients of liquid alumina cloud which are shown in Figures 2.10 and 7.62, respectively.
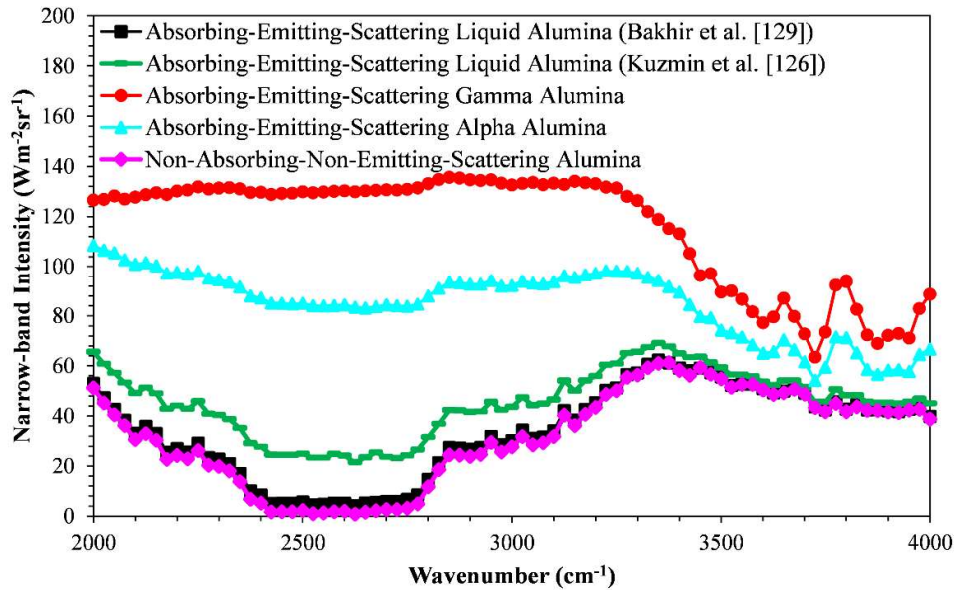
Figure 7.63. Narrow-band integrated radiation intensity distributions at x = 1 m, y = 1 m, and z = 7.9 m and along the direction of 0.0990147, 0.0990147, and 0.990147 predicted by using different alumina refractive and absorption indices

To study the effect of utilizing temperature-dependent refractive and absorption indices of alumina particles on RHT, narrow-band integrated radiation intensity distributions predicted by using temperature-dependent refractive and absorption indices and predicted by using refractive and absorption indices at 1800 K everywhere in the plume are compared and shown in Figure 7.64. It should be noted at this point that, due to the lack of temperature-dependent optical properties of α-Al_2O_3, this comparison is discarded in Figure 7.64. As illustrated by the figure, using refractive and absorption indices at 1800 K everywhere in the plume provides reasonable narrow-band radiation intensity predictions and reduces CPU requirements of the solution of RTE in the coupled codes where repeated solutions of RTE are required.

306
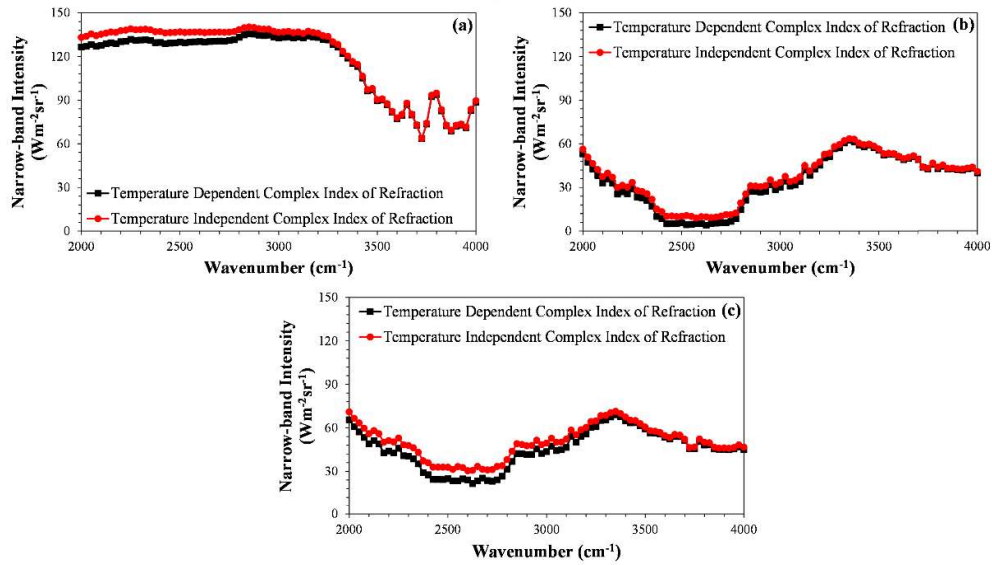
Figure 7.64. Narrow-band integrated radiation intensity distributions at x = 1 m, y = 1 m, and z = 7.9 m and along the direction of 0.0990147, 0.0990147, and 0.990147 predicted by using temperature-dependent refractive and absorption indices (non-uniform particle properties) and predicted by using refractive and absorption indices at 1800 K everywhere in the plume (uniform particle properties) for (a) γ-Al_2O_3 (b) liquid alumina with Anfimov et al. [131] and Bakhir et al. [132] (c) liquid alumina with Kuzmin et al. [129]

The effect of using spectral refractive and absorption indices instead of gray refractive and absorption indices on the RHT under rocket plume conditions is investigated by using the spectral and gray indices given in Figure 2.10 as spectral and gray refractive and absorption indices. Narrow-band integrated radiation intensity distributions predicted by using spectral and gray refractive indices are compared for γ-Al_2O_3, α-Al_2O_3, and liquid alumina in Figure 7.65. As shown in the figure, using gray refractive and absorption indices instead of spectral ones provides reasonably accurate narrow-band intensity distribution between the wavenumber range of $2000 - 4000$ cm^{-1} for the test case under investigation owing to very similar gray and spectral refractive and absorption indices in the same wavenumber interval (see Figure 2.10).
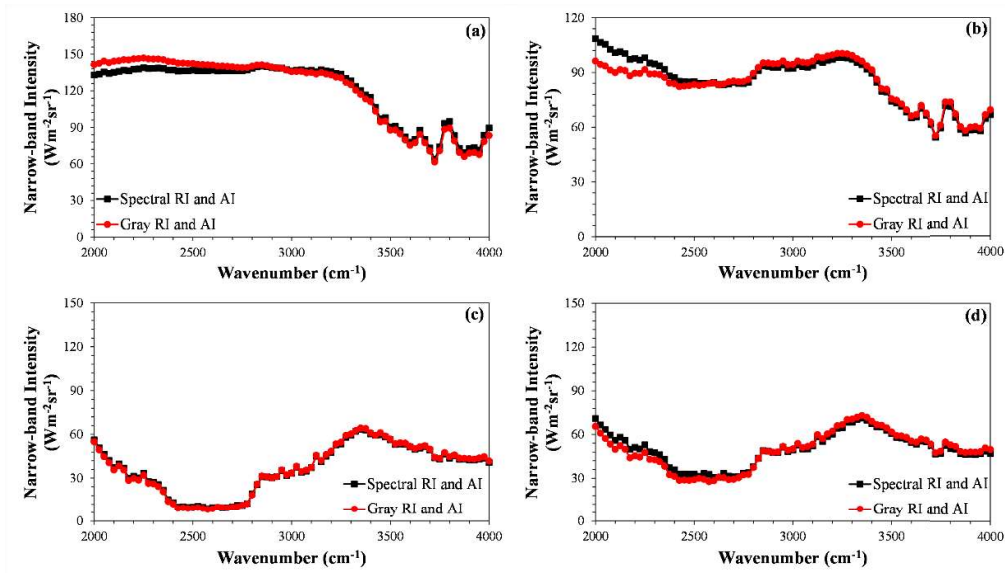
Figure 7.65. Narrow-band integrated radiation intensity distributions at x = 1 m, y = 1 m, and z = 7.9 m and along the direction of 0.0990147, 0.0990147 and 0.990147 predicted by using spectral and gray refractive and absorption indices for (a) γ-Al$_2$O$_3$ (b) α-Al$_2$O$_3$ (c) liquid alumina with Anfimov et al. [131] and Bakhir et al. [132] (c) liquid alumina with Kuzmin et al. [129]

The effect of using a PSD instead of average diameter, such as d_{43}, d_{32}, etc., on the infrared plume signature is also tested in this section. For this purpose, scattering coefficients and asymmetry factors of γ-Al$_2$O$_3$ are calculated using PSD, d_{32}, d_{43}, and 11.6 µm diameter and refractive and absorption indices at 1800 K. The predicted absorption coefficients, scattering coefficients and asymmetry factors are shown by Figure 7.66. As demonstrated by the figure, using d_{32}, d_{43}, and 11.6 µm as average diameter does not significantly influence the radiative properties of the alumina particle cloud.
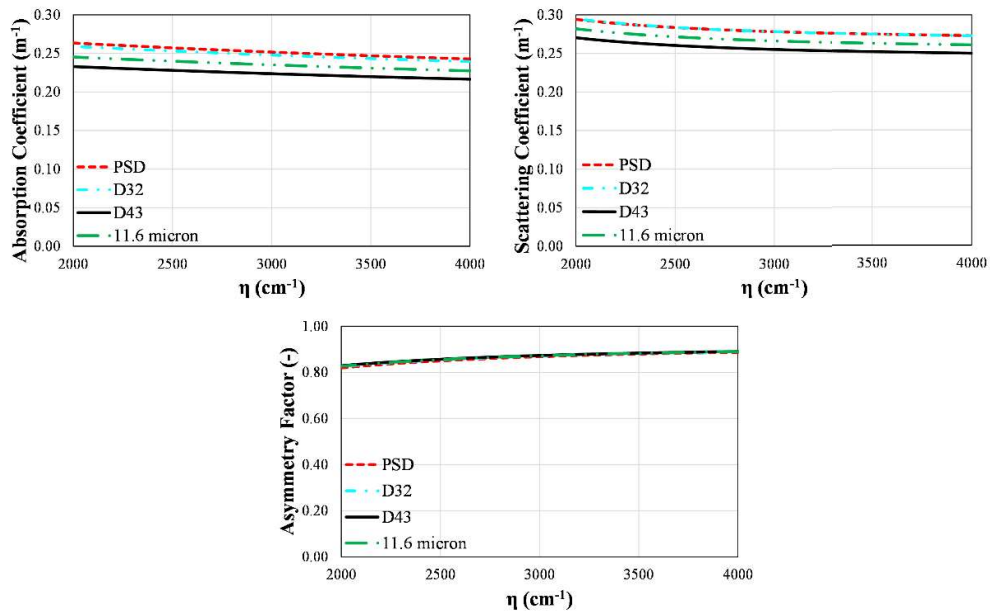
Figure 7.66. Absorption coefficients, scattering coefficients and asymmetry factors of the alumina particle cloud using PSD, d_{32}, d_{43}, and 11.6 μm diameter

Comparison of the narrow-band integrated radiation intensity distributions predicted by using PSD, d_{32}, d_{43}, and 11.6 μm diameter is demonstrated by Figure 7.67. As shown by the figure, using an average particle size (such as d_{32}, d_{43}, or 11.6 μm) instead of PSD does not significantly influence narrow-band integrated radiation intensity distribution between the wavenumber range of 2000 – 4000 cm^{-1}. Furthermore, the mean absolute percentage error in the narrow band intensities (considering the predictions using PSD as the reference solution) are calculated as 1.2 %, 1.4 %, and 1.2 % for d_{32}, d_{43}, and 11.6 μm, respectively. To conclude, using an average particle size instead of PSD provides reasonably accurate narrow-band intensity predictions for the test case under investigation.
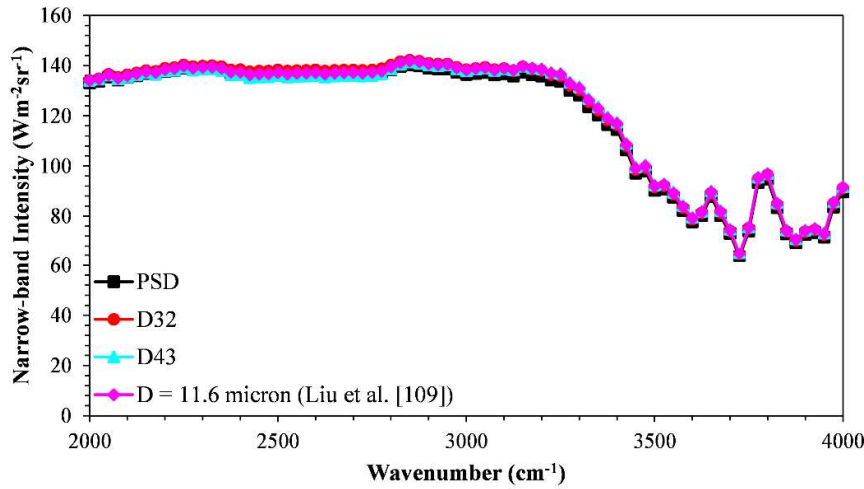
Figure 7.67. Narrow-band integrated radiation intensity distributions at x = 1 m, y = 1 m and z = 7.9 m and along the direction of 0.0990147, 0.0990147 and 0.990147 predicted by using PSD, d_{32}, d_{43}, and 11.6 μm diameter

Finally, the CPU time requirements of the simplified and rigorous approaches for particle radiative property models are investigated. For this purpose, CPU time requirements of the 3-D radiation models (i) using a PSD with temperature-dependent and spectral RI, (ii) using an average particle size with temperature-dependent and spectral RI, and (iii) using a PSD with temperature-independent and spectral RI are compared. Since the 3-D radiation model is already spectral, CPU time requirements of the spectral and gray particle radiative property models are not compared. The comparison of the CPU time requirements of the different approaches for particle radiative property models is shown in Table 7.38. As shown in the table, when using a PSD with temperature-dependent and spectral RI, CPU time for the calculation of particle radiative properties becomes comparable with that for the solution of RTE since it requires the solution of Mie theory for each spatial grid, wavelength, and particle size. However, using an average size instead of a PSD or using temperature-independent RI reduces CPU time for the calculation of particle radiative properties significantly. Since all particle radiative property models are utilized with SNBCK, the CPU time for the solution of RTE does not change

310

significantly with particle radiative property models. On the other hand, using a less sophisticated gas radiative property model instead of SNBCK may further reduce the total CPU time for the radiation model.

Table 7.38 CPU time requirements of the 3-D radiation models (i) using a PSD with temperature-dependent and spectral RI, (ii) using an average particle size with temperature-dependent and spectral RI, and (iii) using a PSD with temperature-independent and spectral RI

	PSD, Temperature-dependent RI, Spectral RI	Average size, Temperature-dependent RI, Spectral RI	PSD, Temperature-independent RI, Spectral RI
CPU Time for the Particle Properties (s)	1600	18.9	0.14
CPU Time for the Solution of RTE (s)	2027	2009	2026
Total CPU Time (s)	3627	2028	2026

7.9.1 Concluding Remarks for the Modeling of Infrared Plume Signatures of Solid Rocket Motors

In this section, the 3-D radiation model is applied to a test case representing the typical conditions of solid rocket motor exhaust plumes. It was found that neglecting the absorption indices of alumina leads to significant inaccuracies in the predictions of infrared plume signatures for the test cases when γ-Al_2O_3, α-Al_2O_3 are present in the rocket plume. However, the inaccuracy becomes insignificant when liquid alumina is present in the plume. Using temperature-dependent complex indices of refraction of alumina instead of temperature-independent complex indices of

refraction at 1800 K does not remarkably improve the accuracy in infrared plume signature predictions between 2000 - 4000 cm^{-1} for the test case under investigation. Therefore, temperature-independent complex indices of refraction can be utilized to reduce CPU requirements of the solution of RTE in the coupled problems by preventing the solution of Mie theory at each spatial grid. Comparisons of the infrared plume signature predictions of gray and spectral complex indices of refraction of alumina particles reveal that gray indices can safely be used for the solution of RTE in the rocket plumes in absence of spectral indices. Using a mean diameter such as Sauter-mean diameter or mass-mean diameter instead of a PSD provides reasonable infrared plume signature predictions.

CHAPTER 8

CONCLUSIONS

Due to the dominance of RHT in the freeboards of BFBCs because of the presence of radiating particles together with radiating gases, RHT characteristics during combustion of coal and coal/biomass blends in BFBCs require special attention. For this purpose, solution of RTE coupled with conservation equations of other transport processes is necessary. However, the solution of RTE in BFBCs is not straightforward due to spectral and directional nature of radiation and it requires robust methods not only for the solution of RTE but also for the estimation of spectral radiative properties of combustion gases, particles, and walls. Hence, the ultimate objective of this thesis is to couple comprehensive steady-state and transient system models for 0.3 MWt ABFBC test rig firing lignite and co-firing lignite/CR blends with limestone addition with a 3-D radiation model using MOL of DOM and robust models for the spectral radiative properties of combustion gases, particles, and walls. To achieve those objectives, the effect of spectral properties of combustion gases, particles, and walls and accuracy and performance of the estimation methods for those properties must be assessed first with the 3-D spectral radiation model without coupling it with the BFBC system model prior to coupling.

On the basis of the application of the 3-D spectral radiation code in isolation from the BFBC system model and coupled steady-state and transient system models with 3-D radiation model, the following conclusions have been reached:

- Bordbar's 10 band model and banded SLW-1 require around 50 and 20 times less CPU than that of banded SLW, respectively.

- Bordbar's 10 band model reduces CPU requirement of the spectral RTE solution for BFBCs with recycle or CFBCs where RHT is dominated by particles.

- Banded SLW-1 accurately predicts the RHT in BFBCs with and without recycle and reduces the CPU requirement of the spectral RTE solution in those systems.

- Using gray wall emissivity instead of spectral emissivity does not lead to significant error in incident wall HF predictions.

- Utilizing gray wall emissivity for hot refractory-lined walls leads to significant inaccuracies in the ST predictions of the combustion tests where particle load is low due to higher share of wall radiation in the RHT.

- Discrepancies between the ST predictions of gray and non-gray cold water wall emissivities and those of gray and non-gray cold slag covered water wall emissivities which are common in industry and utility boilers are found to be insignificant which is attributed to the combined effects of low wall temperatures and similar gray and non-gray water wall emissivities.

- While co-firing high ash content lignites with low ash content biomass in bubbling fluidized bed combustors, the contribution of cyclone particles to thermal radiation decreases. On the other hand, those of combustion gases and fine particles originated from biomass combustion increase.

- The contribution of gas radiation to total RHT in bubbling fluidized beds slightly increases with the addition of biomass due to (i) lower total freeboard (cyclone and bag filter) particle load due to low ash content of biomass and (ii) high hydrogen content of the biomass fuel leading to higher water vapor concentration along the freeboard.

- Co-firing lignite and biomass in a coal-fired power plant instead of only lignite combustion may not deteriorate RHT in the freeboard depending on the ash, hydrogen, and moisture content of the biomass.

- A parametric study carried out in a 1-D slab problem involving combustion gases and soot reveals that soot particle diameter and number of soot particles

314

in a soot aggregate do not significantly affect the net wall HF and ST predictions due to their insignificant effect on absorption coefficient.

- The presence of soot particles in the splash zone of BFBCs significantly improves incident wall HFs and STs due to the combined effects of higher absorption coefficient of soot compared to fly ash particle in the wavelength range of $1 - 7$ μm, which covers 85 % of the thermal radiation, and negligible scattering coefficient of soot throughout the entire thermal spectrum.

- Soot particles have been found to have a noticeable impact on RHT even at very low volume fractions based on a parametric study where different soot volume fractions, observed in different types of diffusion flames, are utilized.

- Planck-mean soot and fly ash particle properties are found to provide reasonably accurate RHT predictions for the freeboard of 0.3 MWt ABFBC test rig and can be used to improve the computational efficiency of the solution of RTE under these conditions.

- Utilization of a sophisticated radiation model, where RTE is explicitly solved in conjunction with the system model for $0.3\ MW_t$ ABFBC test rig instead of using Stefan-Boltzmann law and an empirical correlation for the RHT coefficient, does not significantly influence the freeboard temperature predictions for the test case where freeboard is bounded by hot refractory-lined walls. This insignificant effect is considered to be due to the low temperature difference between the refractory-lined walls and the freeboard medium leading to low heat transfer rates in the freeboard. However, the deviation between the freeboard temperature predictions of the FBC models with and without a sophisticated radiation model is remarkable for the combustion test where freeboard is taken to be enclosed by cold water walls at 537 K.

- Based on the outcomes obtained from the coupled steady-state FBC system model and 3-D radiation model, a combination of SLW-1 for spectral gas

properties, Mie theory for gray fly ash particle properties and gray wall properties provides sufficiently accurate HF, ST and freeboard temperature predictions with a significant saving in the CPU requirement in the coupled solution of RTE. Therefore, the combination of SLW-1 for spectral gas properties, Mie theory for gray fly ash particle properties and gray wall properties can be utilized to improve CPU efficiency of the coupled solution of RTE in BFBCs.

- O_2 and CO_2 emissions are not considerably affected by the use of radiation code in conjunction with the system model for BFBC for the combustion test under investigation as majority of the combustibles are burned in the bed section. However, CO emission predictions increase by the use of the radiation model coupled with BFBC model due to lower freeboard temperature predictions leading to low CO oxidation rates in the freeboard.

- The present transient FBC models coupled with the 3-D radiation model based on MOL of DOM utilizing SLW-1 model for combustion gases and gray radiative properties for particles and walls predicts accurately the transient responses of temperatures and O_2 and CO emissions on step changes imposed to coal and air flow rates for the combustion test with hot refractory-lined walls and with cold water walls.

- Using a sophisticated radiation model coupled with FBC system model provides slightly more accurate temperature predictions for the freeboard of the ABFBC test rig where Çan lignite is co-fired with CR and limestone addition.

- The temperature predictions of FBC models coupled with spectral and gray radiation models do not significantly differ for the co-combustion test under investigation. This slight difference is considered to be due to low temperature difference between the medium and the hot refractory-lined walls leading to low heat transfer rate in the freeboard section.

- At the lower part of the freeboard, the radiation is dominated by particles due to splashing particles whereas radiation is dominated by combustion gases at the upper part of freeboard. Thus, accurate methods for the estimation of spectral radiative properties of both combustion gases and particles are needed.

- Utilization of a radiation model coupled with the system model for BFBC co-firing lignite with CR and limestone addition does not provide any further accuracy in the predictions of gaseous emission of the species O_2, CO_2, CO, SO_2, NO and N_2O for the co-combustion test under consideration due to combustion of the majority of combustibles in the bed section owing to under bed feeding system.

After the 3-D radiation model based on MOL of DOM using robust models for the spectral radiative properties of combustion gases, particles, and walls is coupled with the steady-state and transient system models for BFBCs, the 3-D radiation model was decided to be applied to a test case representing the typical conditions of solid rocket motor exhaust plumes. The results of this study reveal the followings:

- Neglecting the absorption indices of alumina leads to significant inaccuracies in the predictions of infrared plume signatures for the test cases when γ-Al_2O_3, α-Al_2O_3 are present in the rocket plume. However, the inaccuracy becomes insignificant when liquid alumina is present in the plume.

- Using temperature-dependent complex indices of refraction of alumina instead of temperature-independent complex indices of refraction at 1800 K does not remarkably improve the accuracy in infrared plume signature predictions between $2000 - 4000$ cm^{-1} for the test case under investigation. Therefore, temperature-independent complex indices of refraction can be utilized to reduce CPU requirements of the solution of RTE in the coupled problems by preventing the solution of Mie theory at each spatial grid.

- Comparisons of the infrared plume signature predictions of gray and spectral complex indices of refraction of alumina particles reveal that gray indices can safely be used for the solution of RTE in the rocket plumes in absence of spectral indices.

- Using a mean diameter such as Sauter-mean diameter or mass-mean diameter instead of a PSD provides reasonable infrared plume signature predictions.

8.1   Suggestions for Future Work

Present study focuses on the coupling of radiation model with steady state and transient systems models of BFBC. Based on the above mentioned outcomes of the study, following recommendations are suggested for the future extension of the current work:

- Incorporation of more accurate chemical reaction model for more accurate predictions of the species O_2 and CO_2.
- Extending the 2-D CFD model for the incorporation of sulfur retention and nitrogen oxides formation and reduction mechnanisms for the accurate predictions of the gaseous pollutants SO_2, NO and N_2O, and comparing those predictions with the measurements.
- Extending the 2-D CFD model for the incorporation of co-firing lignite with biomass and comparing the predictions of the model with the measurements.
- Coupling the 2-D CFD model with more sophisticated particle radiative property models to account for the effect of particle size and char burnout.
- Coupling of the 3-D radiation model for the solid rocket motor exhaust plume with a system model to understand the effect of simplifying particle radiative property assumptions on the accuracy and CPU efficiency further.

318

REFERENCES

[1]   British Petroleum (BP), Statistical Review of World Energy 2021, BP Energy Outlook. https://www.bp.com/content/dam/bp/business-sites/en/global/corporate/pdfs/energy-economics/statistical-review/bp-stats-review-2021-full-report.pdf (accessed August 3, 2022).

[2]   International Energy Agency (IAE) - Key World Energy Statistics 2022, (n.d.). https://www.iea.org/reports/key-world-energy-statistics-2021/supply (accessed March 7, 2022).

[3]   L. Wang, J.E. Hustad, Ø. Skreiberg, G. Skjevrak, M. Grønli, A critical review on additives to reduce ash related operation problems in biomass combustion applications, Energy Procedia. 20 (2012) 20–29. https://doi.org/10.1016/j.egypro.2012.03.004.

[4]   O. Batir, N. Selçuk, G. Kulah, Effect of kaolin addition on alkali capture capability during combustion of olive residue, Combust. Sci. Technol. 191 (2019) 43–53. https://doi.org/10.1080/00102202.2018.1452376.

[5]   J. Silvennoinen, A new method to inhibit bed agglomeration problems in fluidized bed boilers, in: Proceesings of FBC2003, Jacksonville, Florida USA, 2003: pp. 1–9.

[6]   A.A. Khan, W. de Jong, P.J. Jansens, H. Spliethoff, Biomass combustion in fluidized bed boilers: Potential problems and remedies, Fuel Process. Technol. 90 (2009) 21–50. https://doi.org/10.1016/j.fuproc.2008.07.012.

[7]   Z. Sun, J. Shen, B. Jin, L. Wei, Combustion characteristics of cotton stalk in FBC, Biomass Bioenergy. 34 (2010) 761–770. https://doi.org/10.1016/j.biombioe.2010.01.019.

[8]   Z. Gogebakan, N. Selçuk, Cofiring lignite with hazelnut shell and cotton

residue in a pilot-scale fluidized bed combustor, Energy Fuels. 22 (2008) 1620–1627. https://doi.org/10.1021/ef700650x.

[9]   D. Vamvuka, M. Pitharoulis, G. Alevizos, E. Repouskou, D. Pentari, Ash effects during combustion of lignite/biomass blends in fluidized bed, Renew. Energy. 34 (2009) 2662–2671. https://doi.org/10.1016/j.renene.2009.05.005.

[10] M. Akram, C.K. Tan, D.R. Garwood, M. Fisher, D.R. Gent, W.G. Kaye, Co-firing of pressed sugar beet pulp with coal in a laboratory-scale fluidised bed combustor, Appl. Energy. 139 (2015) 1–8. https://doi.org/10.1016/j.apenergy.2014.11.008.

[11] Turkish Statistical Institute (TSI), (n.d.). http://www.turkstat.gov.tr/PreTablo.do?alt_id=1001 (accessed July 21, 2022).

[12] N. Sılgır, An investigation on the determination of nutrient contents of cottonseed meals produced in Çukurova Region (in Turkish) MSc Thesis, Mustafa Kemal University, Hatay, Turkey, 2015.

[13] Turkish Ministry of Trade, (2018). http://koop.gtb.gov.tr/data/5ad06bb9ddee7dd8b423eb23/2017 Fındık Raporu.pdf. (accessed August 26, 2018).

[14] S.M. Hocaoğlu, H.G. Haksevenler, İ. Baştürk, C. Aydöner, Zeytin Sektörü Atıklarının Yönetimi, TÜBİTAK-MAM Project No: 5148602, 2015.

[15] C. Hu, K. Luo, M. Zhou, J. Lin, D. Kong, J. Fan, Influences of secondary gas injection pattern on fluidized bed combustion process: A CFD-DEM study, Fuel. 268 (2020) 117314. https://doi.org/10.1016/j.fuel.2020.117314.

[16] C. Chen, L. Zhao, X. Wu, J. Wang, Numerical and experimental study on oxy-fuel coal and biomass co-firing in a bubbling fluidized bed, Energy Fuels. 33 (2019) 5829–5839. https://doi.org/10.1021/acs.energyfuels.8b04163.

[17] H. Zhou, G. Flamant, D. Gauthier, Y. Flitris, Simulation of coal combustion

in a bubbling fluidized bed by distinct element method, Chem. Eng. Res. Des. 81 (2003) 1144–1149. https://doi.org/10.1205/026387603770866308.

[18]   M.S. Yasar, N. Selçuk, G. Kulah, Modeling of fluidized bed combustion of lignite with high nitrogen content cotton residue, Combust Sci. Technol. 194 (2022) 435–448. https://doi.org/10.1080/00102202.2019.1688630.

[19]   F. Okasha, Modeling combustion of straw-bitumen pellets in a fluidized bed, Fuel Process. Technol. 88 (2007) 281–293. https://doi.org/10.1016/j.fuproc.2006.10.012.

[20]   F. Scala, P. Salatino, Modelling fluidized bed combustion of high-volatile solid fuels, Chem. Eng. Sci. 57 (2002) 1175–1196. https://doi.org/10.1016/S0009-2509(02)00004-0.

[21]   A. Saario, A. Oksanen, Comparison of global ammonia chemistry mechanisms in biomass combustion and selective noncatalytic reduction process conditions, Energy Fuels. 22 (2008) 297–305. https://doi.org/10.1021/ef700238a.

[22]   D.E. Alagoz, G. Kulah, N. Seluk, A comprehensive fluidized bed combustion model coupled with a radiation model, Combust Sci. Technol. 180 (2008) 910–926. https://doi.org/10.1080/00102200801894356.

[23]   Y. Hu, J. Wang, C.K. Tan, C. Sun, H. Liu, Coupling detailed radiation model with process simulation in Aspen Plus: A case study on fluidized bed combustor, Appl. Energy. 227 (2018) 168–179. https://doi.org/10.1016/j.apenergy.2017.08.030.

[24]   S.A. El-Sayed, E.H. Noseir, Simulation of combustion of sesame and broad bean stalks in the freeboard zone inside a pilot-scale bubbling fluidized bed combustor using CFD modeling, Appl. Therm. Eng. 158 (2019). https://doi.org/10.1016/j.applthermaleng.2019.113767.

[25]   M.F. Diba, M.R. Karim, J. Naser, Numerical modelling of a bubbling

fluidized bed combustion: A simplified approach, Fuel. 277 (2020). https://doi.org/10.1016/j.fuel.2020.118170.

[26]   D.E. Beasley, L.P. Golan, Dynamic response of fluidized beds, Chem. Eng. Commun. 79 (1989) 115–130. https://doi.org/10.1080/00986448908940030.

[27]   E. Ikonen, U. Kortela, Dynamic model for a bubbling fluidized bed coal combustor, Control Eng. Pract. 2 (1994) 1001–1006. https://doi.org/10.1016/0967-0661(94)91622-5.

[28]   N. Selçuk, E. Degirmenci, Dynamic simulation of fluidized bed combustors and its validation against measurements, Combust. Sci. Technol. 167 (2001) 1–27. https://doi.org/10.1080/00102200108952175.

[29]   A. Galgano, P. Salatino, S. Crescitelli, F. Scala, P.L. Maffettone, A model of the dynamics of a fluidized bed combustor burning biomass, Combust. Flame. 140 (2005) 371–384. https://doi.org/10.1016/j.combustflame.2004.12.006.

[30]   T. Kataja, P.O. Box, F.- Tampere, Dynamic Model of a Bubbling Fluidized Bed Boiler, (n.d.) 140–149.

[31]   V.K. Surasani, F. Kretschmer, P. Heidecke, M. Peglow, E. Tsotsas, Biomass combustion in a fluidized-bed system: An integrated model for dynamic plant simulations, Ind. Eng. Chem. Res. 50 (2011) 9936–9943. https://doi.org/10.1021/ie200537m.

[32]   L. Sun, D. Li, K.Y. Lee, Enhanced decentralized PI control for fluidized bed combustor via advanced disturbance observer, Control Eng. Pract. 42 (2015) 128–139. https://doi.org/10.1016/j.conengprac.2015.05.014.

[33]   M. Huttunen, J. Peltola, S. Kallio, L. Karvonen, T. Niemi, V. Ylä-Outinen, Analysis of the processes in fluidized bed boiler furnaces during load changes, Energy Procedia. 120 (2017) 580–587. https://doi.org/10.1016/j.egypro.2017.07.175.

[34]   G.M. Castilla, R.M. Montanés, D. Pallares, F. Johnsson, Dynamic modeling

of the reactive side in large-scale fluidized bed boilers, Ind. Eng. Chem. Res. 60 (2021) 3936–3956. https://doi.org/10.1021/acs.iecr.0c06278.

[35] F. Di Natale, R. Nigro, F. Scala, Heat and mass transfer in fluidized bed combustion and gasification systems, 2013. https://doi.org/10.1533/9780857098801.1.177.

[36] C. Ates, N. Selçuk, G. Kulah, Effect of changing biomass source on radiative heat transfer during co-firing of high-sulfur content lignite in fluidized bed combustors, Appl. Therm. Eng. 128 (2018) 539–550. https://doi.org/10.1016/j.applthermaleng.2017.09.011.

[37] C. Ates, N. Selçuk, G. Kulah, Effect of limestone addition on radiative heat transfer during co-firing of high-sulfur content lignite with biomass in fluidized bed combustors, Combust. Sci. Technol. 190 (2018) 1377–1391. https://doi.org/10.1080/00102202.2018.1452122.

[38] N. Selçuk, A. Batu, I. Ayranci, Performance of method of lines solution of discrete ordinates method in the freeboard of a bubbling fluidized bed combustor, J. Quant. Spectrosc. Radiat. Transf. 73 (2002) 503–516. https://doi.org/10.1016/S0022-4073(01)00225-4.

[39] G. Demirkaya, F. Arinç, N. Selçuk, I. Ayranci, Comparison between performances of Monte Carlo method and method of lines solution of discrete ordinates method, J. Quant. Spectrosc. Radiat. Transf. 93 (2005) 115–124. https://doi.org/10.1016/j.jqsrt.2004.08.016.

[40] C. Ates, G. Ozen, N. Selçuk, G. Kulah, Radiative heat transfer in strongly forward scattering media of circulating fluidized bed combustors, J. Quant. Spectrosc. Radiat. Transf. 182 (2016) 264–276. https://doi.org/10.1016/j.jqsrt.2016.06.009.

[41] C. Ates, N. Selçuk, G. Ozen, G. Kulah, Benchmarking grey particle approximations against nongrey particle radiation in circulating fluidized bed combustors, Numer. Heat Transf. B Fundam. 71 (2017) 467–484.

https://doi.org/10.1080/10407790.2017.1309144.

[42] C. Ates, O. Sen, N. Selçuk, G. Kulah, Influence of spectral particle properties on radiative heat transfer in optically thin and thick media of fluidized bed combustors, Int. J. Therm. Sci. 122 (2017) 266–280. https://doi.org/10.1016/j.ijthermalsci.2017.08.023.

[43] C. Ates, N. Selçuk, G. Kulah, Significance of particle concentration distribution on radiative heat transfer in circulating fluidized bed combustors, Int. J. Heat Mass Transf. 117 (2018) 58–70. https://doi.org/10.1016/j.ijheatmasstransfer.2017.09.138.

[44] C. Ates, N. Selçuk, G. Kulah, Influence of gray particle assumption on the predictive accuracy of gas property approximations, J. Quant. Spectrosc. Radiat. Transf. 220 (2018) 67–83. https://doi.org/10.1016/j.jqsrt.2018.09.010.

[45] C. Ates, N. Selçuk, G. Kulah, Influence of fly ash composition on non-gray particle radiation in combusting systems, J. Quant. Spectrosc. Radiat. Transf. 215 (2018) 25–40. https://doi.org/10.1016/j.jqsrt.2018.05.004.

[46] M.F. Modest, Radiative Heat Transfer, third ed., Elsevier, New York, 2013.

[47] M.F. Modest, The treatment of nongray properties in radiative heat transfer: From past to present, J. Heat Transfer. 135 (2013) 061801. https://doi.org/10.1115/1.4023596.

[48] V.P. Solovjov, B.W. Webb, F. Andre, Radiative properties of gases. In: Kulacki FA, editor. Handbook of thermal science and engineering, Cham: Springer; 2017, pp. 1–74. https://doi.org/10.1007/978-3-319-32003-8_59-1.

[49] H. Chu, F. Liu, H. Zhou, Calculations of gas thermal radiation transfer in one-dimensional planar enclosure using LBL and SNB models, Int. J. Heat Mass Transf. 54 (2011) 4736–4745. https://doi.org/10.1016/j.ijheatmasstransfer.2011.06.002.

[50] H.C. Hottel, A.F. Sarofim, Radiative Transfer, McGraw-Hill, New York,

1967.

[51] M.K. Denison, B.W. Webb, An absorption-line blackbody distribution function for efficient calculation of total gas radiative transfer, J. Quant. Spectrosc. Radiat. Transf. 50 (1993) 499–510. https://doi.org/10.1016/0022-4073(93)90043-H.

[52] M.K. Denison, A spectral line-based weighted-sum-of-gray-gases model for arbitrary RTE solvers, PhD thesis, Brigham Young University, Provo, UT, 1994.

[53] M.K. Denison, B.W. Webb, The spectral-line weighted-sum-of-gray-gases model for H_2O/CO_2 mixtures, J. Heat Transfer. 117 (1995) 788–792. https://doi.org/10.1115/1.2822652.

[54] M.F. Modest, H. Zhang, The full-spectrum correlated-k distribution for thermal radiation from molecular gas-particulate mixtures, J. Heat Transfer. 124 (2002) 30–38. https://doi.org/10.1115/1.1418697.

[55] F.N. Çayan, N. Selçuk, A comparative study of modeling of radiative heat transfer using MOL solution of DOM with gray gas, wide-band correlated-k, and spectral line-based weighted sum of gray gases models, Numer. Heat Transf. B Fundam. 52 (2007) 281–296. https://doi.org/10.1080/10407790701372728.

[56] V. Kez, J.L. Consalvi, F. Liu, J. Ströhle, B. Epple, Assessment of several gas radiation models for radiative heat transfer calculations in a three-dimensional oxy-fuel furnace under coal- fired conditions, Int. J. Therm. Sci. 120 (2017) 289–302. https://doi.org/10.1016/j.ijthermalsci.2017.06.017.

[57] V. Kez, J.L. Consalvi, F. Liu, T. Gronarz, J. Ströhle, R. Kneer, B. Epple, Investigation of gas and particle radiation modelling in wet oxy-coal combustion atmospheres, Int. J. Heat Mass Transf. 133 (2019) 1026–1040. https://doi.org/10.1016/j.ijheatmasstransfer.2019.01.013.

[58] X. Yang, Z. He, S. Dong, H. Tan, Evaluation of the non-gray weighted sum of gray gases models for radiative heat transfer in realistic non-isothermal and non-homogeneous flames using decoupled and coupled calculations, Int. J. Heat Mass Transf. 134 (2019) 226–236. https://doi.org/10.1016/j.ijheatmasstransfer.2019.01.038.

[59] H. Bordbar, G.C. Fraga, S. Hostikka, An extended weighted-sum-of-gray-gases model to account for all CO_2 - H_2O molar fraction ratios in thermal radiation, Int. Commun. Heat Mass Transf. 110 (2020) 104400. https://doi.org/10.1016/j.icheatmasstransfer.2019.104400.

[60] G. Ozen, N. Selçuk, Sensitivity of radiation modeling to property estimation techniques in the freeboard of lignite-fired bubbling fluidized bed combustors (BFBCs), Combust. Sci. Technol. 186 (2014) 684–697. https://doi.org/10.1080/00102202.2014.883848.

[61] H. Bordbar, A. Maximov, T. Hyppänen, Improved banded method for spectral thermal radiation in participating media with spectrally dependent wall emittance, Appl. Energy. 235 (2019) 1090–1105. https://doi.org/10.1016/j.apenergy.2018.11.033.

[62] V.P. Solovjov, B.W. Webb Radiative transfer model parameters for carbon monoxide at high temperature, in 11th International Heat Transfer Conference (IHTC), Kyongju, Korea: 1998, pp. 445–450. https://doi:10.1615/ihtc11.4520.

[63] V.P. Solovjov, B.W. Webb, SLW modeling of radiative transfer in multicomponent gas mixtures, J. Quant. Spectrosc. Radiat. Transf. 65 (2000) 655-672. https://doi:10.1016/S0022-4073(99)00133-8.

[64] V.P. Solovjov, B.W. Webb, Global spectral methods in gas radiation: The exact limit of the SLW model and its relationship to the ADF and FSK methods, J. Heat Transfer. 133 (2011) 042701. https://doi:10.1115/1.4002775.

[65] J.T. Pearson, The development of updated and improved SLW model parameters and its application to comprehensive combustion predictions, PhD thesis, Brigham Young University, Provo, UT, 2013.

[66] J.T. Pearson, B.W. Webb, V.P. Solovjov, J. Ma, Efficient representation of the absorption line blackbody distribution function for H_2O, CO_2, and CO at variable temperature, mole fraction, and total pressure. J. Quant. Spectrosc. Radiat. Transf. 138 (2014) 82-96. https://doi:10.1016/j.jqsrt.2014.01.019.

[67] R. Demarco, J.L. Consalvi, A. Fuentes, S. Melis, Assessment of radiative property models in non-gray sooting media, Int. J. Therm. Sci. 50 (2011) 1672-1684. https://doi:10.1016/j.ijthermalsci.2011.03.026.

[68] V.P. Solovjov, F. Andre, D. Lemonnier, B.W. Webb, The rank correlated SLW model of gas radiation in non-uniform media, J. Quant. Spectrosc. Radiat. Transf. 197 (2017) 26-44. https://doi:10.1016/j.jqsrt.2017.01.034.

[69] V.P. Solovjov, F. Andre, D. Lemonnier, B.W. Webb, The Scaled SLW model of gas radiation in non-uniform media based on Planck-weighted moments of gas absorption cross-section, J. Quant. Spectrosc. Radiat. Transf. 206 (2018) 198-212. https://doi:10.1016/j.jqsrt.2017.11.012.

[70] B.W. Webb, V.P. Solovjov, F. Andre, An exploration of the influence of spectral model parameters on the accuracy of the rank correlated SLW model. J. Quant. Spectrosc. Radiat. Transf. 218 (2018) 161-170. https://doi:10.1016/j.jqsrt.2018.06.023.

[71] V.P. Solovjov, B.W. Webb, F. André, D. Lemonnier, Locally correlated SLW model for prediction of gas radiation in non-uniform media and its relationship to other global methods, J. Quant. Spectrosc. Radiat. Transf. 245 (2020) 106857. https://doi:10.1016/j.jqsrt.2020.106857.

[72] G. Colomer, R. Cònsul, A. Oliva, Coupled radiation and natural convection: Different approaches of the SLW model for a non-gray gas mixture, J. Quant. Spectrosc. Radiat. Transf. 107 (2007) 30-46.

https://doi:10.1016/j.jqsrt.2006.12.011.

[73] A. Ibrahim, D. Saury, D. Lemonnier, Coupling of turbulent natural convection with radiation in an air-filled differentially-heated cavity at Ra = 1.5 x 10^9, Comput. Fluids. 88 (2013) 115-125. https://doi:10.1016/j.compfluid.2013.09.006.

[74] M. Cherifi, S. Laouar-Meftah, A. Benbrik, D. Lemonnier, D. Saury, Interaction of radiation with double-diffusive natural convection in a three-dimensional cubic cavity filled with a non-gray gas mixture in cooperating cases, Numer. Heat Transf. A Appl. 69 (2016) 479-496. https://doi:10.1080/10407782.2015.1090233.

[75] Y. Billaud, D. Saury, D. Lemonnier, Numerical investigation of coupled natural convection and radiation in a differentially heated cubic cavity filled with humid air. Effects of the cavity size, Numer. Heat Transf. A Appl. 72 (2017) 495-518. https://doi:10.1080/10407782.2017.1386509.

[76] P.D. Nguyen, A. Danda, M. Embouazza, M. Gazdallah, P. Evrard, V. Feldheim, Application of the spectral line-based weighted-sum-of-gray-gases model (SLWSGG) to the calculation of radiative heat transfer in steel reheating furnaces firing on low heating value gases, J. Phys. Conf. Ser. 369 (2012) 012008. https://doi:10.1088/1742-6596/369/1/012008.

[77] B. Garten, F. Hunger, D. Messig, B. Stelzner, D. Trimis, C. Hasse, Detailed radiation modeling of a partial-oxidation flame, Int. J. Therm. Sci. 87 (2015) 68-84. https://doi:10.1016/j.ijthermalsci.2014.07.022.

[78] G. Ozen, N. Selçuk, SLW model for computational fluid dynamics modeling of combustion systems: Implementation and validation, Numer. Heat Transf. B Fundam. 70 (2016) 47-55. https://doi:10.1080/10407790.2016.1173499.

[79] B.W. Webb, J. Ma, J.T. Pearson, V.P Solovjov, SLW modeling of radiation transfer in comprehensive combustion predictions, Combust. Sci. Technol. 190 (2018) 1392-1408. https://doi:10.1080/00102202.2018.1452123.

[80] J. Badger, B.W. Webb, V.P. Solovjov, An exploration of advanced SLW modeling approaches in comprehensive combustion predictions, Combust. Sci. Technol. 194 (2019) 225-241. https://doi:10.1080/00102202.2019.1678907.

[81] V.P. Solovjov, D. Lemonnier, B.W. Webb, The SLW-1 model for efficient prediction of radiative transfer in high temperature gases, J. Quant. Spectrosc. Radiat. Transf. 112 (2011) 1205−1212. https://doi.org/10.1016/j.jqsrt.2010.08.009.

[82] V.P. Solovjov, D. Lemonnier, B.W. Webb, SLW-1 modeling of radiative heat transfer in nonisothermal nonhomogeneous gas mixtures with soot, J. Heat Transfer. 133 (2011) 102701. https://doi:10.1115/1.4003903.

[83] P. Evrard, V. Feldheim, P. Lybaert, An alternative method to optimise the SLW Grey Gases, J. Phys. Conf. Ser. 395 (2012) 012007. https://doi:10.1088/1742-6596/395/1/012007.

[84] J. Meulemans, An assessment of some non-gray global radiation models in enclosures, J. Phys. Conf. Ser. 676 (2016) 012017. https://doi:10.1088/1742-6596/676/1/012017.

[85] H. Amiri, K. Lari, Comparison of global radiative models in two-dimensional enclosures at radiative equilibrium, Int. J. Therm. Sci. 104 (2016) 423-436. https://doi:10.1016/j.ijthermalsci.2016.01.020.

[86] S. Cholake, S.P. Venkateshan, T. Sundararajan, Combined convection and radiation heat transfer in non-gray participating media in a differentially heated square cavity, Comput. Therm. Sci. 11 (2019) 489-507. https://doi:10.1615/ComputThermalScien.2019026257.

[87] G. Ozen, C. Ates, N. Selçuk, G. Kulah, Assessment of SLW-1 model in the presence of gray and non-gray particles. Int. J. Therm. Sci. 136 (2019) 420-432. https://doi:10.1016/j.ijthermalsci.2018.10.038.

[88] H. Bordbar, T. Hyppänen, Line by line based band identification for non-gray gas modeling with a banded approach, Int. J. Heat Mass Transf. 127 (2018) 870–884. https://doi.org/10.1016/j.ijheatmasstransfer.2018.06.093.

[89] A. Maximov, Theoretical analysis and numerical simulation of spectral radiative properties of combustion gases, PhD thesis, Lappeenranta University of Technology, Finland, 2012.

[90] K. Andersson, R. Johansson, S. Hjärtstam, F. Johnsson, B. Leckner, Radiation intensity of lignite-fired oxy-fuel flames, Exp. Therm. Fluid Sci. 33 (2008) 67–76. https://doi.org/10.1016/j.expthermflusci.2008.07.010.

[91] J. Guo, F. Hu, W. Luo, P. Li, Z. Liu, A full spectrum k-distribution based non-gray radiative property model for fly ash particles, Int. J. Heat Mass Transf. 118 (2018) 103–115. https://doi.org/10.1016/j.ijheatmasstransfer.2017.10.092.

[92] N. Selçuk, E. Degirmenci, Y. Gogebakan, Modeling of a Bubbling AFBC with Volatiles Release, J. Energy Resour. Technol. 125 (2003) 72. https://doi.org/10.1115/1.1506937.

[93] Y. Gogebakan, N. Selçuk, Assessment of a model with char attrition for a bubbling atmospheric fluidized-bed combustor, Combust Sci. Technol. 176 (2004) 799–818. https://doi.org/10.1080/00102200490428413.

[94] H. Altindag, Y. Gogebakan, N. Selçuk, Sulfur capture for fluidized-bed combustion of high-sulfur content lignites, Appl. Energy. 79 (2004) 403–424. https://doi.org/10.1016/j.apenergy.2004.01.006.

[95] O. Afacan, Y. Gogebakan, N. Selçuk*, Modeling of NOx emissions from fluidized bed combustion of high volatile lignites, Combust Sci. Technol. 179 (2007) 227–247. https://doi.org/10.1080/00102200600809191.

[96] G. Kulah, E.M. Morali, N. Selçuk, Mathematical modeling of a bubbling fluidized bed combustor cofired with lignite and biomass, Combust Sci.

Technol. 182 (2010) 600–612. https://doi.org/10.1080/00102200903466244.

[97] G. Kulah, Validation of a FBC model for co-firing of hazelnut shell with lignite against experimental data, Exp. Therm. Fluid Sci. 34 (2010) 646–655. https://doi.org/10.1016/j.expthermflusci.2009.12.006.

[98] ANSYS Inc., ANSYS Fluent, (2020). https://www.ansys.com/products/fluids/ansys-fluent (accessed May 1, 2023).

[99] W.A. Fiveland, Three-dimensional radiative heat-transfer solutions by the discrete-ordinates method, J. Thermophys. 2 (1988) 309–316. https://doi.org/10.2514/3.105.

[100] W.A. Fiveland, A.S. Jamaluddin, Three-dimensional spectral radiative heat transfer solutions by the discrete-ordinates method, J. Thermophys. 5 (1991) 335–339. https://doi.org/10.2514/3.268.

[101] B.G. Carlson, K.D. Lathrop, Transport theory-the method of discrete ordinates, in: H. Greenspan, C.N. Kelber, D. Okrent (Eds.), Computing Methods in Reactor Physics, Gordon & Breach, New York, 1968: pp. 165–266.

[102] C. Ateş, Nongray Gas and Nongray Particle Effects in Modeling Fluidied Bed Combustor, PhD thesis, Middle East Technical University, Ankara, TR, 2018.

[103] C.P. Thurgood, A. Pollard, H.A. Becker, The T_N quadrature set for the discrete ordinates method, J. Heat Transfer. 117 (1995) 1068–1070. https://doi.org/10.1115/1.2836285.

[104] A. Yücel, Solution of the discrete ordinates equations for a radiatively participating medium by the method of lines, in: Vichnevexsky, R., Knight, D., Richter, G. (Eds.), Advances in Computer Methods for Partial Differential Equations VII, IMACS, New Brunswick, NJ, 1992, pp. 838–844.

[105] R. Weiner, B.A. Schmitt, H. Podhaisky, ROWMAP - A ROW-code with Krylov techniques for large stiff ODEs, Appl. Numer. Math. 25 (1997) 303–319. https://doi.org/10.1016/S0168-9274(97)00067-6.

[106] I. Ayrancı, The method of lines solution of discrete ordinates method for radiative heat transfer in 3-D rectangular enclosures containing scattering media, MSc thesis, Middle East Technical University, Ankara, TR, 2001.

[107] W.E. Schiesser, The Numerical Method of Lines in Integration of Partial Differential Equations, Academic Press Inc., 1991.

[108] P. Saucez, W.E. Schiesser, A.V. Wouwer, Upwinding in the method of lines, Math. Comput. Simul. 56 (2001) 171–185. https://doi.org/10.1016/S0378-4754(01)00288-9.

[109] C.B. Ludwig, W. Malkmus, J.E. Reardon, J.A.L. Thomson, Handbook of infrared radiation from combustion gases, NASA SP-3080, 1973.

[110] A. Soufiani, J. Taine, High temperature gas radiative property parameters of statistical narrow-band model for H_2O, CO_2 and CO, and correlated-K model for H_2O and CO_2, Int. J. Heat Mass Transf. 40 (1997) 987–991. https://doi.org/10.1016/0017-9310(96)00129-9.

[111] A.A. Lacis, V. Oinas, A description of the correlated k distribution method for modeling nongray gaseous absorption, thermal emission, and multiple scattering in vertically inhomogeneous atmospheres, J. Geophys. Res. Atmos. 96 (1991) 9027–9063. https://doi.org/10.1029/90JD01945.

[112] F. Liu, G.J. Smallwood, Ö.L. Gülder, Application of statistical narrowband model to three-dimensional absorbing-emitting-scattering media, J. Thermophys. Heat Trans. 13 (1999) 285–291. https://doi.org/10.2514/2.6453.

[113] M.H. Bordbar, G. Wecel, T. Hyppänen, A line by line based weighted sum of gray gases model for inhomogeneous CO_2-H_2O mixture in oxy-fired

combustion, Combust Flame. 161 (2014) 2435–2445. https://doi.org/10.1016/j.combustflame.2014.03.013.

[114] L.S. Rothman, I.E. Gordon, R.J. Barber, H. Dothe, R.R. Gamache, A. Goldman, V.I. Perevalov, S.A. Tashkun, J. Tennyson, HITEMP, the high-temperature molecular spectroscopic database, J. Quant. Spectrosc. Radiat. Transf. 111 (2010) 2139–2150. https://doi.org/10.1016/j.jqsrt.2010.05.001.

[115] T.F. Smith, Z.F. Shen, J.N. Friedman, Evaluation of coefficients for the weighted sum of gray gases model, J. Heat Transf. 104 (1982) 602–608. https://doi.org/10.1115/1.3245174.

[116] V.P. Solovjov, D. Lemonnier, B.W. Webb, 2011. SLW-1 modeling of radiative heat transfer in nonisothermal nonhomogeneous gas mixtures with soot, J. Heat Transfer. 133, 102701. https://doi.org/10.1115/1.4003903.

[117] C.F. Bohren, D.R. Huffman, Absorption and scattering of light by small particles, John Wiley & Sons, New York, 1983.

[118] H. Tyagi, Radiative and combustion properties of nanoparticle-laden liquids, PhD thesis, Arızona State University, Tempe, AZ, 2008.

[119] L.A. Dombrovsky, The use of transport approximation and diffusion-based models in radiative transfer calculations, Comput. Therm. Sci.. 4 (2012) 297–315. https://doi.org/10.1615/ComputThermalScien.2012005050.

[120] K. Tian, K.A. Thomson, F. Liu, D.R. Snelling, G.J. Smallwood, D. Wang, Determination of the morphology of soot aggregates using the relative optical density method for the analysis of TEM images, Combust. Flame. 144 (2006) 782–791. https://doi.org/10.1016/j.combustflame.2005.06.017.

[121] D.W. Mackowski, A simplified model to predict the effects of aggregation on the absorption properties of soot particles, J. Quant. Spectrosc. Radiat. Transf. 100 (2006) 237–249. https://doi.org/10.1016/j.jqsrt.2005.11.041.

[122] T.L. Farias, M.G. Carvalho, U.O. Koylu, G.M. Faeth, Computational evaluation of approximate Rayleigh-Debye-Gans/fractal-aggregate theory for the absorption and scattering properties of soot, J. Heat Transfer. 117 (1995) 152–159. https://doi.org/10.1115/1.2822296.

[123] D.G. Goodwin, Infrared optical constants of coal slags, PhD thesis, Stanford University, Stanford, CA, 1986.

[124] J.L. Ebert, Infrared optical properties of coal slag at high temperatures, PhD thesis, Stanford University, Stanford, CA, 1994.

[125] H. Chang, T.T. Charalampopoulos, Determination of the wavelength dependence of refractive indices of flame soot, Proc. Math. Phys. Eng. Sci. 430 (1990) 577–591. https://doi.org/10.1098/rspa.1990.0107.

[126] S.C. Lee, C.L. Tien, Optical constants of soot in hydrocarbon flames, Symp. (Int.) Combust. 18 (1981) 1159–1166. https://doi.org/10.1016/S0082-0784(81)80120-8.

[127] M.R. Querry, Optical Constants, AD-A158 623, University of Missouri Kansas City, Missouri, 1985.

[128] L.A. Dombrovsky, Radiation heat transfer in disperse systems, Begell House, New York, 1996.

[129] V.A. Kuzmin, E.I. Maratkanova, I.A. Zagrai, Modeling of thermal radiation of heterogeneous combustion products in the model solid rocket engine plume, Procedia Eng. 206 (2017) 1801–1807. https://doi.org/10.1016/j.proeng.2017.10.716.

[130] Y.A. Plastinin, H.P. Sipatchev, G.F. Karabadzhak, B.A. Khmelinin, A.G. Khiebnikov, Y.N. Shishkin, Influence of alumina particles' phase transition on its radiation in the middle infrared and ultraviolet regions of spectrum, 38th Aerospace Sciences Meeting and Exhibit. (2000). https://doi.org/10.2514/6.2000-735.

[131] N.A. Anfimov, G.F. Karabadjak, B.A. Khmelinin, Y.A. Plastinin, A. V. Rodionov, Analysis of mechanisms and nature of radiation from aluminum oxide in different phase states in solid rocket exhaust plumes, AIAA 28th Thermophysics Conference C. (1993). https://doi.org/10.2514/6.1993-2818.

[132] L.P. Bakhir, G.I. Levashenko, V. V. Tamanovich, Refinement of the imaginary part of the complex refractive index of liquid aluminum oxide, J. Appl. Spectrosc. 26 (1977) 378–383.

[133] J. Kischkat, S. Peters, B. Gruska, M. Semtsiv, M. Chashnikova, M. Klinkmüller, O. Fedosenko, S. MacHulik, A. Aleksandrova, G. Monastyrskyi, Y. Flores, W.T. Masselink, Mid-infrared optical properties of thin films of aluminum oxide, titanium dioxide, silicon dioxide, aluminum nitride, and silicon nitride, Appl Opt. 51 (2012) 6789–6798. https://doi.org/10.1364/AO.51.006789.

[134] J.Y. Ko, E. Lee, S. Kwon, Influence of optical properties of alumina particles on the radiative base heating from solid rocket plume, Adv. Space Res. 64 (2019) 514–526. https://doi.org/10.1016/j.asr.2019.04.024.

[135] Q. Binauld, J.M. Lamet, L. Tessé, P. Rivière, A. Soufiani, Numerical simulation of radiation in high altitude solid propellant rocket plumes, Acta Astronaut. 158 (2019) 351–360. https://doi.org/10.1016/j.actaastro.2018.05.041.

[136] G. Cai, D. Zhu, X. Zhang, Numerical simulation of the infrared radiative signatures of liquid and solid rocket plumes, Aerosp. Sci. Technol. 11 (2007) 473–480. https://doi.org/10.1016/j.ast.2007.02.008.

[137] R. Duval, A. Soufiani, J. Taine, Coupled radiation and turbulent multiphase flow in an aluminised solid propellant rocket engine, J. Quant. Spectrosc. Radiat. Transf. 84 (2004) 513–526. https://doi.org/10.1016/S0022-4073(03)00268-1.

[138] S. Carlotti, F. Maggi, Experimental techniques for characterization of particles in plumes of sub-scale solid rocket motors, Acta Astronaut. 186 (2021) 496–507. https://doi.org/10.1016/j.actaastro.2021.06.011.

[139] J.D. Jackson, C.C. Yen, Measurements of total and spectral emissivities of some ceramic fibre insulation materials, in: P. Kirkwood (Ed.), Ceramics in Energy Applications, The Institute of Energy, London, UK, 1994, pp. 159–174. https://doi.org/10.1016/B978-0-08-042133-9.50016-2.

[140] H. Jo, J.L. King, K. Blomstrand, K. Sridharan, Spectral emissivity of oxidized and roughened metal surfaces, Int. J. Heat Mass Transf. 115 (2017) 1065–1071. https://doi.org/10.1016/j.ijheatmasstransfer.2017.08.103.

[141] N. Selçuk, Ü. Sivrioğlu, Mathematical modeling of coal-fired fluidized beds, J. Therm. Sci. Technol. (in Turkish), 3 (1980) 31–38.

[142] M.S. Yasar, N. Selçuk, G. Kulah, Modeling of fluidized bed combustion of lignite with high nitrogen content cotton residue, Combust. Sci. Technol. 194 (2022) 435–448. https://doi.org/10.1080/00102202.2019.1688630.

[143] J.R. Grace, R. Clift, on the Two-Phase Theory of Fluidization, Chem. Eng. Sci. 29 (1974) 327–334. https://doi.org/10.1016/0009-2509(74)80039-4.

[144] J.R. Grace, D. Harrison, The behaviour of freely bubbling fluidised beds, Chem. Eng. Sci. 24 (1969) 497–508. https://doi.org/10.1016/0009-2509(69)85021-9.

[145] P.E.G. Gogolek, H.A. Becker, Calculation of the expansion of a bubbling fluidised bed of coarse particles, Powder Technol. 71 (1992) 107–110. https://doi.org/10.1016/0032-5910(92)88010-F.

[146] J.F. Davidson, D. Harrison, Fluidized particles 1st edn., Cambridge University Press, New York, 1963.

[147] S. Mori, C.Y. Wen, Estimation of bubble diameter in gaseous fluidized beds, AIChE J. 21 (1975) 109–115. https://doi.org/10.1002/aic.690210114.

[148] J.H. Choi, I.Y. Chang, D.W. Shun, C.K. Yi, J.E. Son, S.D. Kim, Correlation on the particle entrainment rate in gas fluidized beds, Ind. Eng. Chem. Res. 38 (1999) 2491–2496. https://doi.org/10.1021/ie980707i.

[149] J.P. Hannes, Mathematical modelling of circulating fluidized bed combustion, RWTH Aachen, Aachen, DE, 1996.

[150] J.D. Hazlett, M.A. Bergougnou, Influence of bubble size distribution at the bed surface on entrainment profile, Powder Technol. 70 (1992) 99–107. https://doi.org/10.1016/0032-5910(92)85038-W.

[151] J.F. Stubington, S.W. Chan, S.J. Clough, A model for volatiles release into a bubbling fluidized-bed combustor, AIChE J. 36 (1990) 75–85. https://doi.org/10.1002/aic.690360110.

[152] D.B. Anthony, J.B. Howard, Coal devolatilization and hydrogastification, AIChE J. 22 (1976) 625–656. https://doi.org/10.1002/aic.690220403.

[153] H.C. Hottel, G.C. Williams, N.M. Nerheim, G.R. Schneider, Kinetic studies in stirred reactors: Combustion of carbon monoxide and propane, Symp. (Int.) Combust. 10 (1965) 111-121. https://doi.org/10.1016/S0082-0784(65)80155-2.

[154] E. Değirmenci, Dynamic simulation of fluidized bed combustors, PhD thesis, Middle East Technical University, Ankara, TR, 2000.

[155] K. Jung, R.D. La Nauze, Sherwood numbers for burning particles in fluidized beds, in: 4th Conference (International) on Fluidization, Engineering Foundation, Koshikojima, Japan, 1983: pp. 427–434.

[156] M.A. Field, D.W. Gill, B.B. Morgan, P.G.W. Hawksley, Combustion of pulverized coal, British Coal Utilization Research Association, England, 1967.

[157] J. Adánez, L.F. De Diego, F. García-Labiano, A. Abad, J.C. Abanades, Determination of biomass char combustion reactivities for FBC applications

by a combined method, Ind. Eng. Chem. Res. 40 (2001) 4317–4323. https://doi.org/10.1021/ie0102394.

[158] H. Altindağ, Mathematical modeling of sulfur retention in fluidized bed combustors, MSc thesis, Middle East Technical University, Ankara, TR, 2003.

[159] M.S. Yasar, Mathematical modeling of a bubbling fluidized bed combustor co-fired with cotton residue and lignite, MSc thesis, Middle East Technical University, Ankara, TR 2018.

[160] Z. Wu, Y. Ohtsuka, Remarkable formation of N_2 from a Chinese lignite during coal pyrolysis, Energy Fuels. 10 (1996) 1280–1281. https://doi.org/10.1021/ef960050i.

[161] S. Yuan, X. li Chen, W.-F. Li, H.-F. Liu, F.-C. Wang, Nitrogen conversion under rapid pyrolysis of two types of aquatic biomass and corresponding blends with coal, Bioresour. Technol. 102 (2011) 10124–10130. https://doi.org/10.1016/j.biortech.2011.08.047.

[162] T. Shimizu, Y. Tachiyama, A. Kuroda, M. Inagaki, Effect of SO_2 removal by limestone on NO_x and N_2O emissions from a bubbling fluidized-bed combustor, Fuel. 71 (1992) 841–844. https://doi.org/10.1016/0016-2361(92)90140-J.

[163] M.A. Wojtowicz, J.R. Pels, J.A. Moulijn, Combustion of coal as a source of N_2O emission, Fuel Processing Technology. 34 (1993) 1–71. https://doi.org/10.1016/0378-3820(93)90061-8.

[164] J.E. Johnsson, K. Dam-Johansen, Formation and reduction of NO_x in a fluidized bed combustor, in: Proc of the 11th International Conference on Fluidized Bed Combustion, New York, USA, 1991: pp. 1389–1396.

[165] D. Kunii, O. Levenspiel, Fluidization engineering, second ed., Butterworth-Heinemann, 1991.

[166] F.P. Incropera, D.P. DeWitt, Fundementals of Heat and Mass Transfer, third ed., John Wiley & Sons, Inc., New York, 1990.

[167] M. Schiemann, T. Gronarz, P. Graeser, J. Gorewoda, R. Kneer, V. Scherer, 2019. A correlation between char emissivity and temperature, Fuel. 256, 115889. https://doi.org/10.1016/j.fuel.2019.115889.

[168] M. Kozan, N. Selçuk, Investigation of radiative heat transfer in freeboard of a 0.3 MW_t AFBC test rig, Combust. Sci. Technol. 153 (2000) 113–126. https://doi.org/10.1080/00102200008947254.

[169] N. Selçuk, O. Oymak, E. Değirmenci, Basic requirement for modelling fluidized beds: Fast computation of particle size distributions (PSDs), Powder Technol. 87 (1996) 269–271. https://doi.org/10.1016/0032-5910(96)03112-9.

[170] A.O.O. Denloye, J.S.M. Botterill, Bed to surface heat transfer in a fluidized bed of large particles, Powder Technol. 19 (1978) 197–203. https://doi.org/10.1016/0032-5910(78)80028-X.

[171] C.K.K. Lun, S.B. Savage, D.J. Jeffrey A.N. Chepurniy, Kinetic theories for granular flow: inelastic particles in Couette flow and slightly inelastic particles in a general flowfield, J. Fluid Mech. 140 (1984) 223-256. https://doi.org/10.1017/S0022112084000586.

[172] ANSYS Inc., ANSYS Fluent User Guide, (2023). https://www.ansys.com/products/fluids/ansys-fluent (accessed May 1, 2023).

[173] D. Gidaspow, R. Bezburuah, J. Ding, Hydrodynamics of circulating fluidized beds kinetic theory approach, in: Proc of the 7th international conference on fluidization, Gold Coast, AU, 1984.

[174] M. Syamlal, W. Rogers, T.J. O'brien, (DE94000087) MFIX Documentation Theory Guide Technical Note, 1993.

[175] D.G. Schaeffer, Instability in the evolution equations describing incompressible granular flow, J. Differ. Equ. 66 (1987) 19-50. https://doi.org/10.1016/0022-0396(87)90038-6.

[176] B.G.M. van Wachem, J.C. Schouten, C.M. van den Bleek, R. Krishna, J.L. Sinclair, Comparative analysis of CFD models of dense gas-solid systems, AIChE J. 47 (2004) 1035–1051. https://doi.org/10.1002/aic.690470510.

[177] W.E. Ranz, W.R. Marshall, Vaporation from drops: Part I, Chem. Eng. Prog. 48 (1952) 141-146.

[178] C.-Y. Wen, Y.H. Yu, Mechanics of fluidization, Chem. Eng. Prog. Symp. Ser. 162 (1966) 100–111.

[179] S. Ergun, Fluid flow through packed columns, Chem. Eng. Prog. 48 (1952) 89–94.

[180] M. Lopez de Bertodano, Turbulent bubbly flow in a triangular duct, PhD thesis, Rensselaer Polytechnic Institute, Troy, NY, 1991.

[181] B.E. Launder, D.B. Spalding, The numerical computation of turbulent flows, Comput. Methods Appl. Mech. Eng. 3 (1974) 269-289. https://doi.org/10.1016/0045-7825(74)90029-2.

[182] H. Kobayashi, J.B. Howard, A.F. Sarofim, Coal devolatilization at high temperatures, Symp. (Int.) Combust. 16 (1977) 411-425. https://doi.org/10.1016/S0082-0784(77)80341-X.

[183] S.K. Ubhayakar, D.B. Stickler, R.E. Gannon, Modelling of entrained-bed pulverized coal gasifiers, Fuel. 56 (1977) 281-291. https://doi.org/10.1016/0016-2361(77)90009-6.

[184] Y.C. Guo, C.K. Chan, K.S. Lau, Numerical studies of pulverized coal combustion in a tubular coal combustor with slanted oxygen jet, Fuel. 82 (2003) 893-907. https://doi.org/10.1016/S0016-2361(02)00367-8.

[185] Y. Wu, D. Liu, D. Zheng, J. Ma, L. Duan, X. Chen, Numerical simulation of circulating fluidized bed oxy-fuel combustion with Dense Discrete Phase Model, Fuel Process. Technol. 195 (2019) 106219. https://doi.org/10.1016/j.fuproc.2019.106129.

[186] S.-P. Gao, J.-T. Zhao, Z.-Q. Wang, J.-F. Wang, Y.-T. Fang, J.-J. Huang, Effect of CO_2 on pyrolysis behaviors of lignite, J. Fuel Chem. Technol. 41 (2013) 257–264. https://doi.org/10.1016/S1872-5813(13)60017-1.

[187] N. Howaniec, Combined effect of pressure and carbon dioxide activation on porous structure of lignite chars, Materials. 12 (2019) 1326. https://doi.org/10.3390/ma12081326.

[188] J.M. Heikkinen, B.C.H. Venneker, G. di Nola, W. de Jong, H. Spliethoff, CFD simulation and experimental validation of co-combustion of chicken litter and MBM with pulverized coal in a flow reactor, Fuel Process. Technol. 89 (2008) 874–889. https://doi.org/10.1016/j.fuproc.2008.02.004.

[189] J. Xie, W. Zhong, Y. Shao, Q. Liu, L. Liu, G. Liu, Simulation of combustion of municipal solid waste and coal in an industrial-scale circulating fluidized bed boiler, Energy Fuels. 31 (2017) 14248–14261. https://doi.org/10.1021/acs.energyfuels.7b02693.

[190] Y. Huang, Z. Bao, L. Duan, Y. Duan, Bed-to-tube heat transfer characteristics with an immersed horizontal tube in the pressurized fluidized bed at high temperature, Int. Commun. Heat Mass Transf. 124 (2021) 105270. https://doi.org/10.1016/j.icheatmasstransfer.2021.105270.

[191] W.P. Adamczyk, K. Myöhänen, E.U. Hartge, J. Ritvanen, A. Klimanek, T. Hyppänen, R.A. Białecki, Generation of data sets for semi-empirical models of circulated fluidized bed boilers using hybrid Euler-Lagrange technique, Energy. 143 (2018) 219–240. https://doi.org/10.1016/j.energy.2017.10.029.

[192] M.M. Farid, H.J. Jeong, K.H. Kim, J. Lee, D. Kim, J. Hwang, Numerical investigation of particle transport hydrodynamics and coal combustion in an

industrial-scale circulating fluidized bed combustor: Effects of coal feeder positions and coal feeding rates, Fuel. 192 (2017) 187–200. https://doi.org/10.1016/j.fuel.2016.12.025.

[193]   H. Harmandar, Effect of recycling on the performance of bubbling fluidized bed combustors, MSc thesis, Middle East Technical University, Ankara, TR, 2003.

[194]   N. Selçuk, Y. Gogebakan, H. Harmandar, H. Altindag, Effect of recycle on fluidized-bed combustion and emission characteristics of high-sulfur lignite, Combust. Sci. Technol. 176 (2004) 959–975. https://doi.org/10.1080/00102200490428576.

[195]   Z. Gogebakan, Co-firing biomass with coal in bubbling fluidized bed combustors, PhD thesis, Middle East Technical University, Ankara, TR, 2007.

[196]   Z. Gogebakan, Y. Gogebakan, N. Selçuk, Co-firing of olive residue with lignite in bubbling FBC, Combust. Sci. Technol. 180 (2008) 854–868. https://doi.org/10.1080/00102200801894117.

[197]   Z. Gogebakan, Y. Gogebakan, N. Selçuk, E. Selçuk, Investigation of ash deposition in a pilot-scale fluidized bed combustor co-firing biomass with lignite, Bioresour. Technol. 100 (2009) 1033–1036. https://doi.org/10.1016/j.biortech.2008.07.037.

[198]   Z. Gogebakan, N. Selçuk, Trace elements partitioning during co-firing biomass with lignite in a pilot-scale fluidized bed combustor, J. Hazard. Mater. 162 (2009) 1129–1134. https://doi.org/10.1016/j.jhazmat.2008.05.149.

[199]   C. Ates, G. Ozen, N. Selçuk, G. Kulah, Assessment of gas radiative property models in the presence of nongray particles, Numer. Heat Transf. A Appl. 73 (2018) 385–407. https://doi.org/10.1080/10407782.2018.1447196.

[200] L.G. Blevins, T.H. Cauley, Fine particulate formation during switchgrass/coal cofiring, J. Eng. Gas Turbines Power. 127 (2005) 457–463. https://doi.org/10.1115/1.1804540.

[201] N. Selçuk, N. Kayakol, Evaluation of angular quadrature and spatial differencing schemes for discrete ordinates method in rectangular furnaces, in: Proc. of 31st National Heat Transfer Conference, ASME HTD, Houston, Texas, USA, 1996: pp. 151–158.

[202] L.S. Rothman, R.R. Gamache, R.H. Tipping, C.P. Rinsland, M.A.H. Smith, D.C. Benner, V.M. Devi, J.M. Flaud, C. Camy-Peyret, A. Perrin, A. Goldman, S.T. Massie, L.R. Brown, R.A. Toth, The HITRAN molecular database: Editions of 1991 and 1992, J. Quant. Spectrosc. Radiat. Transf. 48 (1992) 469–507. https://doi.org/10.1016/0022-4073(92)90115-K.

[203] M.S. Yasar, G. Ozen, N. Selçuk, G. Kulah, Assessment of improved banded model for spectral thermal radiation in presence of non-gray particles in fluidized bed combustors, Appl. Therm. Eng. 176 (2020) 115322. https://doi.org/10.1016/j.applthermaleng.2020.115322.

[204] J. Cai, M.F. Modest, Radiation modeling in fluidized-bed coal combustion, in: Proc. of the 50th AIAA aerospace sciences meeting including the new horizons forum and areospace exposition, Tennessee, USA, 2012. https://doi.org/10.2514/6.2012-525.

[205] M.S. Yasar, G. Ozen, N. Selçuk, G. Kulah, Performance of banded SLW-1 in presence of non-gray walls and particles in fluidized bed combustors, J. Quant. Spectrosc. Radiat. Transf. 257 (2020) 107370. https://doi.org/10.1016/j.jqsrt.2020.107370.

[206] H.G. Wagner, Soot Formation — An Overview, in: D.C. Siegla, G.W. Smith (Eds.), Particulate Carbon, Springer, 1981: pp. 1–29. https://doi.org/10.1007/978-1-4757-6137-5.

[207] W. Prins, R. Siemons, W.P.M. Van Swaaij, M. Radovanovic, Devolatilization and ignition of coal particles in a two-dimensional fluidized bed, Combust. Flame. 75 (1989) 63–79. https://doi.org/10.1016/0010-2180(89)90087-4.

[208] B. Andersson, B. Leckner, L. Åmand, Fluidized bed combustion of coals and alternative fuels, in: Proc. of the 8th International Conference on Fluidized Bed Combustion, Houston, USA, 1985: pp. 1019–1029.

[209] B.W. Butler, M.K. Denison, B.W. Webb, Radiation heat transfer in a laboratory-scale, pulverized coal-fired reactor, Exp. Therm. Fluid Sci. 9 (1994) 69–79. https://doi.org/10.1016/0894-1777(94)90010-8.

[210] S. Bard, P.J. Pagni, Carbon particulate in small pool fire flames, J. Heat Transfer. 103 (1981) 357–362. https://doi.org/10.1115/1.3244466.

[211] G. Svensson, B. Leckner, The fluidised bed boiler at Chalmers University of Technology, in: Proc of the 7th Conference (International) on Fluidized Bed Combustion, Philadelphia, USA, 1982: pp. 625–636.

[212] M.S. Yasar, N. Selçuk, G. Kulah, Performance and validation of a radiation model coupled with a transient bubbling fluidized bed combustion model, Int. J. Therm. Sci. 176 (2022) 107496. https://doi.org/10.1016/j.ijthermalsci.2022.107496.

[213] J. Everson, H.F. Nelsont, Rocket plume radiation base heating by reverse Monte Carlo simulation, J. Thermophys. Heat Trans. 7 (1993) 717–723. https://doi.org/10.2514/3.482.

[214] S.W. Baek, M.Y. Kim, Analysis of radiative heating of a rocket plume base with the finite-volume method, Int. J. Heat Mass Transf. 40 (1997) 1501–1508. https://doi.org/10.1016/S0017-9310(96)00257-8.

[215] F. Liu, G.J. Smallwood, Ö.L. Gülder, Application of statistical narrowband model to three-dimensional absorbing-emitting-scattering media, J.

Thermophys. Heat Trans. 13 (1999) 285–291. https://doi.org/10.2514/2.6453.

[216] P.E. Baudoux, A. Roblin, P. Chervet, New approach for radiative-transfer computations in axisymmetric scattering hot media, J. Thermophys. Heat Trans. 15 (2001) 317–325. https://doi.org/10.2514/2.6628.

[217] G. Cai, D. Zhu, X. Zhang, Numerical simulation of the infrared radiative signatures of liquid and solid rocket plumes, Aerosp. Sci. Technol. 11 (2007) 473–480. https://doi.org/10.1016/j.ast.2007.02.008.

[218] M.Y. Kim, Assessment of the axisymmetric radiative heat transfer in a cylindrical enclosure with the finite volume method, Int. J. Heat Mass Transf. 51 (2008) 5144–5153. https://doi.org/10.1016/j.ijheatmasstransfer.2008.03.012.

[219] M. Shusser, E. Mograbi, I. Immer, Modeling gas radiative properties in a rocket motor plume, ASME 2012 Summer Heat Transfer C, 1–9.

[220] V.A. Kuzmin, E.I. Maratkanova, I.A. Zagray, R. V. Rukavishnikova, Modeling of thermal radiation of heterogeneous combustion products in the model solid rocket engine plume, Procedia Eng. 206 (2017) 1801–1807. https://doi.org/10.1016/j.proeng.2017.10.716.

[221] V. Rialland, A. Guy, D. Gueyffier, P. Perez, A. Roblin, T. Smithson, Infrared signature modelling of a rocket jet plume - Comparison with flight measurements, J. Phys. Conf. Ser. 676 (2016) 012020. https://doi.org/10.1088/1742-6596/676/1/012020.

[222] R. Yadav, C. Balaji, S.P. Venkateshan, Implementation of SLW model in the radiative heat transfer problems with particles and high temperature gradients, Int. J. Numer. Methods Heat Fluid Flow. 27 (2017) 1128–1141. https://doi.org/10.1108/HFF-03-2016-0095.

[223] Q. Binauld, J.M. Lamet, L. Tessé, P. Rivière, A. Soufiani, Numerical simulation of radiation in high altitude solid propellant rocket plumes, Acta Astronaut. 158 (2019) 351–360. https://doi.org/10.1016/j.actaastro.2018.05.041.

[224] J.Y. Ko, E. Lee, S. Kwon, Influence of optical properties of alumina particles on the radiative base heating from solid rocket plume, Adv. Space Res. 64 (2019) 514–526. https://doi.org/10.1016/j.asr.2019.04.024.

[225] B. Gu, M.Y. Kim, S.W. Baek, Analysis of the IR signature and radiative base heating from a supersonic solid rocket exhaust plume, Int. J. Aeronaut. Space Sci. 20 (2019) 423–432. https://doi.org/10.1007/s42405-018-0135-y.

[226] M.Y. Kim, M.J. Yu, J.H. Cho, S.W. Baek, Influence of particles on radiative base heating from the rocket exhaust plume, J. Spacecr. Rockets. 45 (2008) 454–458. https://doi.org/10.2514/1.32229.

[227] D. Zhang, L. Bai, Y. Wang, Q. Lv, T. Zhang, An improved SHDOM coupled with CFD for simulating infrared radiation signatures of rocket plumes, Infrared Phys. Technol. 122 (2022) 104054. https://doi.org/10.1016/j.infrared.2022.104054.

[228] G. Ozen, Thermal radiation from solid propellant rocket motor plume, PhD thesis, Middle East Technical University, Ankara, TR, 2015.

[229] R.W. Hermsen, Aluminum oxide particle size for solid rocket motor performance prediction, J. Spacecraft, 18 (1981) 483–490. https://doi.org/10.2514/3.57845.

[230] J.K. Sambamurthi, Al_2O_3 collection and sizing from solid rocket motor plumes, J. Propuls. Power. 12 (1996) 598–604. https://doi.org/10.2514/3.24075.

[231] J. Rissler, M.E. Messing, A.I. Malik, P.T. Nilsson, E.Z. Nordin, M. Bohgard, M. Sanati, J.H. Pagels, Effective density characterization of soot

agglomerates from various sources and comparison to aggregation theory, Aerosol Sci. Technol. 47 (2013) 792–805. https://doi.org/10.1080/02786826.2013.791381.

[232] G.N. Pretorius, J.R. Bunt, M. Gräbner, H. Neomagus, F.B. Waanders, R.C. Everson, C.A. Strydom, Evaluation and prediction of slow pyrolysis products derived from coals of different rank, J. Anal. Appl. Pyrolysis. 128 (2017) 156–167. https://doi.org/10.1016/j.jaap.2017.10.014.

APPENDICES

A. Ordinates and Weights for S_N and T_N Approximations

Table A.1 Ordinates and weights for S_N approximations

Order of Approximation	Ordinates			Weights
	μ	η	ξ	w
S_2	0.5000000	0.7071068	0.5000000	3.1415927
S_4	0.2958759	0.2958759	0.9082483	1.0471976
	0.2958759	0.9082483	0.2958759	1.0471976
	0.9082483	0.2958759	0.2958759	1.0471976
S_6	0.1838670	0.1838670	0.9656013	0.3219034
	0.1838670	0.6950514	0.6950514	0.7252938
	0.6950514	0.1838670	0.6950514	0.7252938
	0.1838670	0.9656013	0.1838670	0.3219034
	0.6950514	0.6950514	0.1838670	0.7252938
	0.9656013	0.1838670	0.1838670	0.3219034
S_8	0.1422555	0.1422555	0.9795543	0.3424718
	0.1422555	0.5773503	0.8040087	0.1984568
	0.5773503	0.1422555	0.8040087	0.1984568
	0.1422555	0.8040087	0.5773503	0.1984568
	0.5773503	0.5773503	0.5773503	0.9234358
	0.8040087	0.1422555	0.5773503	0.1984568
	0.1422555	0.9795543	0.1422555	0.3424718
	0.5773503	0.8040087	0.1422555	0.1984568
	0.8040087	0.5773503	0.1422555	0.1984568
	0.9795543	0.1422555	0.1422555	0.3424718

Table A.1 Ordinates and weights for S_N approximations (Cont'd)

Order of Approximation	Ordinates			Weights
	μ	η	ξ	w
S_10	0.9809754	0.1372719	0.1372719	0.0944411
	0.8523177	0.1372719	0.5046889	0.1483950
	0.8523177	0.1372719	0.5046889	0.1483950
	0.7004129	0.1372719	0.7004129	0.0173700
	0.7004129	0.5046889	0.5046889	0.1149972
	0.7004129	0.7004129	0.1372719	0.0173701
	0.5046889	0.1372719	0.8523177	0.1483950
	0.5046889	0.5046889	0.7004129	0.1149972
	0.5046889	0.7004129	0.5046889	0.1149972
	0.5046889	0.8523177	0.1372719	0.1483950
	0.1372719	0.1372719	0.9809754	0.0944411
	0.1372719	0.5046889	0.8523177	0.1483950
	0.1372719	0.7004129	0.7004129	0.0173701
	0.1372719	0.8523177	0.5046889	0.1483950
	0.1372719	0.9809754	0.1372719	0.0944411

Table A.2 Ordinates and weights for T_4 approximations

Order of Approximation	Ordinates			Weights
	μ	η	ξ	w
T₄	0.5773503	0.5773503	0.5773503	0.1552105
	0.9901475	0.0990148	0.0990148	0.0526558
	0.0990148	0.0990148	0.9901475	0.0526558
	0.0990148	0.9901475	0.0990148	0.0526558
	0.9428090	0.2357022	0.2357022	0.0880364
	0.2357023	0.2357022	0.9428090	0.0880364
	0.2357023	0.9428090	0.2357022	0.0880364
	0.8616404	0.1230915	0.4923660	0.0995716
	0.8616404	0.4923660	0.1230915	0.0995716
	0.1230915	0.4923660	0.8616404	0.0995716
	0.4923660	0.1230915	0.8616404	0.0995716
	0.4923660	0.8616404	0.1230915	0.0995716
	0.1230915	0.8616404	0.4923660	0.0995716
	0.6804138	0.2721655	0.6804138	0.1320254
	0.2721655	0.6804138	0.6804138	0.1320254
	0.6804138	0.6804138	0.2721655	0.1320254

B. Calculation of Planck Mean Properties

Spectral dependences of blackbody emissive power was first defined by Max Planck by the following expression:

$$E_b(T, \eta) = \frac{2\pi h c_0 \eta^3}{n^2 \left[\exp\left(\frac{hc_0\eta}{nkT} \right) - 1 \right]} = \frac{3.7419x10^{-8} \, \eta (cm^{-1})^3}{\exp\left(\frac{1.4388\eta}{T} \right) - 1} \tag{B.1}$$

This function of spectral blackbody emissive power is usually referred to as Planck's law in the radiation literature.

In RHT modeling, spectral radiative properties of combustion gases, particles and walls are often represented as gray radiative properties for the sake of simplicity and computational efficiency as given by Eq. (B.2):

$$\bar{\varphi} = \frac{\int_0^\infty w(\lambda)\varphi(\lambda)d\lambda}{\int_0^\infty w(\lambda)d\lambda} \tag{B.2}$$

For the sake of simplicity, a parameter, f, is generally used as weighing factor which stands for the fraction of blackbody emissive power between 0 and λ to the total blackbody emissive power as given below;

$$f(n\lambda T) = \frac{\int_0^\lambda E_{b,\lambda}d\lambda}{\int_0^\infty E_{b,\lambda}d\lambda} \tag{B.3}$$

By definition, the fractional blackbody emissive power between wavelengths j' and $j'+1$ becomes:

$$\Delta f_{j'} = f\left(n\lambda_{j'+1}T \right) - f\left(n\lambda_{j'}T \right) \tag{B.4}$$

By utilizing the properties of particle laden combustion gases and fraction of blackbody emissive power, the integrals in Eq. (B.2) takes the following form;

$$\bar{\varphi} = \frac{\sum_{j'=1}^{NB'} \varphi_{\lambda,j'} \Delta f_{j'}}{\sum_{j'=1}^{NB'} \Delta f_{j'}} \qquad (B.7)$$

where NB$'$ is the number of discrete spectral points utilized.

C. Banded SLW Paremeters

Table C.1 $\tilde{b}_{lm\iota}$ coefficients used for H_2O used in banded SLW model [52]

$$\iota = 1; \eta = 400 \text{ cm}^{-1}$$

l/m	0	1	2	3
0	1.034880	-3.205320	5.233910	-2.444240
1	0.162518	1.057830	-1.898120	1.000310
2	0.062300	-0.438688	0.523441	-0.168893
3	-0.004470	0.054700	-0.030200	-0.011900

$$\iota = 2; \eta = 800 \text{ cm}^{-1}$$

l/m	0	1	2	3
0	4.698810	-13.646200	18.485580	-8.075800
1	0.701356	-1.049090	0.767759	-0.119224
2	0.012400	0.234308	-0.474880	0.248892
3	-0.003380	0.042000	-0.060400	0.026000

$$\iota = 3; \eta = 1200 \text{ cm}^{-1}$$

l/m	0	1	2	3
0	2.793600	-6.650720	8.673610	-3.884290
1	0.538776	-0.512367	0.835504	-0.296496
2	0.017500	0.330223	-0.792430	0.504712
3	-0.003590	0.062000	-0.129340	0.078200

$\iota = 4; \eta = 1600 \text{ cm}^{-1}$

l/m	0	1	2	3
0	0.661548	0.239577	-0.345370	0.278664
1	0.352983	0.292861	-0.159180	0.068200
2	-0.027700	0.200190	-0.325120	0.205232
3	0.010200	-0.030000	0.079000	-0.032100

$\iota = 5; \eta = 2000 \text{ cm}^{-1}$

l/m	0	1	2	3
0	2.270170	-3.143220	4.174130	-1.723130
1	0.397199	0.258657	-0.243020	0.155146
2	0.012600	0.245277	-0.468750	0.277731
3	-0.002900	0.055700	-0.088600	0.048000

$\iota = 6; \eta = 2400 \text{ cm}^{-1}$

l/m	0	1	2	3
0	1.712930	11.871950	-25.363200	16.155170
1	-1.563070	12.657640	-22.586900	13.132240
2	-0.319807	2.097910	-3.862000	2.333820
3	-0.016000	0.103039	-0.194080	0.124317

$\iota = 7; \eta = 2800 \text{ cm}^{-1}$

l/m	0	1	2	3
0	4.415900	1.297330	-6.910150	6.344960
1	0.149179	4.513580	-9.102810	6.369330
2	-0.070600	0.871753	-1.880240	1.347930
3	-0.004950	0.046100	-0.104470	0.080100

$\iota = 8; \eta = 3200 \text{ cm}^{-1}$

l/m	0	1	2	3
0	5.887600	-14.450000	17.203710	-7.019270
1	2.232590	-6.892200	9.587360	-4.252810
2	0.357981	-1.310450	1.971870	-0.934688
3	0.023000	-0.083400	0.154301	-0.074900

$\iota = 9; \eta = 3600 \text{ cm}^{-1}$

l/m	0	1	2	3
0	1.090980	-0.667602	1.196970	-0.478035
1	0.453609	-0.392997	0.989952	-0.480344
2	-0.011400	0.232239	-0.528280	0.327719
3	-0.013800	0.138361	-0.197270	0.100174

$\iota = 10; \eta = 4000 \text{ cm}^{-1}$

l/m	0	1	2	3
0	1.285040	-0.354062	1.042850	-0.535162
1	0.337819	0.221254	0.221063	-0.209401
2	0.031300	0.016800	0.024300	-0.007910
3	0.001410	0.010200	-0.014200	0.008100

$\iota = 11; \eta = 4400 \text{ cm}^{-1}$

l/m	0	1	2	3
0	3.973380	-0.013100	-2.728890	2.230120
1	0.079900	2.308260	-4.123120	2.117290
2	-0.022100	0.191051	-0.323460	0.148445
3	0.000000	0.000000	0.000000	0.000000

$$\iota = 12; \eta = 4800 \text{ cm}^{-1}$$

l/m	0	1	2	3
0	10.725170	-20.868900	17.106140	-3.421950
1	1.809420	-2.151990	-0.568700	2.168500
2	0.106192	0.110237	-0.804140	0.761877
3	0.002070	0.018200	-0.068100	0.061700

$$\iota = 13; \eta = 5200 \text{ cm}^{-1}$$

l/m	0	1	2	3
0	2.058830	-0.428569	2.440140	-1.647670
1	0.397563	0.300877	2.021340	-1.717100
2	-0.041100	0.304618	0.427193	-0.490756
3	-0.007510	0.042400	0.066400	-0.068200

$$\iota = 14; \eta = 5600 \text{ cm}^{-1}$$

l/m	0	1	2	3
0	2.105800	1.240950	-2.251570	1.498620
1	0.295851	1.776270	-2.941700	1.690860
2	-0.015800	0.432065	-0.763440	0.448476
3	-0.003030	0.038600	-0.064100	0.036100

$$\iota = 15; \eta = 6000 \text{ cm}^{-1}$$

l/m	0	1	2	3
0	2.081290	32.439890	-66.296100	41.888740
1	-1.065630	15.139630	-29.336200	18.256870
2	-0.177146	1.808770	-3.587660	2.289470
3	-0.006740	0.068200	-0.140950	0.094600

$$\iota = 16;\ \eta\ =\ 6400\ \text{cm}^{-1}$$

l/m	0	1	2	3
0	5.082400	4.616290	-11.998000	9.546210
1	-0.293260	4.842200	-7.907770	6.288870
2	-0.118469	0.670423	-1.439000	1.352390
3	-0.005970	0.033500	-0.096700	0.101685

$$\iota = 17;\ \eta\ =\ 6800\ \text{cm}^{-1}$$

l/m	0	1	2	3
0	3.780730	1.433880	-5.651670	4.424550
1	0.403788	4.348350	-8.058300	5.202870
2	-0.059000	1.179140	-2.151490	1.461670
3	-0.005620	0.082500	-0.132660	0.106878

$$\iota = 18;\ \eta\ =\ 7200\ \text{cm}^{-1}$$

l/m	0	1	2	3
0	2.044820	-0.615712	3.885660	-1.870360
1	0.804910	-1.342360	3.700580	-1.777270
2	0.114626	-0.200450	0.608866	-0.293221
3	0.010400	0.018300	-0.009360	0.002290

$$\iota = 19;\ \eta\ =\ 7600\ \text{cm}^{-1}$$

l/m	0	1	2	3
0	4.055340	-4.446000	5.382510	-1.940980
1	0.391165	1.449000	-2.918080	1.658260
2	-0.028300	0.460623	-0.825080	0.453146
3	-0.002590	0.030200	-0.054000	0.030800

$\iota = 20; \eta = 8000 \text{ cm}^{-1}$

l/m	0	1	2	3
0	1.366600	47.315280	-77.684700	34.657790
1	-0.566972	10.616220	-16.133700	6.796900
2	-0.056900	0.587717	-0.880860	0.348555
3	0.000000	0.000000	0.000000	0.000000

$\iota = 21; \eta = 8400 \text{ cm}^{-1}$

l/m	0	1	2	3
0	7.732610	-9.435820	4.204410	6.972740
1	0.938640	0.887361	-5.462150	7.154400
2	-0.001590	0.417897	-1.253370	1.360910
3	-0.001280	0.018500	-0.049800	0.064000

$\iota = 22; \eta = 8800 \text{ cm}^{-1}$

l/m	0	1	2	3
0	7.538020	-15.028500	34.833880	-19.021200
1	3.116390	-8.276220	17.514700	-9.468230
2	0.496985	-1.366210	2.733900	-1.476530
3	0.029300	-0.072100	0.140141	-0.076900

$\iota = 23; \eta = 9200 \text{ cm}^{-1}$

l/m	0	1	2	3
0	10.932840	-31.292600	45.381960	-21.114300
1	1.858530	-6.247740	8.768050	-4.105970
2	0.082500	-0.330505	0.461993	-0.223626
3	0.000000	0.000000	0.000000	0.000000

$$\iota = 24;\ \eta\ =\ 9600\ \text{cm}^{-1}$$

l/m	0	1	2	3
0	60.375380	-161.185000	179.419600	-70.244600
1	10.826800	-32.392600	38.989250	-16.184900
2	0.498208	-1.562520	1.917650	-0.816269
3	0.000000	0.000000	0.000000	0.000000

$$\iota = 25;\ \eta\ =\ 10000\ \text{cm}^{-1}$$

l/m	0	1	2	3
0	7.424940	-9.192230	29.908380	-15.834900
1	1.283460	-5.603710	15.744170	-7.813150
2	0.142384	-1.104000	2.538140	-1.164180
3	0.007630	-0.063200	0.132586	-0.057900

$$\iota = 26;\ \eta\ =\ 10400\ \text{cm}^{-1}$$

l/m	0	1	2	3
0	4.205970	5.801680	2.077100	-2.296060
1	0.390288	4.638900	-2.722770	0.694151
2	-0.052300	0.977768	-0.872260	0.313460
3	-0.004580	0.061200	-0.060500	0.022000

$$\iota = 27;\ \eta\ =\ 10800\ \text{cm}^{-1}$$

l/m	0	1	2	3
0	5.540220	-6.559960	14.146900	-8.096800
1	1.250370	-2.777260	5.215090	-3.002880
2	0.114194	-0.410314	0.716019	-0.402913
3	0.005300	-0.020900	0.034300	-0.018700

$\iota = 28; \eta = 11200 \text{ cm}^{-1}$

l/m	0	1	2	3
0	24.538120	-95.260000	153.348200	-71.410100
1	7.931800	-36.049400	57.340110	-27.184100
2	0.908331	-4.408880	6.992400	-3.358540
3	0.035600	-0.175753	0.277693	-0.134244

$\iota = 29; \eta = 11600 \text{ cm}^{-1}$

l/m	0	1	2	3
0	204.139600	-858.380000	1221.677000	-526.127000
1	57.365870	-264.126000	386.514400	-168.827000
2	5.648940	-27.797300	41.400020	-18.248500
3	0.190010	-0.983824	1.483700	-0.658178

$\iota = 30; \eta = 12000 \text{ cm}^{-1}$

l/m	0	1	2	3
0	12.680370	6.374270	-25.087300	34.224280
1	3.383720	0.847623	-7.940330	11.387990
2	0.358656	-0.055200	-0.799880	1.237670
3	0.014100	-0.007450	-0.025100	0.043500

Table C.2 $\tilde{c}_{lm\iota}$ coefficients used for H_2O used in banded SLW model [52]

$$\iota = 1; \eta = 400 \text{ cm}^{-1}$$

l/m	0	1	2	3
0	6.012490	-0.983854	0.004890	-0.018200
1	-11.052900	2.572710	-0.574373	0.057300
2	11.500000	-3.684840	1.281550	-0.134567
3	-4.500000	1.800000	-0.744000	0.083500

$$\iota = 2; \eta = 800 \text{ cm}^{-1}$$

l/m	0	1	2	3
0	4.962500	-1.562990	-0.321975	-0.025600
1	-11.628000	2.311180	0.643499	0.074100
2	12.800000	-2.182030	-0.817465	-0.114893
3	-5.180000	0.790000	0.367000	0.057300

$$\iota = 3; \eta = 1200 \text{ cm}^{-1}$$

l/m	0	1	2	3
0	2.439670	-1.389870	-0.233354	-0.017400
1	-5.645830	1.135900	-0.006770	-0.000178
2	6.580000	0.010300	0.340257	0.021300
3	-2.780000	-0.372000	-0.265149	-0.020500

$$\iota = 4;\ \eta\ =\ 1600\ \text{cm}^{-1}$$

l/m	0	1	2	3
0	1.748300	-1.073150	-0.105330	0.000954
1	-2.472870	1.629210	-0.094000	-0.006290
2	2.470000	-1.964670	0.095500	-0.006730
3	-1.010000	0.945000	-0.024000	0.001050

$$\iota = 5;\ \eta\ =\ 2000\ \text{cm}^{-1}$$

l/m	0	1	2	3
0	1.833480	-1.252170	-0.246067	-0.021500
1	-3.677340	2.457670	0.761219	0.096000
2	3.640000	-3.637600	-1.590450	-0.224196
3	-1.400000	1.820000	0.915000	0.134000

$$\iota = 6;\ \eta\ =\ 2400\ \text{cm}^{-1}$$

l/m	0	1	2	3
0	-4.902690	-2.482410	-0.207389	-0.008280
1	5.500340	3.203440	0.305713	0.022700
2	-21.576100	-12.550800	-2.059200	-0.128794
3	12.800000	7.247030	1.205320	0.072100

$$\iota = 7;\ \eta\ =\ 2800\ \text{cm}^{-1}$$

l/m	0	1	2	3
0	-8.367560	-3.419930	-0.261490	-0.006170
1	-3.694880	-1.602830	-0.506064	-0.022100
2	-7.640000	-5.540790	-0.881401	-0.063600
3	9.460000	5.860000	1.010870	0.063100

$$\iota = 8; \ \eta \ = \ 3200 \ \mathrm{cm}^{-1}$$

l/m	0	1	2	3
0	-0.293299	-1.206150	-0.122646	-0.012400
1	1.675040	5.278390	1.420790	0.151646
2	-10.092700	-15.215400	-4.593220	-0.462659
3	8.390000	10.800000	3.304630	0.326000

$$\iota = 9; \ \eta \ = \ 3600 \ \mathrm{cm}^{-1}$$

l/m	0	1	2	3
0	1.694690	-0.431034	-0.200718	-0.113743
1	-3.319310	-0.741880	0.671423	0.454133
2	3.940000	1.727160	-1.377570	-0.826218
3	-1.770000	-0.960430	0.846151	0.473281

$$\iota = 10; \ \eta \ = \ 4000 \ \mathrm{cm}^{-1}$$

l/m	0	1	2	3
0	1.702760	-1.387570	-0.187650	-0.009690
1	-3.254100	2.988730	0.582187	0.048200
2	3.440000	-3.880000	-1.040000	-0.103000
3	-1.390000	1.750000	0.537000	0.055600

$$\iota = 11; \ \eta \ = \ 4400 \ \mathrm{cm}^{-1}$$

l/m	0	1	2	3
0	-16.968400	-8.450000	-1.138480	-0.052000
1	38.500000	21.710890	3.465760	0.184189
2	-62.100000	-33.425700	-5.348800	-0.281705
3	31.154060	16.258760	2.581590	0.134630

$$\iota = 12; \eta = 4800 \text{ cm}^{-1}$$

l/m	0	1	2	3
0	-3.333650	-1.353700	-0.009120	0.004310
1	-5.291160	-1.405110	-0.296025	-0.004160
2	4.057400	-0.913207	-0.407280	-0.052300
3	-0.991000	1.050000	0.361000	0.036200

$$\iota = 13; \eta = 5200 \text{ cm}^{-1}$$

l/m	0	1	2	3
0	-1.649250	-2.260310	-0.517058	-0.058400
1	-0.088000	2.619520	1.137500	0.172320
2	2.300000	-0.664808	-0.793314	-0.164811
3	-2.020000	-0.934000	-0.019700	0.037700

$$\iota = 14; \eta = 5600 \text{ cm}^{-1}$$

l/m	0	1	2	3
0	-3.337940	-3.723400	-0.549166	-0.025900
1	7.356000	9.234270	1.574720	0.083900
2	-11.200000	-14.924500	-2.980620	-0.179267
3	4.850000	7.330000	1.580000	0.099300

$$\iota = 15; \eta = 6000 \text{ cm}^{-1}$$

l/m	0	1	2	3
0	-13.879000	-3.011590	-0.106739	0.0
1	-37.192000	-10.361600	-0.788729	0.0
2	70.469810	19.114000	1.351090	0.0
3	-34.000000	-9.160000	-0.635453	0.0

$\iota = 16;\ \eta\ =\ 6400\ \mathrm{cm}^{-1}$

l/m	0	1	2	3
0	-37.278300	-14.352400	-1.801920	-0.079400
1	149.382000	64.243430	9.005160	0.423066
2	-199.686000	-87.369500	-12.442200	-0.589144
3	78.600000	34.800000	5.000000	0.239166

$\iota = 17;\ \eta\ =\ 6800\ \mathrm{cm}^{-1}$

l/m	0	1	2	3
0	-16.466800	-10.229000	-1.946220	-0.130937
1	59.447040	41.382830	9.000380	0.649267
2	-90.500000	-66.419000	-15.280000	-1.144270
3	44.800000	33.800000	7.994260	0.610093

$\iota = 18;\ \eta\ =\ 7200\ \mathrm{cm}^{-1}$

l/m	0	1	2	3
0	-0.400976	-0.111904	0.152273	0.0
1	-2.827980	-2.652460	-0.769741	0.0
2	4.619140	4.374310	1.161200	0.0
3	-1.910000	-1.920000	-0.530000	0.0

$\iota = 19;\ \eta\ =\ 7600\ \mathrm{cm}^{-1}$

l/m	0	1	2	3
0	-1.827830	-2.542780	-0.432174	-0.023900
1	-7.547320	-3.062940	-0.881314	-0.069300
2	12.000000	7.147530	1.922260	0.147857
3	-6.350000	-4.560000	-1.230000	-0.094600

$$\iota = 20; \eta = 8000 \text{ cm}^{-1}$$

l/m	0	1	2	3
0	0.069200	0.681132	0.088700	0.0
1	-189.364000	-42.437500	-2.387110	0.0
2	449.000000	100.831100	5.651170	0.0
3	-260.113000	-58.569500	-3.284450	0.0

$$\iota = 21; \eta = 8400 \text{ cm}^{-1}$$

l/m	0	1	2	3
0	-3.661120	-1.376370	-0.176879	-0.012500
1	-6.963100	-1.690810	0.021400	0.023600
2	-28.300000	-15.922500	-2.895560	-0.176382
3	29.400000	14.900000	2.490000	0.138000

$$\iota = 22; \eta = 8800 \text{ cm}^{-1}$$

l/m	0	1	2	3
0	-13.575100	-7.124090	-1.205540	-0.074100
1	34.154620	22.093390	4.492610	0.300477
2	-67.931300	-43.415400	-8.815610	-0.581553
3	39.600000	25.100000	5.063530	0.331000

$$\iota = 23; \eta = 9200 \text{ cm}^{-1}$$

l/m	0	1	2	3
0	-16.130600	-8.250340	-1.235750	-0.060800
1	-71.000800	-29.968500	-4.197180	-0.188165
2	106.000000	44.678790	6.105040	0.265461
3	-50.057200	-20.497200	-2.701910	-0.112441

$$\iota = 24; \eta = 9600 \text{ cm}^{-1}$$

l/m	0	1	2	3
0	0.0	0.0	0.0	0.0
1	0.0	0.0	0.0	0.0
2	0.0	0.0	0.0	0.0
3	0.0	0.0	0.0	0.0

$$\iota = 25; \eta = 10000 \text{ cm}^{-1}$$

l/m	0	1	2	3
0	-29.731000	-6.266250	-0.305489	0.0
1	79.494210	17.485740	0.920417	0.0
2	-89.415900	-19.312600	-0.998899	0.0
3	25.900000	5.180000	0.239055	0.0

$$\iota = 26; \eta = 10400 \text{ cm}^{-1}$$

l/m	0	1	2	3
0	-17.707500	-7.965980	-1.191510	-0.064000
1	99.649070	49.212600	7.836400	0.410387
2	-174.000000	-86.524900	-13.892100	-0.727189
3	90.200000	45.300000	7.330000	0.385000

$$\iota = 27; \eta = 10800 \text{ cm}^{-1}$$

l/m	0	1	2	3
0	1.378170	1.360840	0.311756	0.015800
1	-58.090400	-25.789300	-3.690060	-0.165159
2	107.895500	47.282630	6.674770	0.301313
3	-61.100000	-26.800000	-3.780000	-0.173000

$\iota = 28;\ \eta\ =\ 11200\ cm^{-1}$

l/m	0	1	2	3
0	-36.225200	-13.956000	-1.808310	-0.081100
1	241.133300	103.105400	14.429900	0.664769
2	-1154.190000	-462.464000	-61.330300	-2.692800
3	841.000000	334.109800	43.977790	1.917480

$\iota = 29;\ \eta\ =\ 11600\ cm^{-1}$

l/m	0	1	2	3
0	0.0	0.0	0.0	0.0
1	0.0	0.0	0.0	0.0
2	0.0	0.0	0.0	0.0
3	0.0	0.0	0.0	0.0

$\iota = 30;\ \eta\ =\ 12000\ cm^{-1}$

l/m	0	1	2	3
0	-23.407500	-4.772890	-0.219870	0.0
1	38.407420	8.318280	0.414096	0.0
2	-35.042100	-7.180000	-0.327761	0.0
3	15.900000	3.260000	0.151000	0.0

Table C.3 $\tilde{d}_{lm\iota}$ coefficients used for CO_2 used in banded SLW model [52]

$$\iota = 1; \eta = 300 \text{ cm}^{-1}$$

l/m	0	1	2	3
0	14.092100	-45.008300	76.586150	-38.507000
1	3.587140	-16.342200	32.337760	-17.444000
2	5484479.0	-3.153210	6.033820	-3.220100
3	0.030000	-0.181700	0.334136	-0.175400
4	0.0	0.0	0.0	0.0

$$\iota = 2; \eta = 600 \text{ cm}^{-1}$$

l/m	0	1	2	3
0	1.151580	-3.265180	2.597530	-0.365200
1	0.163145	1.436120	-2.045980	1.102660
2	0.026500	-0.035200	0.805636	-0.570800
3	0.020700	-0.192220	0.492278	-0.290800
4	0.001140	-0.005450	-0.015200	0.011900

$$\iota = 3; \eta = 900 \text{ cm}^{-1}$$

l/m	0	1	2	3
0	5.986200	-18.087700	20.661590	-7.761100
1	0.304536	3.320310	-6.212690	3.423500
2	-0.077600	0.914673	-0.810710	0.198430
3	-0.008460	0.042600	0.232125	-0.213300
4	0.0	0.0	0.0	0.0

$$\iota = 4; \eta = 1200 \text{ cm}^{-1}$$

l/m	0	1	2	3
0	-8.543650	85.961180	-138.220000	67.863300
1	-10.699600	73.400070	-110.148000	51.705700
2	-2.881480	17.963190	-25.615100	11.567900
3	-0.293640	1.731380	-2.334090	1.006100
4	-0.010200	0.057400	-0.072700	0.029500

$$\iota = 5; \eta = 1500 \text{ cm}^{-1}$$

l/m	0	1	2	3
0	6.470500	-0.579890	0.0	0.0
1	0.432575	0.010800	0.0	0.0
2	0.0	0.0	0.0	0.0
3	0.0	0.0	0.0	0.0
4	0.0	0.0	0.0	0.0

$$\iota = 6; \eta = 1800 \text{ cm}^{-1}$$

l/m	0	1	2	3
0	-22.640900	175.141400	-211.511000	86.966300
1	-9.237000	60.508930	-74.237700	31.363200
2	-1.097880	6.579290	-8.052780	3.450550
3	-0.041400	0.233599	-0.279510	0.120020
4	0.0	0.0	0.0	0.0

$\iota = 7$; $\eta = 2100$ cm^{-1}

l/m	0	1	2	3
0	5.191580	-18.176200	23.113750	-10.017500
1	0.295888	0.169255	-1.136530	0.894114
2	-0.081400	0.775819	-1.325230	0.683492
3	-0.014500	0.152943	-0.246466	0.117372
4	-0.000576	0.006630	-0.011100	0.004710

$\iota = 8a$; $\eta = 2400$ cm^{-1}

l/m	0	1	2	3
0	3.712510	-9.299260	68.205710	-41.907100
1	1.592330	-12.654800	46.653980	-26.532700
2	0.385473	-3.356290	9.169920	-4.846200
3	0.024500	-0.206470	0.508616	-0.254430
4	0.0	0.0	0.0	0.0

$\iota = 8b$; $\eta = 2400$ cm^{-1}

l/m	0	1	2	3
0	2.435250	-23.426900	36.063010	-16.610600
1	-0.606820	6.659310	-10.337400	4.728690
2	-0.043400	0.440435	-1.300560	0.735770
3	0.026000	-0.189210	0.455025	-0.224240
4	0.0	0.0	0.0	0.0

$$\iota = 9; \eta = 2700 \text{ cm}^{-1}$$

l/m	0	1	2	3
0	19.532940	6.882670	-27.539500	13.012140
1	2.538740	4.135320	-8.258670	3.518680
2	0.119748	0.142277	-0.295336	0.114518
3	0.0	0.0	0.0	0.0
4	0.0	0.0	0.0	0.0

$$\iota = 10; \eta = 3000 \text{ cm}^{-1}$$

l/m	0	1	2	3
0	57.108820	-89.496600	53.883800	-6.564940
1	8.018190	-7.490780	-1.535140	3.550530
2	0.303043	-0.085500	-0.406005	0.301169
3	0.0	0.0	0.0	0.0
4	0.0	0.0	0.0	0.0

$$\iota = 11; \eta = 3300 \text{ cm}^{-1}$$

l/m	0	1	2	3
0	15.702420	-38.601200	41.134810	-15.349200
1	5.588770	-14.005900	16.229660	-6.684180
2	1.183270	-3.276450	3.909660	-1.658080
3	0.108180	-0.262760	0.259329	-0.095500
4	0.003220	-0.004870	0.000399	0.001190

$\iota = 12; \eta = 3600 \text{ cm}^{-1}$

l/m	0	1	2	3
0	1.057720	-1.122970	1.485520	-0.294350
1	0.225422	2.111910	-1.032800	0.582535
2	-0.037800	1.040450	-2.650590	2.307730
3	0.001690	-0.011100	0.178781	0.014600
4	0.0	0.0	0.0	0.0

$\iota = 13; \eta = 3900 \text{ cm}^{-1}$

l/m	0	1	2	3
0	2.215390	1.570390	-2.648370	1.489110
1	-0.863730	6.428930	-5.788340	1.565060
2	-0.122490	0.513625	0.351379	-0.523360
3	-0.003150	0.001900	0.082000	-0.066200
4	0.0	0.0	0.0	0.0

$\iota = 14; \eta = 4200 \text{ cm}^{-1}$

l/m	0	1	2	3
0	37.130500	-97.351500	144.747400	-72.977200
1	11.334070	-36.488400	57.952520	-30.066300
2	1.366080	-5.050910	8.126220	-4.203330
3	0.056100	-0.222630	0.358408	-0.184290
4	0.0	0.0	0.0	0.0

375

$\iota = 15;\ \eta\ =\ 4500\ \text{cm}^{-1}$

l/m	0	1	2	3
0	17.605640	16.589840	-28.286800	15.679650
1	0.754699	17.708070	-22.697300	10.319910
2	-0.223320	2.603830	-3.176030	1.388810
3	-0.015500	0.111595	-0.133760	0.057700
4	0.0	0.0	0.0	0.0

$\iota = 16;\ \eta\ =\ 4800\ \text{cm}^{-1}$

l/m	0	1	2	3
0	5.230980	0.412313	0.087500	-0.850750
1	0.596114	2.869110	2.366290	-3.675700
2	0.022600	-0.103760	2.235560	-1.807050
3	0.002340	-0.046200	0.243823	-0.175500
4	0.0	0.0	0.0	0.0

$\iota = 17;\ \eta\ =\ 5100\ \text{cm}^{-1}$

l/m	0	1	2	3
0	3.439480	14.242520	-33.744100	20.074140
1	0.823179	7.014010	-15.166700	8.680000
2	0.078200	1.027030	-2.045410	1.134080
3	-0.002210	0.094900	-0.143430	0.067800
4	0.0	0.0	0.0	0.0

$\iota = 18; \eta = 5400$ cm^{-1}

l/m	0	1	2	3
0	4.695960	2.173860	-10.468800	7.574500
1	0.844226	1.361500	-3.334060	1.971780
2	0.490874	-2.410590	3.799970	-1.880680
3	0.088800	-0.507390	0.807579	-0.399060
4	0.004440	-0.025900	0.041000	-0.020100

$\iota = 19; \eta = 5700$ cm^{-1}

l/m	0	1	2	3
0	14.732150	-38.101600	56.027930	-23.199300
1	1.007730	-2.492330	3.811200	-1.586930
2	0.0	0.0	0.0	0.0
3	0.0	0.0	0.0	0.0
4	0.0	0.0	0.0	0.0

$\iota = 20; \eta = 6000$ cm^{-1}

l/m	0	1	2	3
0	88.607910	-212.170000	699.795200	30.424190
1	18.018770	-6.091520	166.079200	86.837080
2	-0.042000	13.496060	3.062210	27.002870
3	-0.214000	2.095820	-1.661690	2.958710
4	-0.011600	0.088700	-0.099100	0.108894

$$\iota = 21; \ \eta = 6300 \ \text{cm}^{-1}$$

l/m	0	1	2	3
0	17.048500	-55.696300	180.482100	-127.229000
1	4.658140	-21.975200	93.665510	-70.286500
2	0.693567	-4.465100	20.009380	-15.154700
3	0.058300	-0.409840	1.852720	-1.408740
4	0.001890	-0.013300	0.061600	-0.047300

$$\iota = 22; \ \eta = 6600 \ \text{cm}^{-1}$$

l/m	0	1	2	3
0	-38.733300	334.794100	-582.748000	293.589500
1	-21.823200	177.223400	-308.523000	154.997400
2	-4.112960	33.788470	-59.144000	29.763900
3	-0.334990	2.830980	-4.993560	2.525040
4	-0.010200	0.088300	-0.157415	0.080200

$$\iota = 23; \ \eta = 6700 \ \text{cm}^{-1}$$

l/m	0	1	2	3
0	24.080930	-142.762000	401.246300	-237.612000
1	10.965720	-72.785100	184.083900	-106.488000
2	2.002100	-13.247600	30.769560	-17.391800
3	0.161970	-1.020680	2.219610	-1.229620
4	0.004860	-0.028800	0.059200	-0.032200

D. Estimation of Mean Beam Length

In the present work, the approach based on two emissivities is used to determine the gray gas parameters of SLW-1 model. For this approach, Solovjov et al. [81] recommended that all L_1 and L_2 values must capture a range of path lengths that are both smaller and greater than the length defined by the physical boundaries. In order to define the physical boundaries of the system under consideration, three different definitions are utilized, and their predictive accuracies are tested against the benchmark solutions and measurements. The first one is the height of the freeboard. The second one is the spectrally averaged mean beam length which is estimated by the following expression;

$$L_m = 3.6 \times \frac{V}{A} \tag{D.1}$$

where V is the volume of the test rig and A is the surface area of the walls surrounding the test rig. Furthermore, Ozen et al. [87] recommended a band-wise selection of pathlengths for the banded SLW-1 model to achieve higher accuracy since the optical thickness of the medium varies substantially at each wavelength. Therefore, spectrally dependent mean beam length is also utilized as the physical boundary in this study. The following expression is used to determine the spectrally dependent mean beam length;

$$1 - e^{-\kappa_j L_e} = \int_V e^{-\kappa_j S} \frac{\kappa_j \cos\theta dV}{\pi S^2} \tag{D.2}$$

where L_e is the spectrally dependent mean beam length, κ_j is the gas absorption coefficient in the jth band and S is the distance between an infinitesimal surface element dA located in the walls of the test rig and an arbitrary volume element dV inside the medium. It should be noted that Eq. (D.2) is applicable to an arbitrary volume irradiating an infinitesimal surface element. Hence, Eq. (D.2) is applied to different infinitesimal surface elements placed on surfaces of the METU 0.3 MWt ABFBC test rig. Spectrally dependent mean beam length is then calculated by

averaging the solutions of Eq. (D.2) applied to those infinitesimal surface elements. Calculation of mean beam length requires an iterative solution as illustrated in Figure D.1 since both spectrally dependent mean beam length and gas absorption coefficient depend on each other. Side walls are divided into 3 x 11 infinitesimal surfaces whereas bottom and top walls are divided into 3 x 3 surfaces which means that the boundaries of METU 0.3 MWt ABFBC test rig is represented as 150 infinitesimal surfaces for the calculation of spectrally dependent mean beam length. In this study, spectrally dependent mean beam lengths are calculated separately from the radiation code and are given as input data to the model as their calculation requires iterative solution of triple integrals for various infinitesimal surfaces. Calculated spectrally dependent mean beam lengths for the combustion tests under investigation are summarized in Table D.1. Spectrally dependent mean beam lengths are also compared with the mean beam lengths for optically thin media (L_0) calculated using Eq. (D.3). As shown by the table, spectrally dependent mean beam lengths are very close to L_0 in the spectral bands where gas absorption coefficients are very small (see Figure D.2).

$$L_m = 4 \times \frac{V}{A} \qquad (D.3)$$

where V is the volume of the freeboard and A is the total freeboard surface area.
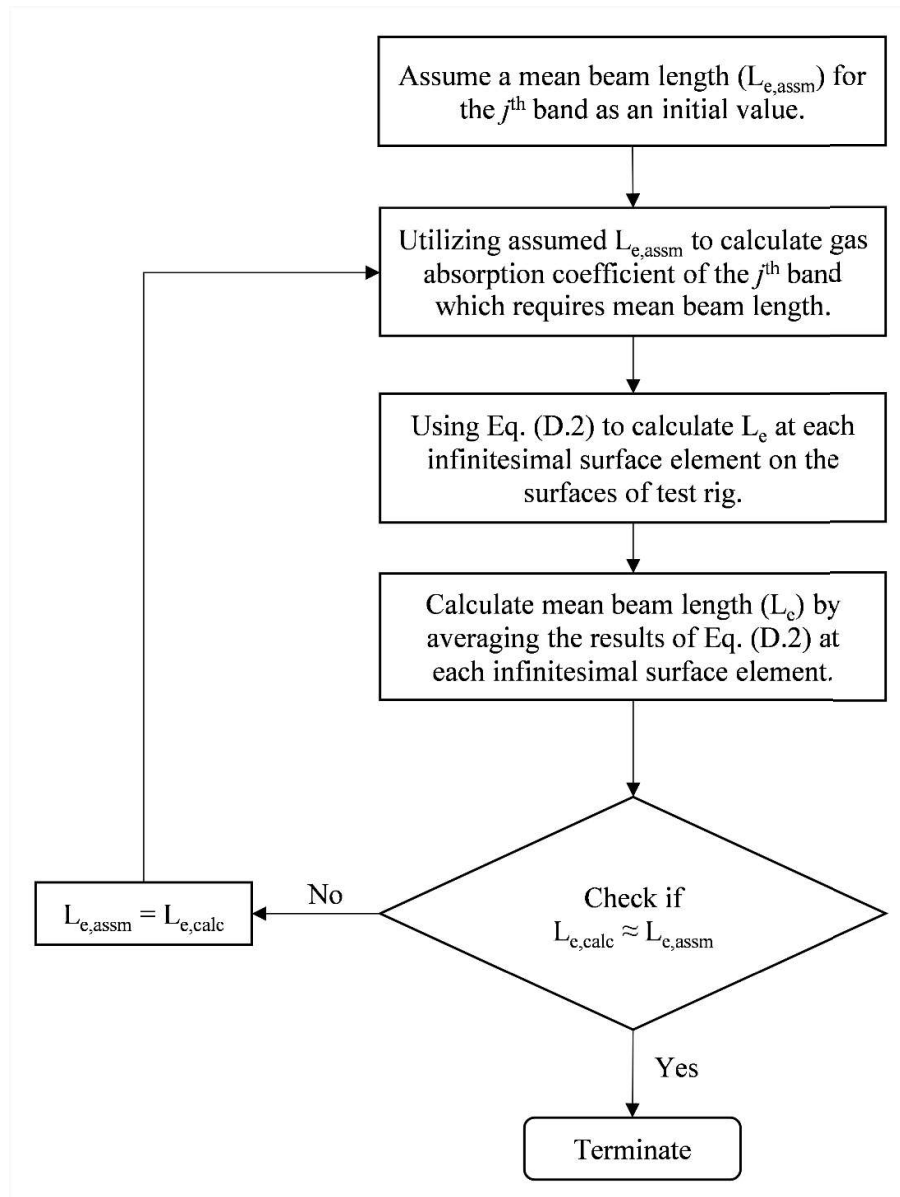
Figure D.1. Solution procedure for calculation of spectrally dependent mean beam length
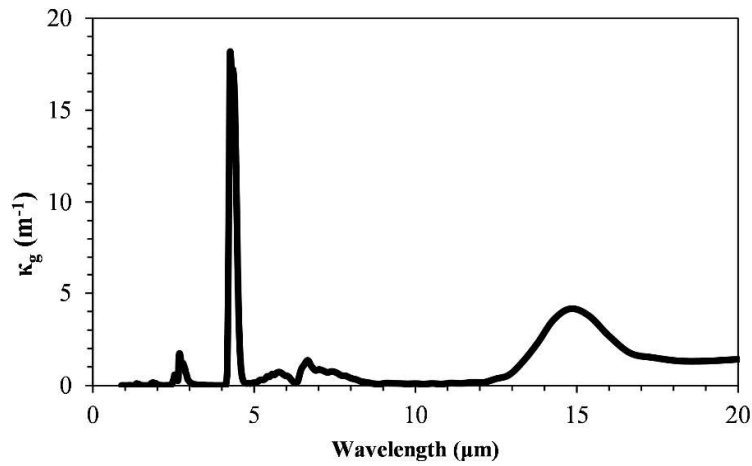
Figure D.2. Spectral variation in the gas absorption coefficient of the flue gas under the conditions of Test 2 and Test 3

Table D.1 Spectrally dependent mean beam lengths and mean beam lengths for optically thin media for Test 2 and Test 3

Band No.	Band Interval (μm)	Spectrally Dependent Mean Beam Length Eq. (D.2)	Mean Beam Length for Optically Thin Media Eq. (D.3)
1	1 – 2.4	0.41	0.42
2	2.4 – 3.1	0.36	0.42
3	3.1 – 4.1	0.42	0.42
4	4.1 – 4.8	0.16	0.42
5	4.8 – 6.3	0.38	0.42
6	6.3 – 8.9	0.36	0.42
7	8.9 – 12.1	0.41	0.42
8	12.1 – 20.0	0.29	0.42

E. Complex Index of Refraction Models for Ash Particles

E.1. Complex Index of Refraction Model Proposed by Goodwin

E.1.1. Calculation of Spectral Refractive Indices (n) between 1-8 μm

In the wavelength interval $1 - 8$ μm, Goodwin estimated the refractive index of coal slags by using a mixture tule and by assuming refractive index of coal slags are uniform with respect to composition:

$$\frac{n^2 - 1}{n^2 + 2} = \rho \sum_i X_{m,i} F_i(\lambda) \tag{E.1}$$

By rearranging Eq. (E.1), the refractive index, n, can be determined as follows:

$$n(\lambda) = \left(\frac{1 + 2\rho \sum_i X_{m,i} F_i(\lambda)}{1 - \sum_i X_{m,i} F_i(\lambda)} \right)^{0.5} \tag{E.2}$$

where $F_i(\lambda)$ is the fitting function for each oxide which can be estimated as:

$$F_i(\lambda) = \frac{(a_i \lambda^2 - b_i)}{(c_i \lambda^2 - d_i)} \tag{E.3}$$

The coefficients of the fitting function, $F_i(\lambda)$, for each species in the coal slag are listed in Table E.1.

Table E.1 The coefficients of the fitting function, $F_i(\lambda)$, for each species in the coal slag

	a	b	c	d
F(SiO₂)	0.9389	53	5.001	420
F(Al₂O₃)	1.914	174	10.36	1633.8
F(CaO)	4.250	827.7	16.63	6102.3
F(Fe₂O₃)	1.647	0.00	11.36	0.00
F(MgO)	1.278	136.9	7.433	1200.9
F(TiO₂)	2.72	260.0	15.80	1954.4

The mixture rule that Goodwin proposed is only available for six oxides listed in Table E.1. Fortunately, these oxides usually accounts for the 95% - 97% of typical coal ashes. The oxides not listed in Table E.1. are not included in the RI model of Goodwin. However, Goodwin suggested two approaches to extend his model for the inclusion of other components.

- Utilization of Eq. (E.2) by neglecting all other component (by setting the refractive index of other components to 1.0)
- Normalization of the mass fractions of the six oxides listed in Table E.1 to unity.

It was stated by Goodwin that both approaches provide similar results.

E.1.2. Calculation of Spectral Absorption Indices (k) between 1-4 μm

The dominant absorbing species in the coal slags for the wavelengths less than 4 μm is Fe₂O₃. The following simple correlation, suggested by Goodwin, describes the interaction between Fe absorption;

$$k(\lambda) = a_1 e^{b/\lambda} + a_2 g(\lambda) \tag{E.4}$$

where the exponent b and the function $g(\lambda)$ are independent of composition. Goodwin related the coefficients of Eq. (E.4), which are a_1 and a_2, to the mass fraction of Fe_2O_3 and the ferrous ratio (r) as follows:

$$k(\lambda) = 3.61 \text{ x } 10^{-7}\rho^2(1-r)(Fe_2O_3)^2 e^{\frac{1.75}{\lambda}}$$
$$+ \rho r(Fe_2O_3)[0.0963 + 0.0011\rho r(Fe_2O_3)]g(\lambda) \qquad (E.5)$$

where ρ is the density of slag, (Fe_2O_3) is the weigth percent of iron oxide in the slag, and r is the ferrous ratio which is described by the following expression:

$$r = \frac{Fe^{2+}}{Fe^{2+} + Fe^{3+}} \qquad (E.6)$$

$g(\lambda)$ characterizes the Fe^{2+} absorption spectrum and provided in Table E.2.

Table E.2 Data for the function $g(\lambda)$

λ	$g(\lambda)$	λ	$g(\lambda)$	λ	$g(\lambda)$
0.7	0.304	1.9	2.463	3.0	1.919
0.8	0.727	2	2.424	3.1	1.928
0.9	1.355	2.1	2.332	3.2	1.94
1.0	2.025	2.2	2.213	3.3	1.948
1.1	2.488	2.3	2.094	3.4	1.97
1.2	2.641	2.4	2.002	3.5	1.994
1.3	2.521	2.5	1.941	3.6	2.015
1.4	2.318	2.6	1.898	3.7	2.048
1.5	2.202	2.7	1.891	3.8	2.077
1.6	2.213	2.8	1.892	3.9	2.115
1.7	2.32	2.9	1.904	4.0	2.153
1.8	2.422				

E.1.3. Calculation of Spectral Absorption Indices (k) between 4-8 μm

In the wavelength interval 4-8 μm, the absorption is originated by the existance of silica content in the ash, via vibration. Other oxides have a negligible impact on absorption in this wavelength interval [123]. Therefore, the following expression is used to represent the absorption index (k) in terms of SiO_2 content of the ash;

$$k(\lambda) = \frac{\rho}{\rho_{SiO2}} X_{SiO2} k_0(\lambda) \qquad (E.7)$$

where $k_0(\lambda)$ is the SiO_2 absorption index data which is provided in Table E.3.

Table E.3 SiO_2 absorption index data

λ	$k_0(\lambda)$	λ	$k_0(\lambda)$	λ	$k_0(\lambda)$
4	0.0000579	5	0.00398	6.452	0.00657
4.082	0.0000799	5.063	0.00512	6.667	0.00716
4.167	0.000107	5.128	0.00518	6.897	0.00851
4.255	0.000132	5.263	0.00549	7.143	0.0106
4.348	0.000213	5.333	0.00569	7.407	0.0148
4.396	0.000265	5.405	0.00572	7.692	0.0372
4.444	0.000284	5.556	0.00563	7.752	0.0474
4.494	0.000284	5.882	0.00594	7.813	0.0768
4.545	0.000256	6.061	0.00632	7.874	0.132
4.651	0.000262	6.154	0.00646	7.937	0.216
4.762	0.000485	6.25	0.00652	8	0.323
4.878	0.00182				

In the radiation model, polynomial expressions fitted to this experimental data [Eq. (E.8) to Eq. (E.14)] is utilized:

for $4 \leq \lambda \leq 4.4$:

$$k_0(\lambda) = -0.0705119\lambda + 0.0514052\lambda^2 - 0.0125009\lambda^3 + 0.0010144\lambda^4 \quad (E.8)$$

for $4.4 \leq \lambda \leq 4.8$:

$$k_0(\lambda) = -0.4879839\lambda + 0.3234942\lambda^2 - 0.0714526\lambda^3 + 0.0052591\lambda^4 \quad (E.9)$$

for $4.8 \leq \lambda \leq 5.4$:

$$k_0(\lambda) = 219.3123 - 173.6359\lambda + 51.49852\lambda^2 - 6.781594\lambda^3$$
$$+ 0.3345718\lambda^4 \qquad (E.10)$$

for $5.4 \leq \lambda \leq 6.4$:

$$k_0(\lambda) = -0.9501931\lambda + 0.6835954\lambda^2 - 0.1834775\lambda^3 + 0.0218031\lambda^4$$
$$- 0.0009681\lambda^5 \tag{E.11}$$

for $6.4 \leq \lambda \leq 7.7$:

$$k_0(\lambda) = 20.66834\lambda - 12.00397\lambda^2 + 2.613003\lambda^3 - 0.2526626\lambda^4$$
$$+ 0.0091574\lambda^5 \tag{E.12}$$

for $7.7 \leq \lambda \leq 8.0$:

$$k_0(\lambda) = 146.2145\lambda - 52.81511\lambda^2 + 6.32314\lambda^3 - 0.2506528\lambda^4 \tag{E.13}$$

E.1.4. Calculation of Spectral Refractive (n) and Absorption (k) Indices between 8-13 μm

In the wavelength region between 8-13 μm, absorption of thermal radiation by coal slags is mainly due to the vibration of Si-O-Si and Si-O⁻ bonds. The optical properties of this region is calculated using a multiple oscillator model where RI (m) is determined instead of n and k separately;

$$m^2 = n_\infty^2 + \sum_j \frac{\omega_{pj}^2}{\omega_{0j}^2 - \omega^2 - i\gamma_j\omega} \tag{E.14}$$

where $\omega = 1/\lambda$, ω_{pj}, ω_{0j} and γ_j are the strength, position and width of the jth oscillator, respectively.

By representing the RI (m) explicitly, Eq. (14) can be rewritten as two equations:

$$n^2 - k^2 = n_\infty^2 + \sum_j \frac{\omega_{pj}^2\left(\omega_j^2 - \omega^2\right)}{\left(\omega_j^2 - \omega^2\right)^2 + \gamma_j^2\omega^2} \tag{E.15}$$

$$-2nk = \sum_j \frac{\omega_{pj}^2\gamma_j\omega}{\left(\omega_j^2 - \omega^2\right)^2 + \gamma_j^2\omega^2} \tag{E.16}$$

Goodwin found that the region between 8-12 μm can be represented with three peaks by the following expressions:

$$\left(\frac{\omega_{p1}}{\omega_{0,1}}\right)^2 = (0.425 - 0.60X_{Fe2O3})\left(\frac{X_{SiO2}}{0.52}\right) \tag{E.17}$$

$$\left(\frac{\omega_{p2}}{\omega_{0,2}}\right)^2 = (0.175 + 0.75X_{Fe2O3})\left(\frac{X_{SiO2}}{0.52}\right) \tag{E.18}$$

$$\left(\frac{\omega_{p3}}{\omega_{0,3}}\right)^2 = (0.053)\left(\frac{X_{SiO}}{0.52}\right) \tag{E.19}$$

The parameters of these peaks are listed in Table E.4.

Table E.4 Fitting parameters for the multiple oscillator model

	n_∞^2	$\omega_{0,j}$	γ_j
1st oscillation		1062.8	164.7
2nd oscillation	2.15	955.8	79.1
3rd oscillation		762	27.5

Finally, n and k can be found analytically by the following expressions:

$$n^2 - k^2 = n_\infty^2 + \sum_j \frac{\omega_{pj}^2\left(\omega_j^2 - \omega^2\right)}{\left(\omega_j^2 - \omega^2\right)^2 + \gamma_j^2\omega^2} = A \tag{E.20}$$

$$2nk = \sum_j \frac{\omega_{pj}^2\gamma_j\omega}{\left(\omega_j^2 - \omega^2\right)^2 + \gamma_j^2\omega^2} = B \tag{E.21}$$

$$n = \sqrt{\frac{A}{2} + \frac{\sqrt{A^2 + B^2}}{2}} \tag{E.22}$$

$$k = \frac{B}{2\sqrt{\frac{A}{2} + \frac{\sqrt{A^2 + B^2}}{2}}} \tag{E.23}$$

E.1.5. Calculation of Spectral Refractive (n) and Absorption (k) Indices between 13-20 μm

No experimental measurement is available for the wavelengths greater than 13 μm. Nevertheless, Goodwin suggested that the optical properties of coal slags is dominated by the Reststrahlen bands of Al_2O_3 and MgO in this region. For this reason, RI for this wavelength region can simply be estimated by a simple summation rule as given below;

$$n(\lambda) = \sum x_i n_i(\lambda) \tag{E.24}$$

$$k(\lambda) = \sum x_i k_i(\lambda) \tag{E.25}$$

where the refractive and absorption indices of Al_2O_3 and MgO can be found in [233].

E.2. Complex Index of Refraction Model Proposed by Ebert

E.2.1. Density Calculation

The Ebert's model of RI requires the skeletal density of particles. If the skeletal density of the particle is not available, Ebert suggested a simple summation rule as a function of effective densities of each oxide in the particle;

$$\frac{1}{\rho} = \sum x_i / \rho_i \tag{E.26}$$

where x_i and ρ_i are the mass fraction and density of component i provided in Table E.5.

Table E.5 Oxide densities in glass at room temperature

Oxide	Oxide density in glass (g/cm^3)	Oxide	Oxide density in glass (g/cm^3)
SiO_2	2.28	TiO_2	3.8
Al_2O_3	2.5	Na_2O	3.1
CaO	3.9	K_2O	2.8
Fe_2O_3	5.24	BaO	7
MgO	3.3		

E.2.2. Calculation of Spectral Refractive Indices (n) between 1-8 µm

Similar to the Goodwin's model, the refractive index is estimated by applying a summation rule between the wavelength interval of 1-8 µm according to the Ebert's model;

$$\frac{n^2 - 1}{n^2 + 2} = \rho \sum_i \frac{X_{m,i}}{\rho_i} \frac{n_i{}^2 - 1}{n_i{}^2 + 2} \tag{E.27}$$

where $X_{m,i}$ and n_i are the mass fraction and refractive index of the component i. For each species, n_i is calculated by the following expressions:

$$n_i{}^2 = 1 + C_i - \frac{B_i \lambda^2}{\lambda_{0,i}^2 - \lambda^2} \tag{E.28}$$

C_i, B_i and $\lambda_{0,i}$ values are given in Table E.6.

Table E.6 Dispersion equation (C.23) parameters for oxides

	SiO_2	Al_2O_3	MgO	CaO	TiO_2	Fe_2O_3
ρ_i	2.20	3.97	3.58	3.31	4.86	5.24
C_i	1.104	2.082	1.9625	2.31	5.031	8.3636
B_i	0.8975	5.281	2.47	11.32	7.764	0
$\lambda_{0,i}$	9.896	17.93	15.56	33.9	15.6	0

Ebert used the following expressions to take into account the effect of decreasing SiO₂ content on λ_0;

$$n_{SiO2}{}^2 = 1 + C_{SiO2} - \frac{B_{SiO2}\lambda^2}{(\lambda_{0,SiO2} + \delta\lambda_{0,SiO2})^2 - \lambda^2} \tag{E.29}$$

$$\delta\lambda_{0,SiO2} = 2.82 - 2.90\hat{x}_{SiO2} \tag{E.30}$$

where $\hat{x}_{SiO2}$ is the mole fraction of SiO₂.

Finally, the refractive index, n, can explicitly be found by the following expressions:

$$\frac{n^2 - 1}{n^2 + 2} = \rho \sum_i \frac{X_{m,i}}{\rho_i} \frac{n_i{}^2 - 1}{n_i{}^2 + 2} = \alpha \tag{E.31}$$

$$n = \left| \frac{\sqrt{\alpha + 1 - 2\alpha^2}}{\alpha - 1} \right| \tag{E.32}$$

E.2.3. Calculation of Absorption Indices (k) between 1-4 μm

According to Ebert's model, the absorption index, k, can simply be found using an empirical correlation deduced from 16 samples with different iron oxide contens;

$$k(\text{Fe}) = \left(4.02X_{\text{Fe}_2\text{O}_3} + 16.9X_{\text{Fe}_2\text{O}_3}^2\right)10^{-3} \tag{E.33}$$

where $X_{\text{Fe}_2\text{O}_3}$ is the iron oxide mass fraction.

E.2.4. Calculation of Absorption Indices (k) between 4-8 μm

In the wavelength interval under consideration, the spectral absorption indices are represented by two-phonon model;

$$k = k_0 + k_b \left[1 + \frac{2}{exp\left(\frac{C_2}{2\lambda T}\right) - 1}\right] \tag{E.34}$$

$$k_b = \frac{A_0}{\omega} \exp\left(-\frac{\omega}{B_0}\right), \qquad \omega < \omega^* \tag{E.35}$$

$$k_b = \frac{A_1}{\omega} \exp\left(-\frac{\omega}{B_1}\right), \qquad \omega > \omega^* \tag{E.36}$$

$$\omega^* = \frac{\ln(A_1/A_0)}{\dfrac{1}{B_1} - \dfrac{1}{B_0}} \tag{E.37}$$

$$k_0 = A_{k_0} \exp\left[-\left(\frac{\omega - B_{k_0}}{C_{k_0}}\right)^2\right] \tag{E.38}$$

where C_2 is the second blackbody emissive power constant. The constants in Eqs. (E.34) to (E.38) are listed in Table E.7.

Table E.7 Parameters used in the evaluation of absorption index (k) between 4-8 μm

A_{k0}	0.0015
B_{k0} (cm^{-1})	1800
C_{k0} (cm^{-1})	110
A_0 (cm^{-1})	295
B_0 (cm^{-1})	443
A_1 (cm^{-1})	51370
B_1 (cm^{-1})	200
C_2 (μmK)	14388

Frequency ω in Eqs. (E.34) to (E.38) should be modified to consider the effect of SiO$_2$ content on oscillations;

$$\omega = \omega + \delta\omega = \omega + 355(0.678 - \hat{x}_{SiO2}) \tag{E.39}$$

where $\hat{x}_{SiO2}$ is mole fraction of SiO$_2$.

E.2.5. Calculation of Spectral Refractive (n) and Absorption (k) Indices between 8-13 μm

Ebert stated that multiple oscillatory model can be used to estimate the refractive and absorption indices of coal slags in the wavelength interval between 8-13 μm. In this

region, absorption of thermal radiation by coal slags is mainly due to the vibration of Si-O-Si and Si-O⁻ bonds. The optical properties of this region is calculated using a multiple oscillator model where RI (m) is determined instead of n and k separately;

$$m^2 = n_\infty^2 + \sum_j \frac{\omega_{pj}^2}{\omega_{0j}^2 - \omega^2 - i\gamma_j\omega} \tag{E.40}$$

where $\omega = 1/\lambda$, ω_{pj}, ω_{0j} and γ_j are the strength, position and width of the jth oscillator, respectively.

By representing the RI (m) explicitly, Eq. (E.40) can be rewritten as two equations:

$$n^2 - k^2 = n_\infty^2 + \sum_j \frac{\omega_{pj}^2\left(\omega_j^2 - \omega^2\right)}{\left(\omega_j^2 - \omega^2\right)^2 + \gamma_j^2\omega^2} \tag{E.41}$$

$$-2nk = \sum_j \frac{\omega_{pj}^2\gamma_j\omega}{\left(\omega_j^2 - \omega^2\right)^2 + \gamma_j^2\omega^2} \tag{E.42}$$

Goodwin found that the region between 8-12 μm can be represented with three peaks by the following expressions:

$$\left(\frac{\omega_{p1}}{\omega_{0,1}}\right)^2 = (0.425 - 0.60X_{Fe2O3})\left(\frac{X_{SiO2}}{0.52}\right) \tag{E.43}$$

$$\left(\frac{\omega_{p2}}{\omega_{0,2}}\right)^2 = (0.175 + 0.75X_{Fe2O3})\left(\frac{X_{SiO2}}{0.52}\right) \tag{E.44}$$

$$\left(\frac{\omega_{p3}}{\omega_{0,3}}\right)^2 = (0.053)\left(\frac{X_{SiO}}{0.52}\right) \tag{E.45}$$

The parameters of the peaks are listed in Table E.8.

Table E.8 Fitting parameters for the multiple oscillator model

	$n_\infty{}^2$	$\omega_{0,j}$	γ_j
1st oscillation		1062.8	164.7
2nd oscillation	2.15	955.8	79.1
3rd oscillation		762	27.5

Finally, n and k can be found analytically by the following expressions:

$$n^2 - k^2 = n_\infty^2 + \sum_j \frac{\omega_{pj}^2 \left(\omega_j^2 - \omega^2\right)}{\left(\omega_j^2 - \omega^2\right)^2 + \gamma_j^2 \omega^2} = A \qquad (E.46)$$

$$2nk = \sum_j \frac{\omega_{pj}^2 \gamma_j \omega}{\left(\omega_j^2 - \omega^2\right)^2 + \gamma_j^2 \omega^2} = B \qquad (E.47)$$

$$n = \sqrt{\frac{A}{2} + \frac{\sqrt{A^2 + B^2}}{2}} \qquad (E.48)$$

$$k = \frac{B}{2\sqrt{\frac{A}{2} + \frac{\sqrt{A^2 + B^2}}{2}}} \qquad (E.49)$$

E.2.5. Calculation of Spectral Refractive (n) and Absorption (k) Indices between 13-20 μm

No experimental measurement is available for the wavelengths greater than 13 μm in Ebert's model. Nevertheless, according to the Goodwin's recommendation, mentioned in section E.1.5, optical properties of coal slags is dominated by the Reststrahlen bands of Al_2O_3 and MgO in this region. For this reason, RI for this wavelength region can simply be estimated by a simple summation rule as given below;

$$n(\lambda) = \sum x_i n_i(\lambda) \qquad (E.50)$$

$$k(\lambda) = \sum x_i k_i(\lambda) \qquad\qquad (E.51)$$

where the refractive and absorption indices of Al_2O_3 and MgO can be found in [233].

F. Derivation of Freeboard Particle Energy Balance

Estimation of the temperature profile of the particles along the freeboards of BFBCs is crucial for the evaluation of RHT in such systems. For this purpose, accurate treatment of particles distribution along the freeboard is of considerable importance for the modeling of BFBCs. The transfer of particles from the bed surface to the freeboard by the fluidizing gas is called entrainment. Among the entrained particles, large ones return to bed whereas the smaller ones may be carried out of the bed. This separation or fractionation of fines occurring up the freeboard is known as elutriation. Schematic representation of the transfer of particles from the bed surface into the freeboard is illustrated in Figure F.1.
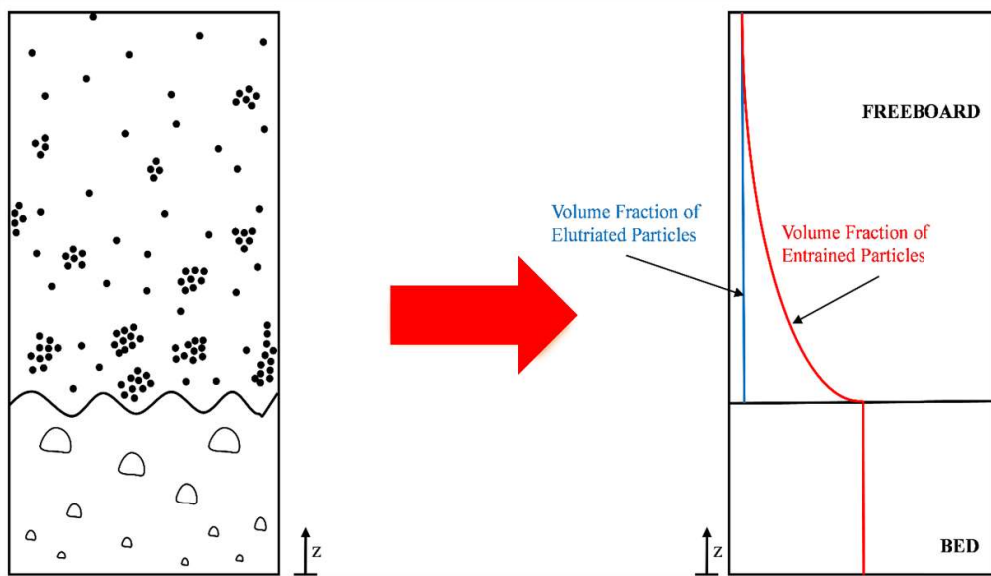
Figure F.1. Schematic representation of the transfer of particles from the bed surface into the freeboard

In this thesis study, the volume fraction of freeboard particles, consisting of fly ash and char, is taken to decrease exponentially with the decay constant a and as a function of freeboard height;

$$\frac{\varepsilon_p}{\varepsilon_{p,0}} = \exp(-a \times z_f) \tag{F.1}$$

The details of the treatment of particles distribution along the freeboard is given in section 3.2.1.

The char particles temperature profile along the freeboard can be calculated by the solution of an energy balance considering convective transport, heat generation due to char combustion and heat transfer between the particles and environment by convection and radiation. Noting that some particles fall back to the bed while others carried by the fluidizing gas, the steady-state energy conservation equation on a differential volume element of thickness Δz (shown in Figure F.2) can be written as;

$$\begin{aligned}
F_{z,d} C_{p,d}(T_d - T_r)\big|_z - F_{z+\Delta z,d} C_{p,d}(T_d - T_r)\big|_{z+\Delta z} \\
- (F_{z,d} - F_{z+\Delta z,d}) C_{p,d}(T_d - T_r)\big|_{z+\Delta z} - A_d h_p(T_d - T_f) \\
- A_f \Delta z(\nabla \cdot q_{r,d}) + A_d r_{C,f} \Delta H^o_{rxn} = 0
\end{aligned} \tag{F.2}$$

where $F_{z,d}$ is the flowrate of char particles at height z, T_d, T_f and T_r are the char particles, freeboard gas, and reference temperatures, respectively, $C_{p,d}$ is the specific heat capacity of char, A_f is the freeboard cross-sectional area, $\nabla \cdot q_{r,d}$ is the radiative ST due to char particles, $r_{C,f}$ and ΔH^o_{rxn} are the rate and reaction enthalpy of char combustion, respectively, and A_d is the total surface area of char particles.
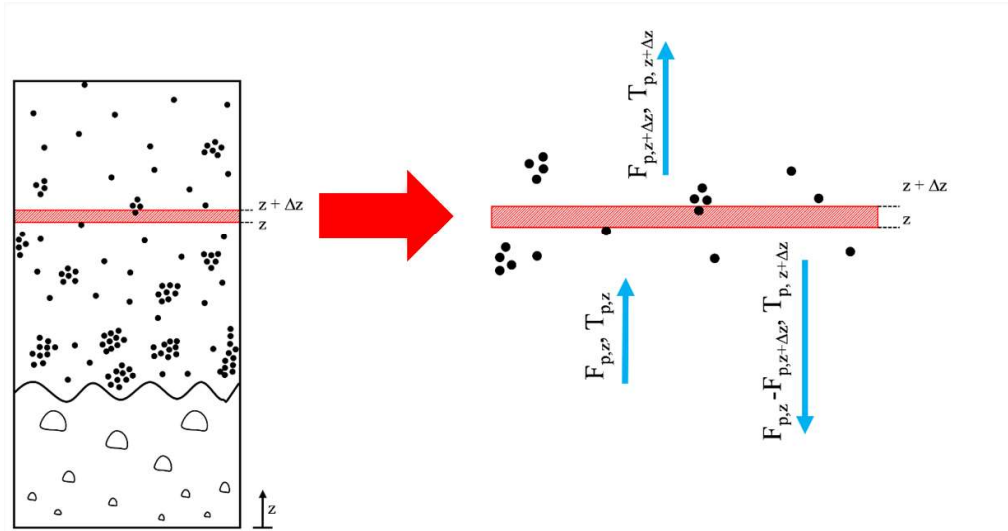
Figure F.2. Schematic representation of the transfer of particles from the bed surface into the freeboard

The char particles' total surface area, A_d, in the differential volume element can be defined as:

$$A_d = \left\{ \begin{array}{c} \text{Number of char} \\ \text{particles in} \\ \text{differential volume} \\ \text{element} \end{array} \right\} \times \left\{ \begin{array}{c} \text{Surface area of} \\ \text{a single char} \\ \text{particle} \end{array} \right\} \tag{F.3}$$

The above verbal form of char particles' total surface area can be rewritten as;

$$A_d = \frac{A_f \Delta z \varepsilon_d}{\frac{4}{3}\pi r_d^3} \times 4\pi r_c^2 = \frac{3 A_f \Delta z \varepsilon_d}{r_d} \tag{F.4}$$

where ε_d is volume fraction occupied by char particles and r_d is char particle radius. Noting that char particles are present in the freeboard with a size distribution, inserting Eq. (F.4) into Eq. (F.2) yields:

$$F_{z,d}C_{p,d}(T_d - T_r)\big|_z - F_{z,d}C_{p,d}(T_d - T_r)\big|_{z+\Delta z}$$

$$- 3A_f\Delta z \int_{r_{min}}^{r_{max}} \frac{\varepsilon_d P_{z,d}(r)}{r_d}h_p(T_d - T_f)dr - A_f\Delta z(\nabla \cdot q_{r,d})$$

$$+ 3A_f\Delta z \frac{x_{FC}}{x_{FC} + x_{ash}} \int_{r_{min}}^{r_{max}} \frac{\varepsilon_d P_{z,d}(r)}{r_d}r_{C,f}\Delta H_{rxn}^o dr = 0 \tag{F.5}$$

The particles in the freeboard are assumed to move upward with the superficial gas velocity. Noting that the freeboard particles consist of both elutriable fines and coarse particles carried by bursting bubbles, the differential form of the char particle energy conservation equation along the freeboard can then be obtained by dividing both sides of Eq. (F.5) by $A_f\Delta z$ and taking the limit as $\Delta z \to 0$.

$$\rho_d\varepsilon_d U_0 C_{p,d}\frac{dT_d}{dz_f} = -\int_{r_{max,e}}^{r_{max}} \frac{3\varepsilon_d P_{z,d}}{r_c}h_p(T_d - T_f)dr - \int_{r_{min}}^{r_{max,e}} \frac{3F_{CO,d}P_{z,d}(r)}{r_d U_0 A_f \rho_d}h_p(T_d - T_f)dr$$

$$- \nabla \cdot q_{r,d} + \frac{x_{FC}}{x_{FC} + x_{ash}} \int_{r_{max,e}}^{r_{max}} \frac{3\varepsilon_d P_{z,d}(r)}{r_d}\Re_{C,f}\Delta H_{rxn}^o dr$$

$$+ \frac{x_{FC}}{x_{FC} + x_{ash}} \int_{r_{min}}^{r_{max,e}} \frac{3F_{CO,d}P_{z,d}(r)}{r_d U_0 A_f \rho_d}\Re_{C,f}\Delta H_{rxn}^o dr \tag{F.6}$$

The radiative ST due to char particles, $\nabla \cdot q_{r,d}$, can be calculated from Eq. (F.7) after calculation of radiative intensity field along the freeboard by solving RTE.

$$\nabla \cdot q_{r,d} = \sum_j \kappa_{j,d}\left(4\pi I_{j,b,d} - \sum_m w_m I_j^m\right) \tag{F.7}$$

In a similar manner, the temperature profile of ash particles along the freeboard can be obtained by solving an energy balance considering convective transport and heat transfer between the particles and environment by convection and radiation:

$$\rho_i \varepsilon_i U_0 C_{p,i} \frac{dT_i}{dz_f} = - \int\limits_{r_{max,e}}^{r_{max}} \frac{3\varepsilon_i P_{z,i}(r)}{r_i} h_p(T_i - T_f) dr$$

$$- \int\limits_{r_{min}}^{r_{max,e}} \frac{3F_{CO,i}P_{z,i}(r)}{r_i U_0 A_f \rho_i} h_p(T_i - T_f) dr - \nabla \cdot q_{r,i} \qquad \text{(F.8)}$$

The radiative ST due to ash particles, $\nabla \cdot q_{r,i}$, can be calculated from Eq. (F.9) after calculation of radiative intensity field along the freeboard by solving RTE.

$$\nabla \cdot q_{r,i} = \sum_j \kappa_{j,i} \left(4\pi I_{j,b,i} - \sum_m w_m I_j^m \right) \qquad \text{(F.9)}$$

G. Estimation of Size Parameters of Rosin-Rammler Size Distribution Model Embedded in ANSYS Fluent

In the ANSYS Fluent software, the size distribution of discrete particles can be represented as a Rosin-Rammler size distribution function:

$$Y_d = e^{-(d/\bar{d})^n} \tag{G.1}$$

where Y_d is the mass fraction of particles with diameter greater than d, $\bar{d}$ is the mean diameter and n is the spread parameter. According to the ANSYS Fluent, the mean diameter ($\bar{d}$) is obtained at which $Y_d = e^{-1} = 0.368$. On the other hand, the spread parameter (n) is estimated by the following relation:

$$n = \frac{\ln(-lnY_d)}{\ln(d/\bar{d})} \tag{G.2}$$

In the Test 4 where the model developed using ANSYS Fluent is applied on, the size distribution of lignite particles fed to the 0.3 MW$_t$ test rig is listed in Table G.1.

Table G.1: PSD of lignite feed for Test 4

Sieve Opening (mm)	Differential Weight (%)	Y_d
19.000	0.00	0.00
16.000	0.00	0.00
12.700	1.08	0.01
8.000	3.04	0.04
6.300	4.90	0.09
4.750	6.10	0.15
3.350	16.86	0.32
2.000	13.57	0.46
1.000	21.48	0.67
0.500	10.85	0.78
0.355	5.82	0.84
0.180	5.55	0.89
0.106	4.09	0.93
0.000	6.66	1.00

Using the information in Table G.1, the mean diameter $(\bar{d})$ is obtained by simply using linear interpolation such that for $\bar{d}$, Y_d must be equal to $e^{-1} = 0.368$. For Test 4, the mean diameter $(\bar{d})$ is calculated as 2.87 mm. Furthermore, the spread parameter (n) can be found by fitting the experimental data provided in Table G.1 into the Eq. (G.2) as illustrated by Figure G.1. Finally, the spread parameter should be equal to the slope of the fitted line which is equal to 0.8766.
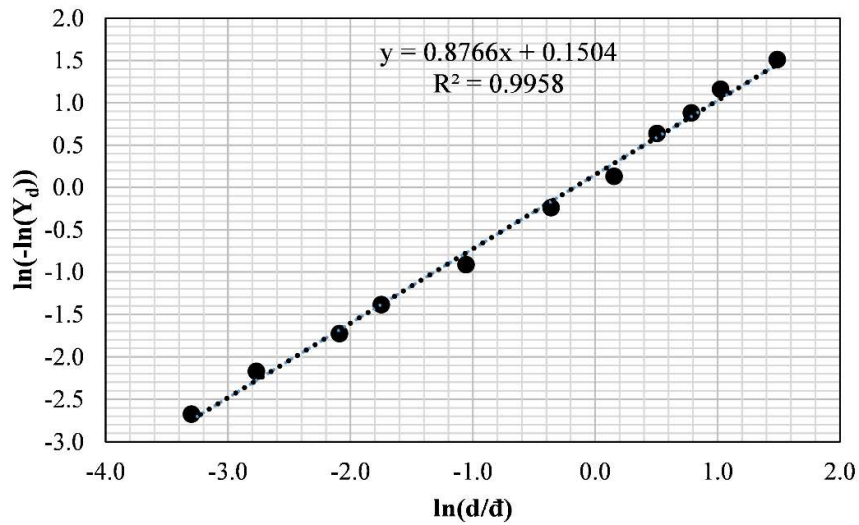
Figure G.1. The experimental size distribution data for the lignite particles used in Test 4 fitted into Eq. (G.2)

The size distribution function of lignite particle feed for Test 4 is then expressed by the following expression:

$$Y_d = e^{-(d/2.87)^{0.8766}} \tag{G.3}$$

The comparison of calculated and measured fuel inlet PSD is illustrated in Figure G.2.
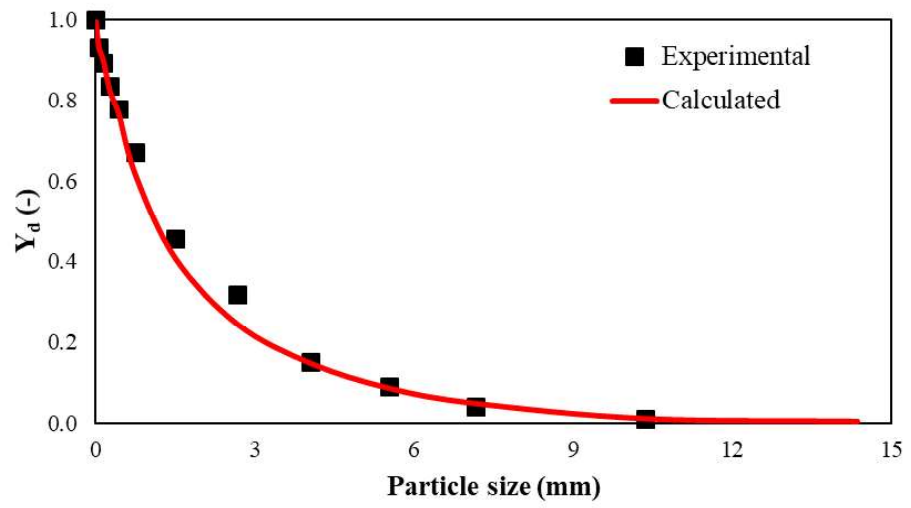
Figure G.2. Calculated and measured fuel inlet PSD for Test 4

H. Estimation of Soot Volume Fraction

The radiative properties of soot and their effect on RHT in BFBCs is investigated by applying the 3-D radiation model based on MOL solution of DOM to Test 5 only in which Çan lignite is burned with limestone addition. Soot particles are taken to be uniformly released only in the splash zone of the 0.3 MW_t ABFBC test rig based on a previous study observing formation of yellow diffusion flames at the bed surface [207]. Splash zone consists of coarse particles (particles with terminal velocities greater than the superficial gas velocity of 1.9 m/s for Test 5) carried by bubble eruption and fine particles. The coarse ones return to bed whereas the smaller ones may be carried out of the bed by the superficial gas velocity. Therefore, the upper limit of the splash zone can be considered as the point where the volume fraction of coarse particles drops to zero. The volume fraction of solid particles decreases exponentially from the surface of the bed as a function of distance with decay constant a;

$$\frac{\varepsilon_p}{\varepsilon_{p,0}} = exp(-a \times z_f) \tag{H.1}$$

where ε_s is the solids volume fraction and $\varepsilon_{s,0}$ is the solids volume fraction at the expanded bed height. Decay constant is estimated by utilizing empirical correlation adopted from Choi et al. [148] which accounts for the variations in gas velocity, column size, particle size, temperature and density;

$$a = \frac{1}{d_p} \times exp\left(-11.2 + 210\frac{d_p}{d_{bed} - d_p}\right) \times \left(\frac{d_p \rho_g (u_0 - u_{mf})}{\mu}\right)^{-0.492}$$

$$\times \left(\frac{d_p g \rho_p}{\rho_g (u_0 - u_{mf})^2}\right)^{0.725} \times \left(\frac{\rho_p - \rho_g}{\rho_g}\right)^{0.731} \times C_D^{-1.47} \tag{H.2}$$

The total volume fraction of solids just above the surface of the expanded bed height, $\varepsilon_{s,0}$, is obtained from;

$$\varepsilon_{p,0} = 1 - \varepsilon_f \tag{H.3}$$

Parameters, u_{mf} and ε_f, are calculated as 0.24 m/s and 0.58, respectively, based on modified two-phase theory which is described in detail in section 3.2.1. Empirical correlation suggested by Choi et al. [148], however, is originally developed for sand and leads to significant inaccuracies in the prediction of volume fraction of ash which is bed material in this study. Therefore, the decay constant is multiplied by 3.5 to comply with the measured particle load (B) at the freeboard exit (15 g/m³) which is calculated by;

$$B = \frac{F_{CO}}{u_0 \times A_f} \tag{H.4}$$

where F_{CO} is the carry over particle flowrate (sum of cyclone and bag filter particle flowrates), u_0 is the superficial gas velocity and A_f is the cross-sectional area of the freeboard. Similarly, the decay constant used for the estimation of coarse particles volume fraction along the freeboard is also multiplied by 3.5 in this study.

The volume fraction of coarse bottom ash particles (whose PSD is given in Appendix I), which represents the bed ash particles due to perfect mixing in the bed, are calculated along the freeboard based on Eq. (H.1). Volume fraction of coarse particle can be considered as negligible when it drops below 1 % of the particles volume fraction at the freeboard exit ($= B/\rho_p = 10^{-5}$). Therefore, that location is taken as the upper limit for splash zone.

Soot volume fraction in the splash zone is calculated by assuming all the tar is converted into soot particles [209];

$$f_v = \frac{M_{coal} x_{tar}(1 - x_{vl})}{u_0 \times A_f} \frac{1}{\rho_p} \tag{H.5}$$

where x_{tar} is the fraction of tar released during pyrolysis, x_{vl} is the fraction of volatiles released to the bed section, which is 0.78 [96], and ρ_p is the soot particles density which is taken as 2000 kg/m³ [231]. The fraction of tar released during

pyrolysis of coal depends on not only the characteristics of the coal but also chemical composition of coal ash due to catalytic effect of mineral content on tar formation [232]. Therefore, the tar content of the lignite under investigation in this study is taken to be 45 % of the volatile matter content based on a previous experimental study conducted on coal with similar characteristics (see Coal B in Ref. [232]).

I. PSD Measurements for the Combustion Tests

Table I.1: PSD of lignite feed for Test 1

Sieve Opening (mm)	Differential Weight (%)	Cumulative Weight (%)
8.000	0.00	100.00
6.300	0.33	99.67
4.750	7.63	92.04
3.350	28.06	63.98
2.360	18.28	45.70
1.700	19.45	26.25
1.180	6.38	19.87
0.850	5.82	14.05
0.600	3.58	10.47
0.425	2.33	8.14
0.300	1.86	6.28
0.180	2.84	3.44
0.000	3.44	0.00

Table I.2: PSD of bed drain ash for Test 1

Sieve Opening (mm)	Differential Weight (%)	Cumulative Weight (%)
6.700	0.00	100.00
6.300	0.00	100.00
4.750	0.46	99.54
3.350	5.33	94.21
2.360	7.78	86.43
2.000	8.65	77.78
1.700	10.93	66.85
1.180	13.99	52.86
0.850	27.05	25.81
0.600	20.42	5.39
0.425	4.77	0.62
0.300	0.50	0.12
0.180	0.04	0.08
0.000	0.08	0.00

Table I.3: PSD of cyclone ash for Test 1

Size (μm)	Cumulative Weight (%)	Size (μm)	Cumulative Weight (%)
2000.00	100.00	46.00	23.93
1700.00	99.98	37.80	18.78
1400.00	99.94	31.00	14.84
1180.00	99.89	25.50	11.82
1000.00	99.80	20.90	9.44
850.00	99.55	17.20	7.50
710.00	98.95	14.10	5.88
600.00	98.11	11.60	4.53
492.50	94.55	9.50	3.42
404.20	91.89	7.80	2.54
331.80	89.85	6.40	1.87
272.30	87.80	5.20	1.39
223.50	84.79	4.30	1.07
183.40	80.08	3.50	0.83
150.60	73.42	2.90	0.64
123.60	65.23	2.40	0.47
101.40	56.18	2.00	0.30
83.30	47.00	1.60	0.15
68.30	38.25	1.30	0.04
56.10	30.44	0.50	0.00

Table I.4: PSD of lignite feed for Test 2

Sieve Opening (mm)	Differential Weight (%)	Cumulative Weight (%)
4.000	0.00	100.00
3.350	11.47	88.53
2.360	20.22	68.31
2.000	17.74	50.57
1.700	16.77	33.80
1.400	8.50	25.30
1.180	7.22	18.08
1.000	7.69	10.39
0.850	2.50	7.89
0.710	1.98	5.91
0.600	0.93	4.98
0.500	0.61	4.37
0.425	0.28	4.09
0.300	0.78	3.31
0.250	0.79	2.52
0.000	2.52	0.00

Table I.5: PSD of bed drain ash for Test 2

Sieve Opening (mm)	Differential Weight (%)	Cumulative Weight (%)
4.000	0.00	100.00
3.350	0.41	99.59
2.360	1.10	98.49
2.000	2.45	96.04
1.700	3.99	92.05
1.400	3.78	88.27
1.180	4.55	83.72
1.000	20.56	63.16
0.850	18.28	44.88
0.710	20.56	24.32
0.600	14.22	10.10
0.500	6.64	3.46
0.425	2.66	0.80
0.300	0.40	0.40
0.250	0.11	0.29
0.000	0.29	0.00

Table I.6: PSD of cyclone ash for Test 2

Size (µm)	Cumulative Weight (%)	Size (µm)	Cumulative Weight (%)
1261.92	100.00	28.25	13.08
1124.68	99.89	25.18	12.27
1002.37	99.59	22.44	11.51
893.37	98.87	20.00	10.79
796.21	97.61	17.83	10.10
709.63	95.49	15.89	9.44
632.46	92.49	14.16	8.80
563.67	88.69	12.62	8.17
502.38	84.23	11.25	7.56
447.74	79.28	10.02	6.97
399.05	74.02	8.93	6.39
355.66	68.63	7.96	5.82
316.98	63.29	7.10	5.27
282.50	58.14	6.33	4.73
251.79	53.29	5.64	4.22
224.40	48.80	5.02	3.73
200.00	44.71	4.48	3.27
178.25	41.04	3.99	2.85
158.87	37.76	3.56	2.48
141.59	34.84	3.17	2.15
126.19	32.24	2.83	1.90
112.47	29.91	2.52	1.69
100.24	27.79	2.24	1.47
89.34	25.87	2.00	1.25
79.62	24.09	1.78	1.03
70.96	22.45	1.59	0.83
63.25	20.93	1.42	0.63
56.37	19.52	1.26	0.45
50.24	18.22	1.13	0.29
44.77	17.02	1.00	0.17
39.91	15.91	0.89	0.07
35.57	14.89	0.80	0.01
31.70	13.95	0.71	0.00

Table I.7: PSD of bag filter ash for Test 2

Size (μm)	Cumulative Weight (%)	Size (μm)	Cumulative Weight (%)
17.83	100.00	1.78	31.39
15.89	100.00	1.59	27.42
14.16	100.00	1.42	23.85
12.62	99.95	1.26	20.65
11.25	99.51	1.13	17.81
10.02	98.42	1.00	15.28
8.93	96.73	0.89	13.01
7.96	94.41	0.80	10.98
7.10	91.44	0.71	9.14
6.33	87.83	0.63	7.49
5.64	83.62	0.56	6.00
5.02	78.87	0.50	4.68
4.48	73.68	0.45	3.52
3.99	68.18	0.40	2.54
3.56	62.50	0.36	1.75
3.17	56.78	0.32	1.14
2.83	51.14	0.28	0.68
2.52	45.71	0.25	0.35
2.24	40.56	0.22	0.12
2.00	35.78	0.20	0.00

Table I.8: PSD of lignite feed for Test 3

Sieve Opening (mm)	Differential Weight (%)	Cumulative Weight (%)
4.000	0.00	100.00
3.350	11.47	88.53
2.360	20.22	68.31
2.000	17.74	50.57
1.700	16.77	33.80
1.400	8.50	25.30
1.180	7.22	18.08
1.000	7.69	10.39
0.850	2.50	7.89
0.710	1.98	5.91
0.600	0.93	4.98
0.500	0.61	4.37
0.425	0.28	4.09
0.300	0.78	3.31
0.250	0.79	2.52
0.000	2.52	0.00

Table I.9: PSD of bed drain ash for Test 3

Sieve Opening (mm)	Differential Weight (%)	Cumulative Weight (%)
4.000	0.00	100.00
3.350	1.47	98.53
2.360	6.14	92.39
2.000	8.96	83.43
1.700	14.89	68.54
1.400	12.83	55.71
1.180	7.60	48.11
1.000	21.38	26.73
0.850	10.02	16.71
0.710	8.85	7.86
0.600	4.28	3.58
0.500	2.22	1.36
0.425	0.69	0.67
0.300	0.31	0.36
0.250	0.10	0.26
0.000	0.26	0.00

Table I.10: PSD of cyclone ash for Test 3

Size (µm)	Cumulative Weight (%)	Size (µm)	Cumulative Weight (%)
1261.92	100.00	28.25	25.14
1124.68	100.00	25.18	23.36
1002.37	100.00	22.44	21.63
893.37	99.97	20.00	19.97
796.21	99.85	17.83	18.36
709.63	99.62	15.89	16.81
632.46	99.14	14.16	15.30
563.67	98.22	12.62	13.85
502.38	96.80	11.25	12.46
447.74	94.95	10.02	11.16
399.05	92.72	8.93	9.94
355.66	90.13	7.96	8.81
316.98	87.23	7.10	7.79
282.50	84.07	6.33	6.88
251.79	80.69	5.64	6.08
224.40	77.14	5.02	5.37
200.00	73.48	4.48	4.75
178.25	69.77	3.99	4.21
158.87	66.06	3.56	3.73
141.59	62.39	3.17	3.30
126.19	58.81	2.83	2.90
112.47	55.35	2.52	2.53
100.24	52.04	2.24	2.18
89.34	48.87	2.00	1.84
79.62	45.87	1.78	1.52
70.96	43.02	1.59	1.22
63.25	40.33	1.42	0.93
56.37	37.80	1.26	0.67
50.24	35.40	1.13	0.44
44.77	33.14	1.00	0.25
39.91	30.99	0.89	0.11
35.57	28.95	0.80	0.02
31.70	27.01	0.71	0.00

Table I.11: PSD of bag filter ash for Test 3

Size (µm)	Cumulative Weight (%)	Size (µm)	Cumulative Weight (%)
17.83	100.00	1.78	28.14
15.89	100.00	1.59	24.40
14.16	100.00	1.42	21.11
12.62	99.93	1.26	18.24
11.25	99.40	1.13	15.73
10.02	98.19	1.00	13.53
8.93	96.33	0.89	11.58
7.96	93.79	0.80	9.83
7.10	90.56	0.71	8.25
6.33	86.64	0.63	6.82
5.64	82.07	0.56	5.51
5.02	76.94	0.50	4.33
4.48	71.38	0.45	3.29
3.99	65.52	0.40	2.39
3.56	59.52	0.36	1.65
3.17	53.54	0.32	1.09
2.83	47.73	0.28	0.65
2.52	42.20	0.25	0.34
2.24	37.06	0.22	0.12
2.00	32.36	0.20	0.00

Table I.12: PSD of lignite feed for Test 4

Sieve Opening (mm)	Differential Weight (%)	Cumulative Weight (%)
19.000	0.00	100.00
16.000	0.00	100.00
12.700	1.08	98.92
8.000	3.04	95.88
6.300	4.90	90.99
4.750	6.10	84.88
3.350	16.86	68.02
2.000	13.57	54.46
1.000	21.48	32.98
0.500	10.85	22.13
0.355	5.82	16.31
0.180	5.55	10.75
0.106	4.09	6.66
0.000	6.66	0.00

Table I.13: PSD of bed drain ash for Test 4

Sieve Opening (mm)	Differential Weight (%)	Cumulative Weight (%)
8.000	0.00	100.00
6.300	0.00	100.00
4.750	0.12	99.87
3.350	4.14	95.73
2.000	6.57	89.16
1.000	47.07	42.10
0.500	37.19	4.90
0.355	4.58	0.33
0.180	0.10	0.22
0.106	0.05	0.18
0.000	0.18	0.00

Table I.14: PSD of cyclone ash for Test 4

Size (µm)	Cumulative Weight (%)	Size (µm)	Cumulative Weight (%)
1261.92	0.00	28.25	1.10
1124.68	0.00	25.18	1.05
1002.37	0.00	22.44	1.00
893.37	0.00	20.00	0.98
796.21	0.01	17.83	0.95
709.63	0.44	15.89	0.93
632.46	1.25	14.16	0.91
563.67	2.06	12.62	0.89
502.38	2.86	11.25	0.86
447.74	3.61	10.02	0.84
399.05	4.29	8.93	0.79
355.66	4.83	7.96	0.74
316.98	5.21	7.10	0.70
282.50	5.41	6.33	0.64
251.79	5.43	5.64	0.59
224.40	5.28	5.02	0.53
200.00	5.00	4.48	0.48
178.25	4.62	3.99	0.44
158.87	4.18	3.56	0.39
141.59	3.73	3.17	0.35
126.19	3.29	2.83	0.32
112.47	2.90	2.52	0.29
100.24	2.55	2.24	0.26
89.34	2.27	2.00	0.23
79.62	2.02	1.78	0.21
70.96	1.84	1.59	0.18
63.25	1.69	1.42	0.17
56.37	1.55	1.26	0.13
50.24	1.45	1.13	0.12
44.77	1.36	1.00	0.09
39.91	1.29	0.89	0.07
35.57	1.21	0.80	0.00
31.70	1.14	0.71	0.00

Table I.15: PSD of bag filter ash for Test 4

Size (μm)	Cumulative Weight (%)	Size (μm)	Cumulative Weight (%)
17.83	100.00	1.78	28.07
15.89	100.00	1.59	24.20
14.16	100.00	1.42	20.82
12.62	99.95	1.26	17.86
11.25	99.68	1.13	15.29
10.02	98.56	1.00	13.05
8.93	96.78	0.89	11.09
7.96	94.35	0.80	9.35
7.10	91.20	0.71	7.79
6.33	87.35	0.63	6.40
5.64	82.83	0.56	5.14
5.02	77.73	0.50	4.02
4.48	72.16	0.45	3.04
3.99	66.27	0.40	2.20
3.56	60.20	0.36	1.51
3.17	54.13	0.32	0.99
2.83	48.20	0.28	0.59
2.52	42.54	0.25	0.30
2.24	37.26	0.22	0.11
2.00	32.42	0.20	0.00

Table I.16: PSD of lignite feed for Test 5

Sieve Opening (mm)	Differential Weight (%)	Cumulative Weight (%)
19.000	0.00	100.00
16.000	0.00	100.00
12.700	2.03	97.97
8.000	8.43	89.53
6.300	9.24	80.30
4.750	10.41	69.89
3.350	23.38	46.51
2.000	13.27	33.24
1.000	14.16	19.08
0.500	5.55	13.53
0.355	2.69	10.84
0.180	2.56	8.29
0.106	2.68	5.61
0.000	5.61	0.00

Table I.17: PSD of bed drain ash for Test 5

Sieve Opening (mm)	Differential Weight (%)	Cumulative Weight (%)
8.000	0.00	100.00
6.300	0.58	99.42
4.750	1.46	97.96
3.350	9.27	88.69
2.000	11.48	77.21
1.000	36.11	41.10
0.500	31.48	9.62
0.355	8.80	0.83
0.180	0.55	0.28
0.106	0.09	0.19
0.000	0.19	0.00

Table I.18: PSD of cyclone ash for Test 5

Size (µm)	Cumulative Weight (%)	Size (µm)	Cumulative Weight (%)
1261.92	100.00	28.25	25.14
1124.68	100.00	25.18	23.36
1002.37	100.00	22.44	21.63
893.37	99.97	20.00	19.97
796.21	99.85	17.83	18.36
709.63	99.62	15.89	16.81
632.46	99.14	14.16	15.30
563.67	98.22	12.62	13.85
502.38	96.80	11.25	12.46
447.74	94.95	10.02	11.16
399.05	92.72	8.93	9.94
355.66	90.13	7.96	8.81
316.98	87.23	7.10	7.79
282.50	84.07	6.33	6.88
251.79	80.69	5.64	6.08
224.40	77.14	5.02	5.37
200.00	73.48	4.48	4.75
178.25	69.77	3.99	4.21
158.87	66.06	3.56	3.73
141.59	62.39	3.17	3.30
126.19	58.81	2.83	2.90
112.47	55.35	2.52	2.53
100.24	52.04	2.24	2.18
89.34	48.87	2.00	1.84
79.62	45.87	1.78	1.52
70.96	43.02	1.59	1.22
63.25	40.33	1.42	0.93
56.37	37.80	1.26	0.67
50.24	35.40	1.13	0.44
44.77	33.14	1.00	0.25
39.91	30.99	0.89	0.11
35.57	28.95	0.80	0.02
31.70	27.01	0.71	0.00

Table I.19: PSD of bag filter ash for Test 5

Size (µm)	Cumulative Weight (%)	Size (µm)	Cumulative Weight (%)
17.83	100.00	1.78	28.14
15.89	100.00	1.59	24.40
14.16	100.00	1.42	21.11
12.62	99.93	1.26	18.24
11.25	99.40	1.13	15.73
10.02	98.19	1.00	13.53
8.93	96.33	0.89	11.58
7.96	93.79	0.80	9.83
7.10	90.56	0.71	8.25
6.33	86.64	0.63	6.82
5.64	82.07	0.56	5.51
5.02	76.94	0.50	4.33
4.48	71.38	0.45	3.29
3.99	65.52	0.40	2.39
3.56	59.52	0.36	1.65
3.17	53.54	0.32	1.09
2.83	47.73	0.28	0.65
2.52	42.20	0.25	0.34
2.24	37.06	0.22	0.12
2.00	32.36	0.20	0.00

Table I.20: PSD of lignite feed for Test 6

Sieve Opening (mm)	Differential Weight (%)	Cumulative Weight (%)
19.000	0.00	100.00
16.000	0.00	100.00
12.700	0.46	99.54
8.000	4.45	95.09
6.300	7.98	87.11
4.750	10.38	76.73
3.350	26.06	50.67
2.000	14.10	36.58
1.000	15.25	21.32
0.500	6.14	15.18
0.355	3.17	12.01
0.180	3.30	8.72
0.106	3.95	4.77
0.000	4.77	0.00

Table I.21: PSD of OR feed for Test 6

Sieve Opening (mm)	Differential Weight (%)	Cumulative Weight (%)
19.000	0.00	100.00
16.000	0.00	100.00
12.700	0.00	100.00
8.000	0.00	100.00
6.300	0.00	100.00
4.750	0.13	99.87
3.350	11.97	87.91
2.000	21.51	66.40
1.000	20.84	45.56
0.500	13.60	31.96
0.355	9.31	22.64
0.180	9.33	13.32
0.106	6.18	7.14
0.000	7.14	0.00

Table I.22: PSD of bed drain ash for Test 6

Sieve Opening (mm)	Differential Weight (%)	Cumulative Weight (%)
8.000	0.00	100.00
6.300	0.63	99.37
4.750	1.76	97.62
3.350	10.24	87.38
2.000	11.30	76.08
1.000	28.82	47.27
0.500	33.93	13.34
0.355	12.31	1.03
0.180	0.85	0.18
0.106	0.18	0.00
0.000	0.00	0.00

Table I.23: PSD of cyclone ash for Test 6

Size (μm)	Cumulative Weight (%)	Size (μm)	Cumulative Weight (%)
1261.92	100.00	28.25	15.61
1124.68	100.00	25.18	14.56
1002.37	100.00	22.44	13.57
893.37	100.00	20.00	12.62
796.21	99.98	17.83	11.71
709.63	99.24	15.89	10.82
632.46	97.71	14.16	9.97
563.67	95.46	12.62	9.13
502.38	92.41	11.25	8.32
447.74	88.61	10.02	7.54
399.05	84.11	8.93	6.80
355.66	79.06	7.96	6.09
316.98	73.63	7.10	5.43
282.50	68.03	6.33	4.81
251.79	62.47	5.64	4.24
224.40	57.13	5.02	3.71
200.00	52.15	4.48	3.23
178.25	47.63	3.99	2.79
158.87	43.61	3.56	2.40
141.59	40.08	3.17	2.04
126.19	37.02	2.83	1.71
112.47	34.35	2.52	1.42
100.24	32.02	2.24	1.16
89.34	29.94	2.00	0.93
79.62	28.06	1.78	0.72
70.96	26.33	1.59	0.54
63.25	24.72	1.42	0.39
56.37	23.20	1.26	0.26
50.24	21.76	1.13	0.15
44.77	20.40	1.00	0.06
39.91	19.10	0.89	0.00
35.57	17.87	0.80	0.00
31.70	16.71	0.71	0.00

Table I.24: PSD of bag filter ash for Test 6

Size (µm)	Cumulative Weight (%)	Size (µm)	Cumulative Weight (%)
17.83	100.00	1.78	27.48
15.89	100.00	1.59	23.79
14.16	100.00	1.42	20.55
12.62	99.79	1.26	17.71
11.25	98.88	1.13	15.24
10.02	97.41	1.00	13.07
8.93	95.31	0.89	11.16
7.96	92.57	0.80	9.45
7.10	89.17	0.71	7.91
6.33	85.13	0.63	6.52
5.64	80.52	0.56	5.26
5.02	75.40	0.50	4.13
4.48	69.88	0.45	3.13
3.99	64.11	0.40	2.27
3.56	58.23	0.36	1.57
3.17	52.37	0.32	1.03
2.83	46.68	0.28	0.62
2.52	41.27	0.25	0.32
2.24	36.23	0.22	0.12
2.00	31.63	0.20	0.00

Table I.25: PSD of lignite feed for Test 7

Sieve Opening (mm)	Differential Weight (%)	Cumulative Weight (%)
19.000	0.00	100.00
16.000	0.00	100.00
12.700	1.27	98.73
8.000	5.06	93.67
6.300	7.10	86.57
4.750	7.81	78.76
3.350	18.75	60.01
2.000	13.20	46.81
1.000	17.78	29.03
0.500	9.07	19.96
0.355	4.93	15.04
0.180	5.17	9.86
0.106	3.50	6.37
0.000	6.37	0.00

Table I.26: PSD of HS feed for Test 7

Sieve Opening (mm)	Differential Weight (%)	Cumulative Weight (%)
19.000	0.00	100.00
16.000	0.00	100.00
12.700	9.04	90.96
8.000	64.45	26.51
6.300	13.87	12.63
4.750	5.84	6.79
3.350	5.16	1.64
2.000	0.63	1.00
1.000	0.31	0.70
0.500	0.19	0.51
0.355	0.00	0.51
0.180	0.06	0.45
0.106	0.00	0.45
0.000	0.45	0.00

Table I.27: PSD of bed drain ash for Test 7

Sieve Opening (mm)	Differential Weight (%)	Cumulative Weight (%)
8.000	0.00	100.00
6.300	1.21	98.79
4.750	2.28	96.51
3.350	10.48	86.03
2.000	10.39	75.64
1.000	26.56	49.08
0.500	36.11	12.97
0.355	12.24	0.73
0.180	0.34	0.39
0.106	0.05	0.34
0.000	0.34	0.00

Table I.28: PSD of cyclone ash for Test 7

Size (µm)	Cumulative Weight (%)	Size (µm)	Cumulative Weight (%)
1261.92	100.00	28.25	13.16
1124.68	100.00	25.18	12.15
1002.37	99.94	22.44	11.21
893.37	99.51	20.00	10.33
796.21	98.51	17.83	9.50
709.63	96.97	15.89	8.71
632.46	94.73	14.16	7.96
563.67	91.74	12.62	7.24
502.38	87.99	11.25	6.55
447.74	83.56	10.02	5.89
399.05	78.58	8.93	5.26
355.66	73.21	7.96	4.66
316.98	67.69	7.10	4.07
282.50	62.21	6.33	3.51
251.79	56.96	5.64	2.96
224.40	52.09	5.02	2.43
200.00	47.67	4.48	1.93
178.25	43.76	3.99	1.46
158.87	40.33	3.56	1.04
141.59	37.33	3.17	0.67
126.19	34.72	2.83	0.36
112.47	32.39	2.52	0.15
100.24	30.27	2.24	0.01
89.34	28.31	2.00	0.00
79.62	26.45	1.78	0.00
70.96	24.66	1.59	0.00
63.25	22.92	1.42	0.00
56.37	21.26	1.26	0.00
50.24	19.66	1.13	0.00
44.77	18.16	1.00	0.00
39.91	16.75	0.89	0.00
35.57	15.45	0.80	0.00
31.70	14.26	0.71	0.00

Table I.29: PSD of bag filter ash for Test 7

Size (µm)	Cumulative Weight (%)	Size (µm)	Cumulative Weight (%)
17.83	100.00	1.78	28.11
15.89	100.00	1.59	24.24
14.16	100.00	1.42	20.85
12.62	99.95	1.26	17.91
11.25	99.68	1.13	15.36
10.02	98.59	1.00	13.14
8.93	96.86	0.89	11.20
7.96	94.48	0.80	9.48
7.10	91.38	0.71	7.94
6.33	87.58	0.63	6.55
5.64	83.10	0.56	5.29
5.02	78.03	0.50	4.16
4.48	72.47	0.45	3.16
3.99	66.56	0.40	2.29
3.56	60.47	0.36	1.59
3.17	54.36	0.32	1.04
2.83	48.38	0.28	0.63
2.52	42.68	0.25	0.33
2.24	37.36	0.22	0.12
2.00	32.49	0.20	0.00

Table I.30: PSD of lignite feed for Test 8

Sieve Opening (mm)	Differential Weight (%)	Cumulative Weight (%)
19.000	0.00	100.00
16.000	0.00	100.00
12.700	1.09	98.91
8.000	3.79	95.12
6.300	5.16	89.97
4.750	6.15	83.82
3.350	16.31	67.51
2.000	13.34	54.17
1.000	21.00	33.17
0.500	11.41	21.76
0.355	6.19	15.58
0.180	6.44	9.14
0.106	3.72	5.42
0.000	5.42	0.00

Table I.31: PSD of CR feed for Test 8

Sieve Opening (mm)	Differential Weight (%)	Cumulative Weight (%)
19.000	0.00	100.00
16.000	1.67	98.33
12.700	6.35	91.98
8.000	31.65	60.33
6.300	12.52	47.81
4.750	7.60	40.22
3.350	14.56	25.65
2.000	7.90	17.76
1.000	7.90	9.86
0.500	2.99	6.87
0.355	0.00	6.87
0.180	5.50	1.37
0.106	0.00	1.37
0.000	1.37	0.00

Table I.32: PSD of bed drain ash for Test 8

Sieve Opening (mm)	Differential Weight (%)	Cumulative Weight (%)
8.000	0.00	100.00
6.300	0.87	99.14
4.750	2.67	96.46
3.350	10.96	85.50
2.000	9.78	75.73
1.000	26.18	49.55
0.500	42.89	6.65
0.355	5.96	0.69
0.180	0.24	0.45
0.106	0.13	0.32
0.000	0.32	0.00

Table I.33: PSD of cyclone ash for Test 8

Size (µm)	Cumulative Weight (%)	Size (µm)	Cumulative Weight (%)
1261.92	100.00	28.25	13.02
1124.68	100.00	25.18	12.08
1002.37	100.00	22.44	11.20
893.37	100.00	20.00	10.36
796.21	99.97	17.83	9.56
709.63	99.05	15.89	8.78
632.46	97.23	14.16	8.03
563.67	94.64	12.62	7.30
502.38	91.16	11.25	6.60
447.74	86.84	10.02	5.92
399.05	81.79	8.93	5.26
355.66	76.18	7.96	4.63
316.98	70.24	7.10	4.03
282.50	64.21	6.33	3.44
251.79	58.34	5.64	2.89
224.40	52.82	5.02	2.36
200.00	47.78	4.48	1.86
178.25	43.31	3.99	1.40
158.87	39.43	3.56	0.99
141.59	36.11	3.17	0.63
126.19	33.27	2.83	0.34
112.47	30.84	2.52	0.14
100.24	28.72	2.24	0.01
89.34	26.82	2.00	0.00
79.62	25.07	1.78	0.00
70.96	23.43	1.59	0.00
63.25	21.86	1.42	0.00
56.37	20.36	1.26	0.00
50.24	18.93	1.13	0.00
44.77	17.57	1.00	0.00
39.91	16.31	0.89	0.00
35.57	15.13	0.80	0.00
31.70	14.03	0.71	0.00

Table I.34: PSD of bag filter ash for Test 8

Size (μm)	Cumulative Weight (%)	Size (μm)	Cumulative Weight (%)
17.83	100.00	1.78	28.77
15.89	100.00	1.59	24.94
14.16	100.00	1.42	21.55
12.62	99.94	1.26	18.57
11.25	99.42	1.13	15.95
10.02	98.24	1.00	13.65
8.93	96.41	0.89	11.72
7.96	93.92	0.80	9.81
7.10	90.73	0.71	8.18
6.33	86.88	0.63	6.72
5.64	82.39	0.56	5.40
5.02	77.35	0.50	4.22
4.48	71.87	0.45	3.19
3.99	66.10	0.40	2.31
3.56	60.18	0.36	1.59
3.17	54.26	0.32	1.04
2.83	48.48	0.28	0.62
2.52	42.96	0.25	0.32
2.24	37.80	0.22	0.11
2.00	33.06	0.20	0.00

CURRICULUM VITAE

Surname, Name: Yaşar, Mehmet Soner

EDUCATION

Degree	Institution	Year of Graduation
MS	METU Chemical Engineering	2018
BS	METU Chemical Engineering	2016
High School	Kırkkonaklar Anadolu High School, Ankara	2009

FOREIGN LANGUAGES

Advanced English

PUBLICATIONS

1. Yasar M.S., Ozen G., Selçuk N. and Kulah G. " Effect of Particle Size Distribution and Complex Refraction Index of Alumina on Infrared Rocket Plume Signatures", Combustion Science and Technology, 00, 1-16 (2023)

2. Yasar M.S., Selçuk N. and Kulah G. "Coupling of Spectral Thermal Radiation Model with a Comprehensive System Model for Co-Combustion of Biomass in Bubbling Fluidized Bed", Fuel, 333(2), 126534 (2023)

3. Yasar M.S., Selçuk N. and Kulah G. "Performance and Validation of a Radiation Model Coupled with a Transient Bubbling Fluidized Bed Combustion Model", International Journal of Thermal Sciences, 176, 107496 (2022)

4. Yasar M.S., Selçuk N. and Kulah G. " Modeling of Fluidized Bed Combustion of Lignite with High Nitrogen Content Cotton Residue", Combustion Science and Technology, 194(2), 435-448 (2022)

5. Yasar M.S., Selçuk N. and Kulah G. "Influence of Soot on Radiative Heat Transfer in Bubbling Fluidized Bed Combustors", Journal of Quantitative Spectroscopy and Radiative Transfer, 270, 107711 (2021)

6. Yasar M.S., Selçuk N. and Kulah G. "Influence of Bag Filter Ash to Spectral Thermal Radiation in Fluidized Bed Combustors Co-Fired with Biomass", International Journal of Thermal Sciences, 167, 107012 (2021)

7. Yasar M.S., Ozen G., Selçuk N. and Kulah G. "Performance of Banded SLW-1 in Presence of Non-Gray Walls and Particles in Fluidized Bed Combustors", Journal of Quantitative Spectroscopy and Radiative Transfer, 257, 107370 (2020)

8. Yasar M.S., Ozen G., Selçuk N. and Kulah G. "Assessment of Improved Banded Model for Spectral Thermal Radiation in Presence of Non-Gray Particles in Fluidized Bed Combustors", Applied Thermal Engineering, 176, 115322 (2020)

Computer Technologies, Movies, Books, Calligraphy